CHARLES UNIVERSITY

Faculty of Science

Department of Physical and Macromolecular Chemistry

STRUCTURAL STUDIES OF SELECTED SIGNALING PROTEIN COMPLEXES

Strukturní studie vybraných komplexů signálních proteinů

RNDr. Katarína Pšenáková

Doctoral thesis

of study program Physical Chemistry

Supervisor: prof. RNDr. Tomáš Obšil, Ph.D.

Consultants: RNDr. Veronika Obšilová, Ph.D.

Ing. Václav Veverka, Ph.D.

Prague 2018

Prohlášení

Prohlašuji, že jsem tuto disertační práci vypracovala samostatně pod vedením mého školitele prof. RNDr. Tomáše Obšila, Ph.D. a všechny použité informační zdroje a literaturu jsem řádně citovala. Tato práce ani její podstatná část nebyla předložena k získání jiného nebo stejného akademického titulu.

V Praze, dne 13.12.2018

_____

Podpis

Poďakovanie

Najväčšie poďakovanie patrí môjmu školiteľovi Tomášovi Obšilovi, za jeho nikdy nekončiacu podporu a za všetko, čo do mňa tak trpezlivo a vytrvalo vštepoval. Po viac než šiestich rokoch práce pod jeho vedením viem, že vedecká kariéra nie je prechádzka ružovou záhradou, ale napriek tomu je to najkrajšie povolanie sveta.

Podľa Studijního řádu sú povinnosti konzultanta doplňovať odborné pôsobenie školiteľa. Moji konzultanti Veronika Obšilová a Václav Veverka toho pre mňa ale robili omnoho viac. Chcela by som poďakovať Veronike za jej láskavý prístup a finančnú podporu. Moje veľké ďakujem patrí tiež Václavovi, za jeho dokonale nezištnú a nikdy neutíchajúcu pomoc a za všetko, čo ma naučil a čo pre mňa urobil.

Moji kolegovia sú moji superhrdinovia. Vždy zachraňujú situáciu, pomáhajú mi a podporujú ma, kde sa len dá a to všetko vždy s úsmevom a láskou. Olívia Petrvalská, Salome Kylarová, Rozálie Hexnerová, Pavel Srb, Lukáš Vrzal, Zdeněk Tošner, Jan Blahút, Klára Kohoutová, Miroslava Alblová, Dana Kalábová, Aneta Šmídová, Markéta Kolcunová, Matej Horváth, Domenico Lentini Santo, Miroslava Kacířová a Dalibor Košek, ďakujem vám za všetko, čo ste pre mňa celé tie roky robili.

Neexistuje nikto na svete, kto by vo mňa veril tak veľmi, ako moji rodičia. Môj doktorský titul patrí mne rovnako, ako vám. Ďakujem.

ABSTRAKT

Schopnost proteinů vázat jiné molekuly v reakci na různé podněty ve svém mikrookolí je základem rozsáhlých regulačních sítí, které koordinují následnou činnost buněk. Správná funkce těchto signálních drah závisí převážně na nekovalentních interakcích, které často ovlivňují strukturu proteinů a proteinových komplexů. Pochopení molekulárního mechanismu funkce proteinu v buněčné signalizaci je proto často závislé na znalosti jeho trojdimenzionální struktury.

V této disertační práci představuji studie, které vedly na molekulární úrovni k pochopení několika protein-proteinových a ligand-proteinových interakcí podílejících se na buněčné signalizaci. Použila jsem nukleární magnetickou rezonanci (NMR), malo-úhlový rozptyl rentgenového záření (SAXS) a další biofyzikální metody pro určení molekulární podstaty inhibice čtyř signálních proteinů: vápník/kalmodulin (Ca^{2+}/CaM)-dependentní proteinkinasy kinasy 2 (CaMKK2); proteasy kaspasa-2; forkhead transkripčního faktoru FOXO3 a proteinkinasy ASK1.

Konkrétněji byla zkoumána role proteinu 14-3-3 a CaM v regulaci CaMKK2 aktivity. Dále byl detailně studován mechanizmus, jakým protein 14-3-3 ovlivňuje schopnost oligomerizace a jaderné lokalizace kaspasy-2 a také byla objasněna podstata modulace transkripční aktivity FOXO transkripčních faktorů díky zkoumání inhibičních schopností malé organické sloučeniny vážící se na DNA-vazbovou doménu proteinu FOXO3. Strukturní studie komplexu TRX vazebné domény proteinkinasy ASK1 s TRX odhalily, že TRX interaguje s ASK1 prostřednictvím redox-aktivního místa a oxidační stres způsobuje strukturní změny na vazebném rozhraní v komplexu ASK1 s TRX. To naznačuje, že oxidace ASK1 je důležitým regulačním signálem pro disociaci komplexu.

Disertační práce poskytuje přehled o vztahu mezi porozuměním molekulárním mechanismům modulace aktivity signálních proteinů a znalostí strukturních detailů jejich složitých interakcí. Integrovaný interdisciplinární přístup potom poukazuje na nové příležitosti oboru studia biologických struktur, kde tradiční metody již dosáhly svých hranic.

ABSTRACT

The ability of proteins to bind other molecules in response to various stimuli in their microenvironment serves as a platform for extensive regulatory networks coordinating downstream cell actions. The correct function of these signaling pathways depends mostly on noncovalent interactions often affecting the structure of proteins and protein complexes. Understanding the molecular mechanism of a protein function in cell signaling therefore often depends on our knowledge of a three-dimensional structure.

In this doctoral thesis, I present the work that led to the understanding of several protein-protein and protein-ligand interactions implicated in cell signaling at the molecular level. I applied nuclear magnetic resonance spectroscopy, small angle X-ray scattering and other biophysical methods to determine the molecular basis of inhibition of four signaling proteins: Calcium/Calmodulin (Ca^{2+}/CaM)-dependent protein kinase kinase 2 (CaMKK2); protease Caspase-2; Forkhead transcription factor FOXO3, and Apoptosis signal-regulating protein kinase 1 (ASK1). In particular, I investigated the distinct roles of 14-3-3 and Ca^{2+}/CaM in the regulation of CaMKK2 activity. I also studied in detail the mechanism how 14-3-3 interferes with the caspase-2 oligomerization and its nuclear localization as well as provided a basis for transcriptional activity modulation of FOXO transcription factors by investigating a small-molecule compound binding to the DNA-binding domain of FOXO3. The structural studies of the complex between TRX binding domain of ASK1 and TRX revealed that TRX interacts with ASK1 through its redox active site and the oxidation induces structural changes in the ASK1 TRX binding interface, suggesting that the ASK1 oxidation is an important regulatory signal for the complex dissociation.

This doctoral thesis provides a comprehensive insight into the intriguing relationship between understanding the molecular mechanisms of activity modulation of signaling proteins and the knowledge of structural details of their complex interactions. The integrative interdisciplinary approach used in this work points at the new opportunities in the world of biological structures, where the traditional methods have already reached their limits.

ABBREVIATIONS

AID ..... Autoinhibitory domain
ASK1 ..... Apoptosis signal-regulating kinase 1
ATP ..... Adenosine triphosphate
CaM ..... Calmodulin
CaMK ..... Ca^{2+}/calmodulin-dependent protein kinase
CaMKK ..... Ca^{2+}/calmodulin-dependent protein kinase kinase
CARD ..... Caspase activation and recruitment domain
CBD ..... Calmodulin binding domain
CD ..... Catalytic domain
CCC ..... C-terminal coiled-coil domain
CRR ..... Central regulatory region
DBD ..... DNA binding domain
ER ..... Endoplasmic reticulum
ERK ..... Extracellular signal-regulated kinase
Eq. ..... Equation
FAD ..... Flavin adenine dinucleotide
Fig. ..... Figure
FOXO ..... Forkhead boxO
HPLC ..... High performance liquid chromatography
JNK ..... c-Jun N-terminal kinase
KD ..... Kinase domain
LPS ..... Lipopolysaccharide molecules
MAPK ..... Mitogen-activated protein kinase
MKK ..... Mitogen-activated kinase kinase
MS ..... Mass spectrometry
NADPH ..... Nicotinamide adenine dinucleotide phosphate
NES ..... Nuclear export sequence
NLS ..... Nuclear localization sequence
NMR ..... Nuclear magnetic resonance

P .....Phosphorylated

P_i .....Inorganic phosphate

PH .....Pleckstrin homology domain

pSer .....Phosphoserine

pThr.....Phosphothreonine

ROS.....Reactive oxygen species

SAXS .....Small angle X-ray scattering

SEC .....Size exclusion chromatography

Tab. .....Table

TBD .....Thioredoxin-1 binding domain

TNFα.....Tumor necrosis factor α

TPR .....Tetratricopeptide repeats

TRAF .....TNF receptor-associated factors

TRX Thioredoxin-1

UV.....Ultraviolet

LIST OF PUBLICATIONS

1. **Psenakova, K.,** Petrvalska, O., Kylarova, S., Lentini, D., Kalabova, D., Herman, P., Obsilova, V. & Obsil, T. 14-3-3 protein directly interacts with the kinase domain of calcium/calmodulin-dependent protein kinase kinase (CaMKK2). *Biochim. Biophys. Acta - Gen. Subj.* **1862**, 1612–1625 (2018).

2. Kylarova, S., **Psenakova, K.,** Herman, P., Obsilova, V. & Obsil, T. CaMKK2 kinase domain interacts with the autoinhibitory region through the N-terminal lobe including the RP insert. *Biochim. Biophys. Acta - Gen. Subj.* **1862**, 2304–2313 (2018).

3. Smidova, A., Alblova, M., Kalabova, D., **Psenakova, K.,** Rosulek, M., Herman, P., Obsil, T. & Obsilova, V. 14-3-3 Protein Masks the Nuclear Localization Sequence of Caspase-2. *FEBS J.* **285**, 4196–4213 (2018).

4. Hagenbuchner, J., Obsilova, V., Kaserer, T., Rass, B., **Psenakova, K.,** Docekal, V., Alblova, M., Kohoutova, K., Spoden, G., Schuster, D., Aneichyk, T., Kofler, R., Vesely, J., Obexer, P., Obsil, T. & Ausserlechner, M.J. Modulation of FOXO3 transcriptional activity by small molecule inhibitors. *Submitted*

5. Kylarova, S., Kosek, D., Petrvalska, O., **Psenakova, K.,** Man, P., Vecer, J., Herman, P., Obsilova, V. & Obsil, T. Cysteine residues mediate high-affinity binding of thioredoxin to ASK1. *FEBS J.* **283**, 3821–3838 (2016).

6. **Psenakova, K.,** Hexnerova, R., Srb, P., Veverka, V., Obsilova, V. & Obsil, T. Integrative structure of the Thioredoxin-binding domain of ASK1 reveals new details in molecular mechanism of the ASK1 activation. *Manuscript in preparation*

Further publications:

Kosek, D., Kylarova, S., **Psenakova, K.,** Rezabkova, L., Herman, P., Vecer, J., Obsilova, V. & Obsil, T. Biophysical and structural characterization of the thioredoxin-binding domain of protein kinase ASK1 and its interaction with reduced thioredoxin. *J. Biol. Chem.* **289**, 24463–24474 (2014).

This work was supported by the Czech Science Foundation (Projects 14-10061S, 16-02739S, 17-00726S, 17-33854L) and the Grant Agency of the Charles University (Project 368216).

TABLE OF CONTENTS

1 INTRODUCTION

1.1 14-3-3 protein

14-3-3 protein belongs to a family of regulatory molecules abundantly expressed in all eukaryotic cells in all tissues. It is a dimeric, acidic and highly conserved 30 kDa protein with seven isoforms identified in mammals (β, γ, ε, ζ, η, σ and τ).[1] 14-3-3 has been first identified in 1965 during the systematic analysis of proteins from bovine brain samples, its name originated from the 14th position of elution fraction and 3.3 coordinates of the starch gel electrophoresis containing the 14-3-3 protein.[2]

Through numerous protein-protein interactions, 14-3-3 can affect a function of many structurally different proteins, playing a key role in cell cycle control, metabolism, apoptosis, or cell signaling.[3] The dimeric molecule of 14-3-3 protein is exclusively *α*-helical; each monomer contains nine antiparallel helices (H1-H9), of those the H3, H5, H7 and H9 helices form an amphipathic binding groove creating a large central channel (*Fig. 1.1*).[1,4] Although there is a high percentage of sequence homology and minimal structural alterations between individual isoforms, they differ in the disordered C-terminal 15-40 amino acid stretch, allowing for a variability in interaction capabilities.[5]

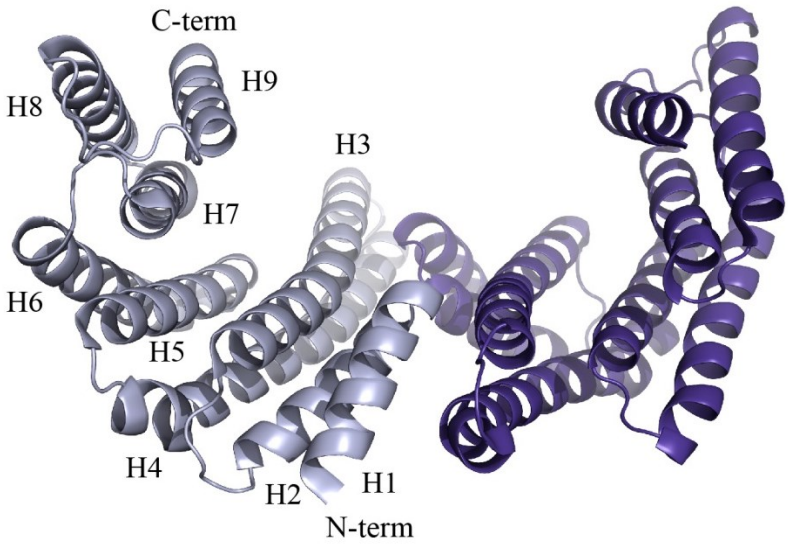

Figure 1.1. X-ray structure of a 14-3-3ζ dimer.[6] Each monomer contains nine antiparallel helices (labeled H1-H9). PDB: 1IB1

1.2 Apoptosis signal-regulating kinase 1

Apoptosis signal-regulating kinase 1 (ASK1) is a human protein kinase at the top of the mitogen-activated protein kinase (MAPK) cascade, the signal transduction pathway that form a cell defense system against stressors. MAPKs are serine/threonine-specific protein kinases with a phosphorylation-dependent activation. The MAPK cascade includes three subgroups characterized in mammals: Extracellular signal-regulated kinase (ERK), p38 MAPK and c-Jun N-terminal kinase (JNK) (*Fig. 1.2*). ERK pathway is regulated by growth factors and is implicated in cell cycle progression, proliferation and differentiation; p38 and JNK pathways respond to environmental stress stimuli such as reactive oxygen species (ROS), UV irradiation, osmotic stress or heat shock, mostly by activating cellular apoptotic processes.[7] ASK1 phosphorylates and activates its downstream targets, MKK3 or MKK6 and MKK4 or MKK7, initiating the p38 and JNK signaling pathways, respectively.[8]

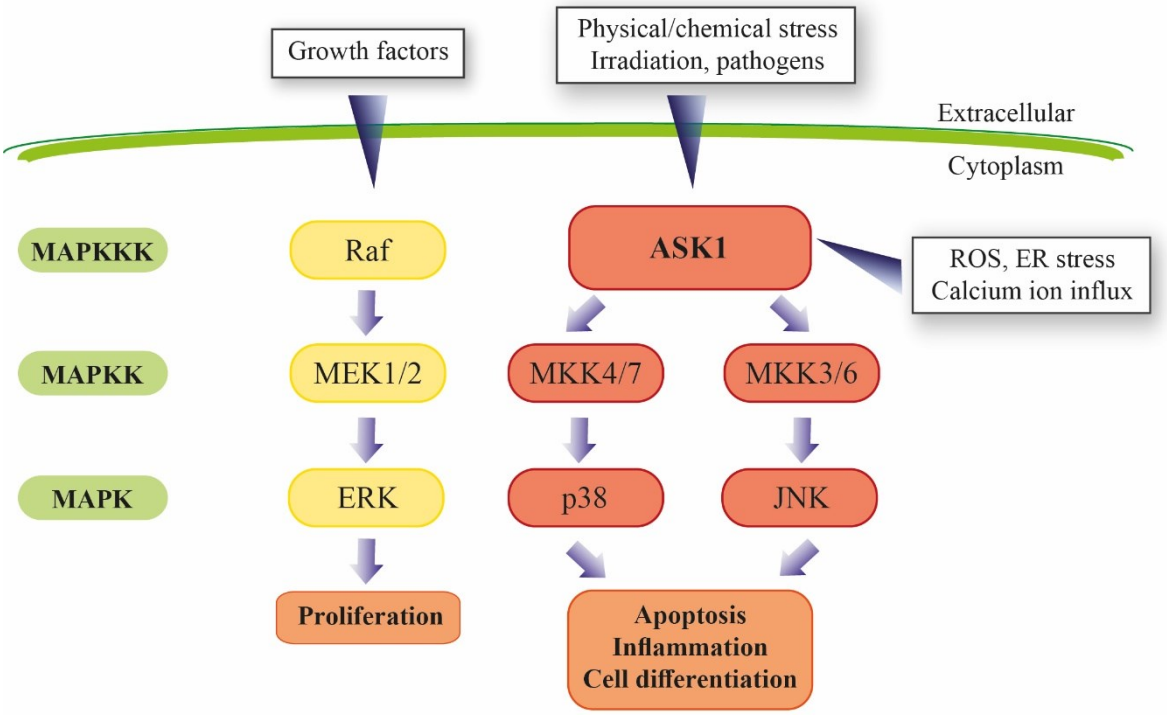

Figure 1.2. Scheme of the MAP kinase signaling pathway. Several extracellular and intracellular stressors activate MAP3Ks that phosphorylate and activate MAP2Ks, further phosphorylating and activating MAPK. The MAPK cascade includes Extracellular signal-regulated kinase (ERK), p38 and c-Jun N-terminal kinase (JNK). Adapted from [9].

In the cell, ASK1 detects ROS and its primary cellular function is the maintenance of a redox balance. Enhanced expression and activation of ASK1 can lead to apoptosis and has been associated with many different diseases; however under suitable circumstances it can also support cell differentiation and survival.[10] The deregulation of ASK1 has been implicated in tumorigenesis, cardiovascular and neurodegenerative diseases, inflammatory and infectious diseases, diabetes, asthma and ageing.[11]

Human ASK1 has a molecular mass of 155 kDa and consists of 1374 amino acids that form three domains (*Fig. 1.3*). The thioredoxin (TRX) binding domain (TBD) found at the N-terminal part of the ASK1 molecule consists of amino acid residues 46-277; the central regulatory region (CRR) and the catalytic domain (CD) of ASK1 are located in the central part of the molecule and include amino acid residues 278-658 and 659-941, respectively. The 14-3-3 binding motif requires phosphorylation on phosphoserine pSer[966], which is located between the CD and C-terminal coiled-coil domain (CCC).[12–14]

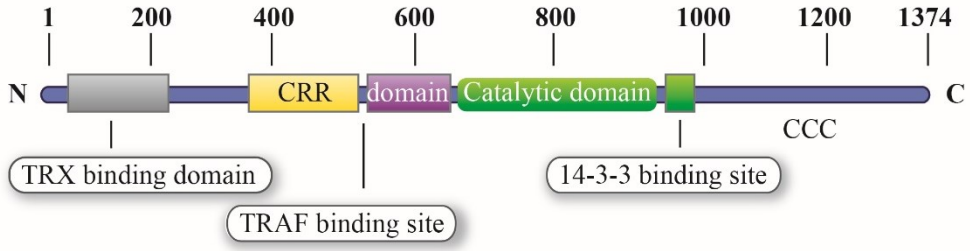

Figure 1.3. ASK1 domain organization. Numbers correspond to the amino acid sequence. The thioredoxin (TRX) binding domain is located at the N-terminus of ASK1, the tumor necrosis factor receptor-associated factor (TRAF) binding site is located in the middle of the central regulatory region (CRR) and the 14-3-3 binding site is located between the catalytic domain and the C-terminal coiled-coil domain (CCC). CRR is divided into two subdomains: tetratricopeptide repeats (yellow part) and a pleckstrin homology domain (violet part). Adapted from [12].

The high resolution structures of the individual ASK1 domains were obtained only for the CD and CRR in 2007 and 2017, respectively (*Fig. 1.4 A, B*).[12,13] The crystal structure of the CD was solved in a complex with staurosporine and revealed a typical kinase fold with the three autophosphorylation sites spontaneously phosphorylated in the presence of ATP and magnesium cations. However, it has been suggested that the

phosphorylation does not directly regulate the catalytic activity of ASK1, but is rather required for the interaction with binding partners.[12] The crystal structure of CRR was solved 10 years later and revealed 14 α-helices arranged into the seven tetratricopeptide repeats (TPR) with a compact and globular conformation followed by a pleckstrin homology (PH) domain with a highly hydrophobic interface.[13]

Structure of the ASK1-TBD complex and the molecular mechanism of the ASK1 inhibition remains unknown, the individual ASK1 domain configuration based on SAXS measurements suggests that the TBD is in the proximity to the CD and the bound TRX may directly inhibit the kinase activity by steric blocking (*Fig. 1.5 C*).[13]

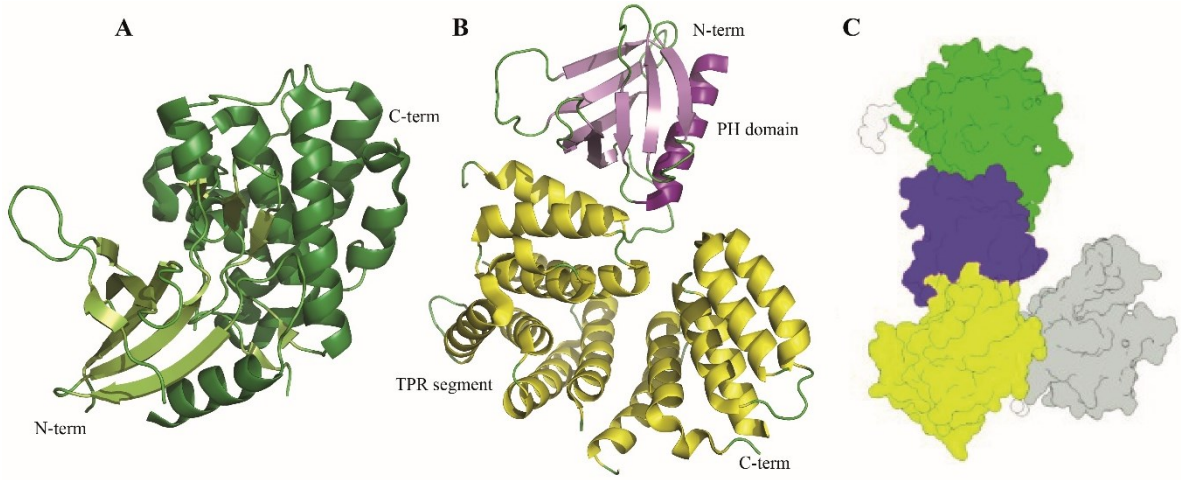

Figure 1.4. ASK1 CD and CRR structure. A) X-ray structure of the catalytic domain (CD) of ASK1.[12] The crystal structure of the CD with a typical kinase fold was solved in a complex with staurosporine. PDB: 2CLQ **B)** X-ray structure of the central regulatory region (CRR).[13] The crystal structure of CRR revealed 14 α-helices in seven tetratricopeptide repeats (TPR - yellow) segment followed by a pleckstrin homology (PH - violet) domain. PDB: 5ULM **C)** Surface representation of the individual ASK1 domain configuration based on SAXS measurements. ASK1-TBD (gray) is in a close vicinity to CD (green), the TPR segment (yellow) is followed by a PH domain (violet). Adapted from [13].

Under reducing conditions, ASK1 directly self-associates through its CCC, forming an inactive oligomeric conformation known as "ASK1 signalosome". In this complex, TRX bound to the kinase's N-terminal part and 14-3-3 bound to the C-terminus ensure the inactive state of the kinase, however the molecular mechanism of the ASK1 activation process is unclear.[15] The typical 14-3-3 binding motif RS[966]ISLP in the ASK1 molecule is located in a close proximity to the CD, thus probably affecting the active site accessibility by a conformational change and/or steric blocking.[16] However, the molecular mechanism of the TRX biding is unknown because of the lack of structural data.

The currently accepted mechanism of the ASK1 activation suggests that oxidative stress causes an intramolecular disulfide bridge formation in the TRX molecule, followed by its immediate dissociation from the complex (*Fig. 1.5*). It results in the 14-3-3 dissociation allowing the recruitment of the two tumor necrosis factor receptor-associated factors TRAF2 and TRAF6 by the CRR. That induces an open conformation of the CRR resulting in the activation loop autophosphorylation and the active kinase.[13,14,17–21] However, the actual mechanism of the ASK1 activation is not yet fully understood.

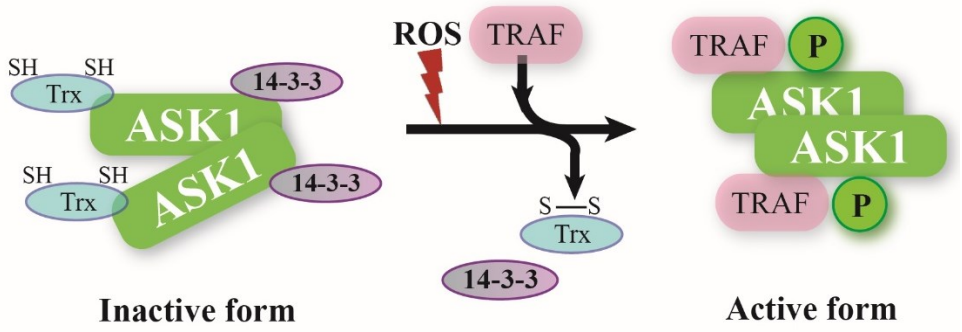

Figure 1.5. Putative model of the ASK1 activation. The ASK1 dimer is homo-oligomerized through the CCC domain; its activity is inhibited by the TRX binding at the N-terminus and 14-3-3 binding at the C-terminus. Reactive oxygen species (ROS) cause dissociation of both TRX and 14-3-3, the binding site is approached by TRAF and the phosphorylated (P) catalytic domain activates ASK1 signaling pathway. Adapted from [22].

1.3 Thioredoxin

Thioredoxins are small 12kDa globular oxidoreductases found from archaea to mammals. They carry two conserved cysteine residues that easily accept and donate electrons establishing the double-catalytic redox active site.[23] Under oxidative conditions, dithiols are reversibly oxidized to disulfides and reduced back to thiols, maintaining the intracellular redox state. In reducing cell environment, the disulfide bridge in the active site of TRX is reduced by FAD-containing thioredoxin reductase, allowing the electron transfer from nicotinamide adenine dinucleotide phosphate (NADPH) to many crucial enzymes, mostly regulating cell proliferation and survival (*Fig. 1.6 A*).[24,25] There are two known mammalian isoforms of thioredoxin: thioredoxin-1 (here denoted as TRX), the essential redox regulator in the cytoplasm and thioredoxin-2, a much less studied isoform preferentially localized in mitochondria.[26,27]

TRX plays an essential role in many key cellular processes including regulation of transcription factors with cysteine residues in the DNA binding site. The change in their redox status directly activates or inhibits the DNA binding, synthesis or repair, and therefore influencing cell differentiation and morphogenesis in embryogenesis. In addition to cytoplasmic proteins dependent on the TRX-derived antioxidant system, it has been found out that TRX can be translocated to the cell nucleus upon oxidation, affecting also the cell proliferation, growth simulation, gene transcription, chemotaxis and apoptosis.[28]

The central core of TRX is formed by a β-sheet with three parallel and two antiparallel β-strands decorated by one longer and three shorter α-helices (*Fig. 1.6 B*).[29] The disulfide ring with a redox active motif consists of 14 amino acids from the C-terminus of $\beta 2$ to the N-terminal part of long $\alpha 2$ helix. Under oxidizing conditions, the disulfide bridge within the catalytic site is formed between Cys^{32} and Cys^{35}; however upon stronger oxidation pressure, there is an additional disulfide bridge formed between Cys^{62} and Cys^{69} that cannot be reduced directly by the TRX reductase.[28]

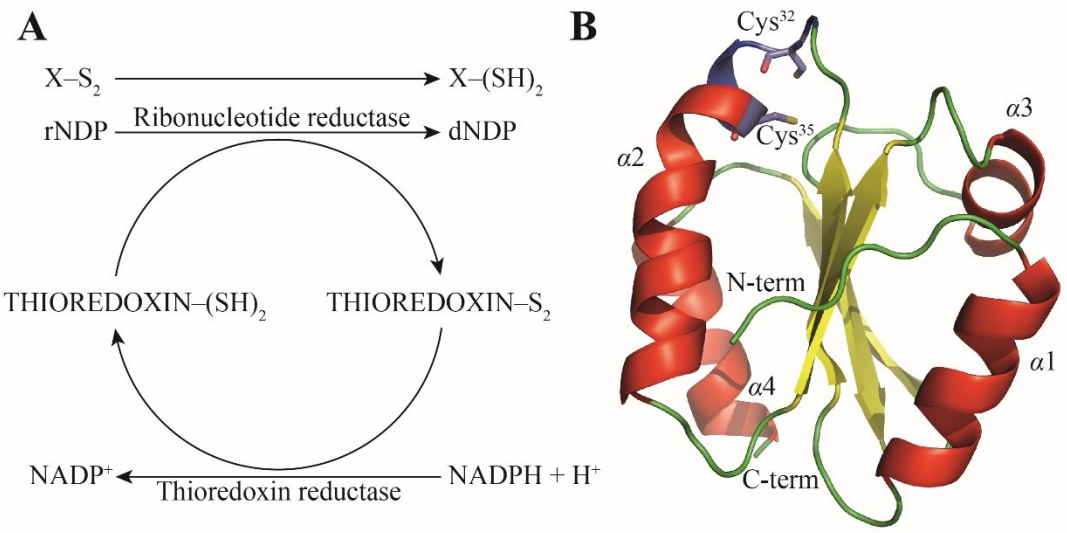

Figure 1.6. A) Electron transport system. TRX facilitates the reduced environment by transferring electrons in a cyclic electron transport process. Adapted from [29,30]. **B) X-ray structure of a reduced TRX.**[31] The TRX structure consists of a central β-sheet decorated by four α-helices. The redox active site $WC^{32}GPC^{35}$ is highlighted in blue. PDB: 1ERT

1.4 Calmodulin

Calcium-modulated protein calmodulin (CaM) is an abundant signaling protein conserved in eukaryotes, where it senses the intracellular Ca^{2+} level. Ca^{2+}/CaM complex determines the initial cellular response to a Ca^{2+} level change by specifically interacting with more than 120 enzymes from most classes of cellular proteins: kinases, phosphatases, plasma membrane Ca^{2+}-ATPase, transcription factors or voltage-gated calcium channels.[32] CaM is a 17 kDa protein with the N- and C-terminal globular domains connected by a relatively long and highly flexible α-helical linker (*Fig. 1.7*).[33] At the resting state, calcium cations bind to four EF-hand motifs with micromolar affinities that increase with the presence of target substrate.[34] The compact and closed structure of the CaM apo-form is extended and opened upon the Ca^{2+} binding with the two α-helices in the EF-hand motifs changing their orientation and exposing amino acids from the hydrophobic cavity.[35] The methyl groups from phenylalanines and methionines are then involved in the interaction with an amphiphilic α-helix from the targeted protein. The substrate binding causes the

CaM hydrophobic pocket to wrap around the target molecule and it simultaneously unfolds the central α-helical linker to form a flexible loop.[36]

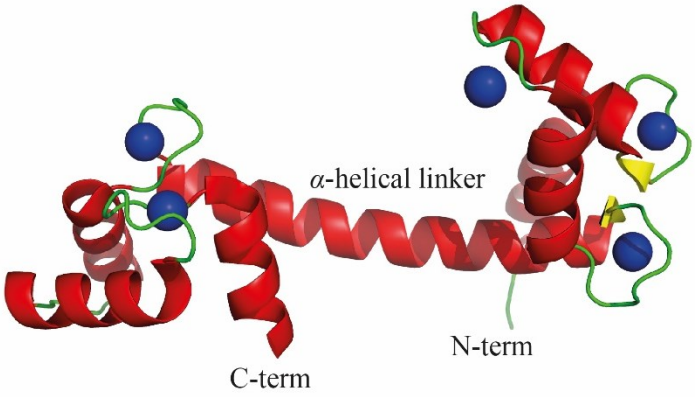

Figure 1.7. X-ray structure of CaM with bound Ca^{2+} ions.[33] The N- and C-terminal globular domains are connected by a flexible α-helical linker. Calcium cations (blue) bind to four EF-hand motifs, the fifth binding site is non-physiological crystallographic artefact. PDB: 1ERT

CaM binding sites and interaction modes are characterized by an immense structural diversity that allows Ca^{2+}/CaM complex to control a large basis of important cellular processes, such as apoptosis, muscle contraction, cell proliferation and fertilization in eukaryotes.[37]

1.5 Ca^{2+}/CaM-dependent protein kinase kinase 2

The Ca^{2+}/CaM-dependent protein kinase kinase 2 (CaMKK2) is a member of the Ca^{2+}/CaM-dependent kinase (CaMK) signaling cascade and belongs to the family of Ser/Thr protein kinases with a similar domain configuration: kinase domain (KD) bearing the catalytic site is followed by the autoinhibitory domain (AID) partially overlapped by the CaM binding domain (CBD) (*Fig. 1.8*).[38] At low intracellular calcium concentrations, the AID interacts with the catalytic site and sterically blocks the KD. The Ca^{2+} influx causes the Ca^{2+}/CaM binding to the CBD, inducing a substantial conformational change releasing the AID binding from the KD and activating the kinase.[39] In the active state, CaMKKs specifically phosphorylate Thr residues inside the activation segment of the two physiological substrates: CaMKI and CaMKIV.[38]

There are two human isoforms on the top of the calcium signaling cascade: CaMKK1 and CaMKK2. Although they are highly sequentially homologous, with the 65% sequence identity and the 80% similarity, CaMKK2 differs in its autonomous activity and in regulating another important substrate, AMP-activated protein kinase (AMPK).[40]

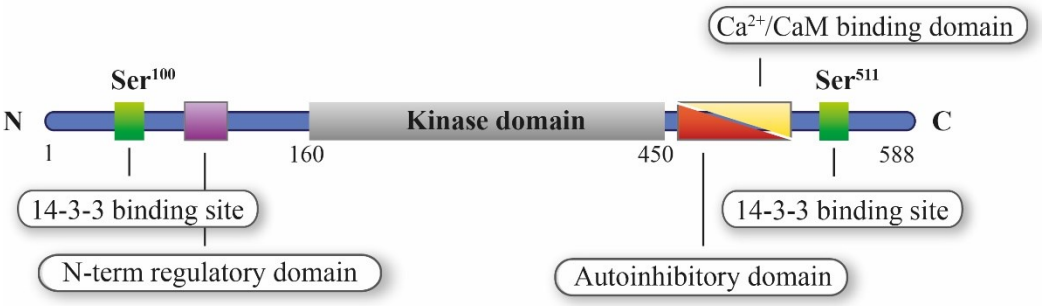

Figure 1.8. Domain organization of CaMKK2. The kinase domain is followed by the autoinhibitory domain that partially overlaps with the Ca^{2+}/CaM binding domain. The N-terminal (N-term) regulatory domain contains three sites phosphorylated by protein kinase GSK3 and CDK5. Ser^{100} and Ser^{511} are the predicted 14-3-3 binding sites. Adapted from [41].

CaMKK2 is therefore one of the most versatile CaMKs, responding to upstream extracellular signals such as insulin from the pancreas, adipogenic stimuli from the white adipose tissue (WAT) and lipopolysaccharide (LPS), amino acids, hormones or glucose from the circulation (*Fig. 1.9*) (reviewed in [32]). Activation of CaMKI is involved in the regulation of a cell growth, axonal elongation or memory formation. CaMKK2-dependent activation of AMPK leads to a regulation of energy balance in the brain, liver or adipose tissue. The whole-body energy homeostasis is then controlled by the CaMKK2 activity, which coordinates actions of the key metabolic pathways involved in an adaptive thermogenesis or muscle hypertrophy (*Fig. 1.10*). Regulation of the CaMKIV activity results in control of protein synthesis and gene expression programs responsive to nutrients and hormones.[32]

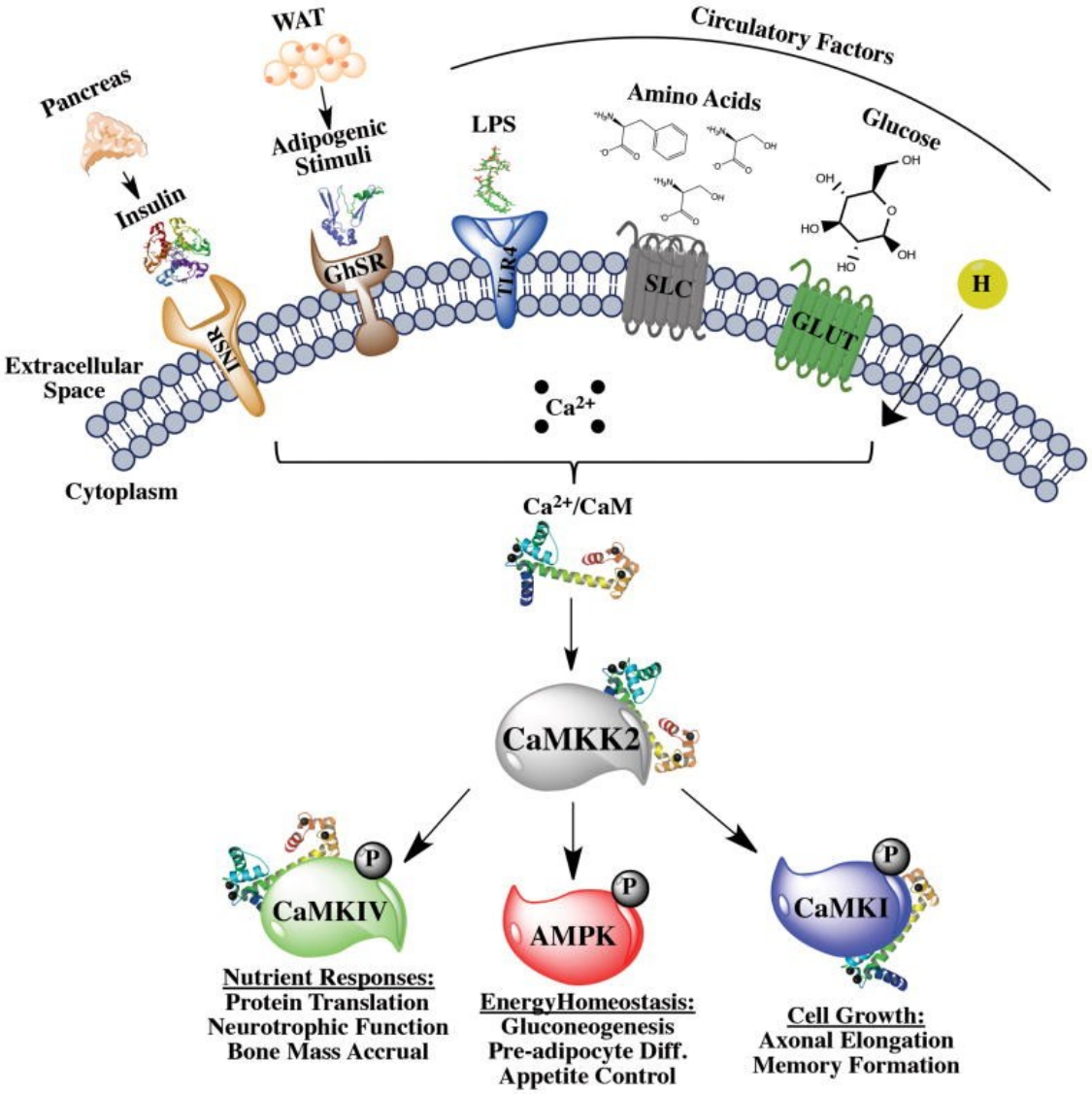

Figure 1.9. The Ca^{2+}/CaM-dependent kinase cascade.[32] CaMKK2 responds to extracellular signals such as insulin from pancreas, adipogenic stimuli from white adipose tissue (WAT) and lipopolysaccharide (LPS), amino acids, hormones or glucose from the circulation. Activation of CaMKI is involved in the regulation of cell growth, AMPK leads to the regulation of energy balance, a regulation of CaMKIV results in control of nutrient and hormone responses. Adapted from [32].

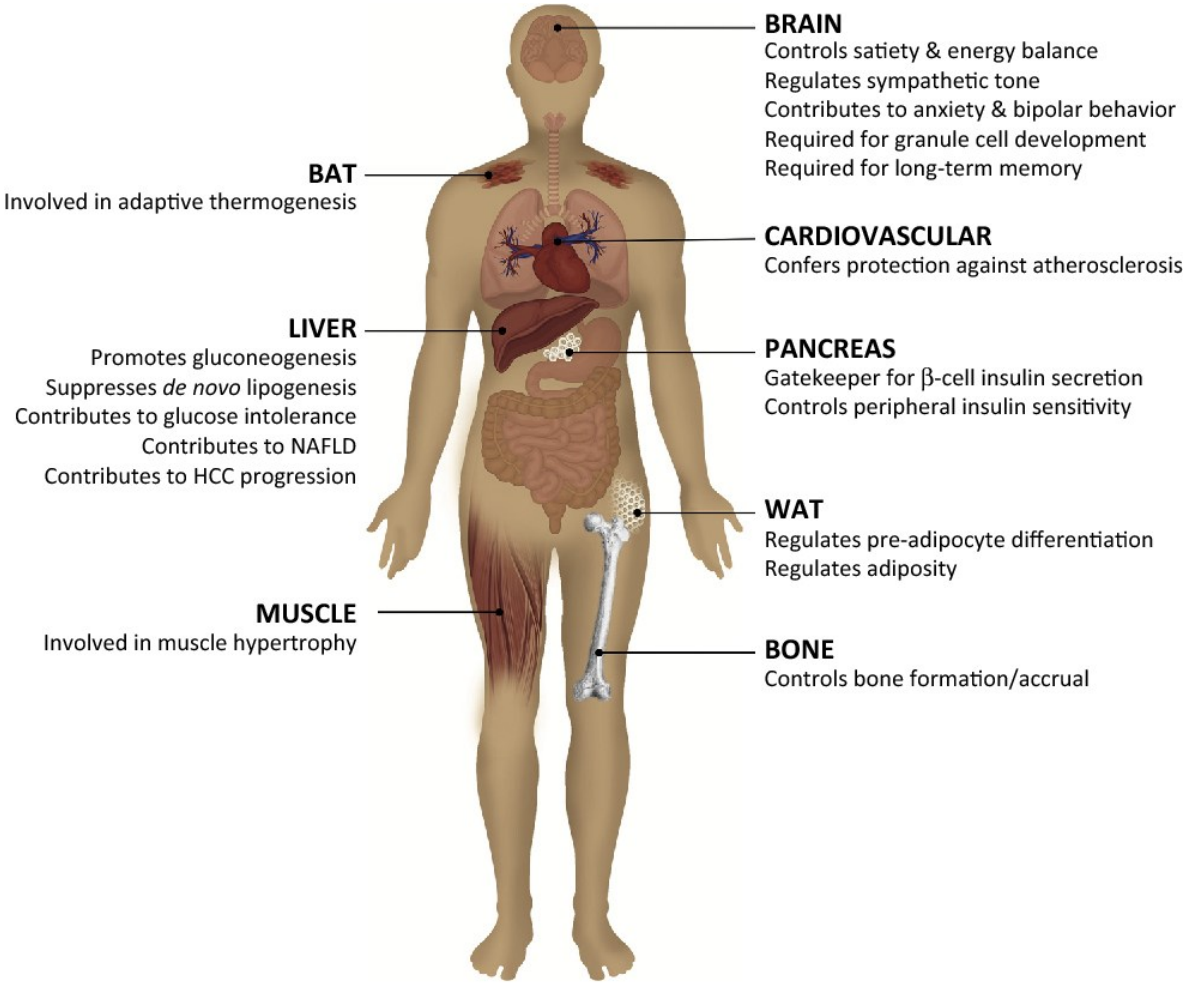

Figure 1.10. The role of CaMKK2 in energy homeostasis.[32] CaMKK2 regulates the whole-body energy homeostasis through coordinating key processes in metabolic tissues. Adapted from [32].

The human isoform of CaMKK2 is a 65 kDa protein; the high-resolution structure has been solved only for the KD (amino acids 158-448) in a complex with its specific ATP-competitive inhibitor STO-609 (*Fig. 1.11 A*).[42] The catalytic domain has a typical protein kinase fold, however the structure revealed unique properties when compared to other CaMKs. The CaMKK2 structure lacks αD helix formed by the conserved Pro residues in other CaMKs, the helical turn is replaced by β5-αE loop with a more hydrophobic substrate binding surface (*Fig. 1.11 B*).[42] In contrast to the structures obtained for CaMKI and CaMKII, the CaMKK2 conformation appeared in a closed form, characteristic for the kinase active state. However, the intrinsically active state of CaMKK2 has been preserved,

even though the proposed phosphorylation sites within the activation loop were not phosphorylated, unlike in many other protein kinases.[43] In the case of CaMKK2 structure, it is because of the Asn^{346} that is spatially equivalent to phosphothreonine and the conserved Phe^{331} within the activation loop stabilizes the catalytically important Lys^{194} and Glu^{236} interaction.[42]

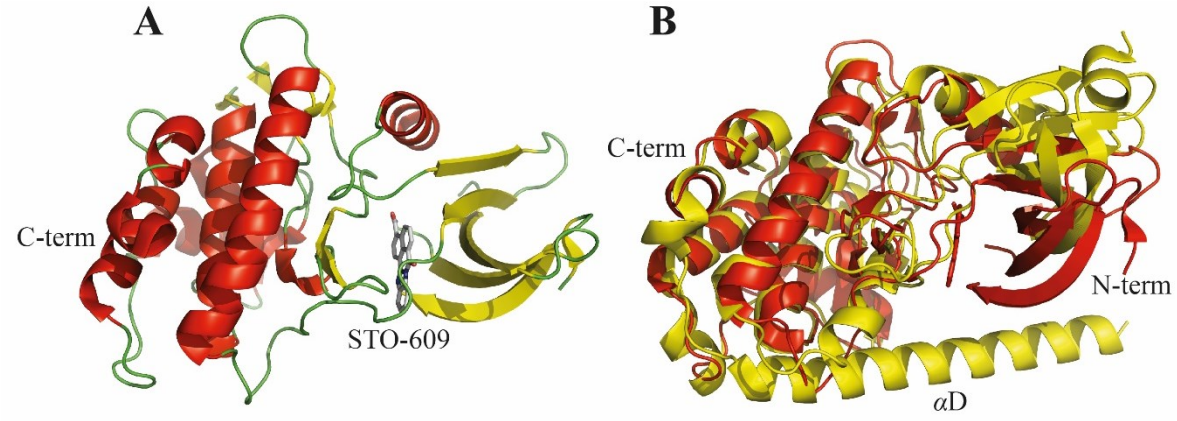

Figure 1.11. A) Crystal structure of the CaMKK2 kinase domain with bound inhibitor STO-609.[42] PDB: 2ZV2 **B) Superposition of CaMKK2 KD (red) with CaMKII KD (yellow).** The CaMKII structure adopts open conformation, opposite to CaMKK2 that misses αD helix. PDB: 2BDW

One of the most important differences in biological function of CaMKK1 and CaMKK2 are in their regulation. The CaMKK1 is strictly inhibited by the AID that is released by the Ca^{2+}/CaM binding to the CBD. CaMKK2 has an autonomous kinase activity independent of the Ca^{2+}/CaM binding. The autocatalytic mechanism is regulated by the three conserved autophosphorylation sites at the N-terminal loop (amino acids 124-142).[44] When these sites are phosphorylated, the Ca^{2+}/CaM-independent kinase activity is prevented and the regulation depends on the phosphorylation status. This regulatory region is sequentially targeted and phosphorylated by the cyclin-dependent kinase 5 (CDK5) and glycogen synthase kinase 3 (GSK3), while one phosphorylation site is recognized by cAMP-dependent protein kinase (PKA).[44,45]

In addition to autoinhibitory mechanisms, both isoforms CaMKK1 and CaMKK2 are partially inhibited by the PKA-dependent phosphorylation and consequently by the 14-3-3 binding. PKA phosphorylates five sites in the CaMKK1 and four sites in the CaMKK2 sequence.[44] The N-terminal phosphorylation regulates interactions of the substrates; the C-terminal phosphorylation blocks the binding of a Ca^{2+}/CaM complex. The two PKA-dependent phosphorylation sites in CaMKK1 and CaMKK2 are also the 14-3-3 binding sites; however the function of 14-3-3 and its involvement in CaMKKs inhibition are not yet fully understood. In the case of CaMKK1, the 14-3-3 binding inhibits the N-terminal dephosphorylation, thus keeping the kinase in the PKA-inhibited state.[46] In addition, it has also been shown that the binding to 14-3-3 decreases the maximum velocity of the kinase suggesting the allosteric modulation of the enzymatic activity.[47]

1.6 Caspase-2

Caspases belong to the family of cysteine endoproteases that cleave target substrates at the site following an aspartic acid residue. Mammalian caspases play a crucial role in the initiation of apoptosis (initiator and executor caspases) and in inflammatory cytokine signaling (inflammatory caspases).[48] All caspases are initially produced as catalytically inactive zymogens called procaspases. Initiator or upstream procaspases become activated after aggregation into dimers or macromolecular complexes followed by the self-cleavage. Executor or downstream procaspases are dimeric molecules that are cleaved by upstream caspases into the three domains: non-active prodomain and an active complex containing p20 and p10 subunits.[49,50]

Caspase-2 is one of the most evolutionary conserved initiator caspases. When activated, it triggers a proteolytic cascade cleaving downstream caspases and mitochondrial, plasma membrane or nuclear proteins, executing apoptotic cell death processes. More than 15 caspase-2 substrates have been identified to date, some of them implicated in human pathophysiology and tumorigenesis. From a functional point of view, caspase-2 influences the metabolic imbalance or DNA damage-induced cell death and endoplasmic reticulum stress response (reviewed in [51]).

The procaspase-2 (proC2) is a 45 kDa protein and its structure consists of the N-terminal caspase activation and recruitment domain (CARD), large subunit p19 and

small subunit p12 (*Fig. 1.12 A*).[52] The fully active enzyme caspase-2 is formed by a noncovalent heterodimer with two p19 and two p12 subunits, the crystal structure of the active caspase-2 has been obtained for the complex with its inhibitor acetyl-Leu-Asp-Glu-Ser-Asp-aldehyde (*Fig. 1.12 B*).[53] The CARD domain mediates a dimerization process and subsequent autoactivation. The domain configuration and structure is analogous to other initiator caspases, however endogenous caspase-2 differs from other caspases in the cell localization.[54] The C-terminus of the prodomain contains a linker between CARD and p19 domains with classical nuclear localization sequence (NLS) that is responsible for import of the protease into nucleus.[55]

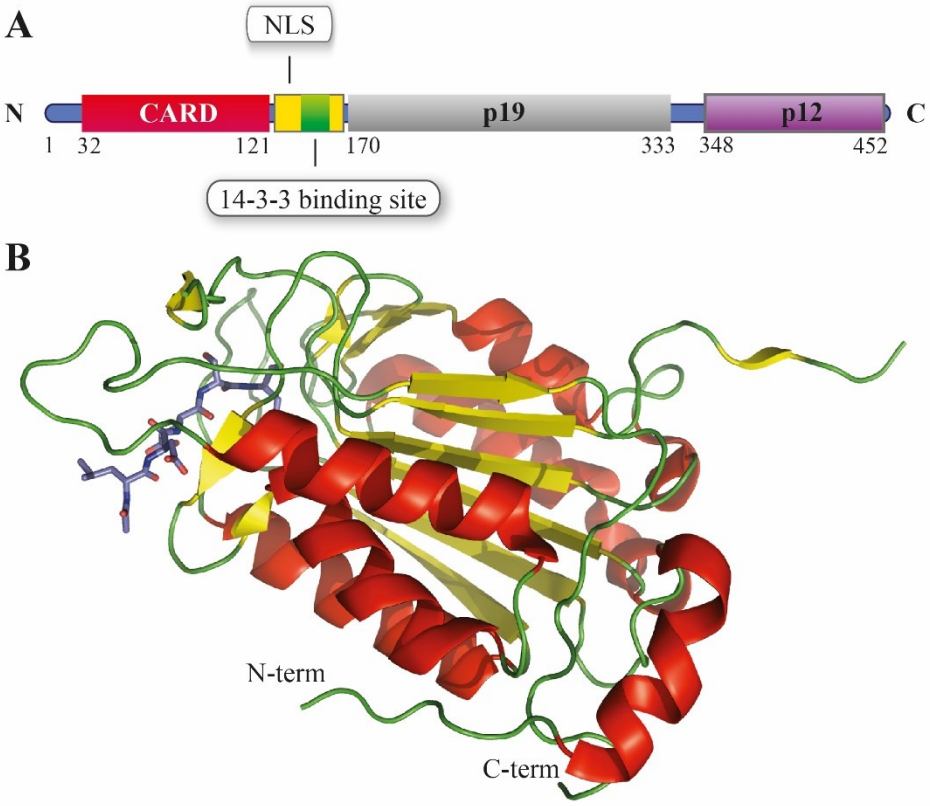

Figure 1.12. A) Caspase-2 domain organization. The N-terminal caspase activation and recruitment domain (CARD) is followed by the nuclear localization sequence (NLS) with a 14-3-3 binding site, large subunit p19 and small subunit p12. Adapted from [56]. **B) Crystal structure of caspase-2.**[53] X-ray structure of active caspase-2 in a complex with its inhibitor acetyl-Leu-Asp-Glu-Ser-Asp-aldehyde (blue sticks). PDB: 1PYO

In addition to autoactivation, procaspase-2 regulation also depends on the phosphorylation status. In *Xenopus leavis*, the NADPH generated by pentose-phosphate cycle is responsible for the phosphorylation of Ser^{135} located several residues upstream from the C-terminus of the CARD domain.[57] This phosphorylation forms a 14-3-3 binding site, where 14-3-3 acts as an inhibitor of a protease activity, presumably by blocking the activation of caspase-2. Under acute nutrient deprivation, the procaspase-2 is dephosphorylated, 14-3-3 dissociates and catalytically active caspase-2 initiates apoptosis.[58] However, the precise role of 14-3-3 in the caspase-2 inhibition is not yet fully understood because of the lack of structural data.

1.7 Transcription factor FOXO3

FOXO proteins belong to the family of forkhead box (FOX) transcription factors that includes more than 100 proteins divided into several classes from FOXA to FOXR, depending on their sequential homology.[59] The "forkhead" nomenclature has its origin in the first identified member, where the mutation in a FOXA gene in *Drosophila melanogaster* caused a characteristic ectopic head structure with fork-like shape.[60] All FOX transcription factors have a highly conserved DNA binding domain with three α-helices flanked by two characteristic loops and the FOX-DNA complexes are involved in a cellular differentiation and proliferation, longevity or tumorigenesis (reviewed in [61]).

Mammalian transcription factors from the O subclass, FOXO proteins, have four members: FOXO1, 3, 4 and 6, with FOXO1 first discovered in human alveolar rhabdomyosarcomas.[62] FOXO proteins are negatively regulated by the insulin-PI3K-Akt signaling pathway. Binding of insulin as a growth factor induces activation of phosphoinositol-3-kinase (PI3K) that serves as an adaptor molecule for protein kinase B (PKB/Akt). PKB signaling then phosphorylates FOXO proteins, what inactivates the target gene transcription.[59] However, the growth factor-mediated regulation of FOXO proteins is overcome when exposed to stress signals. This leads to a relocation of FOXOs from the cytoplasm to the nucleus. Therefore, FOXO proteins play a crucial role not only in apoptotic processes, but also in cell metabolism, oxidative stress response or DNA-damage repair (reviewed in [63]).

The activity of FOXO proteins is regulated by posttranslational modifications, such as phosphorylation, ubiquitination and acetylation (reviewed in [64]). Phosphorylation affects the subcellular localization by forming a 14-3-3 binding site. The binding of 14-3-3 protein causes export from the nucleus and simultaneously restricts the FOXO import into the nucleus.[64] The acetylation affects the DNA binding by decreasing the FOXO-DBD affinity, acetylated systems then sustain expression of proapoptotic genes; deacetylated systems regulate expression of antioxidant genes.[64] Monoubiquitination increases FOXO nuclear localization and transcription activity, polyubiquitination regulates standard proteasome degradation.[64]

FOXO3 protein is a 67 kDa protein expressed in all types of human tissues. Its structure consists of the two distinct domains, the N-terminal typical forkhead DNA binding domain (DBD) that also includes the nuclear localization signal (NLS) and the C-terminal transactivation domain (TAD) that is preceded by a nuclear export sequence (NES) (*Fig. 1.13 A*). The DBD is a 110 amino acids-long segment and it is responsible for recognizing and binding to a specific DNA sequence 5'- (C/A)(A/C)AAA(C/T)AA -3', corresponding to insulin-responsive element (IRE) and 5'- GTAAA(T/C)AA -3' corresponding to Daf-16 family member binding element (DBE) (*Fig. 1.13 B, C*). The NLS domain is responsible for the FOXO3 import to a cell nucleus, NES is involved in a relocation to the cytoplasm (reviewed in [65]).

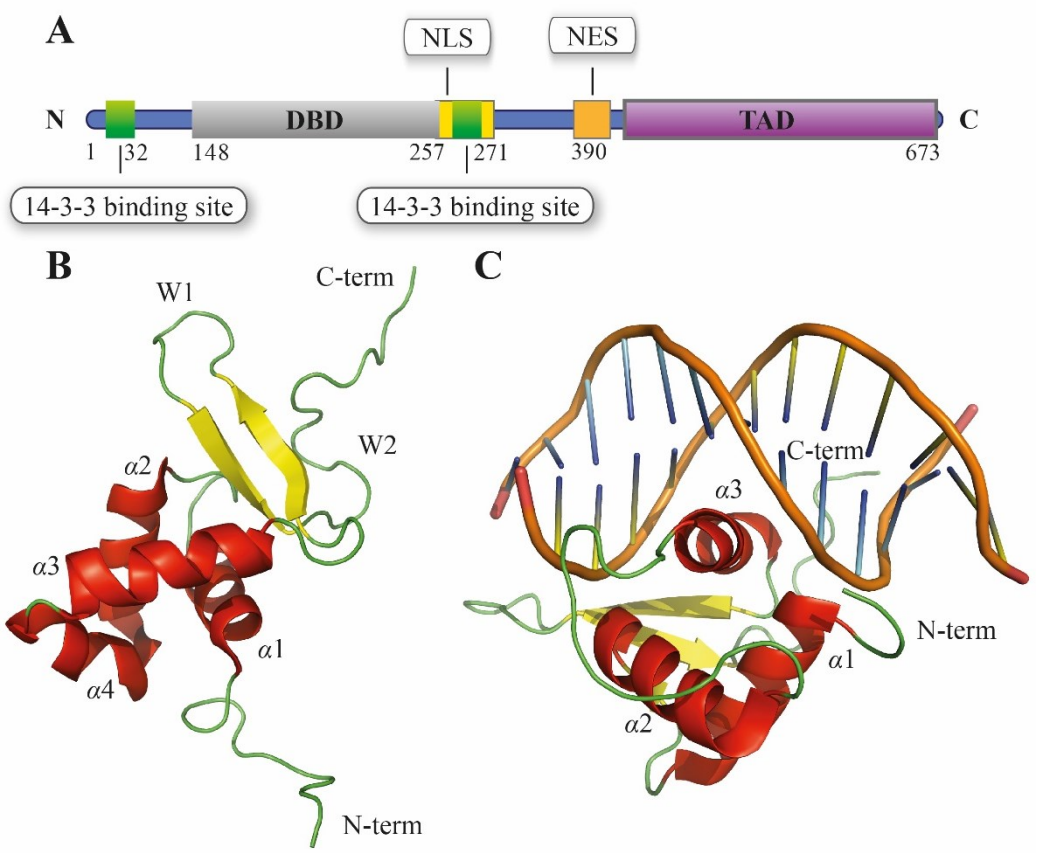

Figure 1.13. A) FOXO3 domain configuration. DNA binding domain (DBD) is surrounded by two 14-3-3 binding sites and followed by nuclear localization signal (NLS), nuclear export sequence (NES) and a C-terminal transactivation domain (TAD). Adapted from [65]. **B) The solution NMR structure of the DNA binding domain of human FOXO3.**[66] PDB: 2K86 **C) The crystal structure of the DNA fragment bound to human FOXO3-DBD.**[67] PDB: 2UZK

FOXO3 also acts as a tumor suppressor when regulating apoptosis induction and cell cycle arrest; however in certain types of cancer, it can promote drug-resistance or chemo-resistance by promoting cancer stem cells and regulating cellular detoxification.[68,69] FOXO3 is therefore an attractive therapeutic target. A reversible inhibition of the DNA binding to FOXO3 by small organic compounds that would compete with the target DNA could directly modulate the FOXO3-DBD transcriptional activity.

2 AIMS

The main aim of this doctoral thesis was to study the molecular mechanism of the inhibition of four signaling proteins: Calcium/Calmodulin (Ca^{2+}/CaM)-dependent protein kinase kinase 2, Caspase-2, Forkhead transcription factor FOXO3 and Apoptosis signal-regulating protein kinase 1.

Specific aims were:

1. To study the role of 14-3-3 and CaM in the regulation of Ca^{2+}/CaM – dependent protein kinase kinase 2 activity,

2. To investigate the role of 14-3-3 in the regulation of Caspase-2 protease activity,

3. To investigate the structural basis of inhibition of the FOXO3-DNA interaction by small molecule inhibitors,

4. To study the molecular mechanism of the Apoptosis signal-regulating kinase 1 activation.

Various biophysical techniques including nuclear magnetic resonance spectroscopy, small angle X-ray scattering, time-resolved fluorescence spectroscopy, analytical ultracentrifugation and mass spectrometry were used as principle tools.

3 METHODS

3.1 Nuclear magnetic resonance

Nuclear magnetic resonance (NMR) spectroscopy is one of the most powerful tools in structural biology. It provides not only information about the three dimensional molecular structure with the atomic resolution complementary to X-ray crystallography, but is also an indispensable technique for studies of biomolecular interactions and time-dependent chemical phenomena, such as intramolecular dynamics or reaction kinetics.[70] Although the solid-phase NMR spectroscopy is becoming more widely used in structural biology, the most of the biomolecular NMR studies are carried out in solution.

In an external magnetic field, the magnetic moments of atomic nuclei with non-zero spin precess around the axis of an external field. When applying a radio frequency pulse matching the frequency of a spin precession, the vector of nuclear magnetization rotates from its equilibrium position. With time, the magnetization vector returns back to the direction of the external field with fluctuating declining amplitude (free induction decay – FID) while inducing electric current that can be recorded by a receiver. The spin relaxation depends on the shielding effect (chemical shift) of locally induced magnetic fields that are determined by the molecular structure and geometry. The Fourier transformation of a FID function shows NMR spectrum of nuclei.[71] Although the method is relatively insensitive compared to other spectroscopic techniques that work with higher energies, it can reveal detailed information about the molecular structure in solution. In biomolecules, NMR spectroscopy exploits the fact that the highly abundant protons are also the most sensitive NMR active nuclei. However, both proteins and nucleic acids contain repetitive subunits, amino acids and nucleotides, bringing extensive overlaps into proton NMR spectra that are proportional to the size of studied systems. This is reduced by acquisition of multidimensional spectra, correlating protons with ^{13}C-carbon and ^{15}N-nitrogen heteronuclei. Due to their low natural abundance, proteins have to be isotopically labelled during their recombinant expression. The size of the system that can be studied by NMR spectroscopy is limited, alongside to increased complexity of the spectra, also by the

unfavorable relaxation properties of the NMR active nuclei, which can be partially overcome by perdeuteration of non-labile proton positions in large proteins.

3.1.1 Sample preparation

For the NMR structure determination of a protein molecule, the in vitro protein sample needs to be isotopically labeled with ^{15}N-nitrogen and ^{13}C-carbon. Isotopes are introduced to *E. coli* expression clones by enriched minimal media for protein expression that contain all salts, trace elements and vitamins together with ^{15}N-labeled ammonium chloride and ^{13}C-labeled glucose as sole nitrogen and carbon sources. The deuterated protein sample is prepared using deuterated minimal media with a prolonged time of *E. coli* expression allowing bacteria to adapt to increased D_2O content.

All protein NMR measurements are conducted using 5mm Shigemi tubes matched to deuterium oxide solvent with 8mm bottom length. The protein NMR sample is concentrated to 100-300 μM and contains 90% H_2O/10% D_2O in a buffer with low salt concentration and neutral or slightly acidic pH.

3.1.2 Experiment design and measurement

A combination of multi-dimensional triple-resonance spectra correlating ^{1}H with ^{13}C and ^{15}N need to be measured and evaluated for a protein structure determination. The sequence-specific backbone resonance assignment is obtained using ^{1}H-^{15}N HSQC and a standard set of three-dimensional spectra: HNCO, HN(CA)CO, HNCACB, and CBCA(CO)NH experiments.

The heteronuclear single quantum coherence (HSQC) spectroscopy is the most frequently used two-dimensional experiment in proteins, where the chemical shift is left to evolve on ^{15}N-nitrogen and the magnetization is transferred back to the hydrogen via the J-coupling for detection. An HSQC experiment includes all N-H correlations from backbone amide groups together with Trp, Asn, Gln, Arg and Lys side-chains.[70,72] The HNCO experiment is a standard 3D experiment, where the chemical shift is left to evolve on all three NMR active nuclei in a protein molecule: ^{1}H-hydrogen, ^{15}N-nitrogen and ^{13}C-carbon from a carbonyl group. The magnetization is transferred from ^{1}H to ^{15}N and then selectively to ^{13}CO via the J-coupling and then back to ^{15}N and ^{1}H for detection. The

complementary HN(CA)CO experiment correlates the same atoms, however the magnetization transfers from ^{1}H to ^{15}N, then it continues to $^{13}C\alpha$ without chemical shift evolvement and only after that to ^{13}CO. The principle of a magnetization transfer is preserved in other 3D experiments, HNCACB and CBCA(CO)NH, where the chemical shift is left to evolve simultaneously on $^{13}C_{\alpha}$ and $^{13}C_{\beta}$, acquiring both signals in one dimension.[70,72]

The specific side-chain resonance assignment can be obtained using a combination of NMR experiments that correlate the backbone with side-chain resonances, such as HBHA(CO)NH, HCCH-TOCSY. The HBHA(CO)NH experiment is a straightforward extension of the CBCA(CO)NH experiment. In this case, the magnetization is further transferred from CA and CB to their directly attached protons, HA and HB. In the HCCH-TOCSY (Total correlation spectroscopy), the magnetization transfer from the side-chain hydrogen to the attached ^{13}C is followed by a TOCSY isotropic mixing that ideally creates correlation between all carbons and protons within the spin system.[70,72]

The final step of the NMR determination of protein structure requires the acquisition of isotopically edited NOESY experiments that allow for the identification of the Nuclear Overhauser effect (NOE), the cross-relaxation through space (mutual dipolar relaxation of nearby spins). The quantified NOEs between specific protons are then introduced as distance restraints to the final structure calculations. The NOE-derived distance restrains can be further complemented by the restraints for dihedral angles obtained using the J-couplings or alternatively the secondary structure effects observed in the backbone resonances.[70,72,73]

3.2 Small angle X-ray scattering

Small angle X-ray scattering (SAXS) is a solution technique, which enables the low resolution structural characterization of proteins and protein complexes. It provides information about the global shape and conformation of biological macromolecules in their native environment, while maintaining their essential flexibility. An inherent limitation of this technique is that SAXS data contain much less structural information compared to the diffraction pattern in protein crystallography. However SAXS requires modest and cheaper sample preparation with a faster and easier data acquisition and evaluation.[74]

In SAXS, the solution of bio-macromolecules is irradiated by a collimated X-ray beam and scattered X-rays are detected on X-ray flat panel detectors. The scattering signal is continuous and radially symmetric due to the averaging of the scattered rays from the randomly oriented distribution of particles in solution. The scattering intensity $I(s)$ is a function of the momentum transfer s:

$$s = 4\pi \sin\frac{\theta}{\lambda} \quad \text{(Eq. 1)}$$

where 2θ corresponds to the scattering angle and λ represents the radiation wavelength.[75] The scattering intensity of a homogeneous solution of target particles is a function of the distance distribution function of the particle $P(r)$:

$$I(s) = \int_0^{D_{\max}} P(r)\frac{\sin(sr)}{sr}dr \quad \text{(Eq. 2)}$$

where $D_{\max}$ is the maximum distance within the particle.[74] The distance distribution function $P(r)$ is radially averaged autocorrelation function calculated from the Fourier transformation of scattering intensities and it shows a distribution of the distances between electrons in the sample. $P(r)$ function has a zero value at $r = 0$ and $r \geq D_{\max}$.[74]

For low s values, the scattering can be described using the Guinier approximation:

$$I(s) = I_0 \exp\left[-(s^2 R_g^2)/3\right] \quad \text{(Eq. 3)}$$

where R_g is the radius of gyration and I_0 is the scattering intensity at $s = 0$.[74]

The Guinier plot of $\ln I(s)$ vs. s^2 enables extraction of R_g and I_0 values and the degree of its linearity describes the interparticle attraction and repulsion force together with the proper background subtraction.[74] Another useful presentation of scattering data is the dimensionless Kratky plot $(sR_g)^2 I(s)/I(0)$ vs. (sR_g). A shape of the Kratky plot curve indicates the conformational flexibility of a protein, regardless of its size.[76]

3.2.1 Sample preparation

For the SAXS experiment, the protein sample should have a high purity and be homogeneous without any signs of aggregation; therefore samples are prepared in a concentration range between 0.5 – 10 mg/mL. To provide a well-defined signal-to-noise ratio, the protein buffer should not contain scattering components such as glycerol or additives and it has to be carefully filtrated.

4 RESULTS AND DISCUSSION

4.1 Publication I: Role of 14-3-3 in the regulation of Ca^{2+}/CaM – dependent protein kinase kinase 2 activity.

Psenakova, K.[+], Petrvalska, O.[+], Kylarova, S.[+], Lentini, D., Kalabova, D., Herman, P., Obsilova, V. & Obsil, T. 14-3-3 protein directly interacts with the kinase domain of calcium/calmodulin-dependent protein kinase kinase (CaMKK2). *Biochim. Biophys. Acta - Gen. Subj.* **1862**, 1612–1625 (2018).

My contribution: expression and purification of CaMKK2, 14-3-3 and CaM; preparation of phosphorylated CaMKK2, single tryptophan mutants of CaMKK2 and dansyl-labeled CaM; sample preparation and further optimization for the small-angle X-ray scattering and time-resolved dansyl and tryptophan fluorescence experiments; small-angle X-ray scattering data analysis.

[+] Equal contribution.

4.1.1 Motivation of the study

There are two human Ca^{2+}/CaM–dependent protein kinase kinase (CaMKK) isoforms: CaMKK1 and CaMKK2. Both isoforms have two common downstream targets: CaMKI and CaMKIV and their activation is regulated by a Ca^{2+}/CaM binding. CaMKK1 shares high sequence identity with CaMKK2, nevertheless CaMKK2 also activates AMPK and exhibits autonomous activity in contrast to CaMKK1. The regulation of CaMKK1 has previously been studied and it has been suggested that its inhibition by the PKA-mediated phosphorylation is further enhanced by 14-3-3 proteins. Although CaMKK2 also contains two 14-3-3 binding motifs in its sequence, the role of 14-3-3 binding in the regulation of CaMKK2 activity is still unclear.

Therefore, the main goal of this work was to investigate the role of 14-3-3 in the regulation of CaMKK2 by performing the structural and biophysical characterization of the complex between CaMKK2 and 14-3-3.

4.1.2 Sample preparation

To determine the role of 14-3-3 in the regulation of CaMKK2 activity, the construct suitable for structural analysis was designed. The DNA encoding human CaMKK2 with amino acid sequence 93-517 was ligated into a selected plasmid, containing the catalytic domain, the Ca^{2+}/CaM binding domain and both suggested 14-3-3 binding motifs. In addition to the two phosphorylation sites at Ser^{100} and Ser^{511}, which are also predicted 14-3-3 binding motifs; the sequence also contained two additional inhibitory PKA phosphorylation sites at Thr^{145} and Ser^{495}, which were mutated to Ala. To avoid autophosphorylation, the catalytic aspartate residue Asp^{330} was mutated to Ala. The modified CaMKK2 construct (CaMKK2-$S^{100,511}$) was recombinantly expressed and phosphorylated *in vitro* by PKA, the HPLC-MS analysis confirmed complete phosphorylation of Ser^{100} and 50% phosphorylation of Ser^{511}, which was consistent with previous reports.[46] Because the N-terminal 14-3-3 binding site is phosphorylated to the significantly higher extent, an additional construct containing only the Ser^{100} with mutated Ser^{511} to Ala was also prepared (CaMKK2-S^{100}).

4.1.3 14-3-3 binds to CaMKK2

To verify the 14-3-3 binding to CaMKK2, analytical ultracentrifugation experiments were performed. The data analysis revealed that a dimer of 14-3-3γ binds to phosphorylated CaMKK2-S^{100} with a 1 ± 0.5 μM affinity, while to phosphorylated CaMKK2-$S^{100,511}$ with a higher affinity of < 0.4 μM, thus suggesting that the phosphorylated C-terminal 14-3-3 binding site increases the stability of the complex.

To characterize the 14-3-3 binding motifs in CaMKK2, the crystallization studies were performed. The 14-3-3ζΔC (construct missing the highly flexible C-terminal tail) isoform was crystalized with a phosphopeptide RKLpSLQER that corresponds to the N-terminal CaMKK2-S^{100} 14-3-3 binding site and the 14-3-3γΔC isoform was crystalized with a phosphopeptide RSLpSAPGN that corresponds to the C-terminal CaMKK2-S^{511}

14-3-3 binding site. The crystal structures revealed that the main chain conformations of both phosphopeptides are highly similar to those observed in the previously determined structures of 14-3-3 complexes.

4.1.4 14-3-3 binding does not inhibit the CaMKK2 activity

To determine whether CaMKK2 is also inhibited by the 14-3-3 binding, as in the case of CaMKK1, the kinase activity measurements were performed. Surprisingly, the data analysis revealed that the 14-3-3 binding does not inhibit the catalytic activity of CaMKK2 toward its physiological substrates. To test the effect of 14-3-3 on the CaMKK2 dephosphorylation, the limited dephosphorylation experiment was performed. The CaMKK2 construct containing all four PKA phosphorylation sites including inhibitory sites Thr^{145} and Ser^{495} was treated by protein phosphatase 1 in the presence or absence of 14-3-3γ and the temporal degree of dephosphorylation was determined by HPLC-MS. The data analysis revealed that the 14-3-3 binding slows down the dephosphorylation of both inhibitory PKA sites in the CaMKK2.

4.1.5 14-3-3 protein is in a direct contact with the CaMKK2 kinase domain

To investigate whether the 14-3-3 protein directly interacts with the kinase domain of CaMKK2 (*Fig. 4.1*), small angle X-ray scattering (SAXS) measurements were performed.

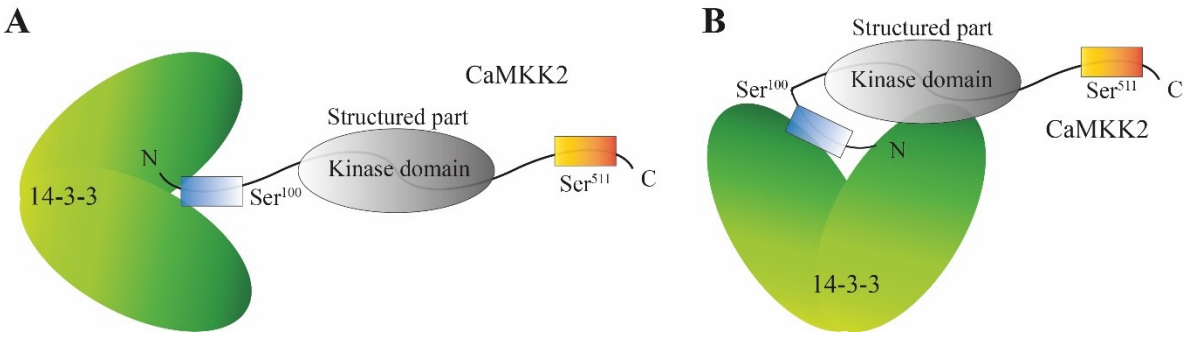

Figure 4.1. The two possible 14-3-3:CaMKK2 complex conformations. A) The 14-3-3:CaMKK2 complex in a loose conformation. A dimer of 14-3-3 (green) binds through the N-terminal Ser^{100} motif (blue) of a stretched CaMKK2. It has

been suggested that the C-terminal 14-3-3 binding motif containing Ser^{511} (orange) is not physiologically relevant. **B)** The 14-3-3:CaMKK2 complex in a compact conformation. A dimer of 14-3-3 (green) binds through the N-terminal Ser^{100} (blue) motif of CaMKK2 and directly interacts with the kinase domain (gray).

Small angle X-ray scattering measurements were performed for CaMKK2-S^{100} and CaMKK2-$S^{100,511}$ alone and in a complex with the dimeric 14-3-3γΔC (*Fig. 4.2 A*). In all samples containing CaMKK2-$S^{100,511}$, the incompletely phosphorylated Ser^{511} led to a mixture of two complexes with either just the N-terminal Ser^{100} or both serines docked within the binding grooves of the 14-3-3 dimer. The absence of attractive interparticle interactions revealed by the linear Guinier plots in all samples confirmed that no aggregation was present within the used concentration range (*Fig. 4.2 B*). The stability of the prepared complexes exhibited no significant concentration dependence of the forward scattering intensity $I(0)$, the Porod volume V_p, and the radius of gyration R_g (*Tab. 4.1*). $P(r)$ functions for CaMKK2s alone and for both complexes are asymmetric and show longer inter-particle distances and a larger maximum distance (D_{max}) compared to the 14-3-3γΔC dimer alone, thus suggesting that CaMKK2 is a significantly more extended protein (*Fig. 4.2 C*). The increased conformational flexibility of CaMKK2 and the complex with 14-3-3 is also showed by the dimensionless Kratky plot ($(sR_g)^2I(s)/I(0)$ versus sR_g) (*Fig. 4.2 D*). In the case of CaMKK2-$S^{100,511}$, the lower R_g and D_{max} values together with the lower maximum of Kratky plot for the complex with 14-3-3γΔC indicate that CaMKK2 phosphorylated at both serines forms a more compact 14-3-3 complex with a decreased conformational flexibility.

Table 4.1. Structural parameters determined from SAXS data.

	c (mg·mL^{-1})	R_g (Å)[a]	R_g (Å)[b]	D_{max} (Å)	V_p[c] (nm^3)	M_w[d,f] (kDa)	M_w[e,f] (kDa)
14-3-3γΔC	3.0	28.7 ± 0.4	28.6 ± 0.4	89	77.8	54 ± 1	49
	1.5	29.0 ± 0.4	29.0 ± 0.4	89	82.8	55 ± 1	52
CaMKK2	2.8	32.6 ± 0.3	32.7 ± 0.3	126	95.6	48 ± 1	60
	2.1	32.1 ± 0.3	32.2 ± 0.3	125	94.0	46 ± 1	59
Complex (S^{100})	16.9	42.3 ± 0.6	42.4 ± 0.6	146	160.4	92 ± 1	100
	12.6	42.5 ± 0.6	42.6 ± 0.6	144	163.4	95 ± 1	102
	9.9	42.4 ± 0.6	42.5 ± 0.6	146	161.1	94 ± 1	101
Complex ($S^{100,511}$)	11.9	39.9 ± 0.7	40.0 ± 0.7	141	164.8	97 ± 1	103
	6.5	39.1 ± 0.6	39.2 ± 0.6	141	159.6	94 ± 1	100

[a]Calculated using Guinier approximation.

[b]Calculated using the program GNOM.

[c]The excluded volume of the hydrated particle (the Porod volume).

[d]Molecular weight estimated by comparing the forward scattering intensity $I(0)$ with that of the reference solution of bovine serum albumin.

[e]Molecular weight estimated from the Porod volume ($M_w \approx V_p \times 0.625$)[77].

[f]Theoretical molecular weights of the 14-3-3γΔC dimer, CaMKK2s and the CaMKK2:14-3-3γΔC complex with 2:1 stoichiometry are 54.3, 48.0 and 102.3 kDa, respectively.

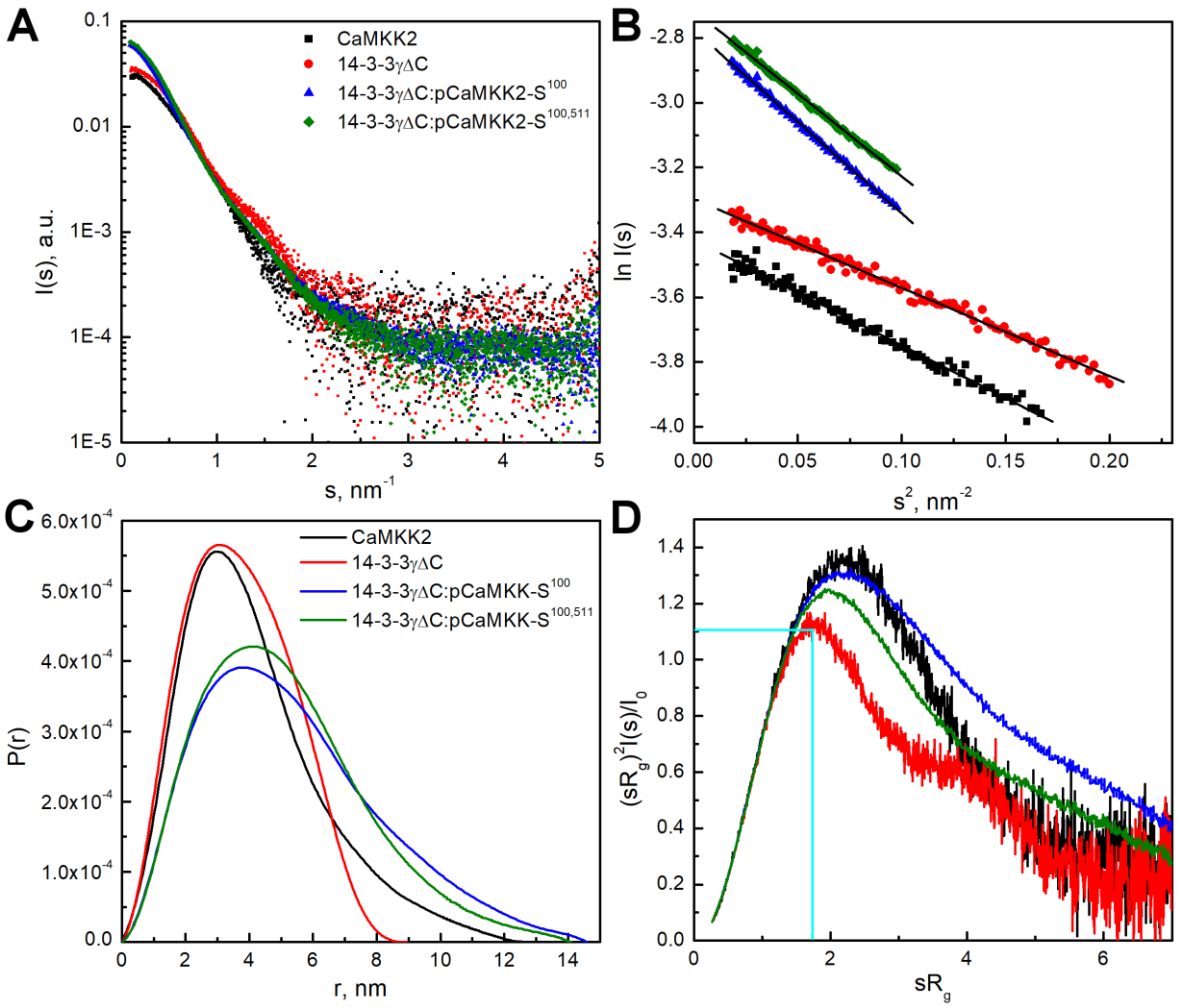

Figure 4.2. SAXS analysis of the CaMKK2 and the complex with 14-3-3. **A)** Scattering intensity as a function of the scattering vector *s* of 14-3-3γΔC alone, CaMKK2-S^{100} alone, the 14-3-3γΔC:CaMKK2-S^{100} and the 14-3-3γΔC:CaMKK2-S^{100,511} complexes mixed at 2:1 molar stoichiometry. **B)** Guinier plots for scattering curves shown in panel A). **C)** Distance distribution functions *P*(*r*) calculated from scattering data using the program GNOM.[78] **D)** Dimensionless Kratky plots. Cyan line shows the compact globular protein's maximum.[76]

Experimental SAXS curves and calculated parameters provide a basis for the structural modeling. To obtain an insight into the relative orientation of CaMKK2 and 14-3-3 within the complex, the program MONSA was used.[79] It utilizes a multiphase modeling with an *ab initio* bead model, which for the complex between 14-3-3γΔC and CaMKK2-S^{100} consists of two phases representing individual proteins within

a low-resolution molecular envelope.[80] The calculated molecular envelope of the 14-3-3:CaMKK2 complex had an asymmetric shape, with most of the CaMKK2 phase stretched out into the solution. Surprisingly, the kinase was attached to the side of the 14-3-3 dimer, instead of being located in the central channel of the 14-3-3 dimer, leaving a deep depression in the center of the 14-3-3 phase (*Fig. 4.3 A*). Next, the program CORAL was used for a rigid body docking of the 14-3-3:CaMKK2 complex.[77] To this end, the crystal structures of the 14-3-3γΔC (PDB: 2B05) and the CaMKK2 kinase domain (PDB: 2ZV2) were used and the unstructured segments missing in the crystal structures were modeled as dummy residue chains. Similarly to MONSA model, the final CORAL model of the complex revealed an asymmetric shape with CaMKK2 located outside the central channel of the 14-3-3γ dimer (*Fig. 4.3 B*). The theoretical SAXS curve of the CORAL model exhibited a χ^2 value of 1.3 when compared to the experimental curve. Therefore, the structural modeling suggested that CaMKK2-S^{100} interacts with 14-3-3γ not only through the N-terminal site containing Ser^{100} but also via a direct interaction with the kinase domain.

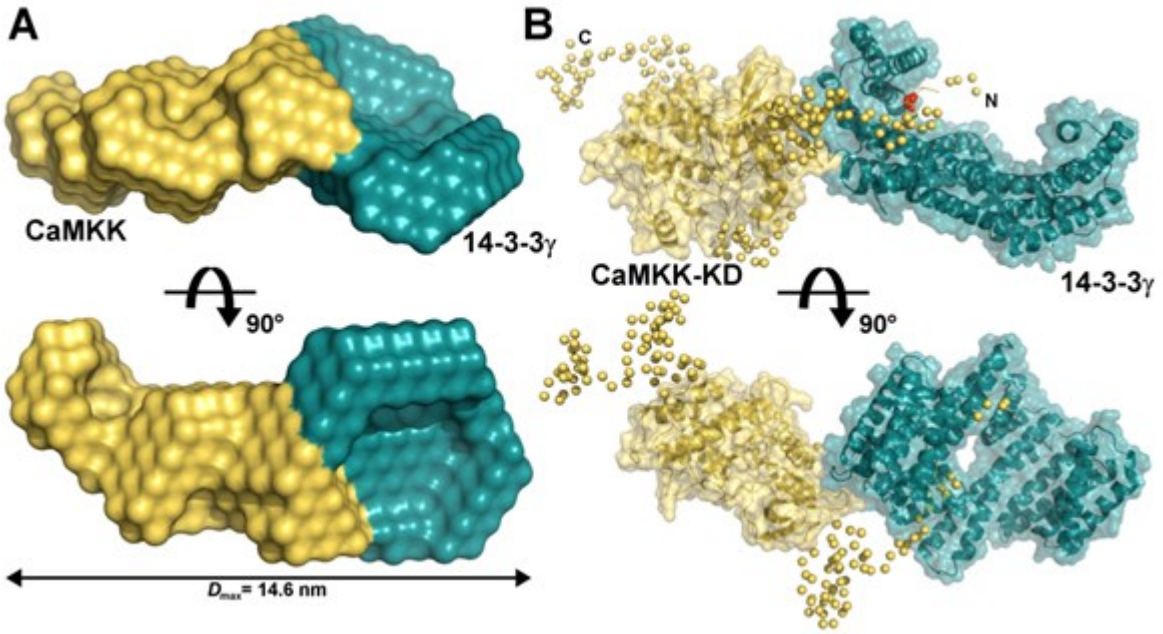

Figure 4.3. SAXS-Based Structural Modeling of the 14-3-3γ:CaMKK2-S^{100} Complex. A) A MONSA multiphase reconstruction for the complex between 14-3-3γΔC (cyan) and CaMKK2-S^{100} (yellow). **B)** The final CORAL model of the complex between 14-3-3γΔC (cyan) and CaMKK2-S^{100} (yellow). For the rigid

body modeling the crystal structure of the 14-3-3γΔC (PDB: 2B05) and the CaMKK2 kinase domain (PDB: 2ZV2)[42] were used, the unstructured CaMKK2 segments missing in the crystal structure were modeled as dummy residue chains. The residue Ser^{100} is shown in red.

4.1.6 14-3-3 does not affect the Ca^{2+}/CaM binding to CaMKK2

To test whether 14-3-3 affects the Ca^{2+}/CaM binding to CaMKK2, time-resolved dansyl fluorescence was measured.[81] The interaction between dansyl-labeled CaM (dans-CaM) and CaMKK2 was investigated in the absence and presence of 14-3-3γ using time-resolved fluorescence intensity and anisotropy decay measurements (*Tab. 4.2*).

Table 4.2. Summary of the time-resolved dans-CaM fluorescence measurements.

Sample	τ_{mean} [a,b] (ns)	K_{SV} [e] (M^{-1})	k_i ($\times 10^{-5}$) ($M^{-1}s^{-1}$) [f]	ϕ_1 [d] (ns)	β_1 [c]	ϕ_2 (ns)	β_2	ϕ_3 (ns)	β_3	ϕ_4 (ns)	β_4
Dansyl-CaM	15.2	0.18	120	< 0.1	0.03	0.6	0.02	2.5	0.10	9.3	0.12
+ 14-3-3γ	15.9	0.19	120	< 0.1	0.03	0.5	0.02	1.9	0.08	8.4	0.15
+ S^{100}	20.5	0.01	4			2.5	0.01	12	0.11	49	0.15
+ S^{100} + 14-3-3γ	20.5	0.00	0			3.0	0.01	11	0.10	49	0.16
+ $S^{100,511}$	20.6	0.01	3			4.7	0.03	16	0.10	52	0.15
+ $S^{100,511}$ + 14-3-3γ	20.2	0.11	53			2.8	0.02	12	0.08	88	0.16

[a]Mean lifetimes were calculated as $\tau_{mean}=\Sigma_i f_i \tau_i$, where f_i is an intensity fraction of the i-th lifetime component τ_i.

[b]S.D. value is ± 0.1 ns.

[c]The anisotropies $r(t)$ were analyzed for a series of exponentials by a model-independent maximum entropy method.

[d]Fast unresolved component.

[e]Stern-Volmer constant of acrylamide quenching.

[f]Bimolecular quenching constant for acrylamide collisional quenching.

The data analysis revealed that the Ca^{2+}/CaM binding to CaMKK2 is accompanied by a significant increase in the mean excited-state lifetime (τ_{mean}) and in the longest correlation time ϕ_4 of the dans-CaM, because the overall rotational diffusion coefficient decreases upon the complex formation. The anisotropy decay measurements showed that the 14-3-3γ binding did not induce any changes in the mobility of dans-CaM when added to the complex with CaMKK2-S^{100} (*Fig. 4.4 A*). On the other hand, the 14-3-3γ binding to CaMKK2-$S^{100,511}$ caused an elevation of the anisotropy decay tail (*Fig. 4.4 B*). These results indicate that the 14-3-3 binding has no effect on the stability of the complex between Ca^{2+}/CaM and CaMKK2. In addition, the binding of the partially phosphorylated C-terminal Ser^{511} of the CaMKK2-$S^{100,511}$ to the second protomer of the 14-3-3 dimer probably affects the conformation of the segment with bound dans-CaM.

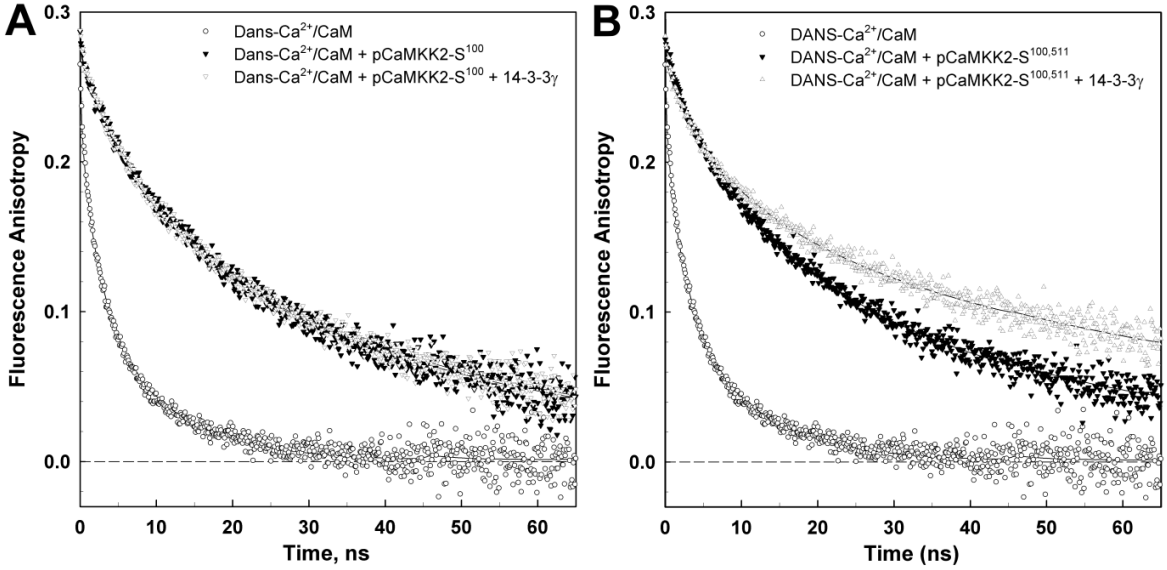

Figure 4.4. Time-resolved dansyl fluorescence measurements. A) Fluorescence anisotropy decays of free dansyl-Ca^{2+}/CaM (open circles) in the presence of CaMKK2-S^{100} (closed triangles), and in the presence of CaMKK2-S^{100} with 14-3-3γ (open triangles). **B)** Fluorescence anisotropy decays of free dansyl-Ca^{2+}/CaM (open circles) in the presence of CaMKK2-$S^{100,511}$ (closed triangles), and in the presence of CaMKK2-$S^{100,511}$ with 14-3-3γ (open triangles).

4.1.7 CaMKK2 conformational changes upon the 14-3-3 binding

To investigate the CaMKK2 conformational changes upon the 14-3-3 binding, four mutants of CaMKK2 carrying single tryptophan residue and the tryptophan lacking 14-3-3γ were prepared. As there are two tryptophan residues present in the wild-type CaMKK2 sequence, Trp^{374} and Trp^{445}, the variants carrying single tryptophan residue were created by mutating the other tryptophan residue to phenylalanine. Because both tryptophans are located at the C-terminus, the artificial single tryptophan residues were introduced to the N-terminus by mutating Phe^{140} and Phe^{267}, respectively, while changing the two naturally occurring tryptophans to phenylalanines. The fluorescently silent 14-3-3γ noW missing all tryptophan residues was used in all tryptophan fluorescence measurements.[82]

The analysis of the fluorescence intensity decay data revealed that the binding of 14-3-3γ noW causes an increase in the mean excited-state lifetime (τ_{mean}) in the case of CaMKK2-S^{100} single tryptophan mutants containing Trp^{140} (*Fig. 4.5 A*) and Trp^{445} (*Fig. 4.5 B*). However, no significant changes were observed for Trp^{267} and Trp^{374} mutants. The increase in τ_{mean} indicates a change of quenching interactions and/or polarity caused by a 14-3-3γ binding near Trp^{140} and Trp^{445} residues. The 14-3-3 binding therefore affects the conformation within the N-terminal regulatory segment in the vicinity of Trp^{140}, which is close to the regulatory phosphorylation site Thr^{145}, and also within the C-lobe of the kinase domain.

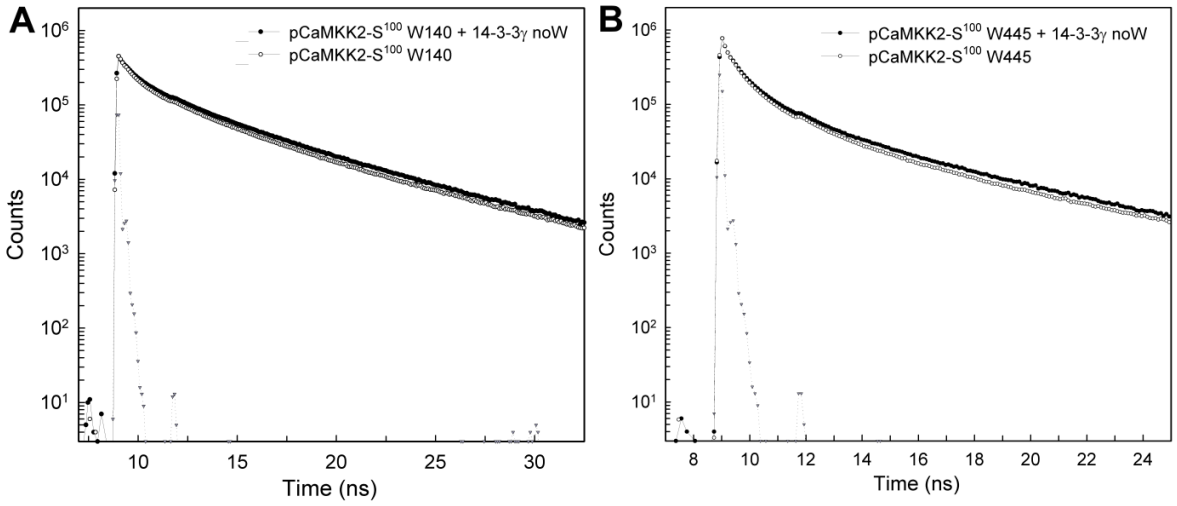

Figure 4.5. Time-resolved tryptophan fluorescence measurements. A) Normalized fluorescence intensity decays of CaMKK2-S^{100} mutant containing single Trp^{140}, in the absence (open circles) and presence (closed circles) of 14-3-3γ noW. Triangles denote instrument response function. **B)** Same as A) for the CaMKK2-S^{100} mutant containing single Trp^{445}.

4.1.8 Conclusion

The main aim of this study was to understand the role of 14-3-3 binding in the regulation of CaMKK2 activity. Analytical ultracentrifugation experiments confirmed 14-3-3ζ binding to phosphorylated CaMKK2 with the binding affinity in the low μM range. The kinase activity measurements revealed that the 14-3-3ζ binding does not inhibit the catalytic activity of CaMKK2; however it slows down the dephosphorylation of the inhibitory PKA phosphorylation sites in the CaMKK2 sequence. The small angle X-ray scattering measurements showed that 14-3-3ζ is directly interacting with the kinase domain of CaMKK2. The data analysis also suggested an asymmetric shape of the complex with the kinase domain of CaMKK2 located outside the central channel of the 14-3-3 dimer. The time-resolved dansyl fluorescence experiments showed that the 14-3-3 does not affect the Ca^{2+}/CaM binding to CaMKK2. And finally, the time-resolved tryptophan fluorescence measurements revealed that the 14-3-3 binding affects the conformation of CaMKK2 in several regions outside the N-terminal phosphorylated 14-3-3 binding motif. In conclusion, the role of 14-3-3ζ in the regulation of CaMKK2 appears to be based on the inhibition of

the dephosphorylation of regulatory PKA phosphorylation sites rather than the direct structural modulation of the kinase domain.

4.2 Publication II: The role of CaM in the regulation of Ca^{2+}/CaM – dependent protein kinase kinase 2 activity

Kylarova, S., **Psenakova, K.,** Herman, P., Obsilova, V. & Obsil, T. CaMKK2 kinase domain interacts with the autoinhibitory region through the N-terminal lobe including the RP insert. *Biochim. Biophys. Acta - Gen. Subj.* **1862**, 2304–2313 (2018).

My contribution: expression and purification of CaMKK2 and CaM; preparation of single tryptophan mutants of CaMKK2; sample preparation and further optimization for the small-angle X-ray scattering and time-resolved tryptophan fluorescence experiments; small-angle X-ray scattering data analysis; all docking calculations and refinement of the structural model based on the experimental data.

4.2.1 Motivation of the study

The Ca^{2+}/CaM – dependent protein kinase kinase 2 (CaMKK2) activates three downstream targets: CaMKI, CaMKIV and AMPKA, involved in key cellular functions. The CaMKK2 activity is regulated by the Ca^{2+}/CaM binding, however, the interaction mechanism remains unclear due to the lack of structural data. The CaMKK2 sequence shows distinct alterations from other CaMKs suggesting that the Ca^{2+}/CaM binding-induced conformational changes different from other CaMKs might occur.

The main goal of this work was to reveal the mechanistic details of the Ca^{2+}/CaM binding-dependent regulation of CaMKK2 by structural characterization of the conformational changes caused by the complex formation.

4.2.2 Sample preparation

To characterize the conformational changes of CaMKK2 caused by the Ca^{2+}/CaM binding, the CaMKK2 construct suitable for structural analysis was designed. The DNA encoding human CaMKK2 with the amino acid sequence 93-517 was ligated into a selected

plasmid, containing the catalytic domain (CD), the autonomous activity region, the Ca^{2+}/CaM binding domain (CBD) and the autoinhibitory domain (AID). To avoid the autophosphorylation, the catalytic aspartate residue Asp^{330} was mutated to Ala. The CaMKK2 construct was recombinantly expressed and purified in a sufficient quantity for detailed characterization.

4.2.3 The Ca^{2+}/CaM binding-induced conformational changes of CaMKK2

To compare changes in solvent accessibility of CaMKK2 upon Ca^{2+}/CaM binding, the hydrogen/deuterium exchange coupled to mass spectrometry (HDX-MS) measurements were performed. In HDX-MS, the deuteration levels of CaMKK2 in the absence and presence of Ca^{2+}/CaM were followed on 22 selected peptides covering the entire CaMKK2 sequence after 60 s (exchange on a short timescale) and 5 h (exchange on a long timescale) of deuteration reaction. The data analysis for both timescales revealed that the most significant change in the deuterium incorporation occurred in the helix αE and strands β1-β2 and β6-β8 of the CaMKK2 kinase domain together with a surface located on the opposite site formed by strands β4-β5 and the helix αC (*Fig. 4.6*). Therefore, results from HDX-MS suggested that the regions surrounding the ATP binding pocket are subjected to the conformational changes upon Ca^{2+}/CaM binding.

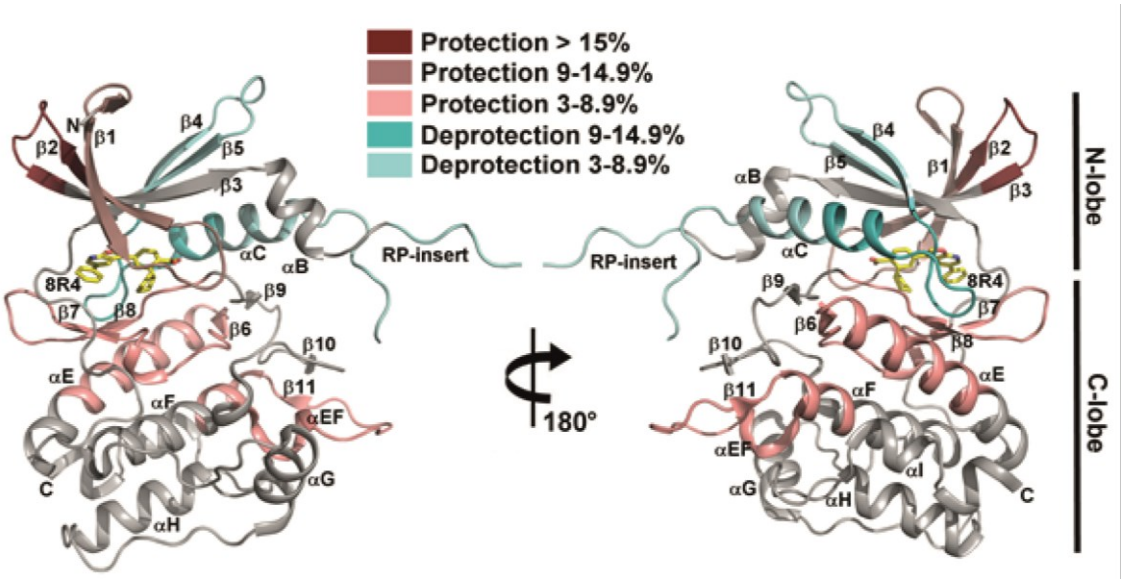

Figure 4.6. Ca^{2+}/CaM binding-induced changes within the kinase domain of CaMKK2. The HDX-MS results of Ca^{2+}/CaM binding to CaMKK2 mapped to the crystal structure of the CaMKK2 kinase domain (PDB: 5UY6). The small molecular inhibitor 8R4 is bound inside the ATP binding pocket.

To investigate the CaMKK2 conformational changes upon the Ca^{2+}/CaM binding, the time-resolved tryptophan fluorescence intensity and anisotropy decays were measured. Six variants of CaMKK2 carrying a single tryptophan residue at different positions were prepared. The tryptophan residues were introduced throughout the whole kinase at these positions: Trp^{128}, Trp^{267}, Trp^{337}, Trp^{366}, Trp^{374} and Trp^{390}. CaM has no tryptophan residue in its sequence, therefore it is naturally fluorescently silent. Fluorescence intensity decay measurements and the lifetime distribution analysis showed that the Ca^{2+}/CaM binding significantly affected the surroundings of Trp^{267}, Trp^{337} and Trp^{366} (*Fig. 4.7*) in contrast to relatively insignificant changes observed in mutants carrying Trp^{128}, Trp^{374}, and Trp^{390}.

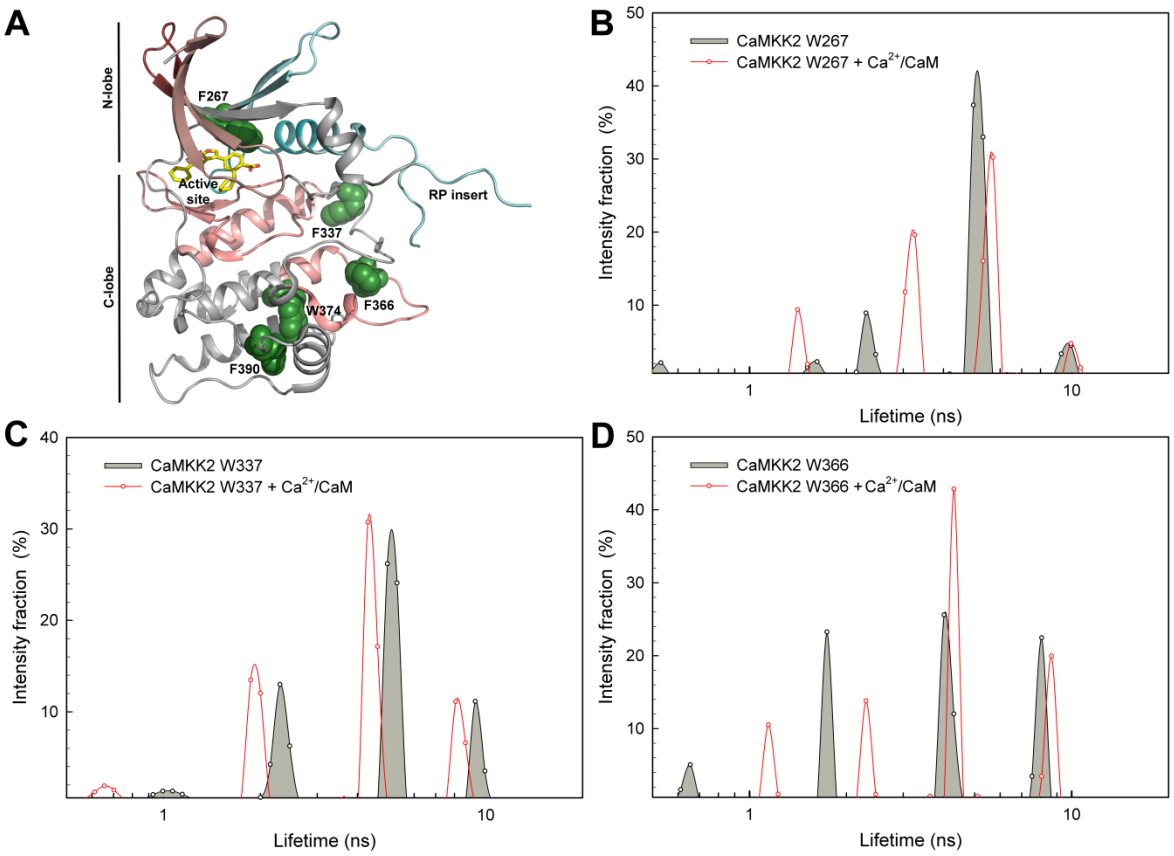

Figure 4.7. Time-resolved tryptophan fluorescence measurements. A) The crystal structure of the CaMKK2 kinase domain (PDB: 5UY6). Green spheres highlight Trp^{374} and phenylalanines F^{267}, F^{337}, F^{366} and F^{390} replaced by tryptophans. **B)-D)** Lifetime distributions of CaMKK2 Trp^{267} (B), Trp^{337} (C) and Trp^{366} (D) in the absence (gray) and presence of Ca^{2+}/CaM (red).

4.2.4 The CaMKK2 kinase domain directly interacts with Ca^{2+}/CaM

Small angle X-ray scattering (SAXS), chemical cross-linking (XL-MS) and molecular docking simulations were performed to study the architecture of the complex between CaMKK2 and Ca^{2+}/CaM. Small angle X-ray scattering was measured for CaMKK2 in a complex with Ca^{2+}/CaM at several protein concentrations. The absence of aggregation was confirmed by the linear Guinier plots in all samples within the used concentration range (*Fig. 4.8 A*). The $P(r)$ functions for CaMKK2s alone and for its complex with Ca^{2+}/CaM showed the similar maximum distance (D_{max}), however the

complex exhibited higher proportion of longer inter-particle distances (*Fig. 4.8 B*). Furthermore, the dimensionless Kratky plot ($(sR_g)^2I(s)/I(0)$ versus sR_g) indicated substantial conformational flexibility of both CaMKK2 and the complex with Ca^{2+}/CaM (*Fig. 4.8 C*).

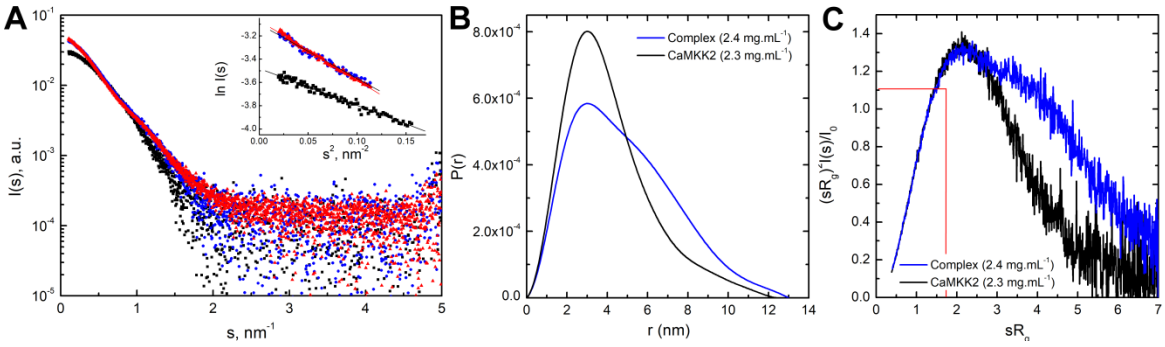

Figure 4.8. SAXS Analysis of the complex between CaMKK2 and Ca^{2+}/CaM. Scattering intensity as a function of the scattering vector *s* of CaMKK2 (2.3 mg·mL^{-1}, black squares) and the CaMKK2:Ca^{2+}/CaM complex prepared with the 2:1 molar stoichiometry (2.4 and 5.8 mg·mL^{-1}, blue circles and red triangles, respectively). Guinier plots for scattering curves are shown in the inset. **B)** Distance distribution functions *P*(r) calculated from the scattering data using the program GNOM.[78] **C)** Dimensionless Kratky plots. Red line shows the compact globular protein's maximum.[76]

The experimental SAXS curves with calculated parameters were further used for the structural modeling of the CaMKK2:Ca^{2+}/CaM complex. To obtain the relative position of CaMKK2 and Ca^{2+}/CaM within the complex, the chemical cross-linking coupled to MS was performed. Two cross-linking agents that react with amine-groups were used: disuccinimidyl glutarate (DSG) and disuccinimidyl suberate (DSS). These experiments revealed three unique regions of CaMKK2 within the kinase domain connected to three different regions of Ca^{2+}/CaM. Cross-links connect the CaMKK2 kinase domain with the N- and C-terminal domains of Ca^{2+}/CaM; the CaMKK2 Ca^{2+}/CaM binding domain to the C-terminus of Ca^{2+}/CaM; and the N-lobe of the CaMKK2 kinase domain to the first N-terminal helix of CaM. The presence of several cross-links between Ca^{2+}/CaM and the kinase domain of CaMKK2 indicates that the Ca^{2+}/CaM bound to CaMKK2 directly interacts with the kinase domain.

The SAXS parameters and obtained cross-links provided the basis and distance restraints for structural modeling of the complex. The docking simulation was performed using the program HADDOCK[83] using the crystal structure of the CaMKK2 kinase domain (PDB: 5UY6) and the solution structure of Ca^{2+}/CaM bound to the CaMKK1 CaM-binding segment (PDB: 1CKK)[84]. The structure with the lowest intermolecular energy chosen as a final model was in a good agreement with the distance restraints obtained from the chemical cross-linking experiments (*Fig. 4.9*) and it suggested that the kinase domain of CaMKK2 interacts with Ca^{2+}/CaM preferentially through surfaces surrounding the C-terminal part of helix αE.

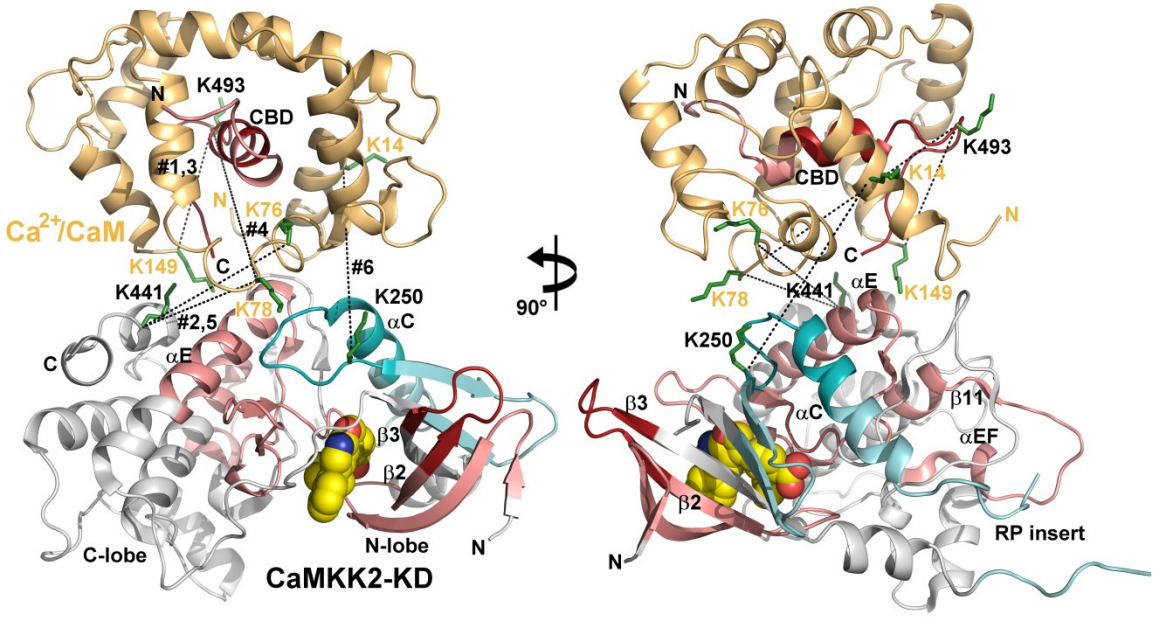

Figure 4.9. Model of the CaMKK2 KD:Ca^{2+}/CaM complex. The structure was modeled using the program HADDOCK[83] with the crystal structure of the CaMKK2 KD (PDB: 5UY6), the solution structure of Ca^{2+}/CaM bound to the CaMKK1 CaM-binding segment (PDB: 1CKK)[84], and intermolecular distance restraints obtained from the chemical cross-linking experiments.

4.2.5 Conclusion

The main aim of this study was to understand the molecular mechanism of the Ca^{2+}/CaM interaction with CaMKK2. The structural study revealed that the interaction between the CaMKK2 kinase domain and the autoinhibitory domain differs from other

CaMKs and involves surfaces of the N-terminal lobe of the kinase domain, including a unique Arg-Pro-rich insert. The HDX-MS results suggested that Ca^{2+}/CaM binding affects the structure of the regions surrounding the ATP binding pocket as well as the activation segment. The SAXS measurements further showed that the complex formed between CaMKK2 and Ca^{2+}/CaM is rather compact, and the Ca^{2+}/CaM bound to the autoinhibitory domain of CaMKK2 transiently interacts with the kinase domain.

Thus, our results indicate that interactions between the CaMKK2 kinase domain and the autoinhibitory domain differ from those of other CaMKs and that the autoinhibitory domain inhibits CaMKK2 by blocking the unique Arg-Pro-rich insert and by affecting the structure of the ATP-binding pocket.

4.3 Publication III: The role of 14-3-3 in the regulation of Caspase-2 protease activity

Smidova, A., Alblova, M., Kalabova, D., **Psenakova, K.,** Rosulek, M., Herman, P., Obsil, T. & Obsilova, V. 14-3-3 Protein Masks the Nuclear Localization Sequence of Caspase-2. *FEBS J.* **285**, 4196–4213 (2018).

My contribution: expression and purification of ^{15}N-labeled 14-3-3; sample preparation and further optimization for the NMR experiments; NMR experimental design and measurements; NMR data evaluation; docking calculations and refinement of the structural model based on the experimental data.

4.3.1 Motivation of the study

Caspase-2 is a human protease involved in the regulation of the apoptotic signaling cascades by proteolysis of cellular substrates. Capase-2 activity is inhibited by phosphorylation followed by 14-3-3 binding. 14-3-3 recognizes two phosphoserines within the caspase-2 sequence located in the linker between the caspase recruitment domain and the p19 domain. However, the mechanistic details of the 14-3-3 binding to caspase-2 and its role in the regulation of the caspase-2 activity remain unclear.

The main goal of this work was to determine the role of 14-3-3 in the regulation of caspase-2 by performing the structural and biophysical characterization of the complex between caspase-2 and 14-3-3.

4.3.2 The 14-3-3 binding surface mapping by NMR

To map the 14-3-3 binding interface in a complex with procaspase-2 (inactive caspase-2), the Nuclear magnetic resonance (NMR) spectroscopy was used. The published sequence-specific backbone resonance assignment of 14-3-3ζΔC construct (missing the flexible 12 residue long C-terminal tail) was used to analyze procaspase-2 biding-induced changes.[85] The NMR titration experiments of ^{15}N-labeled 14-3-3ζΔC by unlabeled procaspase-2 revealed several changes in signal positions and intensities upon the complex formation (*Fig. 4.10*, *4.11*). The most affected regions, involved in the interaction either directly or through conformational change, are helices forming the ligand-binding groove (H3, H5, H7, and H9) together with helices H4, H8 and H6 (*Fig. 4.11 C*). These changes suggest that the p12 and p19 domains of proCaspase-2 are located within the 14-3-3ζ central channel through interaction with the C-terminal helix H9. However, the affected residues of 14-3-3ζΔC are protruding from the inside to the outside of the dimer, suggesting that the binding effect propagates due to allosteric structural changes to the peripheral parts of the molecule that do not directly contribute to the procaspase-2 interaction.[86]

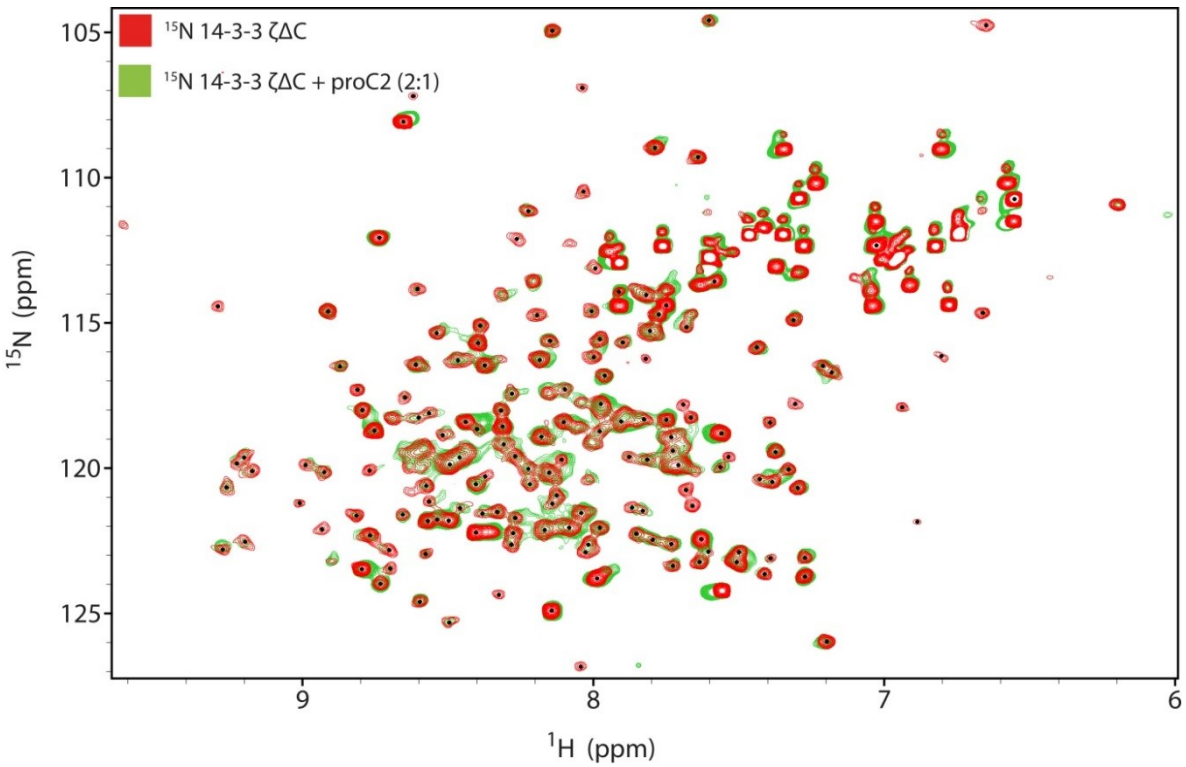

Figure 4.10. Procapse-2 (proC2) binding-induced changes in the ^{1}H-^{15}N HSQC NMR spectra of 14-3-3ζΔC. Comparison of the ^{1}H-^{15}N HSQC spectra of ^{15}N-labeled 14-3-3ζΔC in the absence (red) or in the presence of a two-fold molar excess of unlabeled proC2 (green).

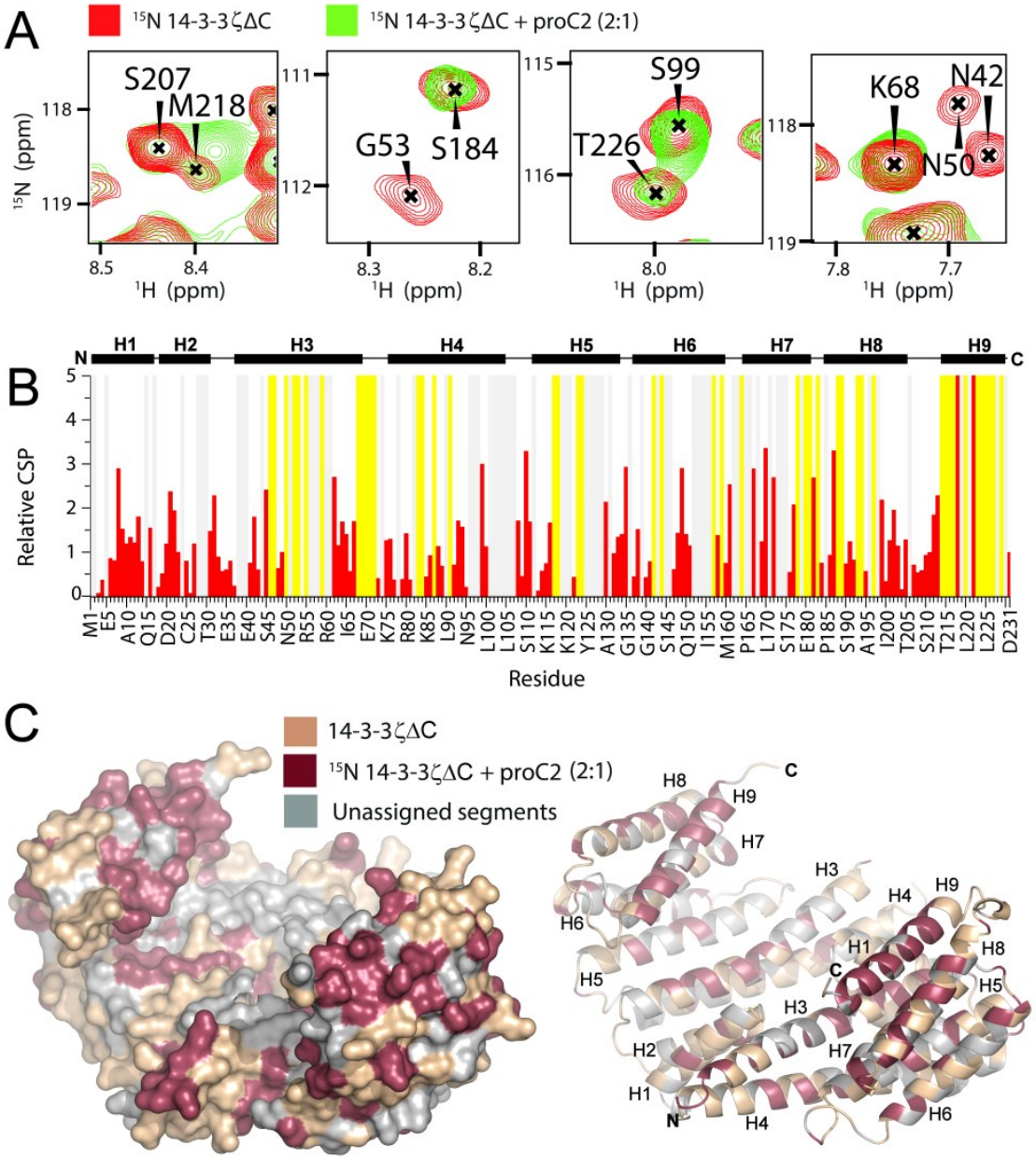

Figure 4.11. Procaspase-2 (proC2) binding-induced changes in the NMR spectra of 14-3-3ζΔC. proC2 binding to 14-3-3ζ was evaluated by NMR titration of ^{15}N-labeled 14-3-3ζΔC with unlabeled proC2 to a final molar ratio 2:1. **A)** Comparison of representative signals of free (red) and proC2-bound (green) 14-3-3ζΔC from the ^{1}H-^{15}N HSQC spectra. **B)** The summary of chemical shift perturbations (CSPs) and intensity change analysis of the 14-3-3ζΔC ^{1}H-^{15}N HSQC spectra induced by proC2 binding. The relative CSPs were calculated as a weighted combination of chemical shifts: $CSP = \sqrt{\left(\Delta\delta_H^2 + \left(\frac{1}{5}\Delta\delta_N\right)^2\right)}$, where

$\Delta\delta_H$ and $\Delta\delta_N$ are differences in chemical shifts of ^{1}H and ^{15}N, respectively, in the free and bound states.[87] The interaction induced both the change in positions (red bars) or intensities (yellow bars) of the signals in the ^{1}H-^{15}N HSQC spectrum of 14-3-3ζΔC. The regions of the protein backbone that could not be unambiguously assigned are highlighted in gray. The helical organization within 14-3-3ζΔC is indicated at the top. **C)** A range of the most significant CSPs and intensity changes mapped onto the 14-3-3ζ structure.[88]

4.3.3 The structural model of a procapase-2 in a complex with 14-3-3

A combined approach based on small angle X-ray scattering, NMR and chemical crosslinking coupled to mass spectrometry was used to obtain a structural model of a procapase-2 in the complex with 14-3-3ζ.

The small angle X-ray scattering (SAXS) data analysis revealed that the procaspase-2 is more flexible than the complex between procapsase-2 and 14-3-3ζ. The experimental SAXS curves with calculated parameters were then used for the structural modeling. To obtain the relative position of procaspase-2 and 14-3-3ζ within the complex, the chemical cross-linking coupled to MS experiment was performed. Two cross-linking agents that react with amine-groups were used: disuccinimidyl glutarate (DSG) and disuccinimidyl suberate (DSS). The data analysis showed three unique regions of procaspase-2 connected to three different regions of 14-3-3.

The SAXS parameters, obtained cross-links and NMR-derived binding surface provided initial platform and distance restraints for structural modeling. The initial structural model of the complex was created using the crystal structures of 14-3-3ζ (PDB: IQJB) and caspase-2 (PDB: 3R7S) (*Fig. 4.12*).[88,89]

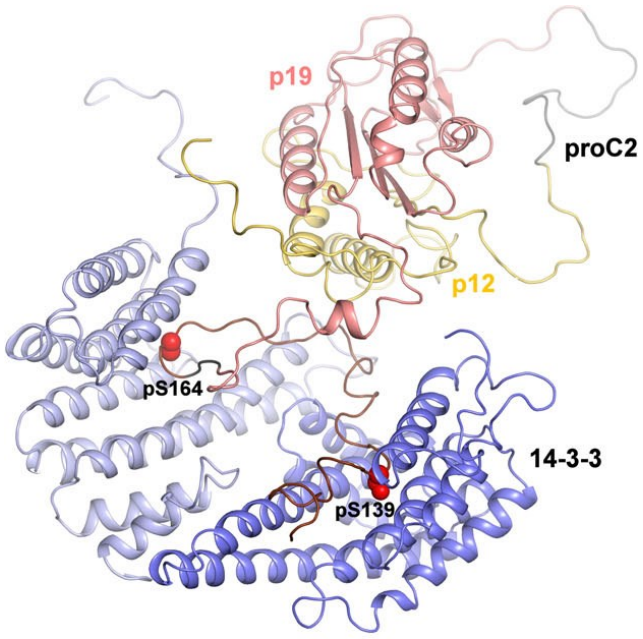

Figure 4.12. Structural model of the proC2:14-3-3ζ complex. The N-terminal procaspase-2 linker containing both 14-3-3 binding motifs is shown in brown with the phosphorylation sites in red; the p12 and p19 domains are shown in yellow and pink, respectively.

4.3.4 Conclusion

The structural analysis of the doubly phosphorylated caspase-2 in a complex with 14-3-3 showed that the p19 and the p12 domains of caspase-2 are positioned within the central channel of the 14-3-3 dimer. In this conformation, the surface of the p12 domain, which is involved in caspase-2 activation by dimerization, is sterically blocked by the 14-3-3ζ dimer, together with masking the nuclear localization sequence of caspase-2, which is located between the two phosphorylated 14-3-3 binding motifs. Therefore, the 14-3-3 binding may inhibit caspase-2 activation by interfering with the caspase-2 oligomerization and/or its nuclear localization.

4.4 Publication IV: Inhibition of the FOXO3-DNA interaction by small molecule inhibitors

Hagenbuchner, J., Obsilova, V., Kaserer, T., Rass, B, **Psenakova, K.,** Docekal, V., Alblova, M., Kohoutova, K., Spoden, G., Schuster, D., Aneichyk, T., Kofler, R., Vesely, J., Obexer, P., Obsil, T. & Ausserlechner, M.J. Modulation of FOXO3 transcriptional activity by small molecule inhibitors. *Submitted*

My contribution: expression and purification of ^{13}C,^{15}N-labeled FOXO3; sample preparation and further optimization for the NMR experiments; NMR experimental design and measurements; NMR assignment and data evaluation.

4.4.1 Introduction

FOXO3 is a member of the O subclass of the Forkhead box (FOX) family of transcription factors. Members of the FOXO subclass are critical regulators of stress resistance, longevity, or apoptosis in mammalian cells. Although other members of the FOXO subclass participate in tumor suppressing actions in cells, it has been shown that FOXO3 is also responsible for the tumor stem cell regeneration, drug- and chemo-resistance and metastases development during cancer advancement.[65,90] However, no inhibitors of FOXO3 transcription factor have been proposed to date.

The main aim of this study was to design and characterize drug-like compounds that would directly bind to the DNA-binding domain (DBD) of FOXO3 and inhibit its transcriptional activity.

4.4.2 Small molecule inhibitor S9 binds to the FOXO3-DBD

By a pharmacophore model-based, virtual *in silico* screening approach, the small molecule compound S9 was identified as a potential inhibitor of the FOXO3:DNA binding.

Structural characterization of the interaction between FOXO3-DBD and S9 was performed using nuclear magnetic resonance (NMR) spectroscopy. The saturation transfer difference (STD) NMR experiments and ^{1}H-^{15}N HSQC titrations were used to determine the actual binding mode of the small molecule and to estimate the dissociation constant of

this interaction. STD signals were detected for several protons of S9 and confirmed its interaction with FOXO3-DBD *in vitro* (*Fig. 4.13*). The data analysis suggested that both aromatic moieties as well as the aliphatic part of S9 are involved in direct interactions with FOXO3-DBD.

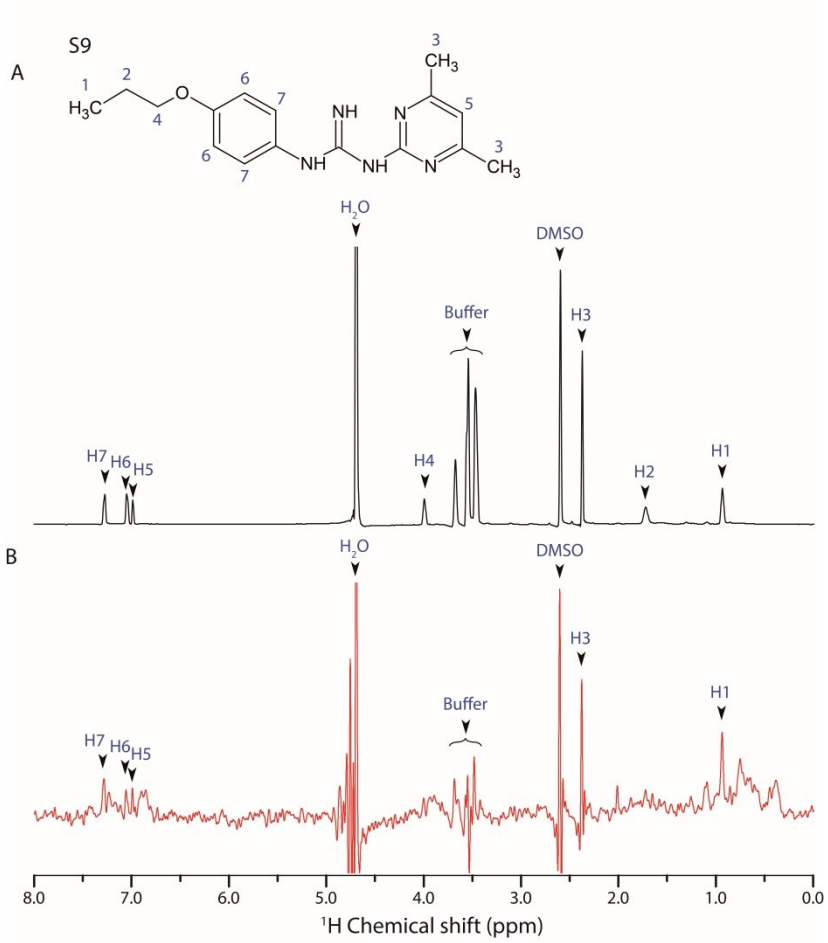

Figure 4.13. 1D ^{1}H STD-NMR experiments for the S9 compound in the presence of the 15 µM protein. A) Reference spectrum for the S9 compound in 10% DMSO (black) and **B)** corresponding STD-NMR spectrum (red). Chemically equivalent hydrogens in S9 molecule are numbered from 1 to 7.

Because the previously published NMR sequential assignment of human FOXO3-DBD[66] was obtained for shorter construct than the construct used in this study, standard triple resonance experiments were used to obtain a sequence specific backbone assignment

of FOXO3-DBD (residues 156–269). The data analysis provided a resonance assignment for the 99 out of the 114 residues (87% of the FOXO3-DBD sequence) (*Fig. 4.14*).

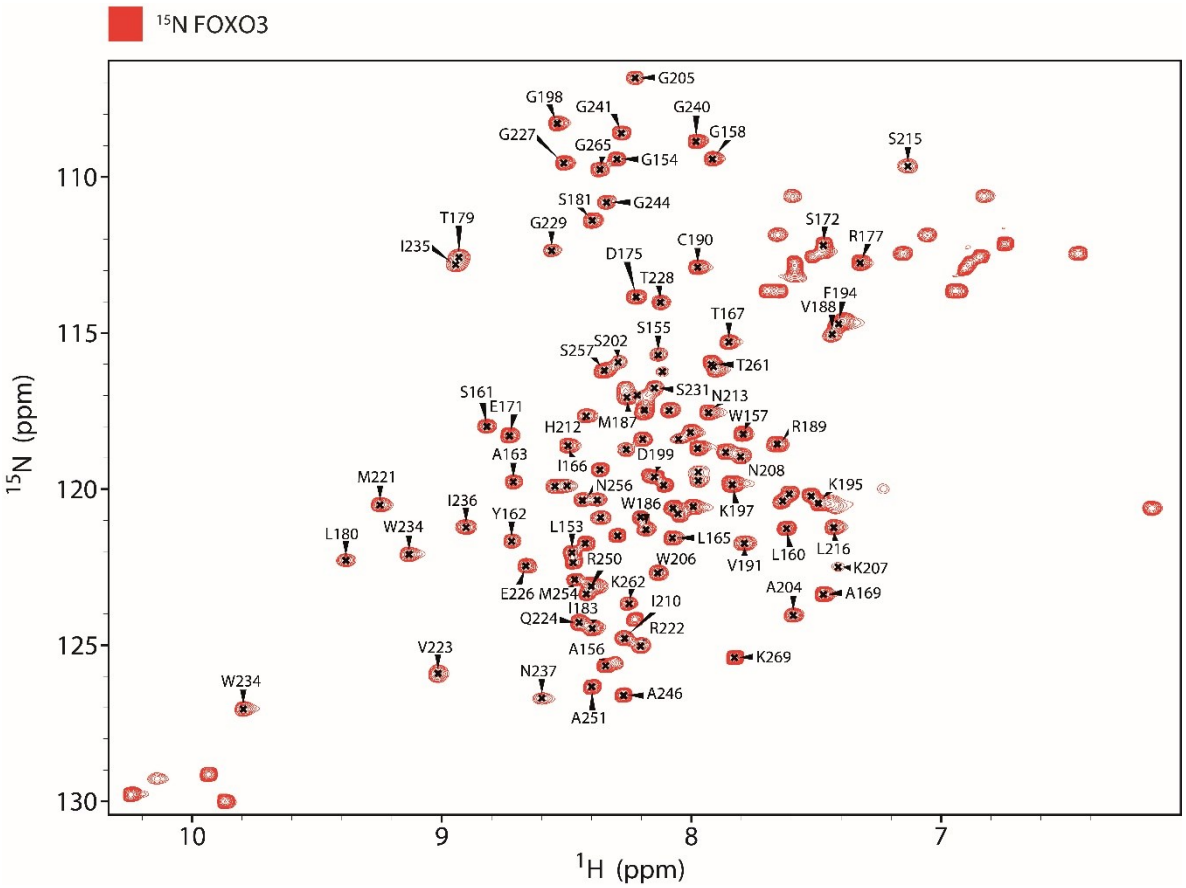

Figure 4.14. ^{1}H-^{15}N HSQC spectrum of ^{15}N-labeled FOXO3-DBD (residues 156-269). The analysis of the set of triple resonance experiments provided a resonance assignment for the 87% of the FOXO3-DBD residues.

To identify the S9-binding site in FOXO3-DBD, the oxalate salt of S9 (S9ox) was used for its higher solubility in water, avoiding the use of DMSO and the associated chemical interference. The ^{15}N-labeled FOXO3-DBD was titrated with four different concentrations of S9ox and ^{1}H and ^{15}N chemical shift perturbations (CSPs) of the backbone amide groups of FOXO3-DBD were followed in the ^{1}H-^{15}N HSQC spectra (*Fig. 4.15*, *4.16 A*). In total, thirteen FOXO3-DBD residues showed the chemical shift change greater than σ^{0}_{corr} above the mean, thus suggesting their contribution to the interaction or their conformational change induced by S9 binding (*Fig. 4.16 B*). The binding surface for S9 was identified by mapping the most affected residues onto the solution structure of

FOXO3-DBD (PDB: 2K86)[66], revealing the region formed by the DNA recognition α-helix H3 and the N-terminal part of β-strand S2 (*Fig. 4.17 A*). The dissociation constant was determined by plotting the normalized chemical shifts against the S9ox concentration, suggesting the binding affinity (K_D value) of 0.5 ± 0.2 mM (*Fig. 4.17 B*).

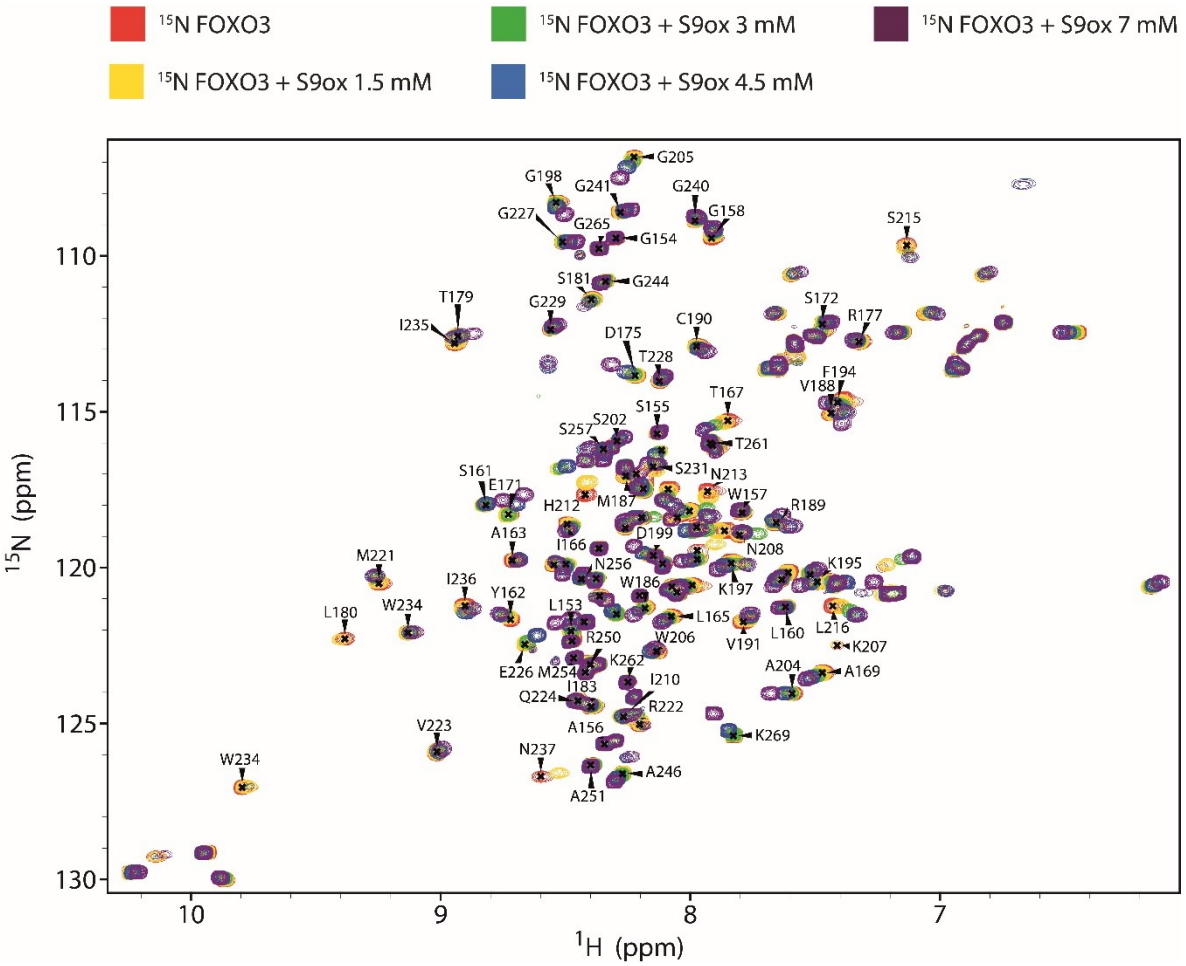

Figure 4.15. S9-oxalate binding to FOXO3-DBD. Comparison of the ^{1}H-^{15}N HSQC spectra of ^{15}N-labeled FOXO3-DBD from the titration of the 1.5 mM (yellow), 3 mM (green), 4.5 mM (blue) and 7 mM (violet) S9-oxalate into the FOXO3-DBD alone (red). The interaction induced both the change in signal positions or significant signal intensity reduction in the ^{1}H-^{15}N HSQC spectrum of FOXO3-DBD.

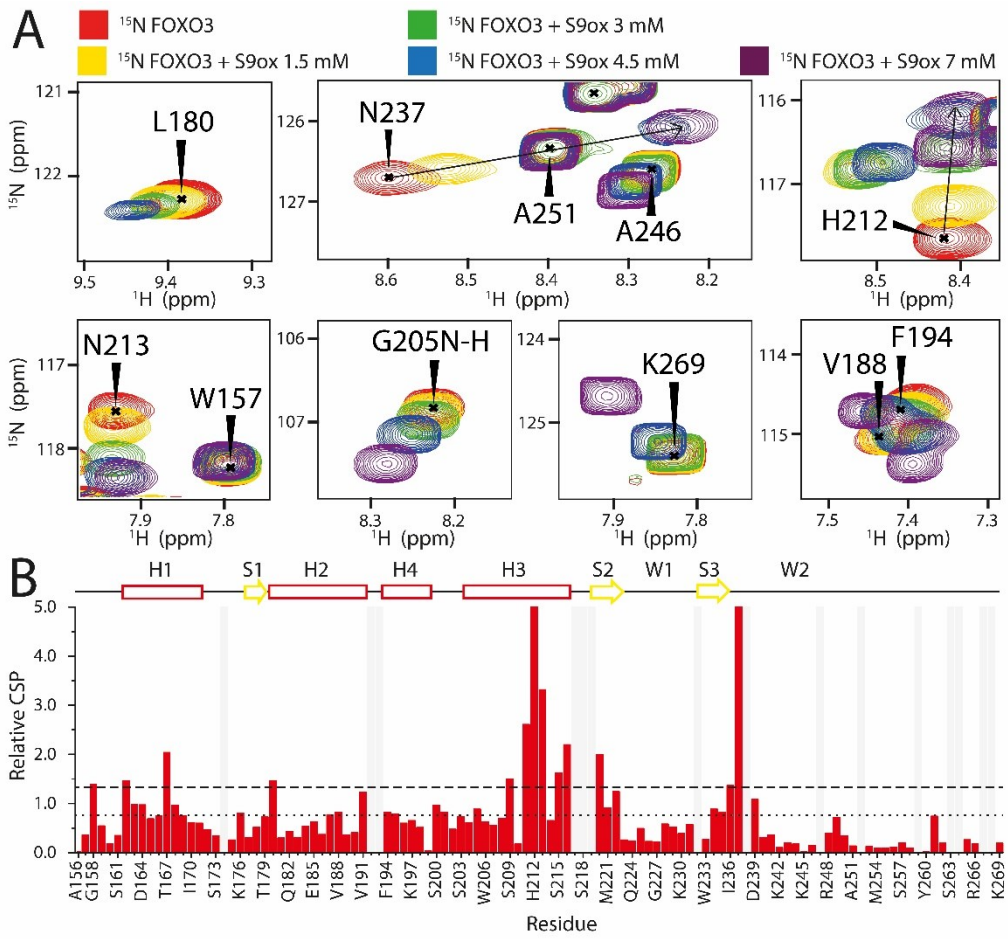

Figure 4.16. S9ox binding-induced changes in the NMR spectra of FOXO3. S9ox binding to FOXO3-DBD was evaluated by NMR titration of ^{15}N-labeled FOXO3 with S9. **A)** Comparison of representative signals of the ^{1}H-^{15}N HSQC spectra of ^{15}N-labeled FOXO3-DBD in the absence of S9ox (red) and in the presence of various concentrations of S9ox. **B)** The summary of quantified chemical shift perturbations (CSPs) obtained for FOXO3-DBD in the presence of 1.5 mM S9ox. The changes in chemical shift resonances were calculated using weighted combination of chemical shifts given by: $CSP = \sqrt{\Delta\delta_H^2 + (\frac{1}{5}\Delta\delta_N)^2}$, where $\Delta\delta_H$ and $\Delta\delta_N$ are differences in chemical shifts of ^{1}H and ^{15}N, respectively, in the free and bound states.[87] The regions of the protein backbone that could not be unambiguously assigned are highlighted in gray. The secondary structure of FOXO3-DBD is indicated on top. The dotted and dashed lines indicate changes greater than the mean and the mean + $1\sigma^{0}_{corr}$, respectively.

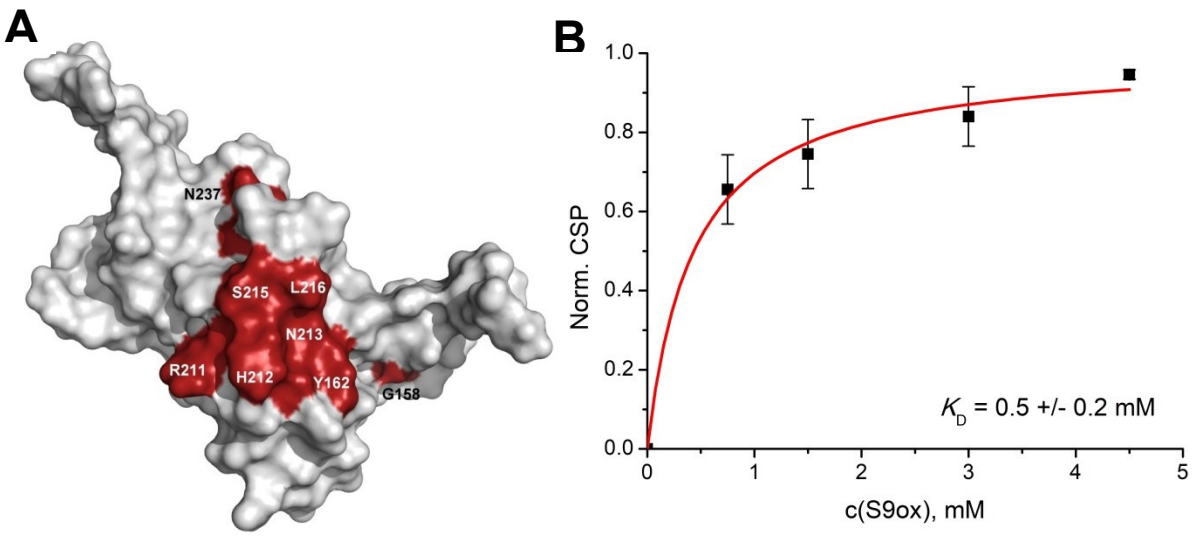

Figure 4.17. A) Observed CSPs mapped onto the surface representation of FOXO3-DBD.[66] Thirteen residues with significantly perturbed ($1\sigma^0_{corr}$ above the mean) ^{1}H-^{15}N resonances are shown in red. PDB: 2K86 **B) Representative binding isotherm of the interaction between FOXO3-DBD and S9ox.** The dissociation constant was determined by plotting the normalized chemical shifts against the S9ox concentration, revealing the binding affinity (K_D value) of 0.5 ± 0.2 mM.

4.4.3 Conclusion

By the *in silico* screening approach, the small molecule inhibitor S9 was identified as a potential compound binding to FOXO3-DBD. The structural studies confirmed the binding of S9 and its oxalate salt S9ox to FOXO3-DBD and the saturation transfer difference (STD) NMR experiments together with ^{1}H-^{15}N HSQC titrations analysis showed that the most affected residues on FOXO3 molecule are the ones responsible for the DNA recognition. The dissociation constant of the interaction between S9ox and FOXO3-DBD was calculated from the normalized chemical shifts. These results showed that it is possible to inhibit the FOXO binding to the target DNA, thus providing basis for the modulation of their transcriptional activity.

4.5 Publication V: The role of cysteines in the regulation of Apoptosis signal-regulating kinase 1 by thioredoxin

Kylarova, S., Kosek, D., Petrvalska, O., **Psenakova, K.,** Man, P., Vecer, J., Herman, P., Obsilova, V. & Obsil, T. Cysteine residues mediate high-affinity binding of thioredoxin to ASK1. *FEBS J.* **283**, 3821–3838 (2016).

My contribution: expression and purification of TRX, ASK1-TBD and cysteine and tryptophan mutants of ASK1-TBD, sample preparation and further optimization for tryptophan fluorescence; native gel electrophoresis experiments.

4.5.1 Motivation of the study

Apoptosis signal-regulating kinase 1 (ASK1) is a human protein kinase that phosphorylates and activates signaling pathways leading to apoptosis. Under reducing conditions, ASK1 forms a complex with thioredoxin (TRX) that dissociates upon oxidation leading to the kinase activation. However, the molecular details of interaction between ASK1 and TRX are not yet fully understood due to the lack of the structural data. It has previously been suggested that cysteine residues may play an important role in this protein-protein interaction.[17,75] Therefore, the main aim of this work was to determine the role of conserved cysteine residues in the interaction between the TRX binding domain of ASK1 (ASK1-TBD) and TRX.

4.5.2 The role of cysteine residues of ASK1-TBD in the ASK1:TRX complex dissociation

The ASK1-TBD sequence (residues 88-302) contains seven conserved cysteine residues: Cys^{120}, Cys^{185}, Cys^{200}, Cys^{206}, Cys^{225}, Cys^{226} and Cys^{250}. Because the 3D structure of this domain is still unknown, we first investigated the solvent accessibility of these cysteine residues. To this end, the protein sample was modified by 2-iodoacetamide (IAA) under native conditions, digested on immobilized pepsin column and directly analyzed by liquid chromatography combined with mass spectrometry (LC-MS/MS). The data analysis

showed that the only inaccessible cysteine is Cys^{120}, residues Cys^{200}, Cys^{206} and Cys^{250} were alkylated almost completely, Cys^{185} was modified by IAA from the 40 % and the adjacent cysteines Cys^{225} and Cys^{226} were alkylated from the 20 % and 80%, respectively (*Fig. 4.18*).

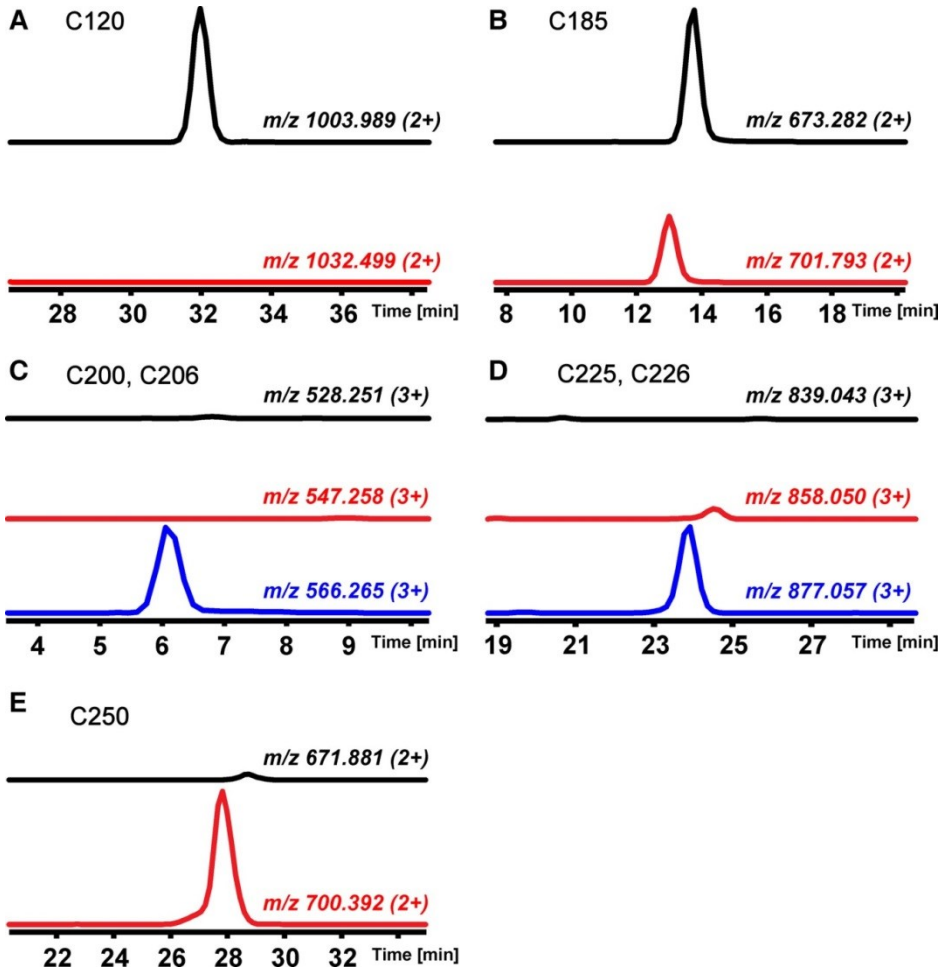

Figure 4.18. Accessibility and reactivity of cysteines in the ASK1-TBD modified with iodoacetamide. Extracted ion chromatograms for selected peptides covering cysteines in the ASK1-TBD sequence are shown: **A)** Cys^{120}, **B)** Cys^{185}, **C)** Cys^{200} and Cys^{206}, **D)** Cys^{225} and Cys^{226}, **E)** Cys^{250}. Traces are colored according to the extent of modification: unmodified (black), singly (red), and doubly (blue) alkylated. Mass-to-charge (m/z) ratios used to plot the chromatograms are indicated above each trace.

To study the importance of the individual cysteine residues of the ASK1-TBD for the TRX binding, the serine-scanning mutagenesis of Cys residues together with the analytical ultracentrifugation (AUC) was used. The AUC data analysis revealed no significant differences in binding affinities of prepared mutants compared to the wild-type ASK1-TBD except the mutant missing the Cys^{250} residue. This was consistent with the previously published data suggesting that this cysteine residue is essential for the TRX binding.[91]

To explore the presence of cysteines at the TRX-binding surface of ASK1-TBD, the catalytically inactive and very reactive mutant of TRX Cys^{35}Ser were prepared and incubated with the ASK1-TBD in a buffer lacking reducing agents. The cross-linked ASK1-TBD:TRX complex was formed and the analysis revealed that the ASK1-TBD and TRX are connected through a disulfide bond between Cys^{32} of TRX and Cys^{200} of the ASK1-TBD. This strongly suggests that the catalytic site of TRX interacts with the ASK1-TBD region containing residue Cys^{200}.

4.5.3 The role of TRX cysteine residues in the ASK1:TRX complex dissociation

To investigate the role of TRX cysteine residues in the ASK1:TRX complex, the AUC was used. The serine mutants of all five cysteines within the TRX sequence (Cys^{32}, Cys^{35}, Cys^{62}, Cys^{69} and Cys^{73}) were prepared. The AUC data analysis revealed that only TRX Cys^{32} to Ser mutant failed to bind ASK1-TBD with high affinity, thus strongly suggesting that from the two catalytic cysteines, the Cys^{32} residue is the one required for the high-affinity binding to the ASK1-TBD. These experiments also revealed that the region containing cysteines Cys^{62} and Cys^{69} is not a part of the ASK1-TBD-binding surface of TRX.

4.5.4 Conclusion

This work revealed that within the ASK1-TBD sequence, the only inaccessible cysteine is Cys^{120}, whereas residues Cys^{200}, Cys^{206} and Cys^{250} were found almost completely solvent accessible. Cys^{185} is accessible from the 40 % and the adjacent cysteines

Cys^{225} and Cys^{226} are accessible from the 20 % and 80%, respectively. The ASK1-TBD serine mutants of cysteine residues (without buried Cys^{120}) showed no significant differences in binding affinities, except of mutant missing Cys^{250} that has been previously shown to be essential for the TRX binding. The cross-linked ASK1-TBD:TRX complex formed under oxidative conditions with the reactive catalytically inactive TRX mutant revealed that the catalytic site of TRX interacts with the ASK1-TBD region containing residue Cys^{200}. In the case of TRX, the AUC data analysis showed that from the two catalytic cysteines, the Cys^{32} is the one responsible for the binding to ASK1-TBD and the region of cysteines Cys^{62} and Cys^{69} does not participate in this protein-protein interaction.

4.6 Publication VI (manuscript in preparation): Molecular mechanism of the Apoptosis signal-regulating kinase 1 activation

Psenakova, K., Hexnerova, R., Srb, P., Veverka, V., Obsilova, V. & Obsil, T. Structural characterization of the Thioredoxin-binding domain of ASK1 reveals molecular mechanism of the ASK1 activation. (2019) *In preparation.*

My contribution: design of all experiments; expression and purification optimization of the unlabeled and $^{2}H,^{13}C,^{15}N$-labeled ASK1-TBD in deuterium oxide, unlabeled and $^{13}C,^{15}N$-labeled TRX and the ^{15}N-labeled ASK1-TBD Cys^{250} to Ser mutant; extensive screening for the stabilizing conditions for NMR samples; optimization of the setup for NMR experiments; NMR data acquisition and processing; sequence-specific NMR resonance assignment for the ASK1-TBD and TRX; docking calculations and refinement of the structural model based on the experimental data.

4.6.1 Motivation of the study

Apoptosis signal-regulating kinase 1 (ASK1) is a human protein kinase at the top of the mitogen-activated protein kinase (MAPK) cascade, the signal transduction pathway that is important for a cell defense system against various stress signals. The ASK1 kinase

activity is inhibited by interaction with two physiological binding partners – mammalian thioredoxin (TRX) and the 14-3-3 protein. In an inactive state, ASK1 forms a dimer with TRX bound at its N-terminal domain and 14-3-3 at the C-terminus of the catalytic domain. Upon oxidative stress conditions, the TRX dissociation is followed by the 14-3-3 dissociation leading to the kinase activation. The detailed molecular mechanism of the ASK1 activation is however still unknown, due to the lack of structural data. The main aim of this work was to determine the structure of the thioredoxin-binding domain of ASK1 (ASK1-TBD) and exploit the structural data for better understanding of the ASK1 activation mechanism.

4.6.2 The ASK1-TBD structure description

Despite an intensive effort, all attempts to crystallize this domain to determine its structure using X-ray crystallography were unsuccessful. Therefore, we decided to prepare the uniformly labeled $^{2}H,^{13}C,^{15}N$ ASK1-TBD (residues 88-267) in a sufficient concentration and purity for NMR characterization. The instability of the protein required prior screening for optimal conditions using various additives. The final sample was prepared in a buffer containing 20 mM HEPES (pH=7.0), 200 mM NaCl, 5 mM EDTA, 5 mM TCEP, 20 mM glycine and 2% glycerol. The sequence-specific NMR resonance assignments were obtained using the TROSY based versions of the standard triple resonance NMR experiments: HNCA, HNCACB, CBCA(CO)NH, HNCO, HN(CA)CO at the 600 MHz and 850 MHz spectrometers.[92,93] The spectra contained resonances for a smaller number of residues than expected for the used construct, suggesting that some protein regions are subjected to a conformational heterogeneity on the NMR timescale. In addition, the signals in several spectral regions were severely overlapped. As a consequence, the complete backbone resonance assignments including H^N, N^H, CO, C^α and C^β were obtained for 116 out of the total 185 residues (63% of the molecule). The additional 11 residues were only partially assigned. The assigned resonances were used as an input for the program TALOS that provides highly reliable prediction of protein backbone torsion angles from NMR chemical shifts.[94] The prediction suggested a globular conformation composed of 6 α-helices and 5 β-strands (*Fig. 4.19*). The organization of the secondary structure elements was also supported by several characteristic H^N-H^N NOE

contacts that were unambiguously assigned in the ^{15}N-edited NOESY spectrum. The close inspection of the NOE contact pattern revealed that all β-strands are folded into a single β-sheet with parallel orientation. Both the N- and C-terminal regions of ASK1-TBD were well defined, however the resonances within several longer regions throughout the molecule were missing, perhaps due to the dynamic behavior that led to unfavorable NMR chemical exchange.[95]

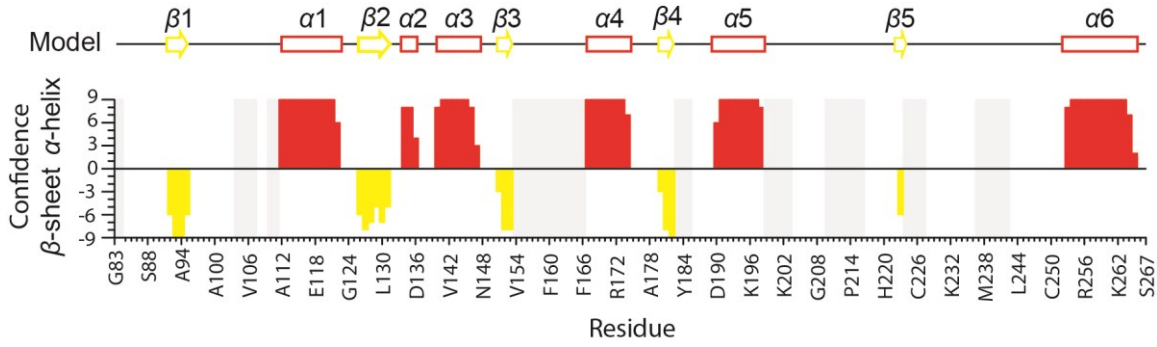

Figure 4.19. ASK1-TBD secondary structure distribution determined from NMR chemical shifts by TALOS.[94] The secondary structure prediction is represented by yellow (β-sheet) and red (α-helices) bars, while the height of the bars reflects the confidence of the prediction. The regions of the protein backbone that could not be unambiguously assigned are highlighted in gray.

Next, we used chemical cross-linking coupled to mass spectrometry (XL-MS) with disuccinimidyl dibutyric urea (DSBU) and adipic acid dihydrazide (ADH) as bifunctional agents to determine the ASK1-TBD intramolecular distance restraints for structural modeling purposes. Identified cross-links provided one distance restraint for DSBU and five for ADH (the length of the spacer arm is 12 Å, thus adding 6.5 Å for each cross-linked lysine side chain and allowing for a conformational dynamics within ~30 Å range) (*Tab. 4.3*).

Table 4.3. Intramolecular cross-links within ASK1-TBD obtained with ADH and DSBU.

		Cross-linked peptides		Cross-linked residues	Observed mass	Theoretical mass	Error (ppm)
ADH[a]	1	135-145	173-196	D136-E173	4152.984	4152.985	-0.2
	2	233-256	173-196	E236-E173	5633.854	5633.86	-1.1
	3	263-268	233-256	C-term[b]-E236	3358.848	3358.847	0.41
	4	197-202	173-196	E197-E173	3677.76	3677.761	-0.1
	5	135-145	91-117	D136-E109	4279.22	4279.22	-0.02
DSBU[a]	6	82-89	257-268	N-term[b]-K262	2078.105	2078.106	-0.6

[a]ADH: adipic acid dihydrazide; DSBU: disuccinimidyl dibutyric urea

[b]C-term: the C-terminal carboxylic group and N-term: the N-terminal amine group

Overall, the data analysis provided the 17 non-redundant H^N-H^N experimental NOE-derived distance constraints, 98 ϕ and 98 ψ dihedral angle constraints and six distance restraints based on cross-links that will be used as an experimental cross-validation for the *ab initio* calculation of the ASK1-TBD structural model using the ROSETTA algorithm.[96]

4.6.3 ASK1-TBD structural changes upon TRX binding, oxidation and Cys^{250} to Ser mutation

In order to determine the TRX binding surface of ASK1-TBD, we performed a titration of the ^{15}N-labeled ASK1-TBD by unlabeled TRX and followed the changes of the residue-specific signals in the 2D ^{1}H-^{15}N HSQC spectra (*Fig. 4.20 A, B*). The analysis of NMR titrations suggested that the TRX binding interface on the ASK1-TBD includes mainly the N-terminal segment, the region containing helix *α*4 and the C-terminal part of the molecule including the very C-terminal *α*-helix (*α*6).

It has previously been speculated that the oxidation of ASK1-TBD may participate in the dissociation of the complex between ASK1 and TRX (Publication V: The role of cysteines in the regulation of Apoptosis signal-regulating kinase 1 by thioredoxin, *Supplement S5*). To investigate the structural changes upon ASK1-TBD oxidation, we collected and analyzed a series of the 2D ^{1}H-^{15}N HSQC spectra under mild oxidative conditions. The oxidation effect on the ASK1-TBD structure was evaluated by the analysis

of spectra acquired at several time points after addition of hydrogen peroxide (*Fig. 4.20 C, D*). The data analysis revealed that the oxidation of ASK1-TBD affects the N-terminal segment, the region containing helix α4 and α5 and the C-terminal part of the molecule including the C-terminal α-helix (α6). These regions also include residues involved in the TRX binding, thus indicating that oxidation of ASK1-TBD is directly involved in the destabilization of the ASK1:TRX complex.

Previous studies have suggested that Cys^{250} located within the C-terminal part of ASK1-TBD plays an important role in the TRX binding as its mutation severely affected this protein-protein interaction.[91] However, the details of Cys^{250} involvement in the TRX binding are unclear, as there is also a possibility that the mutation of Cys^{250} affects the tertiary structure of ASK1-TBD and thus its ability to interact with TRX. To investigate the potential structural changes induced by Cys^{250} to Ser mutation, we analyzed the changes in 2D ^{1}H-^{15}N HSQC spectra induced by this mutation (*Fig. 4.20 E, F*). The changes were mainly observed in regions containing helix α4 and the C-terminal part of the molecule. When compared to the TRX binding-induced CSPs, the structural changes caused by the Cys^{250} mutation include regions involved in the TRX binding. This indicates that the effect caused by C250S mutation is based on the conformational change of ASK1-TBD rather than on direct involvement of this residue in the TRX binding.

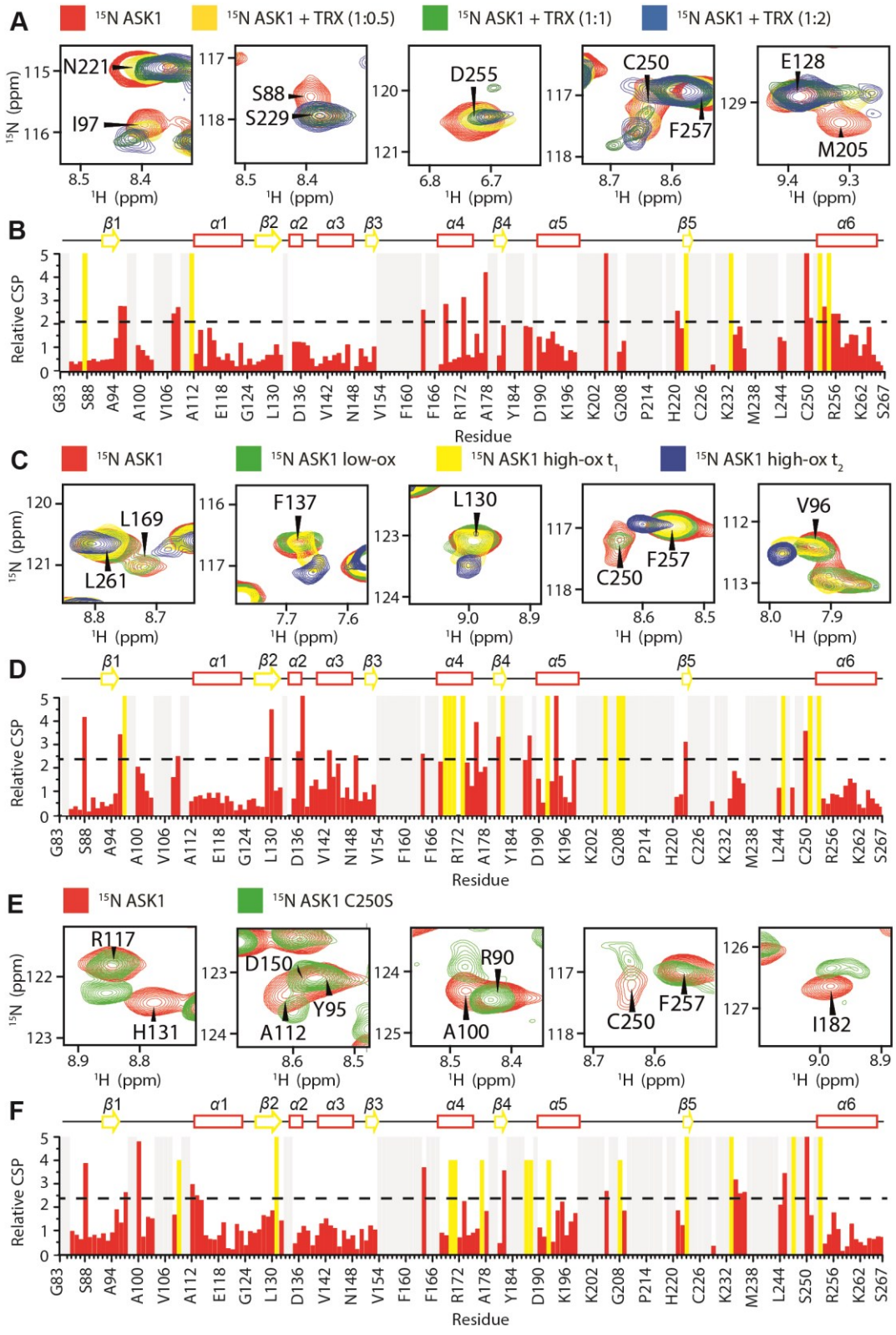

Figure 4.20. Structural changes of ASK1-TBD induced by TRX binding, oxidation and C250S mutation. A) Comparison of representative signals from

the ^{1}H-^{15}N HSQC spectra of the ^{15}N-labeled ASK1-TBD (red) obtained from the titration of 0.5 molar excess (yellow), 1 molar excess (green), and 2 molar excess (blue) of TRX. **B)** The summary of quantified relative chemical shift perturbations (CSPs) obtained for ASK1-TBD in the presence of TRX in 1:2 molar ratio. The changes in chemical shift resonances were calculated using weighted combination of chemical shifts given by: $CSP = \sqrt{\Delta\delta_H^2 + (\frac{1}{5}\Delta\delta_N)^2}$, where $\Delta\delta_H$ and $\Delta\delta_N$ are differences in chemical shifts of ^{1}H and ^{15}N, respectively, in the free and bound states.[87] The relative CSPs were obtained by dividing absolute CSP values by a standard deviation of the whole set of CSPs, the dashed line indicates changes greater than the mean + 1× SD (CSP > 2.1). The interaction induced both the change in positions (red bars) or significant reduction of intensities of signals (yellow bars) in the ^{1}H-^{15}N HSQC spectrum of ASK1. The regions of the protein backbone that could not be unambiguously assigned are highlighted in gray. **C)** Comparison of representative signals in the ^{1}H-^{15}N HSQC spectra obtained from the reduced form of ASK1-TBD (red), ASK1-TBD after O/N dialysis into the buffer without reducing agents (low-ox form, green), ASK1 after the treatment with a 5-fold excess of hydrogen peroxide after 20 minutes (high-ox t_1, yellow) and after 1 hour (high-ox t_2, blue). **D)** The CSP analysis of the ^{1}H-^{15}N HSQC spectrum of ASK1 upon oxidation. The relative CSPs were calculated as in B). The oxidation induced both the change in positions (red bars) or significant reduction of intensities of signals (yellow bars) in the ^{1}H-^{15}N HSQC spectrum of ASK1. The dashed line indicates changes greater than the mean + 1× SD (CSP > 2.4). The unassigned amino-acids are highlighted in gray. **E)** Comparison of the ^{1}H-^{15}N HSQC spectra obtained from the ASK1 molecule (red) and ASK1 C250S mutant (green). **F)** The CSP analysis of the ^{1}H-^{15}N HSQC spectrum of ASK1 after introducing a C250S mutation. The relative CSPs were calculated as in B). The mutation induced both the change in positions (red bars) or significant reduction of intensities of signals (yellow bars) in the ^{1}H-^{15}N HSQC spectrum of ASK1. The dashed line indicates changes greater than the mean + 1× SD (CSP > 2.4). The unassigned amino-acids are highlighted in gray.

4.6.4 TRX directly interacts with ASK1 with its redox-active site

To map the binding interface on TRX by NMR titration of ^{15}N-labeled TRX by the unlabeled ASK1-TBD (*Fig. 4.21 A, B*), we used uniformly labeled ^{13}C,^{15}N TRX with mutated Cys^{73} to Ser to prevent its dimerization. First, we obtained the sequential resonance assignments for TRX under buffer conditions required for the ASK1-TBD stability using the HNCACB, CBCA(CO)NH, HNCO and HN(CA)CO experiments.[92,93] The backbone resonance assignment was obtained for 101 out of the 105 residues. The TRX residues significantly perturbed by ASK1-TBD binding (the relative chemical shift perturbation values CSPs > 2.0, mean + 1× SD) form a distinct patch on the TRX surface highlighting the actual site of the ASK1 interaction (*Fig. 4.21 C, D*). The binding interface is relatively large; the regions most affected by ASK1 binding are centered around the redox-active site WC^{32}GPC^{35} and involve also loops in the vicinity of the α3 helix and the C-terminal α4 helix (residues 71-76 and 89-92, respectively). The observed values of CSPs correlate with the solvent accessibility of these residues and show that buried residues are not involved in the interaction.

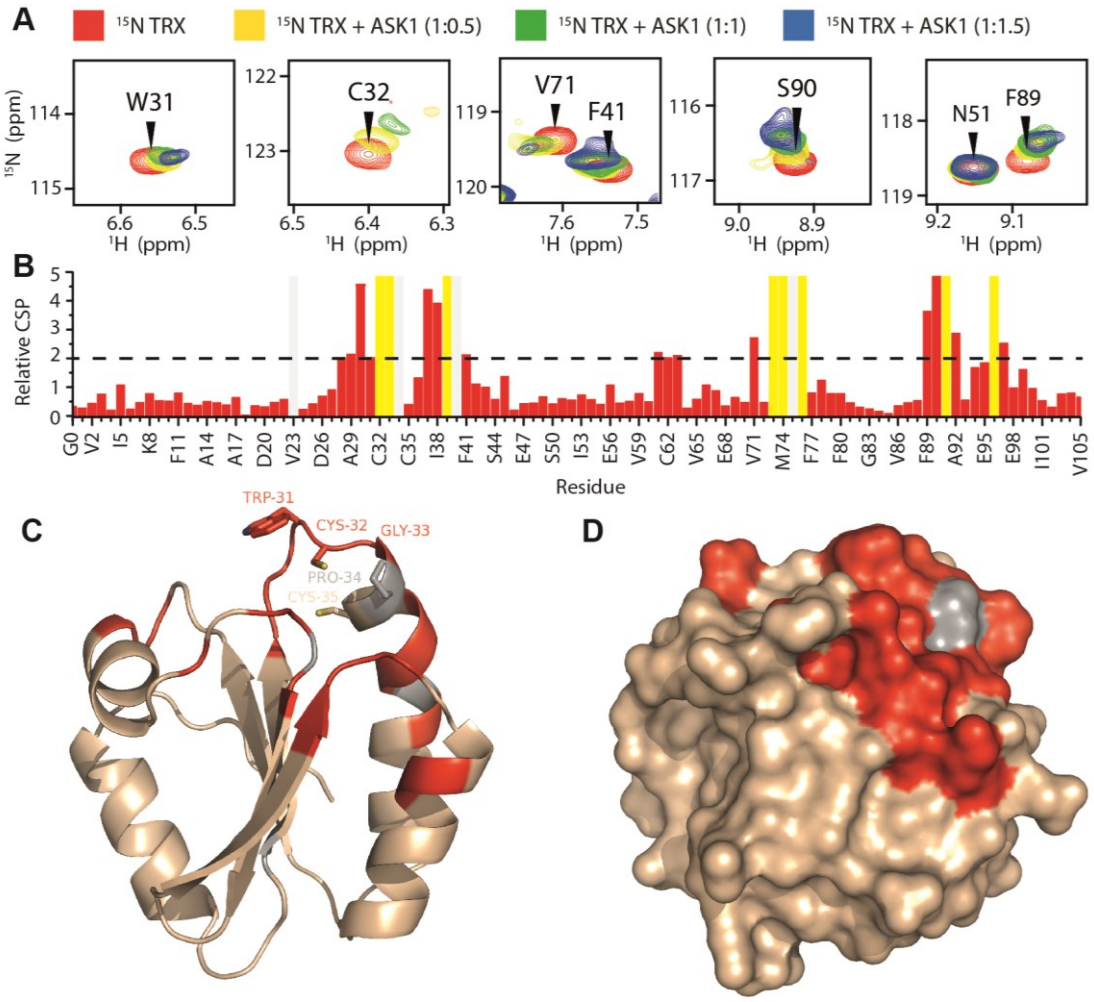

Figure 4.21. The ASK1 binding surface on the TRX molecule. A) Comparison of representative signals of the ^{1}H-^{15}N HSQC spectra obtained from the titration of 0.5 molar excess (yellow), 1 molar excess (green), and 1.5 molar excess (blue) of ASK1 to the free TRX (red). **B)** The CSP analysis of the ^{1}H-^{15}N HSQC spectrum of TRX upon ASK1 binding to the final 1:1.5 molar ratio, calculated as in Fig. 4.21 B). The interaction induced both the change in positions (red bars) or significant reduction of intensities of signals (yellow bars) in the ^{1}H-^{15}N HSQC spectrum of TRX. The dashed line indicates changes greater than the mean + 1× SD. The unassigned amino-acids are highlighted in gray. **C)** A range of the most significant CSPs (CSP > 2.0, mean + 1× SD) mapped onto TRX structure.[31] Unassigned prolines are highlighted in gray; backbone amide signals most affected by ASK1 binding are highlighted in red; the redox-active region $WC^{32}GPC^{35}$ is shown as sticks. PDB: 1ERT **D)** Surface representation of C).

4.6.5 Conclusion

The main objective of this work was the structural characterization of the ASK1-TBD as well as of its complex with TRX. The extensive conformational heterogeneity of the studied ASK1-TBD that was manifested by the lack of signals in the NMR spectra for more than 40% of the residues, and unfavorable stability prevented the attempts for the full structural determination using a standard NMR approach. Overall, the data analysis provided several experimental constraints together with the secondary structure assignment; however the structural model that would fully satisfied the experimental constrains was not yet obtained, mainly due to the extensive sparsity of the accessible NMR data.

The NMR titration analysis showed that TRX interacts with ASK1 with its redox active site and the TRX binding interface on the ASK1-TBD is formed by helix α4 and the C-terminal part of the molecule including the C-terminal α-helix (α6). In addition, the distribution of changes in the NMR spectra associated with the oxidative stress suggested that the ASK1 oxidation is an important signal for the complex dissociation. Introducing the C250S mutation caused conformational changes observed in regions involved in the TRX binding, suggested that the Cys^{250} mutation causes structural changes that prevent the binding, rather than being directly involved in the complex formation.

5 CONCLUSIONS

The main aim of this doctoral thesis was to study the molecular mechanism of the inhibition of four signaling proteins: Calcium/Calmodulin (Ca^{2+}/CaM)-dependent kinase kinase 2, Caspase-2, Forkhead transcription factor FOXO3 and Apoptosis signal-regulating kinase 1. By applying various biophysical techniques including the nuclear magnetic resonance spectroscopy, small angle X-ray scattering, time-resolved fluorescence spectroscopy, analytical ultracentrifugation and mass spectrometry, I investigated:

1. The role of 14-3-3 and CaM in the regulation of CaMKK2 activity. The experimental data revealed that the 14-3-3 binding does not inhibit the CaMKK2 kinase activity, but rather downregulates its dephosphorylation. The interactions between the CaMKK2 kinase domain and the autoinhibitory domain differ from those of other CaMKs and the autoinhibitory domain inhibits CaMKK2 by blocking the unique Arg-Pro-rich insert and by affecting the structure of the ATP-binding pocket.

2. The role of 14-3-3 in the regulation of Caspase-2 protease activity. The study revealed that the 14-3-3-dependent inhibition relies on interfering with the caspase-2 oligomerization and/or its nuclear localization.

3. The small-molecule compound binding to the DNA-binding domain of FOXO3. The study revealed the ability to inhibit FOXO transcription factors by small molecule compounds and provided structural basis for the modulation of their transcriptional activity.

4. The molecular mechanism of the Apoptosis signal-regulating protein kinase 1 activation. The structural studies of the TRX binding domain of ASK1 revealed that TRX directly interacts with ASK1 with its redox active site, the binding interface is relatively large and in ASK1 it includes the C-terminal alpha-helix. Introducing the Cys^{250} mutation causes structural changes that prevent the TRX binding, rather than being directly involved in the complex formation. Oxidative stress induces structural changes in the ASK1 molecule in regions involved in TRX binding, suggesting that the ASK1 oxidation is also involved in the complex dissociation.

6 REFERENCES

1. Liu, D. *et al.* Crystal structure of the zeta isoform of the 14-3-3 protein. *Nature* **376**, 191–194 (1995).

2. MOORE, B. W. & MCGREGOR, D. Chromatographic and Electrophoretic Fractionation of Soluble Proteins. *J. Biol. Chem.* **240**, 1647–1653 (1965).

3. Aitken, A. *et al.* Specificity of 14-3-3 isoform dimer interactions and phosphorylation. *Biochem. Soc. Trans.* **30**, 351–60 (2002).

4. Xiao, B. *et al.* Structure of a 14-3-3 protein and implications for coordination of multiple signalling pathways. *Nature* **376**, 188–91 (1995).

5. Truong, A. B., Masters, S. C., Yang, H. & Fu, H. Role of the 14-3-3 C-terminal loop in ligand interaction. *Proteins* **49**, 321–5 (2002).

6. Obsil, T., Ghirlando, R., Klein, D. C., Ganguly, S. & Dyda, F. Crystal structure of the 14-3-3zeta:serotonin N-acetyltransferase complex. a role for scaffolding in enzyme regulation. *Cell* **105**, 257–67 (2001).

7. Matsuzawa, A. & Ichijo, H. Stress-Responsive Protein Kinases in Redox-Regulated Apoptosis Signaling. *Antioxid. Redox Signal.* **7**, 472–481 (2005).

8. Ichijo, H. *et al.* Induction of apoptosis by ASK1, a mammalian MAPKKK that activates SAPK/JNK and p38 signaling pathways. *Science* **275**, 90–94 (1997).

9. Takeda, K., Matsuzawa, A., Nishitoh, H. & Ichijo, H. Roles of MAPKKK ASK1 in Stress-Induced Cell Death. *Cell Struct. Funct.* **28**, 23–29 (2003).

10. Takizawa, T., Tatematsu, C. & Nakanishi, Y. Double-stranded RNA-activated protein kinase interacts with apoptosis signal-regulating kinase 1: Implications for apoptosis signaling pathways. *Eur. J. Biochem.* **269**, 6126–6132 (2002).

11. Hayakawa, R., Hayakawa, T., Takeda, K. & Ichijo, H. Therapeutic targets in the ASK1-dependent stress signaling pathways. *Proc. Jpn. Acad. Ser. B. Phys. Biol. Sci.* **88**, 434–53 (2012).

12. Bunkoczi, G. *et al.* Structural and Functional Characterization of the Human Protein Kinase ASK1. *Structure* **15**, 1215–1226 (2007).

13. Weijman, J. F. *et al.* Structural basis of autoregulatory scaffolding by apoptosis signal-regulating kinase 1. *Proc. Natl. Acad. Sci.* **114**, E2096–E2105 (2017).

14. Obsil, T. & Obsilova, V. Structural aspects of protein kinase ASK1 regulation. *Adv. Biol. Regul.* **66**, 31–36 (2017).

15. Goldman, E. H., Chen, L. & Fu, H. Activation of Apoptosis Signal-regulating Kinase 1 by Reactive Oxygen Species through Dephosphorylation at Serine 967 and 14-3-3

Dissociation. *J. Biol. Chem.* **279**, 10442–10449 (2004).

16. Petrvalska, O. *et al.* Structural insight into the 14-3-3 protein-dependent inhibition of protein kinase ASK1 (apoptosis signal-regulating kinase 1). *J. Biol. Chem.* **291**, 20753–20765 (2016).

17. Saitoh, M. *et al.* Mammalian thioredoxin is a direct inhibitor of apoptosis signal-regulating kinase (ASK) 1. *EMBO J.* **17**, 2596–2606 (1998).

18. Nishitoh, H. *et al.* ASK1 is essential for JNK/SAPK activation by TRAF2. *Mol. Cell* **2**, 389–395 (1998).

19. Liu, H., Nishitoh, H., Ichijo, H. & Kyriakis, J. M. Activation of apoptosis signal-regulating kinase 1 (ASK1) by tumor necrosis factor receptor-associated factor 2 requires prior dissociation of the ASK1 inhibitor thioredoxin. *Mol. Cell. Biol.* **20**, 2198–2208 (2000).

20. Tobiume, K., Saitoh, M. & Ichijo, H. Activation of apoptosis signal-regulating Kinase 1 by the stress-induced activating phosphorylation of pre-formed oligomer. *J. Cell. Physiol.* **191**, 95–104 (2002).

21. Noguchi, T. *et al.* Recruitment of tumor necrosis factor receptor-associated factor family proteins to apoptosis signal-regulating kinase 1 signalosome is essential for oxidative stress-induced cell death. *J. Biol. Chem.* **280**, 37033–37040 (2005).

22. Shiizaki, S., Naguro, I. & Ichijo, H. Activation mechanisms of ASK1 in response to various stresses and its significance in intracellular signaling. *Adv. Biol. Regul.* **53**, 135–144 (2013).

23. Nagahara, N. Catalytic site cysteines of thiol enzyme: sulfurtransferases. *J. Amino Acids* **2011**, 709404 (2011).

24. Laurent, T. C., Moore, E. C. & Reichard, P. Enzymatic Synthesis of Deoxyribonucletides. *J. Biol. Chem.* **239**, 3436–3444 (1964).

25. Tonissen, K. F. & Trapani, G. D. Thioredoxin system inhibitors as mediators of apoptosis for cancer therapy. *Mol. Nutr. Food Res.* **53**, 87–103 (2009).

26. Holmgren, A. Thioredoxin. (1985).

27. Damdimopoulos, A. E., Miranda-Vizuete, A., Pelto-Huikko, M., Gustafsson, J. Å. & Spyrou, G. Human mitochondrial thioredoxin. Involvement in mitochondrial membrane potential and cell death. *J. Biol. Chem.* **277**, 33249–33257 (2002).

28. Lu, J. & Holmgren, A. Thioredoxin System in Cell Death Progression. *Antioxid. Redox Signal.* **17**, 1738–1747 (2012).

29. Holmgren, A., Söderberg, B. O., Eklund, H. & Brändén, C. I. Three-dimensional structure of Escherichia coli thioredoxin-S2 to 2.8 A resolution. *Proc. Natl. Acad. Sci. U. S. A.* **72**, 2305–2309 (1975).

30. Pšenáková, K. Structural Study of the ASK1:Thioredoxin Complex. *Diploma Thesis* (2015).

31. Weichsel, A., Gasdaska, J. R., Powis, G. & Montfort, W. R. Crystal structures of reduced, oxidized, and mutated human thioredoxins: evidence for a regulatory homodimer. *Structure* **4**, 735–51 (1996).

32. Marcelo, K. L., Means, A. R. & York, B. The Ca2+/Calmodulin/CaMKK2 Axis: Nature's Metabolic CaMshaft. *Trends Endocrinol. Metab.* **27**, 706–718 (2016).

33. Wilson, M. A. & Brunger, A. T. The 1.0 A crystal structure of Ca(2+)-bound calmodulin: an analysis of disorder and implications for functionally relevant plasticity. *J. Mol. Biol.* **301**, 1237–56 (2000).

34. Bayley, P. M., Findlay, W. A. & Martin, S. R. Target recognition by calmodulin: dissecting the kinetics and affinity of interaction using short peptide sequences. *Protein Sci.* **5**, 1215–28 (1996).

35. Zhang, M., Tanaka, T. & Ikura, M. Calcium-induced conformational transition revealed by the solution structure of apo calmodulin. *Nat. Struct. Biol.* **2**, 758–67 (1995).

36. Ikura, M. *et al.* Solution structure of a calmodulin-target peptide complex by multidimensional NMR. *Science (80-.).* **256**, 632–8 (1992).

37. Hoeflich, K. P. & Ikura, M. Calmodulin in action: diversity in target recognition and activation mechanisms. *Cell* **108**, 739–42 (2002).

38. Tokumitsu, H., Wayman, G. A., Muramatsu, M. & Soderling, T. R. Calcium/calmodulin-dependent protein kinase kinase: identification of regulatory domains. *Biochemistry* **36**, 12823–7 (1997).

39. Tidow, H. & Nissen, P. Structural diversity of calmodulin binding to its target sites. *FEBS J.* **280**, 5551–5565 (2013).

40. Anderson, K. A. *et al.* Components of a calmodulin-dependent protein kinase cascade. Molecular cloning, functional characterization and cellular localization of Ca2+/calmodulin-dependent protein kinase kinase beta. *J. Biol. Chem.* **273**, 31880–9 (1998).

41. Psenakova, K. *et al.* 14-3-3 protein directly interacts with the kinase domain of calcium/calmodulin-dependent protein kinase kinase (CaMKK2). *Biochim. Biophys. Acta - Gen. Subj.* **1862**, 1612–1625 (2018).

42. Kukimoto-Niino, M. *et al.* Crystal structure of the Ca2+/calmodulin-dependent protein kinase kinase in complex with the inhibitor STO-609. *J. Biol. Chem.* **286**, 22570–22579 (2011).

43. Johnson, L. N., Noble, M. E. & Owen, D. J. Active and inactive protein kinases: structural basis for regulation. *Cell* **85**, 149–58 (1996).

44. Green, M. F. *et al.* Ca2+/Calmodulin-dependent protein kinase kinase beta is regulated by multisite phosphorylation. *J. Biol. Chem.* **286**, 28066–79 (2011).

45. Wayman, G. A., Tokumitsu, H. & Soderling, T. R. Inhibitory cross-talk by cAMP kinase on the calmodulin-dependent protein kinase cascade. *J. Biol. Chem.* **272**, 16073–6 (1997).

46. Davare, M. A., Saneyoshi, T., Guire, E. S., Nygaard, S. C. & Soderling, T. R. Inhibition of calcium/calmodulin-dependent protein kinase kinase by protein 14-3-3. *J. Biol. Chem.* **279**, 52191–9 (2004).

47. Ichimura, T., Taoka, M., Hozumi, Y., Goto, K. & Tokumitsu, H. 14-3-3 Proteins directly regulate Ca2+/calmodulin-dependent protein kinase kinase α through phosphorylation-dependent multisite binding. *FEBS Lett.* **582**, 661–665 (2008).

48. Pop, C. & Salvesen, G. S. Human caspases: activation, specificity, and regulation. *J. Biol. Chem.* **284**, 21777–81 (2009).

49. Boatright, K. M. *et al.* A Unified Model for Apical Caspase Activation. *Mol. Cell* **11**, 529–541 (2003).

50. Chai, J. *et al.* Crystal Structure of a Procaspase-7 Zymogen: Mechanisms of Activation and Substrate Binding. *Cell* **107**, 399–407 (2001).

51. Fava, L. L., Bock, F. J., Geley, S. & Villunger, A. Caspase-2 at a glance. *J. Cell Sci.* **125**, 5911–5915

52. Butt, A. J., Harvey, N. L., Parasivam, G. & Kumar, S. Dimerization and autoprocessing of the Nedd2 (caspase-2) precursor requires both the prodomain and the carboxyl-terminal regions. *J. Biol. Chem.* **273**, 6763–8 (1998).

53. Schweizer, A., Briand, C. & Grutter, M. G. Crystal structure of caspase-2, apical initiator of the intrinsic apoptotic pathway. *J. Biol. Chem.* **278**, 42441–7 (2003).

54. Mancini, M. *et al.* Caspase-2 is localized at the Golgi complex and cleaves golgin-160 during apoptosis. *J. Cell Biol.* **149**, 603–12 (2000).

55. Baliga, B. C. *et al.* Role of prodomain in importin-mediated nuclear localization and activation of caspase-2. *J. Biol. Chem.* **278**, 4899–905 (2003).

56. Smidova, A. *et al.* 14-3-3 Protein Masks the Nuclear Localization Sequence of Caspase-2. *FEBS J.* **285**, 4196–4213 (2018).

57. Nutt, L. K. *et al.* Metabolic Regulation of Oocyte Cell Death through the CaMKII-Mediated Phosphorylation of Caspase-2. *Cell* **123**, 89–103 (2005).

58. Nutt, L. K. *et al.* Metabolic Control of Oocyte Apoptosis Mediated by 14-3-3ζ-Regulated Dephosphorylation of Caspase-2. *Dev. Cell* **16**, 856–866 (2009).

59. Carter, M. E. & Brunet, A. FOXO transcription factors. *Curr. Biol.* **17**, R113-4 (2007).

60. Weigel, D., Jurgens, G., Kuttner, F., Seifert, E. & Jackle, H. *The Homeotic Gene fork head Encodes a Nuclear Protein and Is Expressed in the Terminal Regions of the Drosophila Embryo*. *Cell* **57**, (1969).

61. Carlsson, P. & Mahlapuu, M. Forkhead Transcription Factors: Key Players in Development and Metabolism. (2002). doi:10.1006/dbio.2002.0780

62. Galili, N. *et al.* Fusion of a fork head domain gene to PAX3 in the solid tumour alveolar rhabdomyosarcoma. *Nat. Genet.* **5**, 230–235 (1993).

63. Burgering, B. M. T. & Kops, G. J. P. L. Cell cycle and death control: long live Forkheads. *Trends Biochem. Sci.* **27**, 352–60 (2002).

64. Wang, Y., Zhou, Y. & Graves, D. T. FOXO Transcription Factors: Their Clinical Significance and Regulation. *Biomed Res. Int.* **2014**, 1–13 (2014).

65. Obsil, T. & Obsilova, V. Structure/function relationships underlying regulation of FOXO transcription factors. *Oncogene* **27**, 2263–2275 (2008).

66. Wang, F. *et al.* Biochemical and Structural Characterization of an Intramolecular Interaction in FOXO3a and Its Binding with p53. *J. Mol. Biol.* **384**, 590–603 (2008).

67. Tsai, K.-L. *et al.* Crystal structure of the human FOXO3a-DBD/DNA complex suggests the effects of post-translational modification. *Nucleic Acids Res.* **35**, 6984–94 (2007).

68. Salcher, S. *et al.* C10ORF10/DEPP, a transcriptional target of FOXO3, regulates ROS-sensitivity in human neuroblastoma. *Mol. Cancer* **13**, 224 (2014).

69. Hui, R. C.-Y. *et al.* Doxorubicin activates FOXO3a to induce the expression of multidrug resistance gene ABCB1 (MDR1) in K562 leukemic cells. *Mol. Cancer Ther.* **7**, 670–8 (2008).

70. Cavanagh, J. *Protein NMR spectroscopy : principles and practice*. (Academic Press, 2007).

71. Atkins, P. W., De Paula, J. & Keeler, J. *Physical chemistry*. (OXFORD University Press, 2014).

72. Higman, V. A. Protein NMR: A Practical Guide. (2018). Available at: http://www.protein-nmr.org.uk/. (Accessed: 27th November 2018)

73. Kumar, A. & Christy Rani Grace, R. Nuclear Overhauser Effect. *Encycl. Spectrosc. Spectrom.* 1643–1653 (1999). doi:10.1006/RWSP.2000.0212

74. Putnam, C. D., Hammel, M., Hura, G. L. & Tainer, J. a. X-ray solution scattering (SAXS) combined with crystallography and computation: defining accurate macromolecular structures, conformations and assemblies in solution. *Q. Rev. Biophys.* **40**, 191–285 (2007).

75. Kosek, D. *et al.* Biophysical and structural characterization of the thioredoxin-

binding domain of protein kinase ASK1 and its interaction with reduced thioredoxin. *J. Biol. Chem.* **289**, 24463–24474 (2014).

76. Receveur-Brechot, V. & Durand, D. How random are intrinsically disordered proteins? A small angle scattering perspective. *Curr. Protein Pept. Sci.* **13**, 55–75 (2012).

77. Petoukhov, M. V. *et al.* New developments in the *ATSAS* program package for small-angle scattering data analysis. *J. Appl. Crystallogr.* **45**, 342–350 (2012).

78. Svergun, D. I. Determination of the regularization parameter in indirect-transform methods using perceptual criteria. *J. Appl. Crystallogr.* **25**, 495–503 (1992).

79. Svergun, D. I. Restoring low resolution structure of biological macromolecules from solution scattering using simulated annealing. *Biophys. J.* **76**, 2879–2886 (1999).

80. Rambo, R. P. Resolving Individual Components in Protein–RNA Complexes Using Small-Angle X-ray Scattering Experiments. in *Methods in enzymology* **558**, 363–390 (2015).

81. Kincaid, R. L., Vaughan, M., Osborne, J. C. & Tkachuk, V. A. Ca2+-dependent interaction of 5-dimethylaminonaphthalene-1-sulfonyl-calmodulin with cyclic nucleotide phosphodiesterase, calcineurin, and troponin I. *J. Biol. Chem.* **257**, 10638–10643 (1982).

82. Rezabkova, L. *et al.* 14-3-3 protein interacts with and affects the structure of RGS domain of regulator of G protein signaling 3 (RGS3). *J. Struct. Biol.* **170**, 451–461 (2010).

83. Cyril Dominguez, Rolf Boelens, and & Bonvin, A. M. J. J. HADDOCK: A Protein−Protein Docking Approach Based on Biochemical or Biophysical Information. *J. Am. Chem. Soc.* (2003). doi:10.1021/JA026939X

84. Ikura, M. *et al.* A novel target recognition revealed by calmodulin in complex with Ca2+-calmodulin-dependent kinase kinase. *Nat. Struct. Biol.* **6**, 819–824 (1999).

85. Killoran, R. C., Fan, J., Yang, D., Shilton, B. H. & Choy, W. Y. Structural analysis of the 14-3-3ζ/Chibby interaction involved in Wnt/β-catenin signaling. *PLoS One* **10**, 1–19 (2015).

86. Milroy, L.-G. *et al.* Stabilizer-Guided Inhibition of Protein-Protein Interactions. *Angew. Chemie Int. Ed.* **54**, 15720–15724 (2015).

87. Williamson, M. P. Using chemical shift perturbation to characterise ligand binding. *Prog. Nucl. Magn. Reson. Spectrosc.* **73**, 1–16 (2013).

88. Rittinger, K. *et al.* Structural analysis of 14-3-3 phosphopeptide complexes identifies a dual role for the nuclear export signal of 14-3-3 in ligand binding. *Mol. Cell* **4**, 153–66 (1999).

89. Tang, Y., Wells, J. A. & Arkin, M. R. Structural and Enzymatic Insights into

Caspase-2 Protein Substrate Recognition and Catalysis. *J. Biol. Chem.* **286**, 34147–34154 (2011).

90. Calnan, D. R. & Brunet, A. The FoxO code. *Oncogene* **27**, 2276–2288 (2008).

91. Nadeau, P. J., Charette, S. J. & Landry, J. REDOX reaction at ASK1-Cys250 is essential for activation of JNK and induction of apoptosis. *Mol. Biol. Cell* **20**, 3628–37 (2009).

92. Renshaw, P. S. *et al.* Sequence-specific assignment and secondary structure determination of the 195-residue complex formed by the Mycobacterium tuberculosis proteins CFP-10 and ESAT-6. *J. Biomol. NMR* **30**, 225–226 (2004).

93. Veverka, V. *et al.* NMR assignment of the mTOR domain responsible for rapamycin binding. *J. Biomol. NMR* **36**, 3 (2006).

94. Shen, Y., Delaglio, F., Cornilescu, G. & Bax, A. TALOS+: A hybrid method for predicting protein backbone torsion angles from NMR chemical shifts. *J. Biomol. NMR* **44**, 213–23 (2010).

95. Arora, A., Abildgaard, F., Bushweller, J. H. & Tamm, L. K. Structure of outer membrane protein A transmembrane domain by NMR spectroscopy. *Nat. Struct. Biol.* **8**, 334–8 (2001).

96. Ovchinnikov, S. *et al.* Structure prediction using sparse simulated NOE restraints with Rosetta in CASP11. *Proteins Struct. Funct. Bioinforma.* **84**, 181–188 (2016).

7 SUPPLEMENTS

7.1 Supplement S1

7.1.1 Publication I: Role of 14-3-3 in the regulation of Ca^{2+}/CaM – dependent protein kinase kinase 2 activity.

Psenakova, K.[+]**,** Petrvalska, O.[+], Kylarova, S.[+], Lentini, D., Kalabova, D., Herman, P., Obsilova, V. & Obsil, T. 14-3-3 protein directly interacts with the kinase domain of calcium/calmodulin-dependent protein kinase kinase (CaMKK2). *Biochim. Biophys. Acta - Gen. Subj.* **1862**, 1612–1625 (2018).

My contribution: expression and purification of CaMKK2, 14-3-3 and CaM; preparation of phosphorylated CaMKK2, single tryptophan mutants of CaMKK2 and dansyl-labeled CaM; sample preparation and further optimization for the small-angle X-ray scattering and time-resolved dansyl and tryptophan fluorescence experiments; small-angle X-ray scattering data analysis.

[+] Equal contribution.

BBA - General Subjects 1862 (2018) 1612–1625

Contents lists available at ScienceDirect

BBA - General Subjects

journal homepage: www.elsevier.com/locate/bbagen

14-3-3 protein directly interacts with the kinase domain of calcium/calmodulin-dependent protein kinase kinase (CaMKK2)

Katarina Psenakova[a,b,1], Olivia Petrvalska[a,b,1], Salome Kylarova[a,b,1], Domenico Lentini Santo[a], Dana Kalabova[b], Petr Herman[c], Veronika Obsilova[b,*], Tomas Obsil[a,b,**]

[a] Department of Physical and Macromolecular Chemistry, Faculty of Science, Charles University, Prague, Czech Republic
[b] BioCeV – Institute of Physiology, The Czech Academy of Sciences, Vestec, Czech Republic
[c] Institute of Physics, Faculty of Mathematics and Physics, Charles University, Prague, Czech Republic

ARTICLE INFO

Keywords:
14-3-3 protein
CaMKK
Protein-protein interaction
SAXS
Fluorescence spectroscopy

ABSTRACT

Background: Calcium/calmodulin-dependent protein kinase kinase 2 (CaMKK2) is a member of the Ca^{2+}/calmodulin-dependent kinase (CaMK) family involved in adiposity regulation, glucose homeostasis and cancer. This upstream activator of CaMKI, CaMKIV and AMP-activated protein kinase is inhibited by phosphorylation, which also triggers an association with the scaffolding protein 14-3-3. However, the role of 14-3-3 in the regulation of CaMKK2 remains unknown.

Methods: The interaction between phosphorylated CaMKK2 and the 14-3-3γ protein, as well as the architecture of their complex, were studied using enzyme activity measurements, small-angle x-ray scattering (SAXS), time-resolved fluorescence spectroscopy and protein crystallography.

Results: Our data suggest that the 14-3-3 protein binding does not inhibit the catalytic activity of phosphorylated CaMKK2 but rather slows down its dephosphorylation. Structural analysis indicated that the complex is flexible and that CaMKK2 is located outside the phosphopeptide-binding central channel of the 14-3-3γ dimer. Furthermore, 14-3-3γ appears to interact with and affect the structure of several regions of CaMKK2 outside the 14-3-3 binding motifs. In addition, the structural basis of interactions between 14-3-3 and the 14-3-3 binding motifs of CaMKK2 were elucidated by determining the crystal structures of phosphopeptides containing these motifs bound to 14-3-3.

Conclusions: 14-3-3γ protein directly interacts with the kinase domain of CaMKK2 and the region containing the inhibitory phosphorylation site Thr^{145} within the N-terminal extension.

General significance: Our results suggested that CaMKK isoforms differ in their 14-3-3-mediated regulations and that the interaction between 14-3-3 protein and the N-terminal 14-3-3-binding motif of CaMKK2 might be stabilized by small-molecule compounds.

1. Introduction

Calcium/calmodulin-dependent protein kinase kinase (CaMKK), a member of the Ca^{2+}/calmodulin-dependent kinase (CaMK) family, specifically phosphorylates Thr residues within the activation loop of two downstream kinases, CaMKI and CaMKIV, considerably increasing their catalytic efficiency, resulting in phosphorylation of multiple downstream targets [1]. Two CaMKK isoforms (CaMKK1 and CaMKK2) have been identified in mammals, which are both highly expressed in the brain. CaMKK2 is also an upstream activator of the AMP-activated protein kinase (AMPK) [2], and studies have shown that the AMPK:-CaMKK2 complex regulates energy balance by acting in the hypothalamus [3]. In fact, CaMKK2 is one of the most versatile CaMKs, which is involved in adiposity regulation, glucose homeostasis, hematopoiesis, inflammation, and cancer, and is considered a potential target for therapeutic intervention (reviewed in [4]).

The members of the CaMK family share a common domain organization consisting of the catalytic domain followed by an autoinhibitory region, which overlaps with the CaM-binding region (Fig. 1A and C) [5]. Although CaMKK1 and CaMKK2 share high similarity and

Abbreviations: AMPK, AMP-activated protein kinase; AUC, Analytical ultracentrifugation; CaM, Calmodulin; CaMKK2, Calcium/calmodulin-dependent protein kinase kinase 2; SAXS, Small-angle x-ray scattering; SV, Sedimentation velocity

* Correspondence to: V. Obsilova, BioCeV – Institute of Physiology, The Czech Academy of Sciences, Prague, Czech Republic.
** Correspondence to: T. Obsil, Department of Physical and Macromolecular Chemistry, Faculty of Science, Charles University, Prague, Czech Republic.
E-mail addresses: veronika.obsilova@fgu.cas.cz (V. Obsilova), obsil@natur.cuni.cz (T. Obsil).

[1] The first three authors KP, OP and SK contributed equally to this work.

https://doi.org/10.1016/j.bbagen.2018.04.006
Received 16 January 2018; Received in revised form 5 April 2018; Accepted 6 April 2018
Available online 10 April 2018

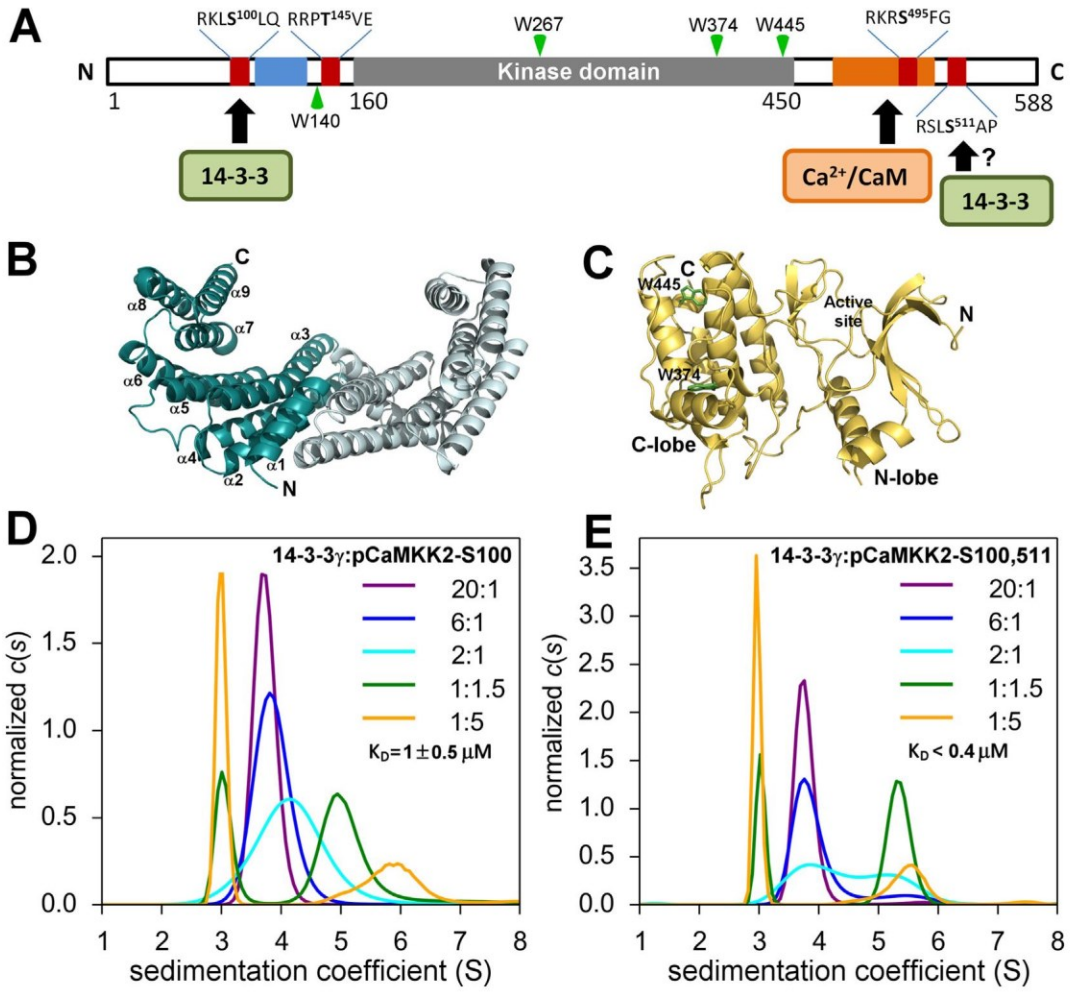

Fig. 1. Phosphorylated CaMKK2 Forms a Stable Complex with 14-3-3γ. (A) Domain structure of CaMKK2. The positions of PKA phosphorylation sites, the N-terminal regulatory site and the CaM binding region are indicated by red, blue and orange rectangles, respectively. The positions of tryptophan residues used in the time-resolved fluorescence experiments are indicated by green triangles. (B) Crystal structure of the 14-3-3γ protein dimer (PDB ID: 2B05) Each protomer is shown in different color. (C) Crystal structure of the kinase domain of CaMKK2 [35]. Tryptophan residues located in the C-lobe are shown as sticks. (D, E) Series of area-normalized $c(s)$ distributions of mixtures of pCaMKK2 and 14-3-3γ at various molar ratios, using 6 μM 14-3-3γ and 0.3 – 30 μM pCaMKK2.

identity in their amino acid sequences (Fig. S1), they differ in their biochemical properties. CaMKK1 activity is strictly regulated by an autoinhibitory mechanism, and Ca^{2+}/CaM binding relieves this autoinhibition [6]. However, in contrast to CaMKK1, CaMKK2 is significantly active in the absence of Ca^{2+}/CaM [7]. This autonomous activity is regulated by a stretch of 23 amino acids (residues 129–151 in rat CaMKK2), which is located N-terminally to the catalytic domain and apparently participates in the release of the autoinhibitory region from the catalytic domain [8]. Moreover, this regulatory region contains three phosphorylation sites targeted by cyclin-dependent kinase 5 and glycogen synthase kinase 3 and one site recognized by cAMP-dependent protein kinase (PKA) [9,10].

Both CaMKKs are partly inhibited upon phosphorylation by PKA [10–12]. CaMKK1 contains five PKA phosphorylation sites, Ser^{52}, Ser^{74}, Thr^{108}, Ser^{458}, and Ser^{475}, four of which are also present in CaMKK2 (Ser^{100}, Thr^{145}, Ser^{495}, and Ser^{511}) (Figs. 1A and S1). Ser^{458} phosphorylation has been shown to block Ca^{2+}/CaM-binding, whereas Thr^{108} phosphorylation plays a role in the regulation of CaMKK1 activity toward CaMKI and CaMKIV [10,13].

In addition to direct, PKA-mediated inhibition, CaMKK1 activity is further regulated through a PKA-dependent mechanism based on interaction with 14-3-3 proteins [14,15]. 14-3-3 proteins, a family of highly conserved dimeric proteins ubiquitously expressed in all eukaryotic cells (Fig. 1B), function as scaffold and chaperone molecules that interact with and regulate the function of several hundred partner proteins by recognizing phosphoserine- (pS) or phosphothreonine (pT)-containing motifs [16]. Mechanistically, 14-3-3 proteins constrain the conformation, occlude sequence-specific and structural features, promote protein-protein interactions, or prevent the aggregation of their binding partners (reviewed in [17,18]). GST pull-down and co-immunoprecipitation assays, together with site-directed mutagenesis, have shown that both CaMKK isoforms bind to various 14-3-3 protein isoforms (mainly γ isoform) and that the conserved motif containing phosphorylated Ser^{74} in CaMKK1 (corresponding to Ser^{100} in CaMKK2, Figs. 1A and S1) functions as the primary 14-3-3 binding site [14,15]. Furthermore, a second 14-3-3 binding motif containing phosphorylated Ser^{475} in CaMKK1 (Ser^{511} in CaMKK2) has also been suggested [15]. The phosphorylation of this site by PKA, however, is low and mainly occurs in the presence of Ca^{2+}/CaM [11,12,14]. The functional role of 14-3-3 binding in CaMKK regulation is apparently twofold. Davare et al. [14] suggested that the 14-3-3 binding inhibits CaMKK1 through two mechanisms, namely inhibition of Thr^{108} dephosphorylation, thus maintaining the kinase in the PKA-mediated inhibited state, and direct inhibition of the kinase activity. Accordingly, Ichimura et al. [15] showed that binding to 14-3-3 decreases the maximum velocity (V_{max}) of CaMKK1. However, the molecular mechanism of this interaction as well as the role of 14-3-3 in the regulation of CaMKK2 remains unclear.

Thus, in this study, we used enzyme activity measurements, small-

angle x-ray scattering (SAXS) and time-resolved fluorescence spectroscopy to characterize the interaction between phosphorylated CaMKK2 and the 14-3-3γ protein. In addition, to elucidate the structural basis of interactions between 14-3-3 and the 14-3-3 binding motifs of CaMKK2, we determined the crystal structures of phosphopeptides containing these motifs bound to 14-3-3.

2. Materials and methods

2.1. Expression, purification and phosphorylation of CaMKK2

DNA encoding human CaMKK2 (residues 93–517) was ligated into pRSFDuet-1 (Novagen) using *Bam*HI and *Not*I sites. Modified pRSFDuet-1 containing the sequence of the His_6-tagged GB1 domain of protein G inserted into the first multiple cloning site was a gift from Evzen Boura (Institute of Organic Chemistry and Biochemistry AS CR, Prague, Czech Republic). CaMKK2 (93–517) was expressed as N-terminal His_6-GB1-tagged fusion protein in *Escherichia coli* BL21 (DE3) cells. Protein expression was conducted in autoinduction media for 5 h at 37 °C and then 16 h at 20 °C, and the protein was purified using Chelating Sepharose Fast Flow (GE Healthcare) according to the standard protocol. The eluted protein was dialyzed against buffer containing 50 mM Tris-HCl (pH 8), 0.5 M NaCl, 4 mM 2-mercaptoethanol, 4 mM EDTA and 10% (*w/v*) glycerol and the His_6-GB1 tag was cleaved by incubation with TEV protease (250 U of TEV/mg of fusion protein) at 30 °C for 1 h. The final purification step was size-exclusion chromatography on a HiLoad 26/600 Superdex 75 column (GE Healthcare) in buffer containing 50 mM Tris-HCl (pH 8), 500 mM NaCl, 5 mM DTT, and 10% (w/v) glycerol. All mutants of CaMKK2 were generated using the QuikChange site-directed mutagenesis kit (Stratagene), and mutations were confirmed by sequencing. The stability of prepared mutants was assessed by measuring the temperature of the unfolding transition (T_m) using differential scanning fluorimetry [19], and no significant differences in T_m were observed. CaMKK2-S^{100} and CaMKK2-$S^{100,511}$ were phosphorylated by incubation at 30 °C for 3 h and then overnight at 4 °C with 170 and 340 units of PKA (Promega), respectively, per mg of protein in the presence of 0.75 mM ATP and 20 mM $MgCl_2$. After phosphorylation, ATP was removed by size-exclusion chromatography. The result of the phosphorylation reaction was assessed by HPLC-MS.

2.2. Expression and purification of 14-3-3 proteins

14-3-3γ, 14-3-3γΔC, 14-3-3ζΔC and 14-3-3γ noW were expressed and purified as described previously [20].

2.3. Expression and purification of CaM

Rat CaM was prepared as described previously [21].

2.4. Preparation of kinase-dead CaMK1D and AMPKA2

DNA encoding human CAMK1D was a gift from Nicola Burgess-Brown (Addgene plasmid # 38834). DNA encoding human AMPKA2 (catalytic α2 subunit of AMPK) was a gift from Cheryl Arrowsmith (Addgene plasmid # 36194). The kinase-dead CAMK1D $D^{165}A$ and AMPKA2 $D^{157}A$ mutants were generated using the QuikChange site-directed mutagenesis kit (Stratagene), and the mutation was confirmed by sequencing. Both N-terminally His_6-tagged proteins were expressed by isopropyl 1-thio-β-D-galactopyranoside induction for 16 h at 15 °C and purified from *E. coli* BL21(DE3) using Chelating Sepharose® Fast Flow (GE Healthcare) according to the standard protocol. The next purification step (only in the case of CaMK1D) was size-exclusion chromatography on a HiLoad 26/600 Superdex 75 column (GE Healthcare) in buffer containing 50 mM HEPES (pH 7.5), 200 mM NaCl, 1 mM $CaCl_2$, 5 mM DTT and 10% glycerol.

2.5. Enzyme activity measurements

The enzymatic activity of $CaMKK2_{93–517}$ was examined using γ-[^{32}P]-ATP assay with inactive CaMKID and AMPKA as physiological kinase substrates. The reaction volume of 45 μL consisted of 10 nM $CaMKK2_{93–517}$ (phosphorylated or not phosphorylated), 10 μM CaMKID (or AMPKA2), 5 μM calmodulin and 100 μM 14-3-3γ (where needed) in buffer containing 50 mM HEPES (pH 7.5), 200 mM NaCl, 20 mM $MgCl_2$, 1 mM $CaCl_2$, 1 mM DTT and 10% glycerol. The reaction was tempered up to 30 °C and initiated by an addition of 5 μL of 1 mM γ-[^{32}P]-ATP (PerkinElmer Life Sciences) to a final ATP concentration 100 μM (~2–3 μCi per reaction). After a 5 min incubation at 30 °C, the reaction was stopped by spotting 45 μL of the reaction mixture onto a P81 phosphocellulose paper strip (Millipore) and washing in 3 × 500 mL of 1% (*w/v*) phosphoric acid for 5 min each. Strips were dried and inserted into vials containing 5 mL of scintillation fluid (Rotiszint™, Carl Roth). Counts were measured using Quantasmart™ liquid analyzer (PerkinElmer Life Sciences). To determine significance for observed changes, a paired two-tail *t*-test was performed. Where indicated in the figures, a single asterisk denotes $p \leq 0.05$ and a double asterisk denotes $p \leq 0.005$.

2.6. HPLC-MS analysis

HPLC-MS analysis was performed as previously described [22,23].

2.7. Analytical ultracentrifugation

Sedimentation velocity (SV) experiments were performed using a ProteomLabTM XL-I analytical ultracentrifuge (Beckman Coulter), as previously described [22]. Samples were dialyzed against buffer containing 50 mM Tris-HCl (pH 7.5), 150 mM NaCl, and 1 mM tris(2-carboxyethyl)phosphine (TCEP) before analysis. SV experiments were conducted in charcoal-filled Epon centerpieces with 12-mm optical path length, at 20 °C, and at 42,000 rpm rotor speed (An-50 Ti rotor, Beckman Coulter), and all sedimentation profiles were recorded with absorption optics. The analysis of mixtures of pCaMKK2 and 14-3-3γ at various molar ratios was performed with 0.3 − 30 μM pCaMKK2 and 6 μM 14-3-3γ.

2.8. Small angle X-ray scattering

SAXS data were collected at the European Molecular Biology Laboratory (EMBL) P12 beamline, at the storage ring PETRA III (Deutsches Elektronen Synchrotron (DESY), Hamburg, Germany). The SAXS measurements were conducted in buffer containing 50 mM Tris-HCl (pH 7.5), 150 mM NaCl, 1 mM TCEP, 1 mM $CaCl_2$, and 3% (*w/v*) glycerol, using 1–2.8 $mg.mL^{-1}$ pCaMKK2, 1.5–3 $mg.mL^{-1}$ 14-3-3γΔC and 9.9–16.9 $mg.mL^{-1}$ pCaMKK2:14-3-3γ complex (1:2 M stoichiometry). The forward scattering $I(0)$ and the radius of gyration R_g were calculated using the Guinier approximation for a s ($s = 4\pi\sin(\theta)/\lambda$, where 2θ is the scattering angle and λ is the wavelength) range that satisfies the $sR_g < 1.3$ condition. The distance distribution functions $P(r)$ and the maximum particle dimensions D_{max} were computed using the program GNOM [24]. The solute apparent molecular mass (MM_{exp}) was estimated by comparing the forward scattering both with that of reference solutions of bovine serum albumin and with that of the excluded volume of the hydrated particle (the Porod volume) V_p [25]. V_p was computed using the program PRIMUS [26]. The two-phase bead modeling of the pCaMKK2:14-3-3γ complex was performed using the program MONSA [27]. The rigid body modeling of the pCaMKK2:14-3-3γ complex was performed using the program CORAL [25], which models flexible loops missing in crystal structures as interconnected dummy residue chains attached to the appropriate Cα atoms in rigid domains. Crystal structures of 14-3-3γ (PDB ID: 2B05) and the kinase domain of CaMKK2 (PDB ID: 5UY6) were used as rigid domains. The

analysis based on the ensemble optimization method was performed using the program EOM [28].

2.9. Fluorescence polarization assay

Various concentrations of 14-3-3γ were incubated for 1 h with 20 nM of FITC-conjugated synthetic peptide GSLSARKL(pS)LQER (FITC-CaMKK2-S100), where pS denotes phosphoserine, with a fluorescein attached to the N-terminus (Pepscan Presto BV, The Netherlands). Fluorescence polarization was measured using a CLARIOstar microplate reader (BMG Labtech) in 10 mM HEPES (pH 7.4), 150 mM NaCl, 0.1% (*v*/v) Tween 20 and 0.1% (*w*/*v*) BSA buffer after incubating for 1 h in a 96-well black plate. Excitation and emission wavelengths were 482 nm and 530 nm, respectively, and K_D was determined using Origin (OriginLab Corp., MA, USA).

2.10. Time-resolved fluorescence measurements

Time-resolved tryptophan fluorescence intensity and anisotropy decay measurements as well as data analysis were performed as previously described [29]. Tryptophan emission was excited at 298 nm by a tripled output of the Ti:Sapphire laser. Tryptophan fluorescence was isolated at 355 nm using a combination of monochromator and a stack of UG1 and BG40 glass filters (Thorlabs) placed in front of the input slit. Dansyl fluorescence was excited at 355 nm and collected at 550 nm. Samples were placed in a thermostatic holder, and all experiments were performed at 23 °C in buffer containing 50 mM Tris-HCl (pH 7.5), 150 mM NaCl, 1 mM TCEP, 1 mM $CaCl_2$ and 10% (*w*/*v*) glycerol. In tryptophan fluorescence experiments, the pCaMKK2 and 14-3-3γ noW concentrations were 12 and 60 μM, respectively. In dansyl fluorescence experiments, the DANS-CaM, CaMKK2 and 14-3-3γ concentrations were 25, 28 and 100 μM, respectively.

2.11. Crystallization, data collection and structure determination

The 14-3-3ζΔC or 14-3-3γΔC proteins and the pepS100 or pepS511 peptides (sequences RKLpSLQER and RSLpSAPGN, respectively) were mixed in a 1:2 M stoichiometry in buffer containing 20 mM HEPES (pH 7), 2 mM $MgCl_2$ and 1 mM TCEP. Crystallization was performed using the hanging-drop vapor-diffusion method at 291 K. Crystals of the 14-3-3ζΔC:pepS100 peptide complex were grown from drops consisting of 2.5 μL of 16.2 mg.mL^{-1} protein and 2.5 μL of 100 mM Tris-HCl (pH 7), 20.8% (*w*/*v*) PEG 2000 and 50 mM sodium fluoride. Crystals of the 14-3-3γΔC:pepS511 peptide complex were grown from drops consisting of 1 μL of 16.5 mg.mL^{-1} protein and 2 μL of 100 mM sodium citrate (pH 5.6), 200 mM potassium sodium tartrate, and 1.8 M ammonium sulfate. Crystals were cryoprotected using 30% (*v*/v) PEG 400 and flash frozen in liquid nitrogen before data collection in oscillation mode at beamline 14.1 of the BESSY synchrotron and the D8 Venture system (Bruker, MA, USA). Diffraction data processing was performed using the packages XDS and XDSAPP [30,31]. Crystal structures of the 14-3-3ζΔC:pepS100 and 14-3-3γΔC:pepS511 complexes were solved by molecular replacement in MOLREP [32], using the structures of 14-3-3ζ (PDB ID: 4FJ3 [33]) and 14-3-3γ (PDB ID: 2B05) as search models, and refined at resolutions of 2.68 and 2.84 Å, respectively, with PHENIX [34]. The atomic coordinates and structure factors of both complexes have been deposited in the RCSB PDB with accession codes 6EWW and 6FEL. All structural figures were prepared with PyMOL (https://pymol.org/2/).

3. Results

3.1. Preparation of phosphorylated CaMKK2

Because the 14-3-3 binding motifs of human CaMKK2 are located around $pSer^{100}$ and $pSer^{511}$, flanking the kinase domain [14,15], we restricted our analysis to the residues 93 − 517 containing these two motifs, the kinase domain, and the Ca^{2+}/CaM binding region (hereafter referred to as CaMKK2). To prepare well-defined protein, suitable for structural analysis, the other two sites phosphorylated by PKA (Thr^{145} and Ser^{495}) were mutated to Ala. In addition, the mutation $D^{330}A$, of the catalytic aspartate residue, was introduced into the kinase domain to avoid autophosphorylation of the recombinant protein during expression and phosphorylation by PKA. Recombinantly expressed $CaMKK2_{93–517}T^{145}A$, $D^{330}A$, $S^{495}A$ (hereafter referred to as CaMKK2-$S^{100,511}$) was phosphorylated in vitro by PKA, and the extent of the phosphorylation reaction was determined by mass spectrometry. HPLC-MS analysis confirmed the stoichiometric phosphorylation of Ser^{100} but only partial (approximately 50%) phosphorylation of Ser^{511} (Fig. S2). Neither the presence of Ca^{2+}/CaM nor the increased concentration of PKA improved the phosphorylation status of Ser^{511}. The weak phosphorylation of Ser^{511} by PKA is consistent with previous reports and indicates that, under physiological conditions, the N-terminal 14-3-3 binding motif would be significantly more phosphorylated than the C-terminal 14-3-3 binding motif [11,12,14]. Therefore, we also prepared a construct containing only the N-terminal 14-3-3 binding motif with Ser^{100} by inserting an additional mutation, Ser^{511} to Ala (hereafter referred to as CaMKK2-S^{100}).

3.2. Phosphorylated CaMKK2 forms a stable complex with 14-3-3γ

The formation of the complex between 14-3-3γ and pCaMKK2 (S^{100} and $S^{100,511}$) was studied using sedimentation velocity (SV) analytical ultracentrifugation (AUC) by analyzing their mixtures at various molar ratios (Fig. 1D and E). The normalized continuous sedimentation coefficient distributions *c*(*s*) based on the SV AUC experiments showed that 14-3-3γ and pCaMKK2-S^{100} formed a complex with a weight-averaged sedimentation coefficient (corrected to 20.0 °C and to the density of water), $s_{w(20,w)}$, of 6.17 S, with a frictional ratio f/f_o of 1.3, whereas 14-3-3γ and pCaMKK2-S^{100} alone showed single peaks, with $s_{w(20,w)}$ values of 3.91 and 3.16 S, respectively. The $s_{w(20,w)}$ value of the 14-3-3γ:pCaMKK2-S^{100} complex corresponds to a molecular mass of ~110 kDa, thus suggesting a 2:1 M stoichiometry for the complex (105.0 kDa theoretical molecular mass). The direct modeling of the SV AUC data using the Lamm equation showed best-fit apparent equilibrium dissociation constants (K_D) of 1 ± 0.5 μM using a Langmuir binding model with a pCaMKK2-S^{100} molecule interacting with a 14-3-3γ dimer.

SV-AUC analysis of mixtures of 14-3-3γ and pCaMKK2-$S^{100,511}$ revealed the formation of a complex with an $s_{w(20,w)}$ value of 5.72 S and with a frictional ratio f/f_o of 1.4. This $s_{w(20,w)}$ value corresponds to a molecular mass of ~111 kDa, thus also suggesting the 2:1 M stoichiometry of the complex. The direct modeling of the SV AUC data showed a best-fit K_D of < 0.4 μM, thus suggesting that the C-terminal motif, when phosphorylated, increases the stability of the complex.

3.3. 14-3-3 Protein binding does not inhibit the activity of pCaMKK2 but slows down its Dephosphorylation

Previous studies have shown that the 14-3-3 binding inhibits the catalytic activity of phosphorylated CaMKK1 [14,15]. To test whether the catalytic activity of pCaMKK2 is also affected by interaction with 14-3-3, the kinase activity measurements were performed. Human CaMK1D and AMPKA2 (catalytic α2 subunit of AMPK) were used as specific substrates. As expected, the phosphorylation by PKA significantly suppressed the activity of pCaMKK2 relative to the non-phosphorylated protein by ~50% and ~30% for CaMK1D and AMPKA2 as substrates, respectively (Fig. 2). Interestingly, the addition of 14-3-3γ did not further suppress the activity of pCaMKK2 but rather resulted in its weak enhancement. When CaMK1D was used as a substrate, the effect was insignificant (the activity increased by 5% on a relative scale compared to the non-phosphorylated enzyme activity), but when

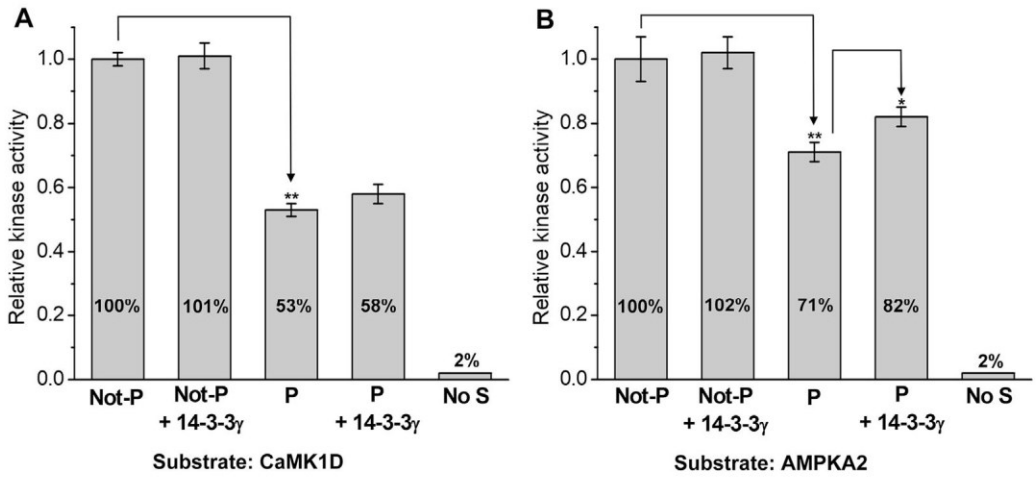

Fig. 2. 14-3-3 Protein Binding Does Not Inhibit the Catalytic Activity of Phosphorylated CaMKK2. The catalytic activity of CaMKK2 and pCaMKK2 both in the absence and the presence of 14-3-3γ was measured using human CaMK1D (kinase-dead mutant $D^{165}A$) and AMPKA2 (kinase-dead mutant $D^{157}A$) as specific substrates. The activities were normalized compared to the non-phosphorylated enzyme activity in the absence of 14-3-3γ (specific activities were 940 ± 20 and 740 ± 50 nmol.min^{-1}.mg^{-1} for CaMK1D and AMPKA2 as substrates, respectively). Results are the means ± S.D., $n = 3$. No S, no substrate; *, $p < 0.05$; **, $p < 0.005$.

AMPKA2 was used as a substrate the pCaMKK2 activity increased significantly by 11%. This indicates that the 14-3-3-mediated regulations of pCaMKK1 and pCaMKK2 differ.

Davare et al. [14] suggested that the 14-3-3 binding inhibits CaMKK1 mainly through inhibition of Thr^{108} (Thr^{145} in CaMKK2) dephosphorylation, thus maintaining the kinase in the PKA-mediated inhibited state. Therefore, we next compared time-dependent overall dephosphorylation of PKA-phosphorylated pCaMKK2 by type 1 protein phosphatase (PP1) in the absence and presence of 14-3-3γ using phos-tag SDS-PAGE. The kinase-dead mutant of pCaMKK2 $D^{330}A$ was used to avoid autophosphorylation of additional residues. Dephosphorylation was assessed by downward shift (Fig. S3) on a phos-tag SDS-PAGE gel. CaMKK2 shifted down gradually with incubation time through several discrete bands, which correspond to various partly phosphorylated forms of CaMKK2. As noticed, an incubation with PP1 for 7 and 30 min resulted in a substantial dephosphorylation of pCaMKK2 in the absence of 14-3-3γ. On the other hand, the presence of 14-3-3γ suppressed the overall dephosphorylation of pCaMKK2 as indicated by a lower abundance of bands corresponding to dephosphorylated CaMKK2 after 7 and 30 min of incubation time.

To assess dephosphorylation of specific regulatory sites Thr^{145} and Ser^{495} (Thr^{108} and Ser^{458} in CaMKK1) an HPLC-MS approach was used. Proteins treated by PP1 for 0, 1.5 and 7 min were collected and directly injected onto an immobilized protease column. After rapid online digestion and desalting, HPLC separation coupled with MS detection was done. Abundances of selected peptides containing Thr^{145} and Ser^{495} were then estimated from intensities of their extracted ion chromatograms (Table S1). The intensity ratios between non-phosphorylated and phosphorylated forms of selected peptides indicated slower dephosphorylation of both phosphoresidues for pCaMKK2 bound to 14-3-3γ compared with pCaMKK2 alone, especially $pSer^{495}$ whose non-phosphorylated form could not be detected. This suggests that the 14-3-3γ binding slows down the dephosphorylation of inhibitory PKA sites of pCaMKK2.

3.4. Structural characterization of the 14-3-3 binding motifs of CaMKK2

Although the putative C-terminal 14-3-3 binding motif (sequence RSLpSer^{511}AP) is a canonical "mode I" 14-3-3 binding site (RXX(pS/pT)XP, wherein pS/pT is phosphoserine or phosphothreonine and X is any residue [36,37]), the N-terminal motif (sequence RKLpS^{100}LQE) contains a Gln residue at the position +2 relative to the phosphorylated residue $pSer^{100}$ (Fig. 1A). Bioinformatics survey of 14-3-3 binding sites revealed that Gln is seldom found at +2 because the Pro residue and, to a lesser extent, Ser, Gly and Asp also, are frequently found at this position [38]. The frequent occurrence of proline at the +2 position is explained by the need to introduce a kink in the peptide chain and to direct the C-terminal portion out of the ligand binding groove of the 14-3-3 protein [36]. To elucidate the structural basis of interactions between 14-3-3 proteins and the 14-3-3 binding motifs of CaMKK2, we solved the crystal structures of phosphopeptides pepS100 (sequence RKLpSLQER) and pepS511 (sequence RSLpSAPGN) bound to 14-3-3ζΔC and 14-3-3γΔC, respectively (ΔC denotes C-terminally truncated versions missing the highly flexible ~15-residues-long C-terminal tail [39]). The 14-3-3 isoforms were selected based on quality of the resulting crystals. The crystal structures were solved by molecular replacement using the structures of 14-3-3ζ (PDB ID: 4FJ3 [33]) and 14-3-3γ (PDB ID: 2B05) as search models, and refined at a resolution of 2.68 and 2.84 Å, respectively (Table 1). The final electron densities allowed us to build seven residues (KLpSLQER, Fig. 3A and B) of pepS100 and six residues (RSLpSAP, Fig. 3C and D) of pepS511.

The main-chain conformations of both phosphopeptides in the 14-3-3 binding grooves are similar to those previously observed in other 14-3-3 protein complexes [33,37,40–42]. The 14-3-3ζ side chains coordinating the $pSer^{100}$ moiety of pepS100 include Arg^{56}, Arg^{127}, and Tyr^{128} (Fig. 3B). Although the side-chain of the Glu residue at the +3 position relative to $pSer^{100}$ is salt-bridged to the Lys^{120} of 14-3-3ζ, the side-chain of the Gln residue at +2 is hydrogen-bonded to the phosphate and to the main-chain carbonyl groups of $pSer^{100}$. These interactions apparently force the direction of the polypeptide chain to change, thus mimicking the role of the Pro residue, as previously observed, for example, in the 14-3-3 binding motifs of yeast neutral trehalase, which also lacks a Pro residue at the +2 position relative to the phosphorylated residue (Fig. 3E) [42]. In the case of pepS511, which contains the canonical "mode I" 14-3-3 binding motif, the coordination of the $pSer^{511}$ moiety and all other contacts are identical to those previously observed in other complexes of peptides with the "mode I" motif.

3.5. The 14-3-3γ:pCaMKK2 complex is flexible and elongated

Because all our attempts to grow crystals of the 14-3-3γ:pCaMKK2-S^{100} and 14-3-3γ:pCaMKK2-S^{100,511} complexes failed, we used SAXS analysis to structurally characterize the interaction between 14-3-3γ and pCaMKK2 in solution. We and other researchers have previously used a similar approach to characterize various 14-3-3 protein complexes [22,41,45]. X-ray scattering data were collected for CaMKK2-S^{100}, 14-3-3γΔC and both complexes prepared with 2:1 M stoichiometry (Table 2). The linearity of the Guinier plots (Fig. 4B), the lack of a significant variation in forward scattering intensity $I(0)$ with the concentration, the Porod volume V_p and the radius of gyration R_g (Table 2) confirmed the absence of aggregation and the stability of the complexes within the concentration range tested. The apparent M_w values of ~47 and ~54 kDa for CaMKK2 and 14-3-3γΔC, respectively, estimated based

Table 1
Crystallographic data collection and refinement statistics.

Complex	14-3-3ζΔC:pepS100	14-3-3γΔC:pepS511
Wavelength (Å)	0.9184	1.3418
Space group	P212121	R3
Unit-cell parameters		
a, *b*, *c* (Å)	56.95, 60.31, 262.19	115.73, 115.73, 203.96
α, β, γ (°)	90, 90, 90	90, 90, 120
Asymmetric unit contents	Two dimers of 14-3-3ζΔC with bound phosphopeptides	Two dimers of 14-3-3γΔC with bound phosphopeptides
Resolution range (Å)[a]	47.71–2.68 (2.84–2.68)	26.82–2.84 (2.94–2.84)
Unique reflections	26,274 (4126)	22,801 (2424)
Data multiplicity	6.42 (6.23)	10.85 (10.81)
Completeness (%)	99.7 (98.9)	94.4 (99.4)
$\langle I/\sigma(I)\rangle$	17.37 (5.21)	11.19 (2.26)
R_{meas}[b]	0.08 (0.3)	0.26 (0.97)
R_{work}	0.208	0.228
R_{free}[c]	0.234	0.280
No. of protein atoms	7118	7402
No. of waters	114	35
Average B factors (Å^2)		
Protein	50.34	40.87
Water	41.77	34.55
R.m.s.[d] deviations from ideal values		
Bond lengths (Å)	0.009	0.004
Bond angles (°)	0.97	0.55
Ramachandran favored (%)	95.51	98.88
Ramachandran allowed (%)	4.49	1.12
Ramachandran outliers (%)	0	0

[a] Values in parentheses are for the highest resolution shell.

[b] $R_{meas} = \sum_{hkl}\{N(hkl)/[N(hkl)-1]\}^{1/2} \times \sum_i |I_i(hkl) - \langle I(hkl)\rangle| \sum_{hkl}\sum_i I_i(hkl)$, where $I(hkl)$ is the intensity of reflection hkl, $\langle I(hkl)\rangle = \frac{1}{N(hkl)}\sum_i I_i(hkl)$, and $N(hkl)$ the multiplicity.

[c] The free R value (R_{free}) was calculated using 5% of the reflections, which were omitted from the refinement.

[d] R.m.s., root mean square.

on the $I(0)$, correspond well with their expected M_w values of 48.0 and 54.3 kDa, respectively. The apparent M_w of 92 − 95 and 94 − 97 kDa of the 14-3-3γΔC:pCaMKK2-S^{100} and 14-3-3γΔC:pCaMKK2-S^{100,511} complexes, respectively, as well as their V_p (~160 nm^3), also indicate a 2:1 M stoichiometry (theoretical M_w 102.3 kDa), thus corroborating the SV AUC results (for globular proteins, $M_w \approx V_p \times 0.625$).

The comparison of the calculated distance distribution functions, $P(r)$, is shown in Fig. 4C. The $P(r)$ functions of CaMKK2 alone and of both complexes show significant asymmetry and longer intra-particle distances and a larger maximum particle distance (D_{max}) than those of the 14-3-3γΔC dimer alone, thus suggesting that their molecules are more extended. This is also supported by their R_g and D_{max} values (Table 2), which are significantly larger than those of spherical proteins consisting of 430 (CaMKK2) and 944 (the 14-3-3γΔC:pCaMKK2 complex) residues ($R_g \sim 3N^{1/3}$, where N is the number of residues; $D_{max} \sim 2.6R_g$). Moreover, the analysis of scattering data showed that the 14-3-3γΔC:pCaMKK2-S^{100,511} complex has lower R_g and D_{max} values than the 14-3-3γΔC:pCaMKK2-S^{100} complex (Table 2), thus indicating that CaMKK2 phosphorylated at both motifs forms a more compact complex with 14-3-3γ. However, it should be noted that the 14-3-3γΔC:pCaMKK2-S^{100,511} complex was prepared using pCaMKK2-S^{100,511}, which was not completely phosphorylated at Ser^{511} (Fig. S2). Therefore, the values of R_g and D_{max} were assessed in a mixture of two complexes where either the N-terminal motif or both motifs are docked within the binding grooves of the 14-3-3 dimer.

14-3-3 binding motifs are frequently located within long intrinsically disordered segments found in most 14-3-3 binding partners [46]. Apparently, CaMKK2 is not an exception because the analysis of protein disorder using the web servers PrDOS [47] and IUPred [48] suggested that its N- and C-terminal segments (residues 1 − 155 and 495 − 588) are significantly disordered (Fig. S4). These segments flank the structured kinase domain and contain both 14-3-3 binding motifs, as well as other regulatory regions (Fig. 1A). Indeed, the analysis of protein disorder using the dimensionless Kratky plot ($(sR_g)^2I(s)/I(0)$ versus sR_g) suggested that CaMKK2 and both complexes have higher conformational flexibility than 14-3-3γΔC (Fig. 4D). The scattering data for compact globular proteins in this plot show a maximum value of 1.104 at sR_g ~1.73 [49]. In addition, only 14-3-3γΔC showed a bell-shaped curve with an $(sR_g)^2I(s)/I(0)$ maximum of ~1.1 at an sR_g value of 1.7 (marked by cyan lines in Fig. 4D). Moreover, a more gradual decrease toward zero at higher sR_g and a higher maximum indicated that the 14-3-3γΔC:pCaMKK2-S^{100} complex has a higher conformational flexibility than the pCaMKK2-S^{100,511} complex, most likely resulting from the absence of interaction between 14-3-3 and the C-terminal segment of pCaMKK2-S^{100}.

3.6. Structural architecture of the 14-3-3γ:pCaMKK2 complex in solution

SAXS-based structural modeling was performed only for the 14-3-3γΔC:pCaMKK2-S^{100} complex. The 14-3-3γΔC:pCaMKK2-S^{100,511} complex was excluded from this analysis due to the heterogeneity caused by the incomplete phosphorylation of the C-terminal motif at Ser^{511} (Fig. S2). Moreover, the 14-3-3γΔC:pCaMKK2-S^{100} complex likely represents a physiologically more relevant form, considering the weak phosphorylation of Ser^{511} [11,12,14]. To determine the relative positions of 14-3-3 and CaMKK2 within the complex, multiphase modeling was performed to obtain ab initio bead models that include two phases representing individual components within a low-resolution shape [50]. Twenty independent models generated using the program MONSA [27] showed similar shape with a mean normalized spatial discrepancy (NSD) value of 0.61. The final model (Fig. 5A), the most typical model selected from all models calculated based on the lowest NSD value, showed a good approximation to the experimental SAXS data (Fig. S5). The calculated molecular envelope had an asymmetric shape, with most of the CaMKK2 phase located not in the central channel of the 14-3-3 dimer (a deep depression in the center of the 14-3-3 phase) but rather attached to the side of the 14-3-3 dimer and stretching out into the solution.

Subsequently, rigid-body modeling of the 14-3-3γΔC:pCaMKK2-S^{100} complex was performed using the program CORAL [25] and the crystal structures of 14-3-3γΔC (PDB ID: 2B05) and of the kinase domain of CaMKK2 [35]. The N-terminal 14-3-3 binding motif was restrained in the ligand-binding groove of 14-3-3γ, as previously observed in the crystal structure of the 14-3-3γΔC:pepS100 complex (Fig. 3A), and unstructured segments missing in the crystal structure were modeled as dummy residue chains. The final CORAL model fitted the SAXS data, with a χ^2 value of 1.33, and showed an asymmetric overall shape similar to that of the kinase domain of CaMKK2 located outside the central channel of the 14-3-3γ dimer (Fig. 5B and D). The model suggests that pCaMKK2-S^{100} interacts with 14-3-3γ not only through the phosphorylated N-terminal motif but also via a direct contact between the kinase domain and the 14-3-3 surface, in contrast to an extended state with CaMKK2 tethered to 14-3-3 only via a single phosphosite. Moreover, the presence of additional contacts between 14-3-3γ and pCaMKK2-S^{100}, outside the phosphorylated motif and the 14-3-3 binding groove, was corroborated by the binding affinity of pCaMKK2-S^{100} (K_D of ~1 μM, Fig. 1B), which was significantly higher than that of the synthetic phosphopeptide containing only the N-terminal 14-3-3 binding motif that binds 14-3-3γ with a K_D of 9 μM (Fig. S6).

Because the 14-3-3 binding motif and the kinase domain of pCaMKK-S^{100} are separated by a 60-residue-long segment, which is predicted to be unstructured (Figs. 1A and S4), in solution, the 14-3-

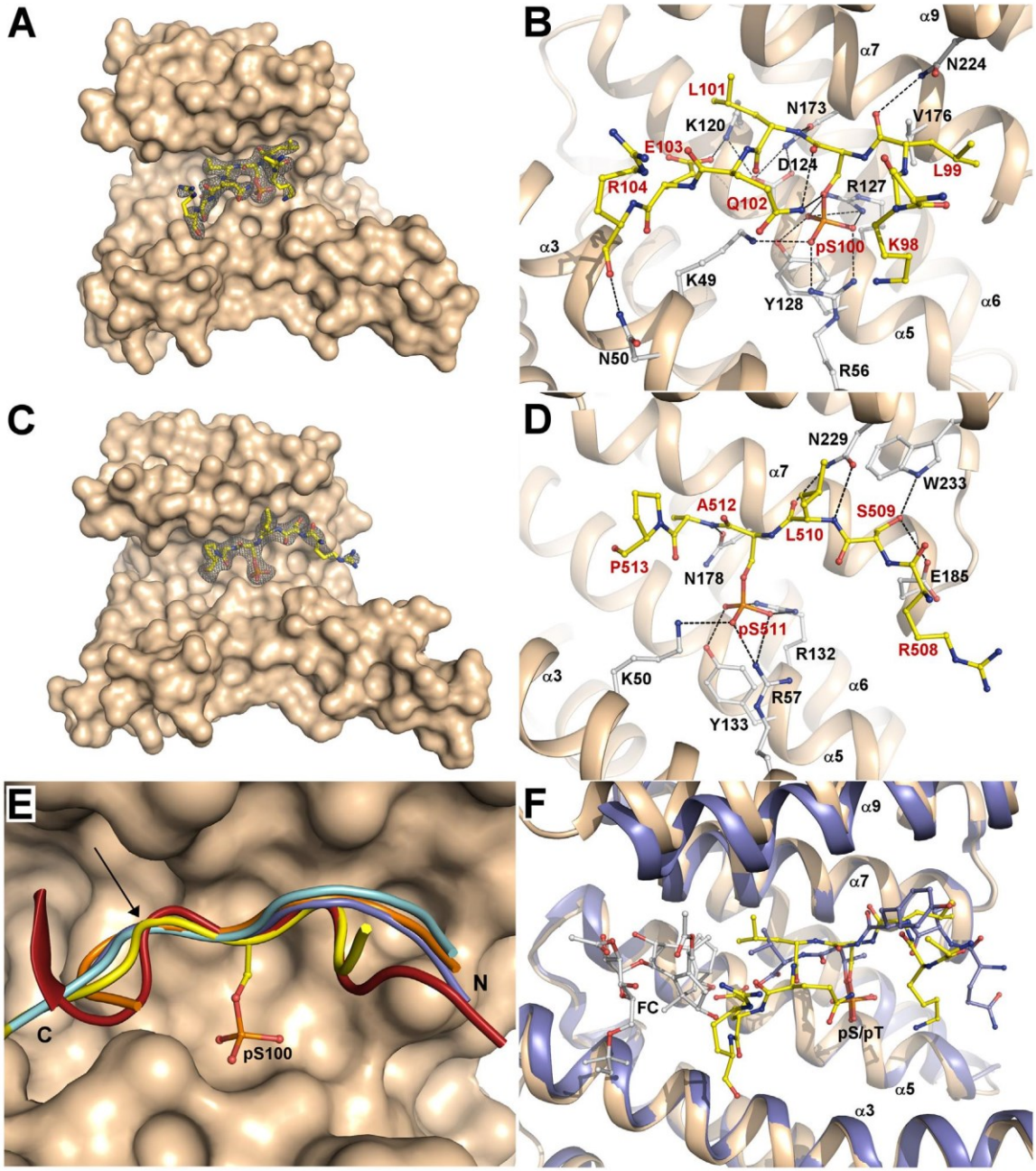

Fig. 3. Contacts between 14-3-3 and the 14-3-3 Binding Motifs of pCaMKK2. (A) Crystal structure of the 14-3-3ζ:pepS100 complex. The $2F_o$-F_c electron density map is contoured at 1σ. (B) Detailed view of contacts between 14-3-3ζ and the pepS100 peptide. The CaMKK2 residues are labeled in red, and the 14-3-3ζ residues are labeled in black. (C) Crystal structure of the 14-3-3γ:pepS511 complex. The $2F_o$-F_c electron density map is contoured at 1σ. (D) Detailed view of contacts between 14-3-3γ and the pepS511 peptide. The CaMKK2 residues are labeled in red, and the 14-3-3γ residues are labeled in black. (E) Comparison of the main-chain conformation of pepS100 (yellow) and pepS511 (violet) peptides with a "mode 1" 14-3-3 peptide (sequence RSHpSYPA, PDB ID: 1QJB, orange) [37], the 14-3-3 binding motifs of AANAT (sequence RRHpTLPA, PDB ID: 1IB1, cyan) [43] and neutral trehalase Nth1 (sequence TRRGpSEDDT, PDB ID: 5N6N, red) [42]. The C-terminal portion of the 14-3-3 binding motifs is indicated by a black arrow. (F) Superimposition of the 14-3-3ζ:pepS100 complex (pepS100 is shown in yellow) with the ternary complex between the "mode 3" phosphopeptide derived from the C-terminus of plant plasma membrane H^+-ATPase (sequence QSYpTV, shown as violet sticks), plant 14-3-3C (violet) and fusicoccin (FC, PDB ID: 1O9F) [44].

3γΔC:pCaMKK2-S^{100} complex may adopt different conformations. Moreover, the presence of conformational flexibility in the complex was indicated by the dimensionless Kratky plot (Fig. 4D). Therefore, we also attempted to model the complex as an ensemble of conformers using the program EOM [28]. The 14-3-3γΔC dimer, the 14-3-3 binding motif and the kinase domain of CaMKK2 were treated as rigid bodies and the flexible N- and C-terminal segments of CaMKK2 as chains of dummy residues. An initial pool of 10,000 conformers was generated and a genetic algorithm was then used to select an ensemble of conformers that collectively fit the experimental SAXS data. The selected ensemble of conformers fits the experimental scattering data with a χ^2 value of 1.22 (Fig. 5D). The R_g and D_{max} distributions calculated from the optimized ensemble are shown in Fig. 5C. The R_g distribution of the EOM-selected ensemble is biased toward more compact structures with lower R_g values than those of the pool. The average R_g and D_{max} values of the ensemble (42.4 and 149 Å, respectively) are consistent with values calculated from the scattering curves (Table 2). In addition, the R_g and D_{max} distributions of the 14-3-3γΔC:pCaMKK2-S^{100} complex have

Table 2
Structural parameters determined from SAXS data.

	c (mg.mL^{-1})	R_g (Å)[b]	R_g (Å)[c]	D_{max} (Å)	V_p[d] (nm^3)	M_w[e,g] (kDa)	M_w[f,g] (kDa)
14-3-3γΔC[a]	3.0	28.7 ± 0.4	28.6 ± 0.4	89	77.8	54 ± 1	49
	1.5	29.0 ± 0.4	29.0 ± 0.4	89	82.8	55 ± 1	52
CaMKK2	2.8	32.6 ± 0.3	32.7 ± 0.3	126	95.6	48 ± 1	60
	2.1	32.1 ± 0.3	32.2 ± 0.3	125	94.0	46 ± 1	59
Complex pSer^{100}	16.9	42.3 ± 0.6	42.4 ± 0.6	146	160.4	92 ± 1	100
	12.6	42.5 ± 0.6	42.6 ± 0.6	144	163.4	95 ± 1	102
	9.9	42.4 ± 0.6	42.5 ± 0.6	146	161.1	94 ± 1	101
Complex pSer^{100,511}	11.9	39.9 ± 0.7	40.0 ± 0.7	141	164.8	97 ± 1	103
	6.5	39.1 ± 0.6	39.2 ± 0.6	141	159.6	94 ± 1	100

[a] 14-3-3γ missing its C-terminal 13 residues.
[b] Calculated using Guinier approximation.
[c] Calculated using the programm GNOM.
[d] The excluded volume of the hydrated particle (the Porod volume).
[e] Molecular weight estimated by comparing the forward scattering intensity $I(0)$ with that of the reference solution of bovine serum albumin.
[f] Molecular weight estimated from the Porod volume ($M_w \approx V_p \times 0.625$) [25].
[g] Theoretical molecular weights of the 14-3-3γΔC dimer, pCaMKK2 and the pCaMKK2:14-3-3γΔC complex (with 2:1 stoichiometry) are 54.3, 48.0 and 102.3 kDa, respectively.

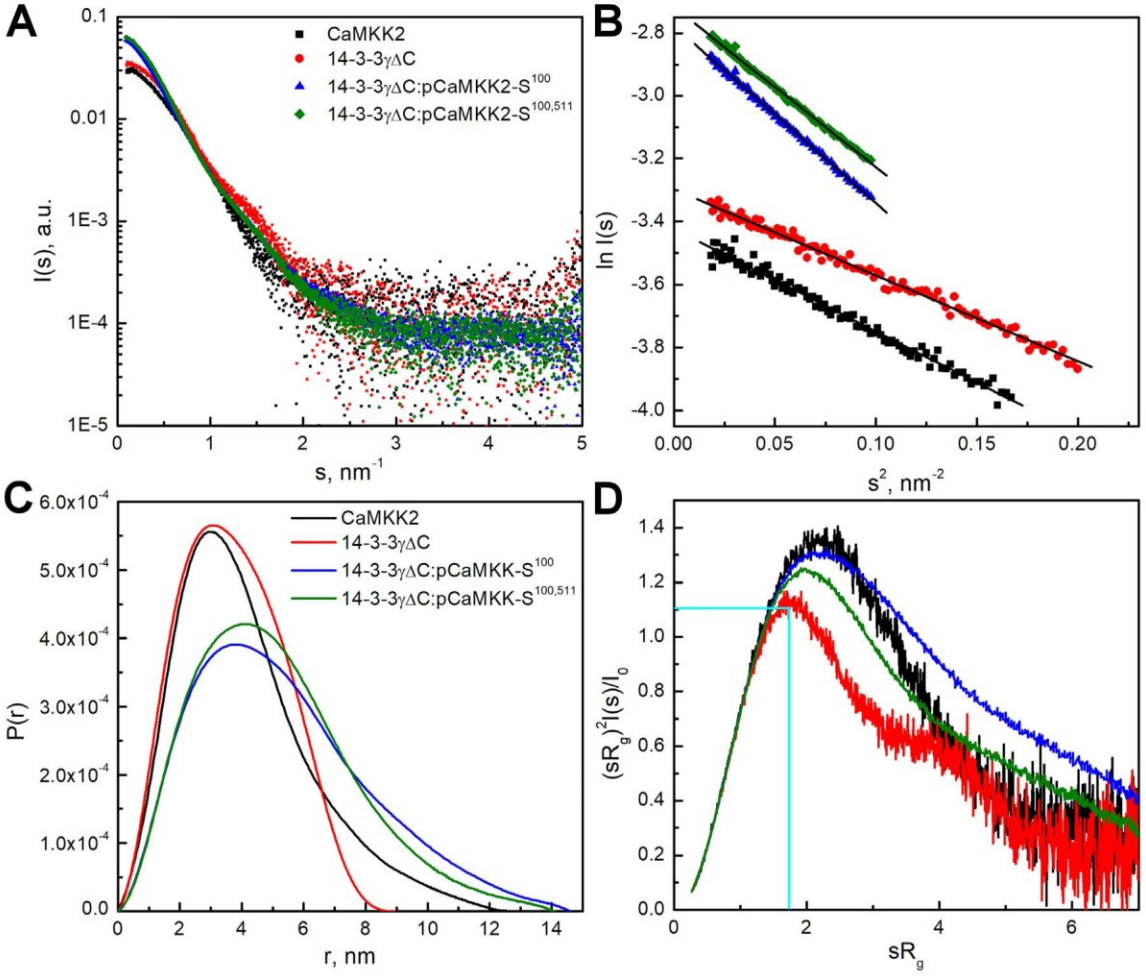

Fig. 4. SAXS Analysis of the 14-3-3ζ:pCaMKK2 Complexes. (A) Scattering intensity as a function of the scattering vector s ($s = 4\pi\sin(\theta/\lambda)$, where 2θ is the scattering angle, and λ is the wavelength) of 14-3-3γΔC, CaMKK-S^{100}, and the 14-3-3γΔC:pCaMKK2-S^{100} and 14-3-3γΔC:pCaMKK2-S^{100,511} complexes were mixed at 2:1 M stoichiometry. (B) Guinier plots for scattering curves shown in panel A. (C) Distance distribution functions P(r) calculated from scattering data using the program GNOM [24]. (D) Dimensionless Kratky plots. Cyan lines mark the maximum at a value of 1.104 for $sR_g = 1.73$, which is characteristic for the scattering data of compact globular proteins [49].

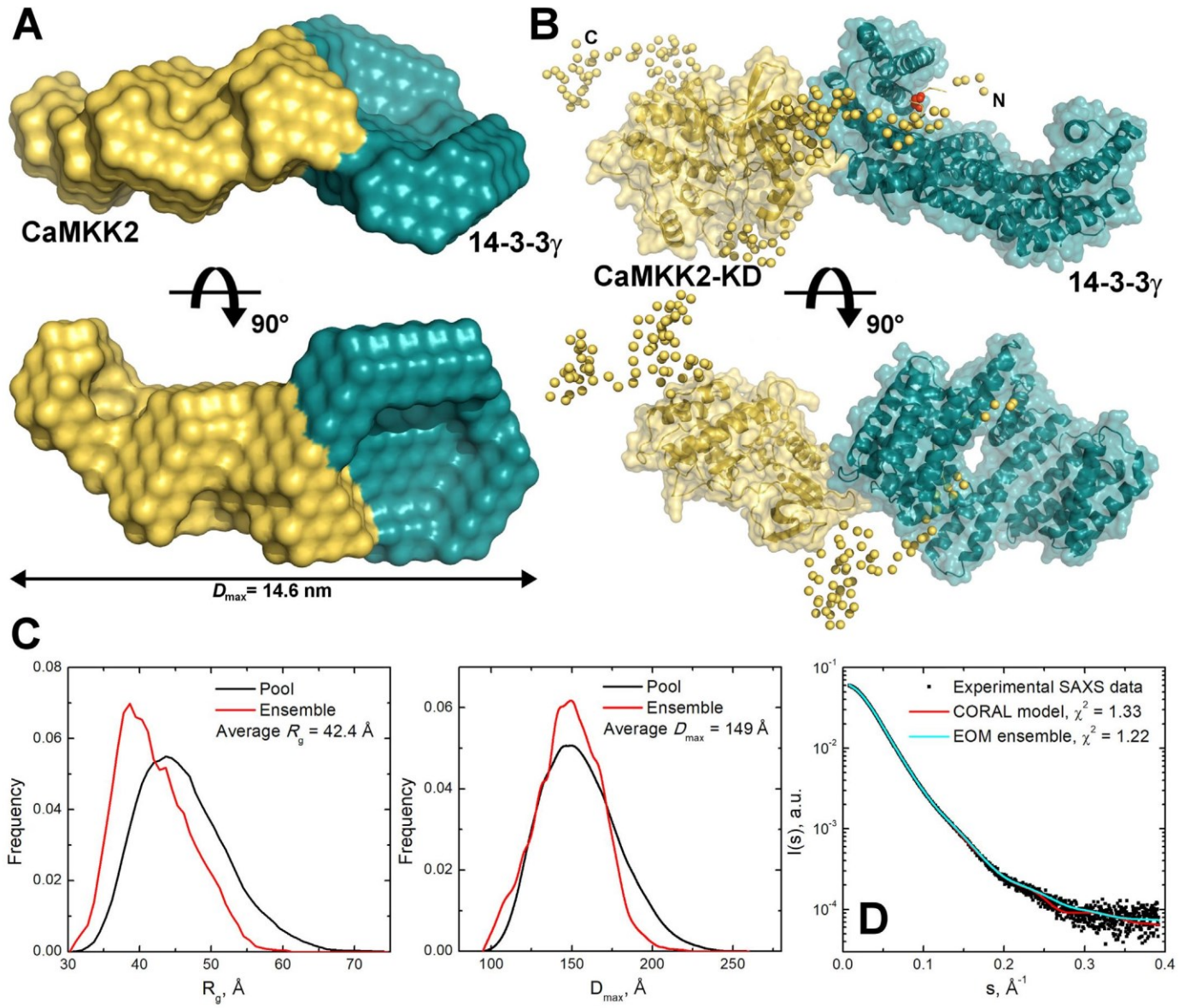

Fig. 5. SAXS-Based Structural Modeling of the 14-3-3γ:pCaMKK2 Complex. (A) Most typical multiphase reconstruction for the 14-3-3γΔC:pCaMKK2-S^{100} complex with the 14-3-3 phase colored in cyan and the CaMKK2 phase colored in yellow. (B) Typical conformation of the 14-3-3γΔC:pCaMKK2-S^{100} complex obtained in the program CORAL using the crystal structures of 14-3-3γΔC (PDB ID: 2B05) and the kinase domain of CaMKK2 (CaMKK-KD, PDB ID: 2ZV2 [35]). The unstructured segments missing in the crystal structure were modeled as dummy residue chains. The residue Ser^{100} is shown in red. (C) Distributions of R_g and D_{max} values of the 14-3-3γΔC:pCaMKK2-S^{100} complex conformations from ensemble selected by the program EOM [28]. (D) Experimental scattering curve of the complex superimposed with the calculated curves of the CORAL model shown in panel B (red) and the ensemble selected by the program EOM (cyan).

smaller extents than those of the pools, indicating that its accessible conformations are not fully randomly distributed and that the complex is unable to be fully extended in solution, thereby suggesting that 14-3-3γΔC interacts with the kinase domain and with pCaMKK2 linkers in solution. Thus, these results are consistent with the MONSA and the CORAL models.

3.7. 14-3-3γ binding does not affect Ca^{2+}/CaM binding to pCaMKK2

A common mechanism of action of the 14-3-3 protein is the interference with protein-protein interactions of its ligand. In the case of CaMKK, 14-3-3 could affect Ca^{2+}/CaM binding to the C-terminus of CaMKK. To test this hypothesis, Ca^{2+}/CaM binding to pCaMKK2-S^{100} and to pCaMKK2-S^{100,511} was investigated in the absence and presence of 14-3-3γ. For such purpose, dansyl-labeled CaM [51] was prepared, and its interaction with pCaMKK2 was monitored using time-resolved fluorescence intensity and anisotropy decay measurements (Table 3 and Fig. 6). The analysis of these measurements showed that Ca^{2+}/CaM binding to pCaMKK2 significantly increased the mean excited-state lifetime (τ_{mean}) and the longest correlation time ϕ_4 of the dansyl moiety, thus reflecting a decrease in the overall rotational diffusion coefficient upon complex formation, which indicates Ca^{2+}/CaM binding to both pCaMKK2 variants. The mutual interaction is clearly visible by the naked eye because the complexes have slower anisotropy decays than free Ca^{2+}/CaM, as shown in Fig. 6A, B. Although 14-3-3γ addition to the pCaMKK2-S^{100}:Ca^{2+}/CaM complex failed to induce any significant change in the dansyl anisotropy decay (open triangles in Fig. 6A), in the case of the pCaMKK2-S^{100,511}:Ca^{2+}/CaM complex, the presence of 14-3-3γ resulted in an additional increase of the rotational correlation time ϕ_4, as clearly seen in the raw data from the elevation of the anisotropy decay tail (open triangles in Fig. 6B). This indicates a significant change in the hydrodynamic properties of the complex,

Table 3
Summary of time-resolved Dans-CaM fluorescence measurements.

Sample	τ_{mean}[a,b] (ns)	K_{SV}[e] (M^{-1})	k_i ($\times 10^{-5}$) ($M^{-1}\,s^{-1}$)[f]	ϕ_1[d] (ns)	β_1[c]	ϕ_2 (ns)	β_2	ϕ_3 (ns)	β_3	ϕ_4 (ns)	β_4
Dansyl-CaM	15.2	0.18	120	< 0.1	0.03	0.6	0.02	2.5	0.10	9.3	0.12
+14-3-3γ	15.9	0.19	120	< 0.1	0.03	0.5	0.02	1.9	0.08	8.4	0.15
$+S^{100}$	20.5	0.01	4			2.5	0.01	12	0.11	49	0.15
$+S^{100}$ + 14-3-3γ	20.5	0.00	0			3.0	0.01	11	0.10	49	0.16
$+S^{100,511}$	20.6	0.01	3			4.7	0.03	16	0.10	52	0.15
$+S^{100,511}$ + 14-3-3γ	20.2	0.11	53			2.8	0.02	12	0.08	88	0.16

[a] Mean lifetimes were calculated as $\tau_{mean} = \Sigma_i f_i \tau_i$, where f_i is an intensity fraction of the i-th lifetime component τ_i.
[b] S.D. value is ± 0.1 ns.
[c] The anisotropies $r(t)$ were analyzed for a series of exponentials by a model-independent maximum entropy method.
[d] Fast unresolved component.
[e] Stern-Volmer constant of acrylamide quenching.
[f] Bimolecular quenching constant for acrylamide collisional quenching.

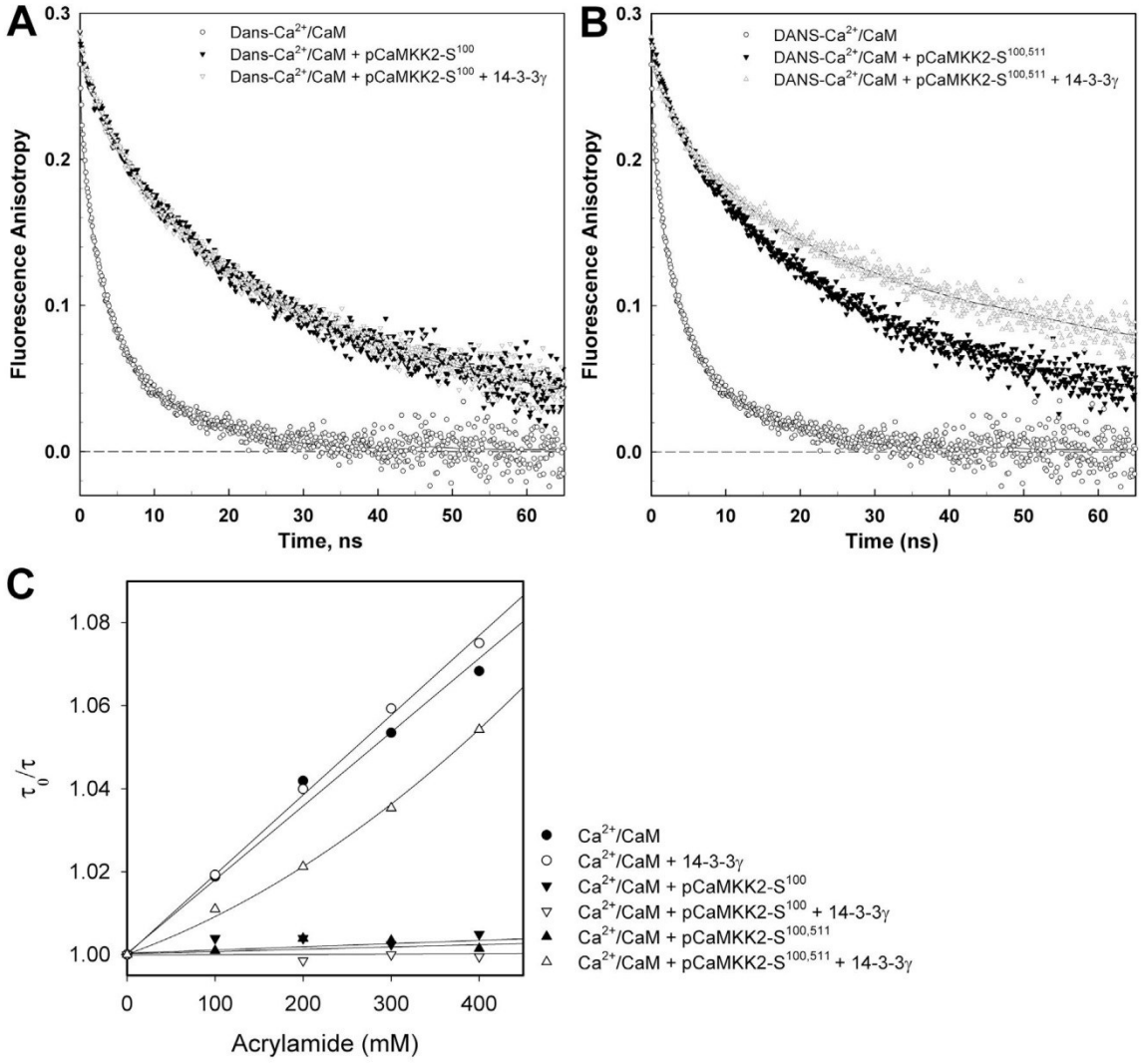

Fig. 6. Time-Resolved Dansyl Fluorescence Measurements. (A) Fluorescence anisotropy decays of free dansyl-Ca^{2+}/CaM (open circles) and dansyl-Ca^{2+}/CaM in the presence of pCaMKK2-S^{100} (closed triangles), and pCaMKK2-S^{100} and 14-3-3γ (open triangles). (B) Fluorescence anisotropy decays of free dansyl-Ca^{2+}/CaM (open circles) and dansyl-Ca^{2+}/CaM in the presence of pCaMKK2-$S^{100,511}$ (closed triangles) and pCaMKK2-$S^{100,511}$ and 14-3-3γ (open triangles). (C) Acrylamide quenching of dansyl-Ca^{2+}/CaM fluorescence. Quenching of free dansyl-Ca^{2+}/CaM (●) is dramatically reduced in the presence of pCaMKK2-S^{100} (▼) and pCaMKK2-$S^{100,511}$ (▲). Although 14-3-3γ addition to the dansyl-Ca^{2+}/CaM/pCaMKK2-S^{100} mixture only slightly increases the shielding of the dansyl fluorophore from the quencher (▽), its addition to the dansyl-Ca^{2+}/CaM/pCaMKK2-$S^{100,511}$ mixture significantly increases dansyl accessibility to acrylamide (Δ), indicating a conformational change of the complex. 14-3-3γ addition to dansyl-Ca^{2+}/CaM causes virtually no effect in the control sample (○).

likely reflecting the binding of the phosphorylated C-terminal motif of pCaMKK2-$S^{100,511}$ to the binding groove of the second 14-3-3γ protomer that results in a formation of apparently larger rotor. Negligible changes in the τ_{mean} of the dansyl moiety, observed in the presence of 14-3-3γ, suggested that 14-3-3γ binding has no effect on the stability of the pCaMKK2:Ca^{2+}/CaM complex. This result was further corroborated by acrylamide quenching of dansyl-CaM fluorescence (Fig. 6C). More specifically, quenching of free dansyl-Ca^{2+}/CaM markedly decreased in the presence of both pCaMKK2 variants. Although 14-3-3γ addition to the pCaMKK2-S^{100}:Ca^{2+}/CaM complex caused only a slight increase in the shielding of the dansyl fluorophore from the quencher, 14-3-3γ addition to the pCaMKK2-$S^{100,511}$:Ca^{2+}/CaM complex resulted in a significant increase of dansyl accessibility to acrylamide, thus indicating a conformational change in the vicinity of bound Ca^{2+}/CaM, most likely due to the interaction between the C-terminal motif and 14-3-3γ.

3.8. Conformational behavior of CaMKK2 and its changes upon 14-3-3γ binding

Time-resolved tryptophan fluorescence measurements were then performed to investigate the conformational behavior of pCaMKK2-S^{100} upon 14-3-3γ binding. Four CaMKK2-S^{100} mutants containing a single tryptophan residue (Trp^{140}, Trp^{267}, Trp^{374} and Trp^{445}) were prepared (Fig. 1A). The sequence of $CaMKK2_{93-517}$ contains two tryptophan residues, Trp^{374} and Trp^{445}, both located within the C-lobe of the kinase domain (Fig. 1C). Therefore, mutants containing single Trp^{374} or Trp^{445} were created by mutating the other residue to Phe. Mutants containing Trp^{140} and Trp^{267} located within the N-terminal linker, close to the regulatory phosphorylation site Thr^{145}, and the N-lobe of the kinase domain, respectively, were generated by mutating both Trp^{374} and Trp^{445} to Phe and by introducing a single Trp residue at the desired position. The fluorescently silent 14-3-3γ noW missing all Trp residues was used in all tryptophan fluorescence measurements [52].

Fluorescence intensity decay measurements showed that the 14-3-3γ noW binding causes a small, albeit significant, increase in the τ_{mean} of Trp^{140} and Trp^{445}, whereas nonsignificant effects were assessed on mutants containing Trp^{267} and Trp^{374} (Table 4). The τ_{mean} prolongation of both mutants is clearly visible in the raw data shown in Fig. 7A and B, wherein the difference between fluorescence decays in the presence and absence of 14-3-3 is undoubtedly higher than the data noise level. The analysis of the lifetime distribution, shown in Fig. 7C and D, indicates an increase in the τ_{mean} of Trp^{140} upon 14-3-3 binding, mainly caused by the appearance of a new lifetime component centered around 8 ns, and a decrease in the intensity fractions associated with the shorter lifetime components. Similarly, 14-3-3 binding induced an increase in the τ_{mean} of Trp^{445}, mainly caused by the extension of the longest lifetime component around 5 ns and by the significant increase in its intensity fraction. The statistical significance of the observed difference is supported by the Monte Carlo confidence-interval analysis [53] shown in Fig. S7. The increase in τ_{mean} indicates a small 14-3-3γ binding-induced change of quenching interactions and/or polarity near these two Trp residues.

Table 4
Summary of time-resolved tryptophan fluorescence measurements.

pCaMKK-S^{100} mutant	τ_{mean} [a,b] (ns)	ϕ_1 (ns)	β_1	ϕ_2 (ns)	β_2	ϕ_3 [c] (ns)	β_3
W140	4.19	1.4	0.037			72	0.170
W140 + 14-3-3γ noW	4.34	0.8	0.021	3.5	0.029	100	0.161
W267	4.88	0.9	0.014			53	0.200
W267 + 14-3-3γ noW	4.97	0.9	0.004	5.3	0.006	79	0.197
W445	2.47	2.3	0.026			84	0.184
W445 + 14-3-3γ noW	2.59	2.8	0.041			> 100 [d]	0.171
W374	4.39	0.9	0.004			44	0.205
W374 + 14-3-3γ noW	4.37	0.5	0.005			61	0.206

[a] Mean lifetimes were calculated as $\tau_{mean} = \Sigma_i f_i \tau_i$, where f_i is an intensity fraction of the *i-th* lifetime component τ_i.

[b] S.D. value is ± 0.05 ns.

[c] S.D. value is about ± 10 ns.

[d] Poorly resolved correlation time of the overall protein rotation; SD is highly asymmetric to longer values. The resolution is primarily limited by a short lifetime value.

Subsequently, the segmental motions of inserted tryptophans were studied using the polarized time-resolved emission measurements. The fluorescence anisotropy decays of all four tryptophans revealed two classes of correlation times (Table 4). Short correlation times, with values up to few nanoseconds (ϕ_1), likely reflect fast segmental motion of the protein near the tryptophan residue, whereas significantly longer correlation times ($\phi_3 > 44$ ns) likely reflect the overall rotational motion of pCaMKK2-S^{100}. In the case of the pCaMKK2-S^{100} W140 and W267 mutants, 14-3-3γ noW binding resulted in the appearance of a new correlation time component located around 3.5 − 5.3 ns (ϕ_2), which could reflect slightly modified internal dynamics of the pCaMKK2-S^{100} complex, induced by 14-3-3γ binding. Changes in the extent of segmental motion were assessed based on the change in the sum of amplitudes of fast anisotropy decay components ($\beta_{fast} = \beta_1 + \beta_2$) [54]. Similarly to the fluorescence lifetime measurements, small but significant changes in β_{fast} were observed only in mutants containing Trp^{140} and Trp^{445}, thus suggesting that complex formation increases protein flexibility in regions surrounding these two tryptophan residues.

Therefore, fluorescence lifetime and anisotropy results indicate that 14-3-3γ binding affects the conformation of CaMKK2 in several regions outside the N-terminal phosphorylated motif, including regions surrounding the Trp^{140} within the N-terminal extension and the Trp^{445} within the C-lobe of the kinase domain.

4. Discussion

The main aim of this study was to characterize the interaction between the 14-3-3 protein and CaMKK2. 14-3-3 proteins regulate the function of many enzymes through various mechanisms. For example, serotonin *N*-acetyltransferase and neutral trehalase Nth1 are activated through 14-3-3 protein-mediated structural modulation of their active sites [42,43]. In the case of phosphorylated tryptophan hydroxylase, 14-3-3 binding slows-down the dephosphorylation of key regulatory phosphosites [55]. Other mechanisms are based on the regulation of sub-cellular localization [56] and on the stabilization of the tertiary and/or quaternary structure of the bound enzyme [57]. Enzymes regulated in a 14-3-3-dependent manner also include many protein kinases [58], although the underlying mechanisms are not fully understood, primarily due to the lack of structural data.

Previous studies on phosphorylated CaMKK1 have shown that the 14-3-3 binding suppresses its catalytic activity [14,15]. Interestingly, enzyme activity measurements revealed that the activity of phosphorylated CaMKK2 is not suppressed but rather weakly enhanced upon complexation with 14-3-3γ (Fig. 2). This indicates that CaMKK isoforms differ in their 14-3-3-mediated regulations, maybe due to differences in their biochemical properties [6,7].

The SAXS results indicated that the complex formed between 14-3-3γ and pCaMKK2-S^{100} had an elongated and flexible conformation in which the kinase domain of CaMKK appears to directly interact with the 14-3-3γ dimer surfaces outside its central channel (Figs. 4C,D and 5A,B). The interaction between the kinase domain of pCaMKK2-S^{100} and 14-3-3γ was also indicated by the analysis, in terms of ensemble of conformations (Fig. 5C), which suggested that the 14-3-3γ:pCaMKK2-S^{100} complex is not as extended as the flexible linkers allow. Moreover,

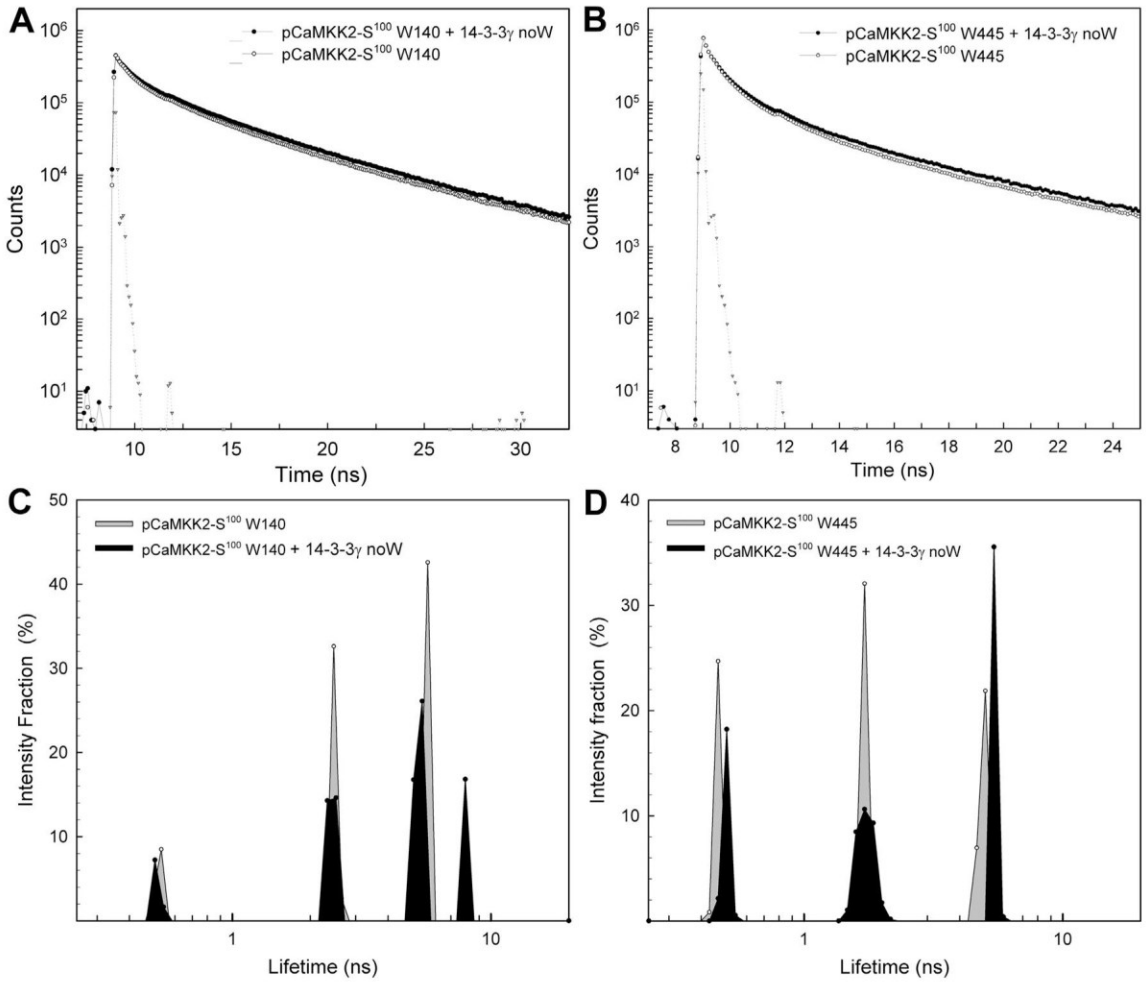

Fig. 7. Time-Resolved Tryptophan Fluorescence Measurements. (A) Normalized fluorescence intensity decays of pCaMKK2-S^{100} W140 mutant, in the absence (open circles) and presence (closed circles) of 14-3-3γ noW. Triangles denote instrument response function. (B) Same as (A) for pCaMKK2-S^{100} W445 mutant. (C) Excited state lifetime distribution of pCaMKK2-S^{100} W140 in the absence (gray-filled distribution) and presence of 14-3-3γ noW (black-filled distribution). (D) Same as (C) for pCaMKK2-S^{100} W445 mutant.

time-resolved fluorescence measurements of the pCaMKK2-S^{100} W445 mutant (Table 4 and Fig. 7) and the binding affinity of pCaMKK2-S^{100}, which was significantly higher than that of pepS100 phosphopeptide (Figs. 1D and S6), further corroborated the existence of contacts between 14-3-3γ and the kinase domain of CaMKK2. Although the second 14-3-3 binding motif at the C-terminus of CaMKK2 may not be significantly phosphorylated in vivo [11,12,14], the presence of this motif increased the overall stability of the complex and reduced its conformational flexibility (Figs. 1E and 4D, 6B). This most likely results from the immobilization of the C-terminal extension when the C-terminal motif is anchored to the second ligand binding groove of the 14-3-3γ dimer. The interaction between 14-3-3 and the kinase domain may be responsible for observed changes in the catalytic activity of CaMKK2 (Fig. 2). We may speculate that the 14-3-3γ binding affects the conformation of the CaMKK2 active site and/or changes its accessibility. Yet another possibility might be that the 14-3-3γ binding affects the interaction between the kinase domain and regulatory regions within the N- and C-terminal segments flanking the kinase domain.

CaMKK1 activity is inhibited by Thr^{108} phosphorylation (Thr^{145} in CaMKK2) [10,13]. In addition, a recent report indicated that the phosphorylation of this residue by AMPK suppresses the autonomous activity of rat CaMKK2 without significant effect on Ca^{2+}/CaM-dependent activity [59]. This threonine residue is located in the linker between the N-terminal 14-3-3 binding motif and the kinase domain (Fig. 1A) [10,13]. CaMKK2 also contains, in this region, serine residues Ser^{129}, Ser^{133}, Ser^{137} phosphorylated by cyclin-dependent kinase 5 and by glycogen synthase kinase 3, which are involved in the regulation of CaMKK2 autonomous activity and stability [9]. Time-resolved fluorescence measurements of the pCaMKK2-S^{100} W140 mutant showed that 14-3-3γ binding affects the structure of this region (Table 4 and Fig. 7). Therefore, structural changes in this region and/or its closeness to 14-3-3 may account for the previously reported protection of CaMKK1 Thr^{145} against dephosphorylation, which keeps CaMKK1 in the PKA-mediated inhibited state [14]. A similar mechanism may also be involved in the regulation of CaMKK2 as suggested by our observation that the 14-3-3γ binding slows down the dephosphorylation of pCaMKK2 by PP1 in vitro (Table S1 and Fig. S3). Alternatively, the 14-3-3 binding may inhibit CaMKK activity by affecting CaM binding to the C-terminus of CaMKK. However, fluorescence measurements with dansyl-CaM showed that this interaction is unaffected by 14-3-3 binding to the pCaMKK2:Ca^{2+}/CaM complex (Table 3 and Fig. 6).

The crystal structures of complexes between 14-3-3 and the 14-3-3 binding motifs of CaMKK showed that both phosphopeptides interact with the amphipathic groove of 14-3-3 similarly to other 14-3-3 complexes [33,37,40–42]. Nevertheless, in the case of the N-terminal motif, the interaction between the side-chain of Gln at the position +2 relative to pSer^{100} and the phosphate group appears to change the direction of the polypeptide chain (Fig. 3B). Interestingly, the superimposition of this structure with that of the ternary complex between the phosphopeptide derived from the C-terminus of plant plasma

membrane H^+-ATPase, plant 14-3-3C, and fusicoccin (Fig. 3F) [44] showed that the fusicoccin binding cavity stays empty due to the abrupt change in the direction of the C-terminal part of pepS100. Therefore, this protein-protein interaction might be stabilized by small-molecule compounds, as previously reported for other 14-3-3 complexes (reviewed in [60]), which is a potential strategy to inhibit the CaMKK activity.

Transparency document

The http://dx.doi.org/10.1016/j.bbagen.2018.04.006 associated this article can be found, in online version.

Acknowledgement

We thank Prof. Jaroslav Vecer for dansyl fluorescence data analysis, Dr. Petr Pompach and Dr. Petr Man for mass spectrometry analyses and Dr. Carlos V. Melo for proofreading the article.

Funding sources

This work was supported by the Czech Science Foundation (grant number 16-02739S), the Czech Academy of Sciences (Research Projects RVO: 67985823 of the Institute of Physiology), EU supported projects BIOCEV (CZ.1.05/1.1.00.02.0109) and Operational Programme "Research and Development for Innovation" (no. CZ.1.05/4.1.00/16.0340), Czech Infrastructure for Integrative Structural Biology (CIISB) project LM2015043, funded by MEYS CR, and by the H2020 Marie Curie Actions of the European Commission through the TASPPI project, Grant Agreement 675179.

Data deposition

The atomic coordinates and structure factors have been deposited in the Protein Data Bank, www.wwpdb.org (PDB ID codes 6EWW and 6FEL).

Author contributions

V.O. and T.O. designed research; K.P., O.P., S.K., D.K., D.L.S., P.H., and T.O. performed research; K.P., S.K., O.P., P.H., V.O., and T.O. analyzed data; and V.O. and T.O. wrote the paper.

Conflict of interest

The authors declare no conflict of interest.

Appendix A. Supplementary data

Supplementary data to this article can be found online at https://doi.org/10.1016/j.bbagen.2018.04.006.

References

[1] B. Haribabu, S.S. Hook, M.A. Selbert, E.G. Goldstein, E.D. Tomhave, A.M. Edelman, R. Snyderman, A.R. Means, Human calcium-calmodulin dependent protein kinase I: cDNA cloning, domain structure and activation by phosphorylation at threonine-177 by calcium-calmodulin dependent protein kinase I kinase, EMBO J. 14 (1995) 3679–3686.
[2] R.L. Hurley, K.A. Anderson, J.M. Franzone, B.E. Kemp, A.R. Means, L.A. Witters, The Ca2+/calmodulin-dependent protein kinase kinases are AMP-activated protein kinase kinases, J. Biol. Chem. 280 (2005) 29060–29066.
[3] K.A. Anderson, T.J. Ribar, F. Lin, P.K. Noeldner, M.F. Green, M.J. Muehlbauer, L.A. Witters, B.E. Kemp, A.R. Means, Hypothalamic CaMKK2 contributes to the regulation of energy balance, Cell Metab. 7 (2008) 377–388.
[4] L. Racioppi, A.R. Means, Calcium/calmodulin-dependent protein kinase kinase 2: roles in signaling and pathophysiology, J. Biol. Chem. 287 (2012) 31658–31665.
[5] H. Tokumitsu, T.R. Soderling, Requirements for calcium and calmodulin in the calmodulin kinase activation cascade, J. Biol. Chem. 271 (1996) 5617–5622.
[6] H. Tokumitsu, M. Muramatsu, M. Ikura, R. Kobayashi, Regulatory mechanism of Ca2+/calmodulin-dependent protein kinase kinase, J. Biol. Chem. 275 (2000) 20090–20095.
[7] K.A. Anderson, R.L. Means, Q.H. Huang, B.E. Kemp, E.G. Goldstein, M.A. Selbert, A.M. Edelman, R.T. Fremeau, A.R. Means, Components of a calmodulin-dependent protein kinase cascade. Molecular cloning, functional characterization and cellular localization of Ca2+/calmodulin-dependent protein kinase kinase beta, J. Biol. Chem. 273 (1998) 31880–31889.
[8] H. Tokumitsu, M. Iwabu, Y. Ishikawa, R. Kobayashi, Differential regulatory mechanism of Ca2+/calmodulin-dependent protein kinase kinase isoforms, Biochemistry 40 (2001) 13925–13932.
[9] M.F. Green, J.W. Scott, R. Steel, J.S. Oakhill, B.E. Kemp, A.R. Means, Ca2+/calmodulin-dependent protein kinase kinase beta is regulated by multisite phosphorylation, J. Biol. Chem. 286 (2011) 28066–28079.
[10] G.A. Wayman, H. Tokumitsu, T.R. Soderling, Inhibitory cross-talk by cAMP kinase on the calmodulin-dependent protein kinase cascade, J. Biol. Chem. 272 (1997) 16073–16076.
[11] M. Matsushita, A.C. Nairn, Inhibition of the Ca2+/calmodulin-dependent protein kinase I cascade by cAMP-dependent protein kinase, J. Biol. Chem. 274 (1999) 10086–10093.
[12] S. Okuno, T. Kitani, H. Fujisawa, Regulation of Ca(2+)/calmodulin-dependent protein kinase kinase alpha by cAMP-dependent protein kinase: I. Biochemical analysis, J. Biochem. 130 (2001) 503–513.
[13] T. Kitani, S. Okuno, H. Fujisawa, Regulation of ca(2+)/calmodulin-dependent protein kinase kinase alpha by cAMP-dependent protein kinase: II. Mutational analysis, J. Biochem. 130 (2001) 515–525.
[14] M.A. Davare, T. Saneyoshi, E.S. Guire, S.C. Nygaard, T.R. Soderling, Inhibition of calcium/calmodulin-dependent protein kinase kinase by protein 14-3-3, J. Biol. Chem. 279 (2004) 52191–52199.
[15] T. Ichimura, M. Taoka, Y. Hozumi, K. Goto, H. Tokumitsu, 14-3-3 proteins directly regulate Ca(2+)/calmodulin-dependent protein kinase kinase alpha through phosphorylation-dependent multisite binding, FEBS Lett. 582 (2008) 661–665.
[16] A.J. Muslin, J.W. Tanner, P.M. Allen, A.S. Shaw, Interaction of 14-3-3 with signaling proteins is mediated by the recognition of phosphoserine, Cell 84 (1996) 889–897.
[17] N.N. Sluchanko, N.B. Gusev, Moonlighting chaperone-like activity of the universal regulatory 14-3-3 proteins, FEBS J. 284 (2017) 1279–1295.
[18] T. Obsil, V. Obsilova, Structural basis of 14-3-3 protein functions, Semin. Cell Dev. Biol. 22 (2011) 663–672.
[19] F.H. Niesen, H. Berglund, M. Vedadi, The use of differential scanning fluorimetry to detect ligand interactions that promote protein stability, Nat. Protoc. 2 (2007) 2212–2221.
[20] V. Obsilova, P. Herman, J. Vecer, M. Sulc, J. Teisinger, T. Obsil, 14-3-3zeta C-terminal stretch changes its conformation upon ligand binding and phosphorylation at Thr232, J. Biol. Chem. 279 (2004) 4531–4540.
[21] B. Holakovska, L. Grycova, J. Bily, J. Teisinger, Characterization of calmodulin binding domains in TRPV2 and TRPV5 C-tails, Amino Acids 40 (2011) 741–748.
[22] O. Petrvalska, D. Kosek, Z. Kukacka, Z. Tosner, P. Man, J. Vecer, P. Herman, V. Obsilova, T. Obsil, Structural insight into the 14-3-3 protein-dependent inhibition of protein kinase ASK1 (apoptosis signal-regulating kinase 1), J. Biol. Chem. 291 (2016) 20753–20765.
[23] L. Rezabkova, P. Man, P. Novak, P. Herman, J. Vecer, V. Obsilova, T. Obsil, Structural basis for the 14-3-3 protein-dependent inhibition of the regulator of G protein signaling 3 (RGS3) function, J. Biol. Chem. 286 (2011) 43527–43536.
[24] D.I. Svergun, Determination of the regularization parameter in indirect-transform methods using perceptual criteria, J. Appl. Crystallogr. 25 (1992) 495–503.
[25] M.V. Petoukhov, D. Franke, A.V. Shkumatov, G. Tria, A.G. Kikhney, M. Gajda, C. Gorba, H.D. Mertens, P.V. Konarev, D.I. Svergun, New developments in the program package for small-angle scattering data analysis, J. Appl. Crystallogr. 45 (2012) 342–350.
[26] P.V. Konarev, V.V. Volkov, A.V. Sokolova, M.H.J. Koch, D.I. Svergun, PRIMUS: a windows PC-based system for small-angle scattering data analysis, J. Appl. Crystallogr. 36 (2003) 1277–1282.
[27] D.I. Svergun, Restoring low resolution structure of biological macromolecules from solution scattering using simulated annealing, Biophys. J. 76 (1999) 2879–2886.
[28] G. Tria, H.D. Mertens, M. Kachala, D.I. Svergun, Advanced ensemble modelling of flexible macromolecules using X-ray solution scattering, IUCrJ 2 (2015) 207–217.
[29] D. Kosek, S. Kylarova, K. Psenakova, L. Rezabkova, P. Herman, J. Vecer, V. Obsilova, T. Obsil, Biophysical and structural characterization of the thioredoxin-binding domain of protein kinase ASK1 and its interaction with reduced thioredoxin, J. Biol. Chem. 289 (2014) 24463–24474.
[30] W. Kabsch, Xds, Acta Crystallogr D Biol Crystallogr, 66 (2010), pp. 125–132.
[31] K.M. Sparta, M. Krug, U. Heinemann, U. Mueller, M.S. Weiss, Xdsapp2.0, J. Appl. Crystallogr. 49 (2016) 1085–1092.
[32] A. Vagin, A. Teplyakov, MOLREP: an automated program for molecular replacement, J. Appl. Crystallogr. 30 (1997) 1022–1025.
[33] M. Molzan, C. Ottmann, Synergistic binding of the phosphorylated S233- and S259-binding sites of C-RAF to one 14-3-3zeta dimer, J. Mol. Biol. 423 (2012) 486–495.
[34] P.D. Adams, P.V. Afonine, G. Bunkoczi, V.B. Chen, I.W. Davis, N. Echols, J.J. Headd, L.W. Hung, G.J. Kapral, R.W. Grosse-Kunstleve, A.J. McCoy, N.W. Moriarty, R. Oeffner, R.J. Read, D.C. Richardson, J.S. Richardson, T.C. Terwilliger, P.H. Zwart, PHENIX: a comprehensive python-based system for macromolecular structure solution, Acta Crystallogr. D Biol. Crystallogr. 66 (2010) 213–221.
[35] M. Kukimoto-Niino, S. Yoshikawa, T. Takagi, N. Ohsawa, Y. Tomabechi, T. Terada, M. Shirouzu, A. Suzuki, S. Lee, T. Yamauchi, M. Okada-Iwabu, M. Iwabu, T. Kadowaki, Y. Minokoshi, S. Yokoyama, Crystal structure of the ca(2)

(+)/calmodulin-dependent protein kinase kinase in complex with the inhibitor STO-609, J. Biol. Chem. 286 (2011) 22570–22579.
[36] M.B. Yaffe, K. Rittinger, S. Volinia, P.R. Caron, A. Aitken, H. Leffers, S.J. Gamblin, S.J. Smerdon, L.C. Cantley, The structural basis for 14-3-3: phosphopeptide binding specificity, Cell 91 (1997) 961–971.
[37] K. Rittinger, J. Budman, J. Xu, S. Volinia, L.C. Cantley, S.J. Smerdon, S.J. Gamblin, M.B. Yaffe, Structural analysis of 14-3-3 phosphopeptide complexes identifies a dual role for the nuclear export signal of 14-3-3 in ligand binding, Mol. Cell 4 (1999) 153–166.
[38] C. Johnson, S. Crowther, M.J. Stafford, D.G. Campbell, R. Toth, C. MacKintosh, Bioinformatic and experimental survey of 14-3-3-binding sites, Biochem. J. 427 (2010) 69–78.
[39] J. Silhan, V. Obsilova, J. Vecer, P. Herman, M. Sulc, J. Teisinger, T. Obsil, 14-3-3 protein C-terminal stretch occupies ligand binding groove and is displaced by phosphopeptide binding, J. Biol. Chem. 279 (2004) 49113–49119.
[40] R. Rose, M. Rose, C. Ottmann, Identification and structural characterization of two 14-3-3 binding sites in the human peptidylarginine deiminase type VI, J. Struct. Biol. 180 (2012) 65–72.
[41] N.N. Sluchanko, S. Beelen, A.A. Kulikova, S.D. Weeks, A.A. Antson, N.B. Gusev, S.V. Strelkov, Structural basis for the interaction of a human small heat shock protein with the 14-3-3 universal signaling regulator, Structure 25 (2017) 305–316.
[42] M. Alblova, A. Smidova, V. Docekal, J. Vesely, P. Herman, V. Obsilova, T. Obsil, Molecular basis of the 14-3-3 protein-dependent activation of yeast neutral trehalase Nth1, Proc. Natl. Acad. Sci. U. S. A. 114 (2017) E9811–E9820.
[43] T. Obsil, R. Ghirlando, D.C. Klein, S. Ganguly, F. Dyda, Crystal structure of the 14-3-3 zeta: serotonin N-acetyltransferase complex. A role for scaffolding in enzyme regulation, Cell 105 (2001) 257–267.
[44] M. Wurtele, C. Jelich-Ottmann, A. Wittinghofer, C. Oecking, Structural view of a fungal toxin acting on a 14-3-3 regulatory complex, EMBO J. 22 (2003) 987–994.
[45] M. Kacirova, J. Novacek, P. Man, V. Obsilova, T. Obsil, Structural basis for the 14-3-3 protein-dependent inhibition of Phosducin function, Biophys. J. 112 (2017) 1339–1349.
[46] D.M. Bustos, The role of protein disorder in the 14-3-3 interaction network, Mol. BioSyst. 8 (2012) 178–184.
[47] T. Ishida, K. Kinoshita, PrDOS: prediction of disordered protein regions from amino acid sequence, Nucleic Acids Res. 35 (2007) W460–464.
[48] Z. Dosztanyi, V. Csizmok, P. Tompa, I. Simon, IUPred: web server for the prediction of intrinsically unstructured regions of proteins based on estimated energy content, Bioinformatics 21 (2005) 3433–3434.
[49] V. Receveur-Brechot, D. Durand, How random are intrinsically disordered proteins? A small angle scattering perspective, Curr. Protein Pept. Sci. 13 (2012) 55–75.
[50] R.P. Rambo, Resolving individual components in protein-RNA complexes using small-angle X-ray scattering experiments, Methods Enzymol. 558 (2015) 363–390.
[51] R.L. Kincaid, M. Vaughan, J.C. Osborne Jr., V.A. Tkachuk, Ca2+ −dependent interaction of 5-dimethylaminonaphthalene-1-sulfonyl-calmodulin with cyclic nucleotide phosphodiesterase, calcineurin, and troponin I, J. Biol. Chem. 257 (1982) 10638–10643.
[52] L. Rezabkova, E. Boura, P. Herman, J. Vecer, L. Bourova, M. Sulc, P. Svoboda, V. Obsilova, T. Obsil, 14-3-3 protein interacts with and affects the structure of RGS domain of regulator of G protein signaling 3 (RGS3), J. Struct. Biol. 170 (2010) 451–461.
[53] P. Herman, J.C. Lee, The advantage of global fitting of data involving complex linked reactions, in: A.W.W. Fenton (Ed.), Allostery: Methods and Protocols, vol. 796, Humana Press Inc., New York, 2012, pp. 399–421.
[54] L. Rezabkova, M. Kacirova, M. Sulc, P. Herman, J. Vecer, M. Stepanek, V. Obsilova, T. Obsil, Structural modulation of phosducin by phosphorylation and 14-3-3 protein binding, Biophys. J. 103 (2012) 1960–1969.
[55] U. Banik, G.A. Wang, P.D. Wagner, S. Kaufman, Interaction of phosphorylated tryptophan hydroxylase with 14-3-3 proteins, J. Biol. Chem. 272 (1997) 26219–26225.
[56] A. Kumagai, W.G. Dunphy, Binding of 14-3-3 proteins and nuclear export control the intracellular localization of the mitotic inducer Cdc25, Genes Dev. 13 (1999) 1067–1072.
[57] C. Ottmann, S. Marco, N. Jaspert, C. Marcon, N. Schauer, M. Weyand, C. Vandermeeren, G. Duby, M. Boutry, A. Wittinghofer, J.L. Rigaud, C. Oecking, Structure of a 14-3-3 coordinated hexamer of the plant plasma membrane H +-ATPase by combining X-ray crystallography and electron cryomicroscopy, Mol. Cell 25 (2007) 427–440.
[58] M. Tinti, F. Madeira, G. Murugesan, G. Hoxhaj, R. Toth, C. Mackintosh, ANIA: ANnotation and integrated analysis of the 14-3-3 interactome, Database (Oxford) 2014 (2014) bat085, , http://dx.doi.org/10.1093/database/bat085.
[59] A. Nakanishi, N. Hatano, Y. Fujiwara, A. Sha'ri, S. Takabatake, H. Akano, N. Kanayama, M. Magari, N. Nozaki, H. Tokumitsu, AMP-activated protein kinase-mediated feedback phosphorylation controls the Ca(2+)/calmodulin (CaM) dependence of Ca(2+)/CaM-dependent protein kinase kinase beta, J. Biol. Chem. 292 19804–19813.
[60] L.M. Stevers, E. Sijbesma, M. Botta, C. MacKintosh, T. Obsil, I. Landrieu, Y. Cau, A.J. Wilson, A. Karawajczyk, J. Eickhoff, J. Davis, M. Hann, R.G. Mahony, L. Doveston, C. Ottmann Brunsveld, Modulators of 14-3-3 protein-protein interactions, J. Med. Chem. (2017 Oct. 19), http://dx.doi.org/10.1021/acs.jmedchem.7b00574 (Epub ahead of print).

Table S1

Dephosphorylation of CaMKK2 at pThr^{145} and pSer^{495} by PP1 in the presence and absence of 14-3-3γ.

Site	peptide form	m/z (charge)	Dephosphorylation time (min)					
			pCaMKK2			pCaMKK2 + 14-3-3γ		
			0	1.5	7	0	1.5	7
Thr145[a]	P	695,9556 (5+)	2.5E+07	2.8E+07	2.2E+07	2.0E+07	4.0E+07	1.6E+07
	not-P	679,9625 (5+)	1.3E+07	3.3E+07	3.7E+07	1.3E+07	1.3E+07	3.2E+07
	ratio non-P/P[c]		**0.52**	**1.2**	**1.7**	**0.65**	**0.33**	**2.0**
Ser495[b]	P	570,2900 (5+)	2.3E+07	2.5E+07	5.4E+06	1.8E+06	4.0E+06	4.2E+06
	not-P	554,2970 (5+)	0.0E+00	2.9E+06	6.2E+06	0.0E+00	0.0E+00	0.0E+00
	ratio non-P/P		**0**	**0.12**	**1.1**	**0**	**0**	**0**

[a]Peptide sequence PSLPYSPVSSPQSSPRLPRRPT^{145}VESHHVSIT

[b]Peptide sequence VKTMIRKRS^{495}FGNPFEGSRREERS

[c]Phosphorylated CaMKK2$_{93\text{-}517}$ D^{330}A (kinase dead mutant) in the presence and absence of 14-3-3γ was dephosphorylated by protein phosphatase 1 (PP1, catalytic subunit α-isoform from rabbit). Dephosphorylation by PP1 (Sigma-Aldrich, USA) with a specific activity 5,000 units/mg) was performed at 30 °C in buffer containing 50 mM HEPES (pH 7.5), 100 mM NaCl, 2 mM DTT, 1 mM $MnCl_2$, and 0.01% NP-40. The reaction mixture contained 11 μM CaMKK2 D^{330}A, 34 μM 14-3-3γ (where needed) and PP1 in an optimized molar ratio of 1:250 (enzyme/substrate). Reactions were stopped after 0, 1.5 and 7 min by adding 100 mM β-glycerolphosphate (Sigma-Aldroch, USA) and immediate freezing in liquid nitrogen. Analysis was started by an online digestion of sample solution containing 64 pmol of CaMKK2 on a pepsin column (66 μL bed volume, flow rate 100 μL.min^{-1}, 3 min). Generated peptides were trapped and desalted online on a Peptide microtrap column (Optimize Technologies, Oregon City, OR) and separated on a C18 reversed phase column (ZORBAX 300SB-C18 3.5 μm, 0.5 × 35 mm, Agilent, Santa Clara, CA) using a linear gradient 10–45% B in 40 min, where solvent A was 2% acetonitrile/0.4% formic acid in water, solvent B 95% acetonitrile/5% water/0.4% formic acid. The column was interfaced with the ESI source of a 15T FT-ICR mass spectrometer (SolariX XR, Bruker Daltonics, Bremen, Germany) operating in MS/MS mode. Peptides were identified by a MASCOT search against a database containing the sequence of human CaMKK2. Intensities of extracted ion chromatograms of first monoisotopes of phosphorylated (P) and non-phosphorylated (not-P) peptides were used to calculate ratios between non-phosphorylated and phosphorylated forms.

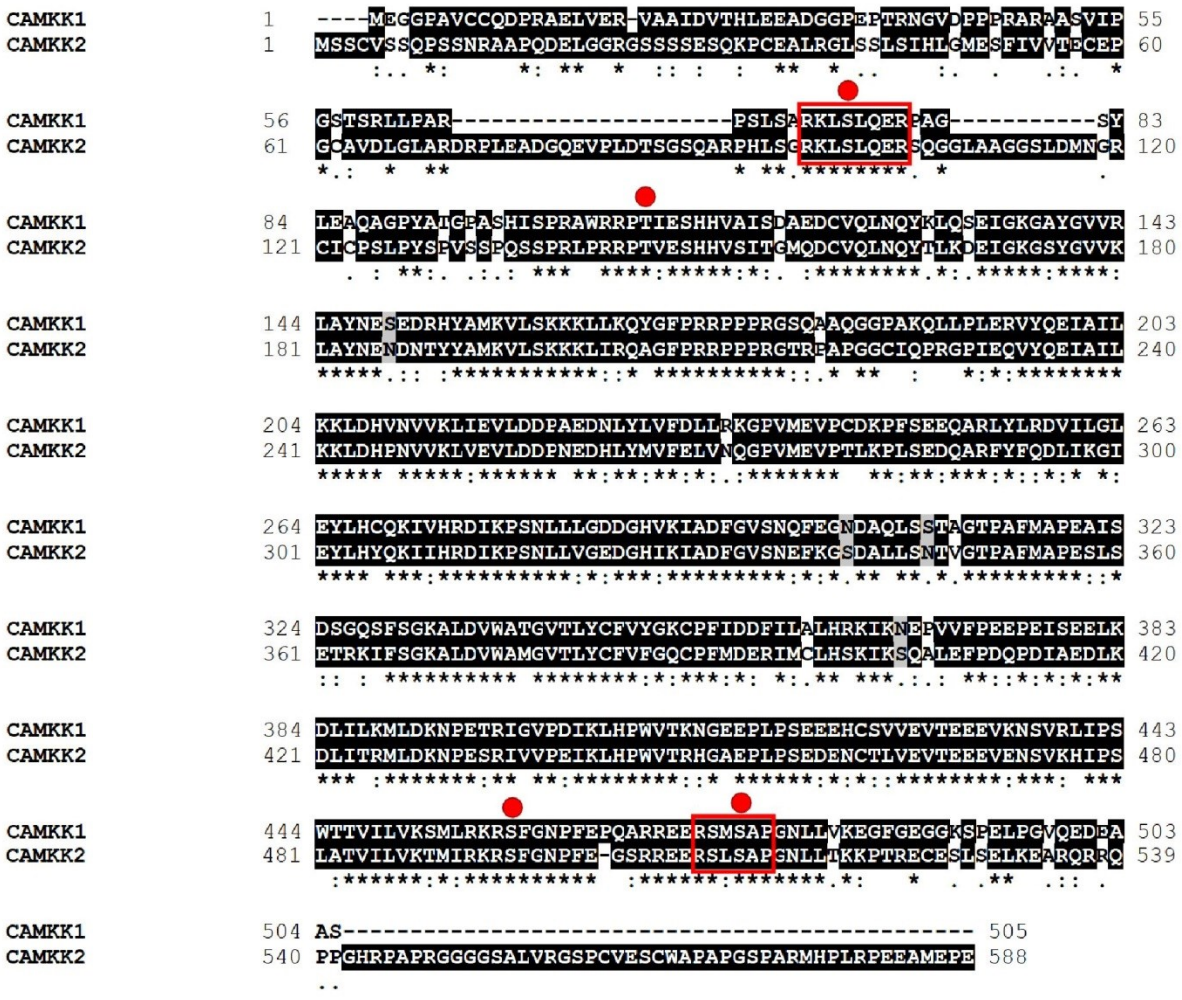

Figure S1. Related to Figure 1A.

Sequence alignment of human CaMKK1 (Q8N5S9) and CaMKK2 (Q96RR4). PKA phosphorylation sites are indicated by red circles. The 14-3-3 binding motifs are indicated by red squares. See also Figure 1A.

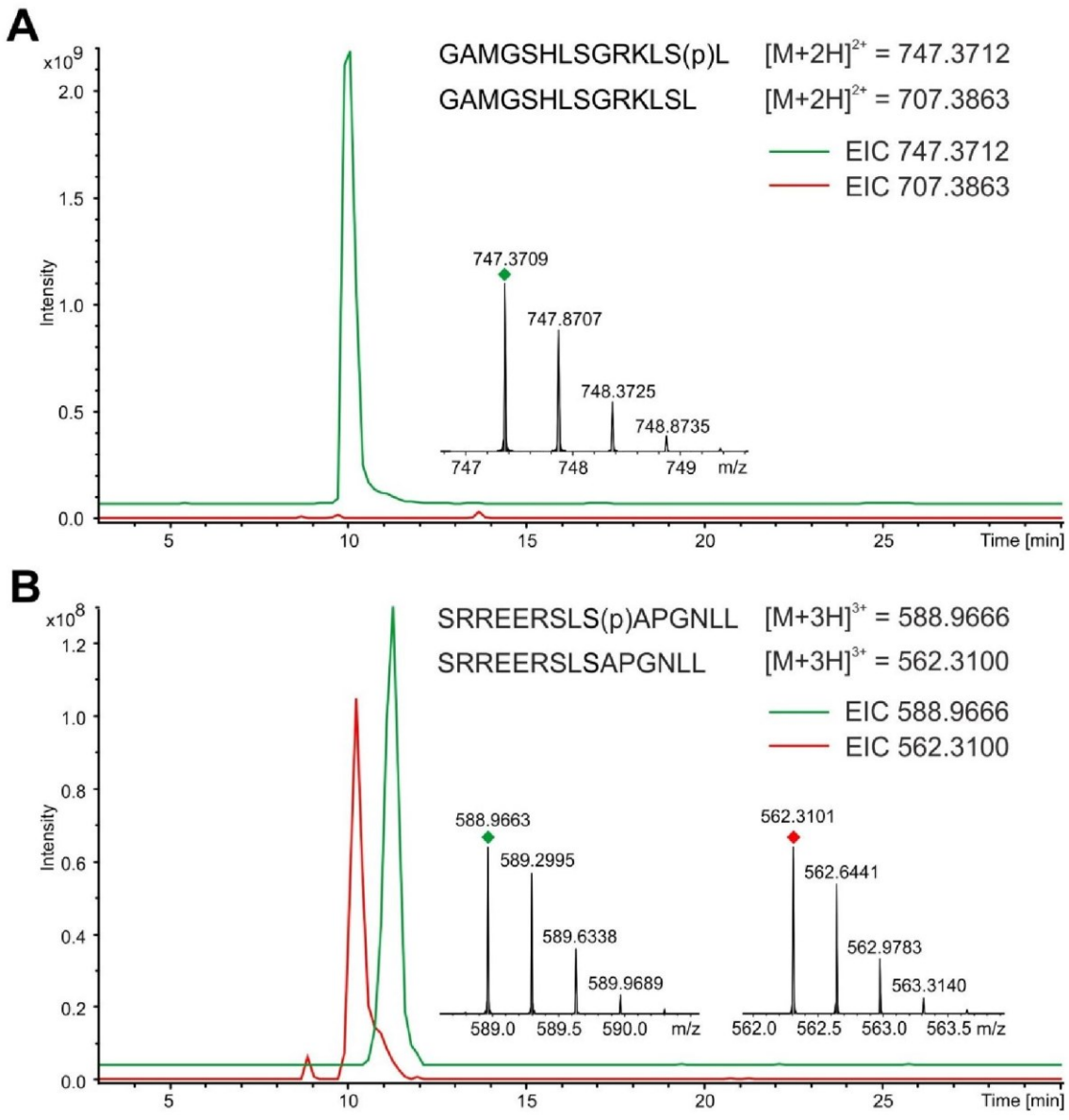

Figure S2. Related to Figure 1.

Detection of CaMKK-S^{100,511} phosphorylated peptides by FT-ICR mass spectrometry. (A) Extract ion chromatogram (EIC) of phosphorylated GAMGSHLSGRKLS^{100}L peptide shown in green, observed at m/z 747.3709 (2+). The red line represents the EIC of the non-phosphorylated form of the same peptide observed at m/z 707.3863 (2+). The inset shows the zoomed, high-resolution MS spectrum of phosphorylated GAMGSHLSGRKLS^{100}L. (B) Extract ion chromatograms of the phosphorylated SRREERSLS^{511}APGNLL peptide shown in green, observed at m/z 588.9663 (3+), and of non-phosphorylated form, observed at m/z 562.3101 (3+), which is shown in red. The inset shows the zoomed, high-resolution MS spectra of phosphorylated and non-phosphorylated SRREERSLS^{511}APGNLL peptides. The phosphorylation sites in both peptides were determined based on the collision-induced dissociation spectra. See also Figure S1A.

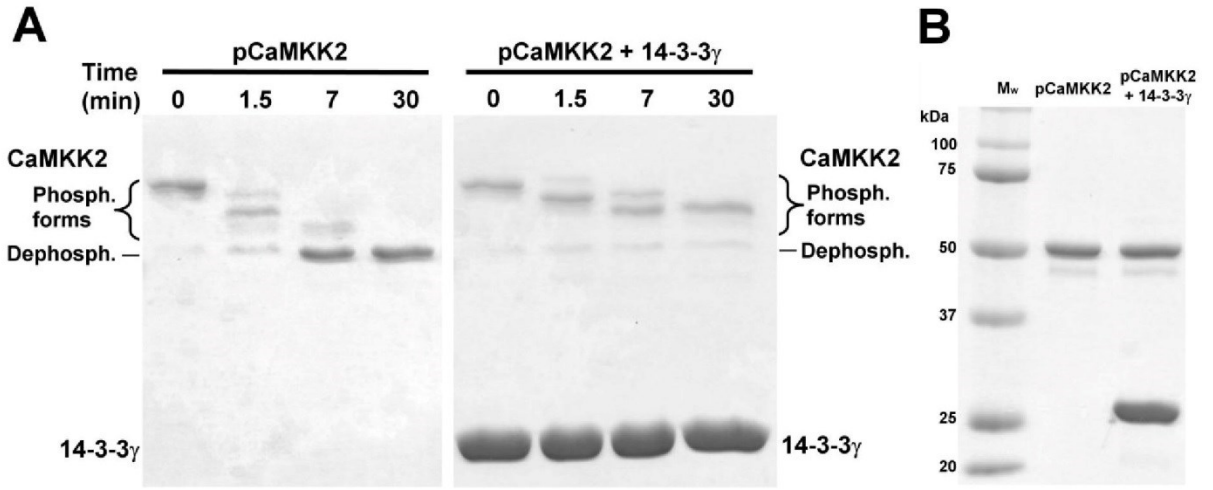

Figure S3. Related to Figure 2.

14-3-3γ Binding Slows Down Dephosphorylation of CaMKK2. (A) Phosphorylated $CaMKK2_{93\text{-}517}$ $D^{330}A$ (kinase dead mutant) in the presence and absence of 14-3-3γ was dephosphorylated by type 1 protein phosphatase (PP1, catalytic subunit α-isoform from rabbit). Dephosphorylation by PP1 (Sigma-Aldrich, USA) with a specific activity 5,000 units/mg) was performed at 30 °C in buffer containing 50 mM HEPES (pH 7.5), 100 mM NaCl, 2 mM DTT, 1 mM $MnCl_2$, and 0.01% NP-40. The reaction mixture contained 11 μM CaMKK2 $D^{330}A$, 34 μM 14-3-3γ (where needed) and PP1 in an optimized molar ratio of 1:250 (enzyme/substrate). Reactions were stopped after 0, 1.5 and 7 min by adding 100 mM β-glycerolphosphate (Sigma-Aldroch, USA), mixing with SDS reducing sample buffer and boiling for 5 min. Sample analysis was performed using 12% Phos-tag SDS-PAGE with 50 μM Phos-tag (FUJIFILM Wako Pure Chemical Corp., Japan). (B) Samples used in (A) resolved on 12% SDS-PAGE. See also Figure 2.

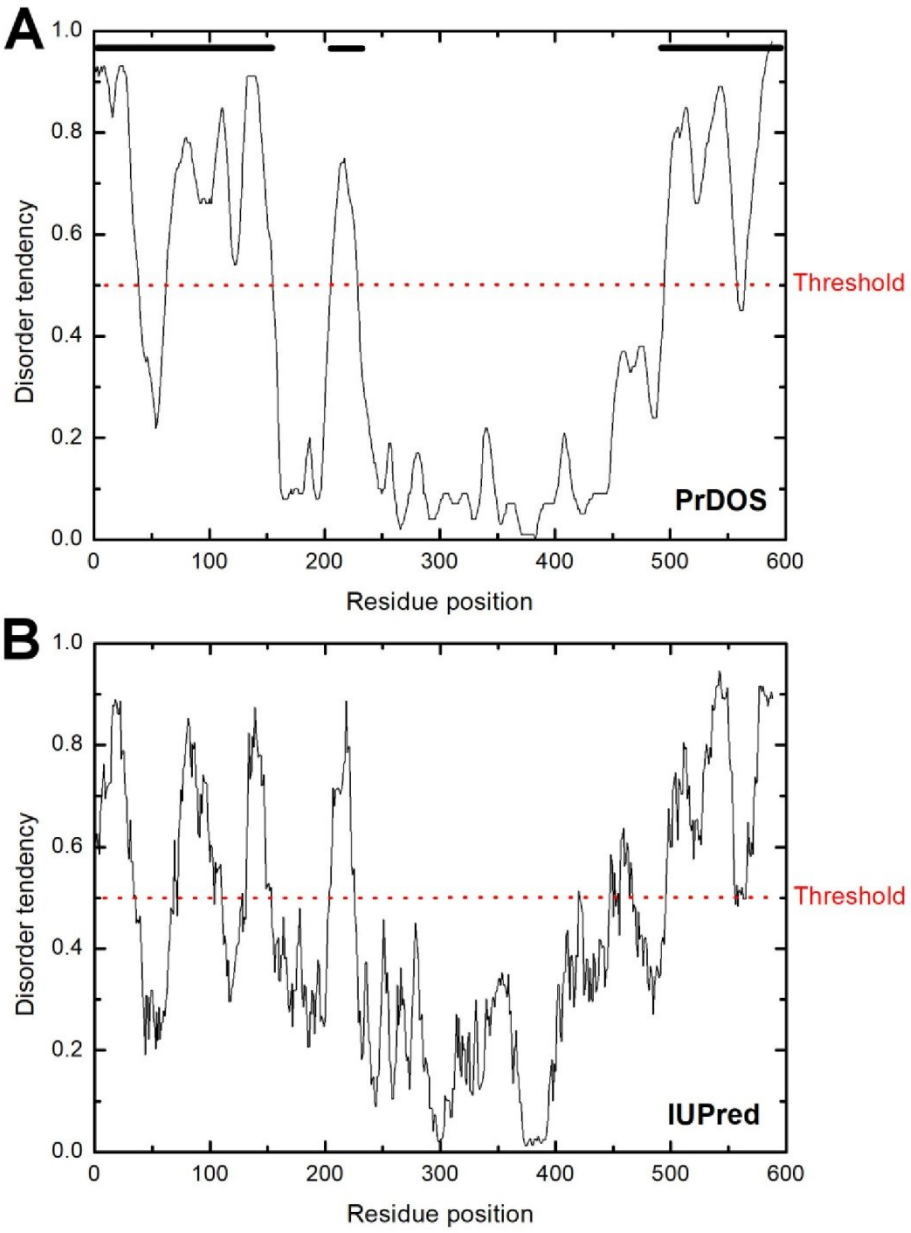

Figure S4. Related to Figure 4D.

Bioinformatics analysis of CaMKK2. Disorder prediction using PrDOS (A) (Ishida and Kinoshita, 2007) and IUPred (B) (Dosztanyi et al., 2005) predictors suggests that both the N-terminal (residues 1-125) and the C-terminal (residues 500-588) tails of CaMKK2 are unstructured. See also Figure 4D.

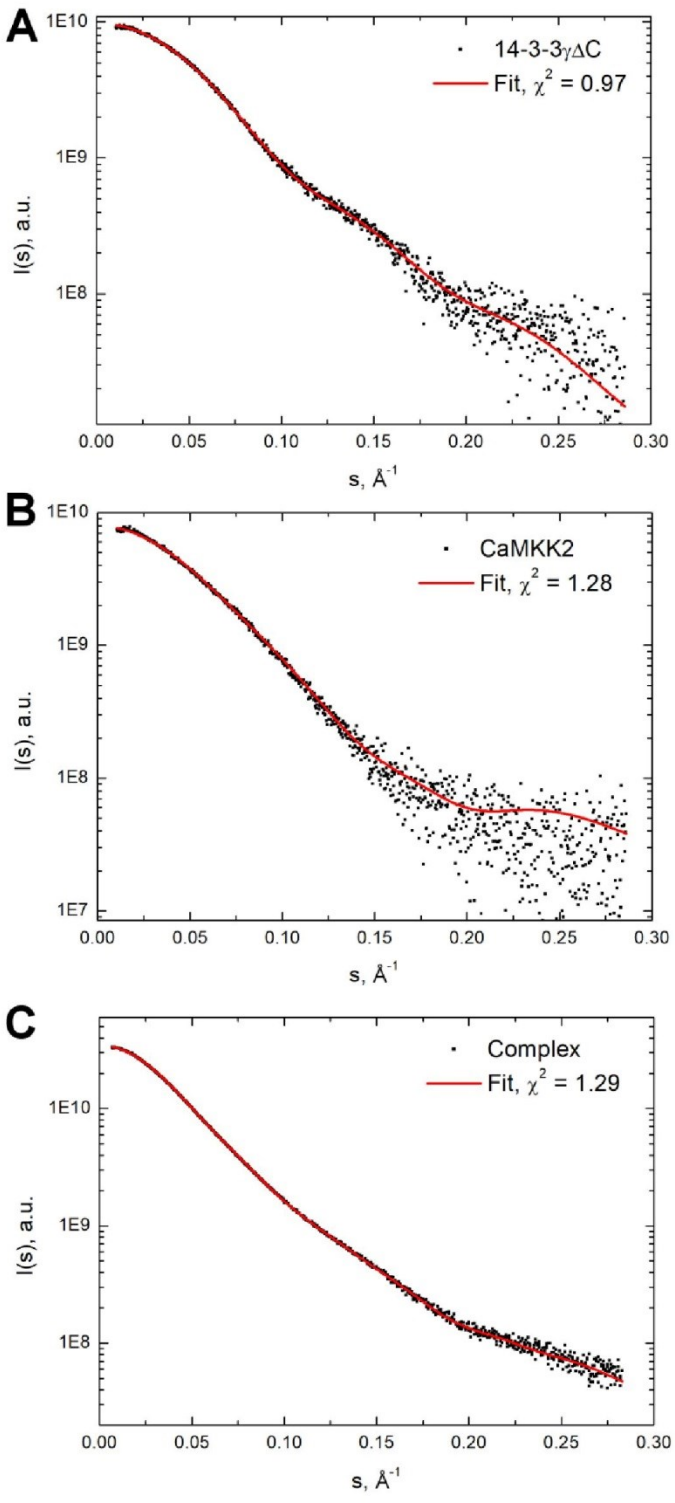

Figure S5. Related to Figure 5A.

Ab initio shape reconstruction of the pCaMKK2-S^{100}:14-3-3γ complex using MONSA. Fits of the simulated scattering curves versus the experimental SAXS data of 14-3-3γΔC (A), CaMKK2-S^{100} (B) and the 14-3-3γΔC:pCaMKK2-S^{100} (2:1) complex (C). See also Figure 5A.

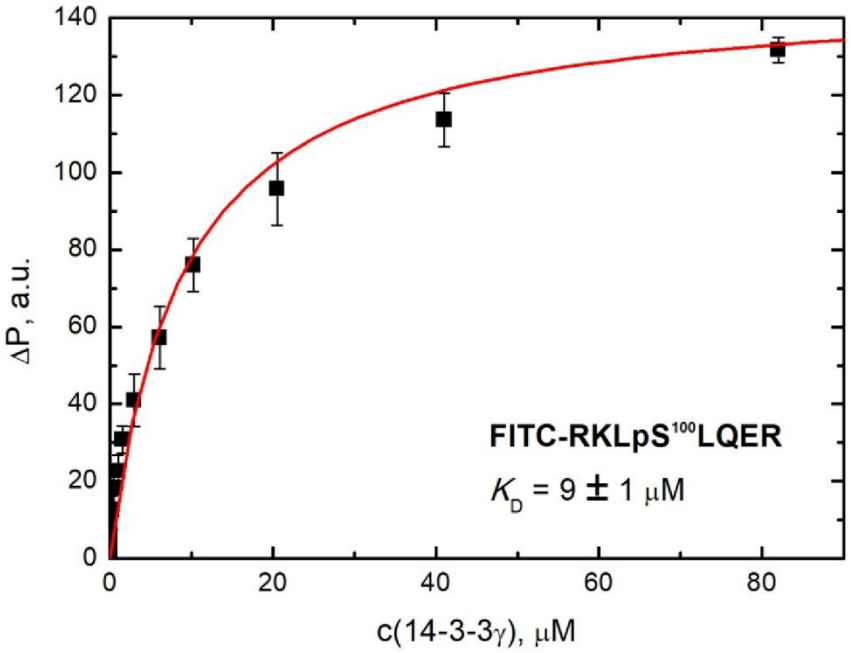

Figure S6. Related to Figures 1D and 5.

Binding isotherm of the synthetic peptide containing the N-terminal 14-3-3 binding motif of CaMKK2. Results are expressed as the mean ± SD of three experiments. See also Figures 1D and 5.

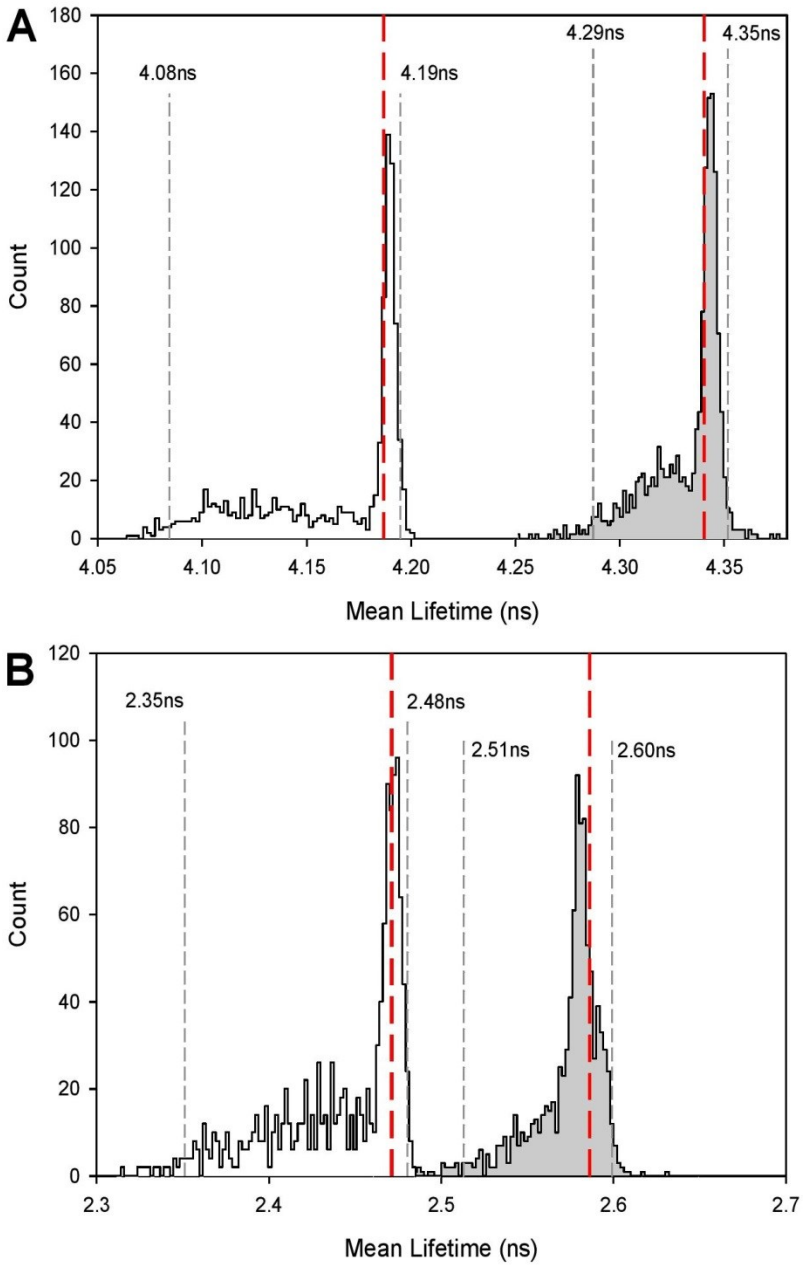

Figure S7. Related to Table 4 and Figure 7.

Statistical significance of observed differences in mean fluorescence lifetimes. Rigorous confidence-interval analysis of the mean fluorescence lifetime of the pCaMKK2-S^{100} W140 (A) and W445 (B) mutants in the absence (white-filled histogram) and presence (gray-filled histogram) of 14-3-3γ noW. Histograms constructed from 1000 Monte-Carlo MEM-fitting cycles (Herman and Lee, 2012) represent the probability of recovering a particular mean fluorescence lifetime from the data shown in Fig. 6 A,B. Dashed lines border 95% confidence intervals (2 standard deviations), the red line indicates the best-fitted value of Table 4. The histograms show that the mean fluorescence lifetime of the complex significantly increases in the presence of 14-3-3γ noW. See also Table 4 and Figure 7.

References

Dosztanyi, Z., Csizmok, V., Tompa, P., and Simon, I. (2005). IUPred: web server for the prediction of intrinsically unstructured regions of proteins based on estimated energy content. Bioinformatics *21*, 3433-3434.

Herman, P., and Lee, J.C. (2012). The advantage of global fitting of data involving complex linked reactions In Allostery: Methods and Protocols, A.W.W. Fenton, ed. (New York: Humana Press Inc.), pp. 399-421.

Ishida, T., and Kinoshita, K. (2007). PrDOS: prediction of disordered protein regions from amino acid sequence. Nucleic Acids Res *35*, W460-464.

7.2 Supplement S2

7.2.1 Publication II: The role of CaM in the regulation of Ca^{2+}/CaM – dependent protein kinase kinase 2 activity

Kylarova, S., **Psenakova, K.,** Herman, P., Obsilova, V. & Obsil, T. CaMKK2 kinase domain interacts with the autoinhibitory region through the N-terminal lobe including the RP insert. *Biochim. Biophys. Acta - Gen. Subj.* **1862**, 2304–2313 (2018).

My contribution: expression and purification of CaMKK2 and CaM; preparation of single tryptophan mutants of CaMKK2; sample preparation and further optimization for the small-angle X-ray scattering and time-resolved tryptophan fluorescence experiments; small-angle X-ray scattering data analysis; all docking calculations and refinement of the structural model based on the experimental data.

BBA - General Subjects 1862 (2018) 2304–2313

Contents lists available at ScienceDirect

BBA - General Subjects

journal homepage: www.elsevier.com/locate/bbagen

CaMKK2 kinase domain interacts with the autoinhibitory region through the N-terminal lobe including the RP insert

Salome Kylarova[a,b], Katarina Psenakova[a,b], Petr Herman[c], Veronika Obsilova[b,**], Tomas Obsil[a,b,*]

[a] Department of Physical and Macromolecular Chemistry, Faculty of Science, Charles University, Prague, Czech Republic
[b] BioCeV – Institute of Physiology, The Czech Academy of Sciences, Vestec, Czech Republic
[c] Institute of Physics, Charles University, Prague, Czech Republic

ARTICLE INFO

Keywords:
CaMKK
Calmodulin
Protein kinase
Protein-protein interaction

ABSTRACT

Background: Calcium/calmodulin-dependent protein kinase kinase 2 (CaMKK2), a member of the Ca^{2+}/calmodulin-dependent kinase (CaMK) family, functions as an upstream activator of CaMKI, CaMKIV and AMP-activated protein kinase. Thus, CaMKK2 is involved in the regulation of several key physiological and pathophysiological processes. Previous studies have suggested that Ca^{2+}/CaM binding may cause unique conformational changes in the CaMKKs compared with other CaMKs. However, the underlying mechanistic details remain unclear.

Methods: In this study, hydrogen-deuterium exchange coupled to mass spectrometry, time-resolved fluorescence spectroscopy, small-angle x-ray scattering and chemical cross-linking were used to characterize Ca^{2+}/CaM binding-induced structural changes in CaMKK2.

Results: Our data suggest that: (i) the CaMKK2 kinase domain interacts with the autoinhibitory region (AID) through the N-terminal lobe of the kinase domain including the RP insert, a segment important for targeting downstream substrate kinases; (ii) Ca^{2+}/CaM binding affects the structure of several regions surrounding the ATP-binding pocket, including the activation segment; (iii) although the CaMKK2:Ca^{2+}/CaM complex shows high conformational flexibility, most of its molecules are rather compact; and (iv) AID-bound Ca^{2+}/CaM transiently interacts with the CaMKK2 kinase domain.

Conclusions: Interactions between the CaMKK2 kinase domain and the AID differ from those of other CaMKs. In the absence of Ca^{2+}/CaM binding the autoinhibitory region inhibits CaMKK2 by both blocking access to the RP insert and by affecting the structure of the ATP-binding pocket.

General significance: Our results corroborate the hypothesis that Ca^{2+}/CaM binding causes unique conformational changes in the CaMKKs relative to other CaMKs.

1. Introduction

The calcium cation (Ca^{2+}) is a ubiquitous second messenger in cellular signaling with many effects mediated through a highly conserved, 17-kDa, Ca^{2+}-sensing protein: calmodulin (CaM). Binding of four Ca^{2+} ions to CaM induces a conformational change, which allows the protein to interact with and activate several target proteins, including a family of Ser/Thr protein kinases known as Ca^{2+}/CaM-dependent protein kinases (CaMKs) (reviewed by [1, 2]). CaMKs are responsible for regulating various cellular functions, such as gene transcription, apoptosis, cytoskeletal reorganization and learning and memory. Studies have suggested that all CaMKs share a similar domain organization with the kinase domain (KD) followed by the C-terminal autoinhibitory region (AID), which slightly overlaps with the CaM-binding domain (CBD) [3]. At low intracellular Ca^{2+} concentrations, CaMKs are inhibited through the AID, which blocks the binding of substrates to the kinase domain and/or affects the structure of the catalytic site. The increase in Ca^{2+} concentrations induces Ca^{2+}/CaM binding to the CBD of CaMKs, thus relieving autoinhibition by disrupting the interaction between the AID and the kinase domain. The CaM molecule consists of two globular N- and C-terminal domains, each containing two EF-hand type Ca^{2+}-binding sites, which are connected by a linker that allows the globular domains to wrap around the helix of CBD within the target protein, thereby affecting the interaction between the AID and the kinase domain of CaMKs (reviewed by [4]). In addition to interactions with the CBD, CaM can also simultaneously

* Correspondence to: T. Obsil, Department of Physical and Macromolecular Chemistry, Faculty of Science, Charles University, Prague, Czech Republic.
** Correspondence to: V. Obsilova, BioCeV – Institute of Physiology, The Czech Academy of Sciences, Prague, Czech Republic.
E-mail addresses: veronika.obsilova@fgu.cas.cz (V. Obsilova), obsil@natur.cuni.cz (T. Obsil).

https://doi.org/10.1016/j.bbagen.2018.07.025
Received 14 May 2018; Received in revised form 18 July 2018; Accepted 22 July 2018
Available online 24 July 2018
0304-4165/

interact with the kinase domain of CaMK, as shown by the crystal structure of the death-associated protein kinase (DAPK) bound to CaM [5]. In this structure, the CaM molecule adopted an extended conformation, which differed from that of CaM:CaMK peptide complexes, with both globular domains involved in interactions with the kinase domain of DAPK and reducing the accessibility of its active site.

Calcium/calmodulin-dependent protein kinase kinase (CaMKK), an upstream element of the CaMK signaling cascade, specifically phosphorylates Thr residues within the activation loop of two downstream kinases, CaMKI and CaMKIV, considerably increasing their catalytic efficiency and phosphorylation of multiple downstream targets [6]. Two CaMKK isoforms (CaMKK1 and CaMKK2) have been identified in mammals in which CaMKK2 also participates in the regulation of energy balance through AMP-activated protein kinase (AMPK) activation [7, 8]. In fact, CaMKK2 is one of the most versatile CaMKs involved in adiposity regulation, glucose homeostasis, hematopoiesis, inflammation, and cancer, and is considered a potential target for therapeutic intervention (reviewed in [9]). Although both CaMKK isoforms share high similarity and identity in their amino acid sequences, they differ in their regulation. CaMKK1 is strictly activated by Ca^{2+}/CaM binding, whereas CaMKK2 is significantly active in the absence of Ca^{2+}/CaM [10, 11]. This autonomous activity is regulated by a stretch of 23 amino acid residues located N-terminally to the catalytic domain (residues 124–142), which may participate in the release of AID from the catalytic domain (Fig. 1) [12, 13]. Several point mutations in this region, which were identified in human genetic studies and in cancer tissues, have been shown to significantly affect both Ca^{2+}/CaM-autonomous and -stimulated CaMKK2 activity [14]. Ca^{2+}/CaM-autonomous CaMKK2 activity is inhibited by phosphorylation of three serine residues, Ser129, Ser133 and Ser137, located within the Ca^{2+}/CaM-autonomous regulatory region, where Ser137 phosphorylation by proline-directed kinases (Pro−K) triggers the phosphorylation of two other serines by glycogen synthase kinase-3 (GSK3) (Fig. 1) [12, 13]. Conversely, Ca^{2+}/CaM-autonomous CaMKK2 activity is increased by autophosphorylation at Thr85 and Thr482, most likely resulting from the disruption of the autoinhibitory mechanism [15, 16].

Furthermore, both CaMKKs are inhibited by cAMP-dependent protein kinase (PKA), which phosphorylates CaMKK2 at Ser100, Thr145, Ser495 and Ser511 [12, 17, 18]. Although Thr145 phosphorylation may play a role in regulating CaMKK2 activity toward its kinase substrates (similarly to homologous Thr108 phosphorylation in CaMKK1), Ser495 phosphorylation likely blocks Ca^{2+}/CaM binding, thereby explaining its inhibitory effect [17, 19]. Phosphorylation of two other serine residues, Ser100 and Ser511, induces binding to the scaffolding 14-3-3 protein [18].

The kinase domain of CaMKK shows distinct differences from catalytic domains of other CaMKs. Sequence comparison showed the presence of a unique Arg-Pro-rich insert (RP insert) within the N-terminal lobe, which enables an efficient targeting and subsequent activation of CaMKI and CaMKIV [20]. In addition, the crystal structure of the CaMKK2 kinase domain revealed that its C-lobe lacks the αD helix involved in hydrophobic interactions with the AID in CaMKI and CaMKII [21, 22]. Furthermore, the solution structure of the complex between Ca^{2+}/CaM and a peptide derived from the CaMKK1 CBD [23] revealed that the binding orientation of this peptide in relation to the CaM globular domains is opposite to that observed in CBD peptides derived from myosin light chain kinase and CaMKII [24–27]. In addition to these structural differences, the sequence and length of the CaMKK AID differ from those of CaMKI and CaMKII, thus suggesting that interactions between the CaMKK kinase domain and the AID substantially differ from those of other CaMKs. However, the underlying mechanistic details remain unclear.

Thus, in this study, we used hydrogen-deuterium exchange coupled to mass spectrometry (HDX-MS), time-resolved fluorescence spectroscopy, small-angle x-ray scattering (SAXS) and chemical cross-linking to characterize structural changes in CaMKK2 induced by Ca^{2+}/CaM binding.

2. Results

2.1. Ca^{2+}/CaM binding affects the ATP-binding pocket of CaMKK2

To assess Ca^{2+}/CaM-induced conformational changes in CaMKK2, HDX-MS was used to compare structural differences and changes in solvent accessibility in the absence and presence of Ca^{2+}/CaM. To this end, a CaMKK2 construct encompassing residues 93−517 (hereafter referred to as CaMKK2) containing the catalytic domain (residues 160–450), the N-terminal region responsible for the Ca^{2+}/CaM-autonomous activity and the C-terminal AID, which partly overlaps with the CBD (Fig. 1), was prepared. In addition, the catalytic aspartate residue of the kinase domain was mutated ($D^{330}A$) to obtain homogeneous protein for structural analysis by avoiding autophosphorylation of the recombinant protein during expression. Therefore, autophosphorylation was prevented throughout this study.

In HDX, destabilization of the secondary structure, greater dynamics and higher solvent exposure increase the exchange rates. Conversely, stabilization of secondary structure elements and decreased access to the solvent manifest as decreased exchange rates. Ca^{2+}/CaM binding-induced changes in the exchange rate of CaMKK2 were followed on 198 peptides from pepsin digest, together covering 100% of the sequence (supplemental Fig. S1). Twenty-two selected peptides covering the entire CaMKK2 93–517 sequence were then used to construct the deuterium uptake profiles after 60 s and 5 h of deuteration (these two deuteration times were selected to examine changes on both short and long timescales). The comparison of the deuteration levels of CaMKK2 in the absence and in the presence of Ca^{2+}/CaM revealed that several regions of the kinase domain and the C-terminal AID showed significant differences in exchange rate upon Ca^{2+}/CaM binding (Figs. 2 and S2).

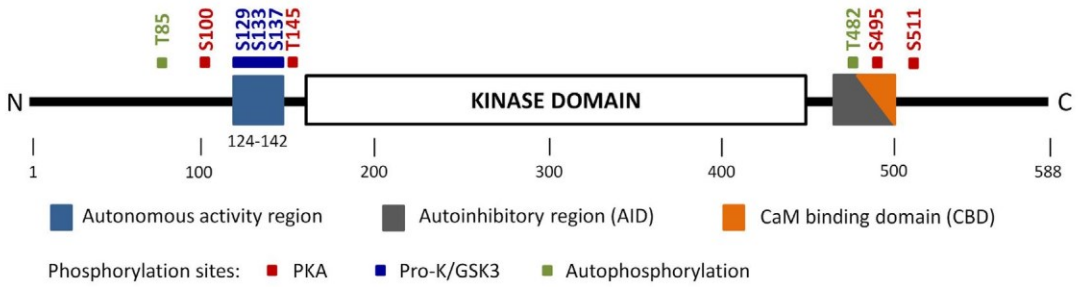

Fig. 1. Domain organization of CaMKK2. The N-terminal Ca^{2+}/CaM-autonomous activity region (residues 124–142) regulates CaMKK2 activity in the absence of Ca^{2+}/CaM. The AID, which overlaps with the CBD, blocks substrate binding to the kinase domain and/or affects the structure of the catalytic site at low intracellular Ca^{2+} concentrations. Ca^{2+}/CaM binding disrupts the interaction between the AID and the kinase domain and relieves the autoinhibition. The positions of regulatory phosphorylation and autophosphorylation sites are marked by colored squares. PKA, cAMP-dependent protein kinase; GSK3, glycogen synthase kinase-3; pro-K, proline-directed kinases.

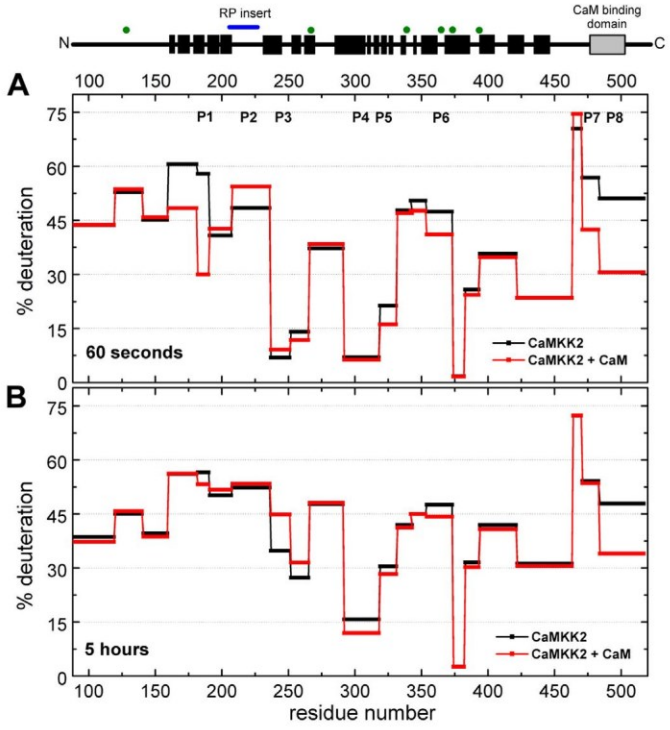

Fig. 2. Ca^{2+}/CaM-binding induced changes in the deuteration levels of CaMKK2. Plots showing the deuteration levels of CaMKK2 (kinase-dead mutant) in the absence (black traces) and presence of Ca^{2+}/CaM (red traces) after 60 s (A) and 5 h (B) of deuteration. The positions of secondary structure elements of the CaMKK2 KD are indicated at the top by black rectangles. The positions of tryptophan residues used in the time-resolved fluorescence experiments are indicated by green dots. P1-P8 indicate peptides whose deuteration kinetics is shown in detail in Fig. S2. See also Figs. S1 and S2.

A significant increase in exchange rate (deprotection) was observed in the strands β4 and β5, in the helix αC and in the RP insert within the N-lobe of the CaMKK2 KD, close to the ATP-binding pocket (Fig. 3A). Because faster deuterium incorporation can be interpreted as increased access to the solvent and/or as structural destabilization, the regions with faster deuteration upon Ca^{2+}/CaM binding are likely involved in interactions with the AID in the absence of CaM.

Conversely, a significant decrease in exchange rate (protection) was observed in the CBD (residues 470–517, peptides P7 and P8 in Fig. S2) and in several regions of the catalytic domain, including the β1 and β2 strands and the loop between the β2 and β3 strands within the N-lobe, as well as two regions within the C-lobe (Figs. 3 and S2). One of these regions within the C-lobe contains the helix αE and the strands β6-β8 that form one side of the ATP binding pocket, whereas the other region is formed by the helix αEF, the β11 strand and the N-terminal part of helix αF. The slower exchange rates observed in these regions likely reflect either structural stabilization and/or decreased access to the solvent caused by the release of the AID from the kinase domain and/or by the interaction with the AID-Ca^{2+}/CaM module. The profound decrease in exchange rate in the CBD region likely reflects its burial within the Ca^{2+}/CaM structure as previously shown by solution structure of the complex between Ca^{2+}/CaM and the CBD peptide derived from CaMKK1 [23]. Accordingly, most of the CaMKK2 KD regions, which were affected by the Ca^{2+}/CaM binding, surround the ATP binding pocket and likely represent conformational changes that participate in the activation of CaMKK2 kinase activity.

2.2. CaMKK2 kinase domain conformational behavior and its changes upon Ca^{2+}/CaM binding

Time-resolved tryptophan fluorescence intensity and anisotropy decay measurements of CaMKK2 were used to investigate the conformational behavior of CaMKK2 and its changes upon Ca^{2+}/CaM binding. Based on the results from the HDX-MS measurements, six CaMKK2 mutants containing a single tryptophan residue in different regions (Trp128, Trp267, Trp337, Trp366, Trp374 and Trp390) were prepared in the background of a kinase-dead CAMKK2 (Fig. 4A). The sequence of CaMKK2 contains two tryptophan residues, Trp374 and Trp445, both located within the C-lobe of the kinase domain. Therefore, the mutant containing single Trp374 was created by mutating Trp445 to Phe. Mutants containing other tryptophans were generated by mutating both Trp374 and Trp445 to Phe and by introducing a single Trp residue at the desired position. The CaM is fluorescently silent because no tryptophan residue is present in its sequence.

Fluorescence intensity decay measurements showed that all tryptophan mutants of CaMKK2 exhibited complex emission decays with multimodal lifetime distributions. Ca^{2+}/CaM binding significantly affected the microenvironment around the indole moiety of Trp267, Trp337 and Trp366, whereas nonsignificant effects were assessed on mutants containing Trp128, Trp374, and Trp390 (Table 1). The Trp267 residue is located within the strand β5 of the N-lobe facing the ATP-binding pocket, the Trp337 is located within the activation segment, between strands β9 and β10, and the Trp366 is part of the strand β11 within the loop connecting helices αEF and αF. Although the mean excited-state lifetime (τ_{mean}) of mutants containing Trp267 and Trp337 decreased upon Ca^{2+}/CaM binding, the mutant containing Trp366 showed an increase in τ_{mean}. The τ_{mean} change of all three mutants is clearly visible in the raw data shown in Fig. S3, wherein the difference between fluorescence decays in the presence and absence of Ca^{2+}/CaM is higher than the data noise level. The analysis of the lifetime distribution, shown in Fig. 4B, indicates that the decrease in the τ_{mean} of Trp267 in the presence of Ca^{2+}/CaM is mainly caused by the decrease in the intensity fraction associated with the dominant lifetime component centered around 5.6 ns and by the corresponding increase in fractions of the shorter components. Conversely, the decrease in the τ_{mean} of Trp337 is mainly caused by the shortening of the four lifetime components present in the distribution without dramatic changes in their individual contributions to the decay (Fig. 4C). In the case of Trp366, the increase in its τ_{mean} value results from the increase in the intensity fraction associated with the dominant lifetime component centered around 4.3 ns and from the shift of the shorter components to larger values (Fig. 4D).

Subsequently, the segmental motions of inserted tryptophans were studied using polarized time-resolved emission measurements. The fluorescence anisotropy decays revealed two classes of correlation times (Table 1). Short correlation times, with values up to few nanoseconds (ϕ_2 and ϕ_3 and a very fast unresolved component with $\phi_1 < 100$ ps), likely reflect the fast segmental motion of the protein near the tryptophan residue and Trp wobbling, whereas significantly longer correlation times ($\phi_4 > 40$ ns) likely reflect the overall rotational motion of CaMKK2. In several cases, an additional, very long correlation time, unresolvable with a Trp lifetime of few ns, was also detected ($\phi_{agg} > 200$ ns), likely reflecting minor protein aggregation. In this case, ϕ_3 shifted somewhat to lower values, which is consistent with the change in shape factors of possible aggregates [30]. Changes in the extent of segmental motion were assessed based on the change in the sum of amplitudes of fast anisotropy decay components ($\beta_{fast}=\beta_1+\beta_2+\beta_3$) [31]. Overall, lower values of β_{fast} indicate a more rigid environment. With some simplification, values of β_{fast} close to zero indicate a stiff protein that behaves like a rigid rotor, whereas β_{fast} values close to the initial anisotropy r_0 ($r_0 = 0.22$ in our case) indicate a loose structure, wherein fluorescence is rapidly depolarized by fast movements. Hence, all tryptophans, except Trp128 and Trp366, are located in rather rigid regions of the kinase domain, and Ca^{2+}/CaM binding caused no significant changes in the flexibility of the study regions. The only exception is the most mobile CaMKK2 Trp366 mutant, which showed a significant decrease in β_{fast} and a decrease in

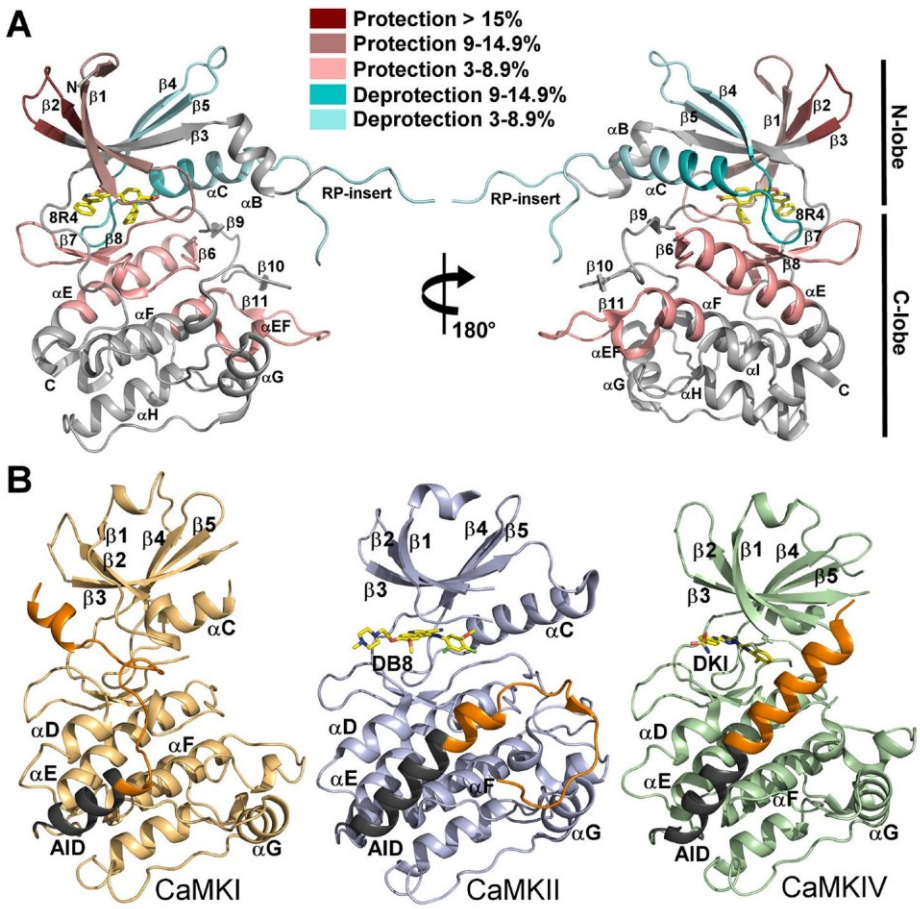

Fig. 3. Ca^{2+}/CaM binding-induced changes within the kinase domain of CaMKK2. (A) Color-coded HDX-MS results of Ca^{2+}/CaM binding-induced changes in CaMKK2 (kinase-dead mutant) mapped to the crystal structure of the CaMKK2 KD (PDB ID: 5UY6). The ATP-binding pocket is occupied by the small molecule 8R4. (B) Comparison with other CaMKs. Structures of the CaMKI KD-AID (PDB ID: 1A06) [28], the CaMKII KD-AID (PDB ID: 3SOA) [29], and the CaMKIV KD-AID (PDB ID: 2W4O) are shown in the same orientation as that of CaMKK2 KD in the left panel of (A). The C-terminal hub domain of CaMKII is not shown for better clarity. The AID regions of CaMKI and CaMKII are shown in dark gray with the CBD in orange.

correlation times ϕ_1 and ϕ_2. This suggested reduced amplitudes and different character of the internal motion in the region surrounding this tryptophan residue upon Ca^{2+}/CaM binding. Signs of microenvironment rigidization were also detected in the Trp128 mutant.

Therefore, fluorescence lifetime and anisotropy results indicate that Ca^{2+}/CaM binding affects the CaMKK2 KD conformation in several regions, such as the β5 strand close to the ATP-binding pocket and two regions within the C-lobe, including the activation segment.

2.3. Molecules of the CaMKK2:Ca^{2+}/CaM complex are compact

The recently reported crystal structure of the DAPK-CaM complex suggested that, in addition to the AID, the Ca^{2+}/CaM can also directly interact with the kinase domain of some CaMKs [5]. To assess whether this direct interaction would also occur in CaMKK2, small angle x-ray scattering, chemical cross-linking and molecular docking were used to study the architecture of the CaMKK2:Ca^{2+}/CaM complex. X-ray scattering data were collected for the CaMKK2, Ca^{2+}/CaM and the CaMKK2:Ca^{2+}/CaM complex prepared at 1:1 M stoichiometry (Table 2 and Fig. 5). The complex samples were prepared at protein concentrations ranging from 2.4 to 10.7 mg.mL^{-1}. However, only samples with low protein concentration (2.4 and 5.8 mg.mL^{-1}) were monodisperse, as indicated by the linearity of Guinier plots at s values lower than $1.3/R_g$ (inset in Fig. 5A). Due to the presence of attractive interparticle interactions, as indicated by the concentration dependence on the radius of gyration (R_g) and by the forward scattering intensity $I(0)$, the scattering curve of the complex at the lowest protein concentration 2.4 mg.mL^{-1} was selected for further analysis. The apparent M_w values of ~46, ~20 and ~64 kDa estimated for CaMKK2, for Ca^{2+}/CaM and for the complex, respectively, based on the forward scattering intensity $I(0)$, match their expected M_w values of 48, 17 and 65 kDa, respectively. The pair-distance distribution function $P(r)$ of CaMKK2 alone and of its complex with Ca^{2+}/CaM showed similar maximum particle distance (D_{max}); however, the $P(r)$-distribution function of the complex showed a higher proportion of inter-atomic distances between 6 and 10 nm (Fig. 5B).

The dimensionless Kratky plot ((sR_g)$2I(s)/I(0)$ versus sR_g) was used to characterize the protein flexibility of the CaMKK2:Ca^{2+}/CaM complex (Fig. 5C). The scattering data of compact globular proteins in this plot show a maximum value of 1.104 at sR_g ~1.73 (marked by red lines in Fig. 5C) [33]. As shown, both CaMKK2 and the CaMKK2:Ca^{2+}/CaM complex had higher maxima, indicating that both molecules show substantial conformational flexibility. Therefore, an ensemble optimization method (EOM) [34] was then used to model the CaMKK2:Ca^{2+}/CaM complex structure as an ensemble of conformers. The CaMKK2 KD and the Ca^{2+}/CaM bound to the CBD were treated as rigid bodies and the flexible N- and C-terminal segments of CaMKK2 as chains of dummy residues. An initial pool of 10,000 conformers was initially generated, and a genetic algorithm was then used to select an ensemble of conformers that collectively fitted the experimental SAXS data with a χ^2 value of 1.12 (Fig. 5D). In addition, its R_g and D_{max} distributions are clearly biased toward more compact structures with lower R_g and D_{max} values than those of the pool (Fig. 5E and F). The average R_g and D_{max} values of the ensemble (36.6 and 121 Å, respectively) are consistent with values calculated using scattering data (Table 2). Moreover, the R_g and D_{max} distributions of the CaMKK2:Ca^{2+}/CaM complex have smaller extents than those of the pools, indicating that its accessible conformations are not fully randomly distributed and that the complex is unable to be fully extended in solution, thereby suggesting that a substantial portion of molecules is rather compact, with a R_g of < 35 Å and a D_{max} of < 120 Å. Furthermore, the presence of compact complexes also suggests that the kinase domain and Ca^{2+}/CaM may directly, but transiently, interact with each other.

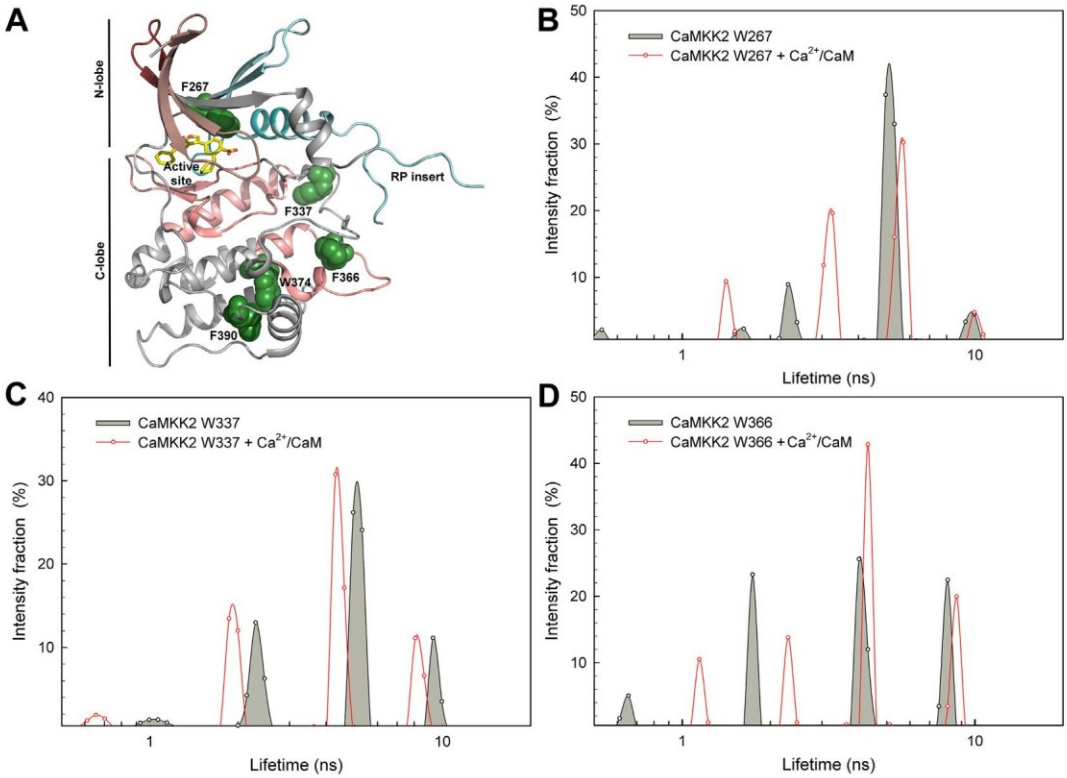

Fig. 4. Time-resolved tryptophan fluorescence measurements of CaMKK2. (A) The crystal structure of the CaMKK2 KD (PDB ID: 5UY6) was colored as in Fig. 3A, according to HDX-MS results. Residues Trp374 and phenylalanines F267, F337, F366 and F390, which were replaced by Trp, are shown as green spheres. (B-D) Excited state lifetime distribution of $CaMKK2_{93–517}$ W267 (panel B), W337 (panel C) and W366 (panel D) in the absence (gray-filled distributions) and presence of Ca^{2+}/CaM (red distributions). All tryptophan mutants were prepared using a kinase-dead CAMKK2. See also Fig. S3.

Table 1
Summary of time-resolved fluorescence measurements.

	τ_{mean}[a,b]	β_1[c,d]	ϕ_2	β_2	ϕ_3	β_3	ϕ_4[f]	β_4	ϕ_{agg}[e]	β_{agg}	β_{fast} =
	(ns)		(ns)		(ns)		(ns)		(ns)		$\beta_1+\beta_2+\beta_3$
W128	4.0	0.03	0.9	0.04	3.3	0.02	61	0.13			0.09
W128 + CaM	4.0	0.02	1.0	0.03	3.2	0.02	70	0.15			0.07
W267	4.8	0.01	1.2	0.01			43	0.20			0.02
W267 + CaM	4.4	0.01	1.6	0.02			67	0.19			0.03
W337	4.6	0.01	1.7	0.03			44	0.18			0.04
W337 + CaM	4.1	0.02	1.3	0.03			23	0.08	> 200	0.09	0.05
W366	4.2	0.05	2.3	0.03	9.2	0.02	40	0.12			0.10
W366 + CaM	4.4	0.04	0.6	0.01	2.9	0.02	22	0.10	> 200	0.05	0.07
W374	4.3	0.03					32	0.15	> 200	0.04	0.03
W374 + CaM	4.3	0.04					42	0.18			0.04
W390	3.8	0.01	1.9	0.03			45	0.18			0.04
W390 + CaM	3.9	0.00	2.0	0.03			25	0.11	> 200	0.08	0.03

[a] Mean lifetimes were calculated as $\tau_{mean} = \Sigma_i f_i \tau_i$, where f_i is an intensity fraction of the i-th lifetime component τ_i.
[b] S.D. value is ± 0.05 ns.
[c] The anisotropies $r(t)$ were analyzed for a series of exponentials by a model-independent maximum entropy method.
[d] Fast unresolved component with $\phi_1 < 100$ ps, amplitude β_1 was calculated to satisfy the requirement of $r_0 = \Sigma_i \beta_i = 0.22$.
[e] Long correlation time resulting from minor protein aggregation; the exact value is inaccessible with ~4 ns Trp lifetime.
[f] S.D. value is ± 10 ns.

2.4. CaMKK2 KD directly interacts with the AID-Ca^{2+}/CaM module

Chemical cross-linking combined with mass spectrometry was used to further investigate the direct contacts between the CaMKK2 KD and Ca^{2+}/CaM and to collect structural data on their relative positions. Two amine-reactive cross-linking agents, disuccinimidyl glutarate (DSG) and disuccinimidyl suberate (DSS), which differ in spacer arm length (~7.7 and ~11.4 Å, respectively), were used. The identified intermolecular cross-links connecting three different regions of CaMKK2 KD to three different regions of CaM are listed in Table 3. In two cases, we were unable to identify the exact cross-linked residue because the corresponding peptide contained two closely located lysine residues. Cross-links #1 and #3 connect CaMKK2 AID-CBD Lys493 to the C-terminus of CaM containing Lys149. Cross-links #2 and #5 were identified between the helix αI at the C-terminus of CaMKK2 KD containing Lys441 and the linker that connects the N- and C-terminal domains of CaM containing Lys76 and Lys78. The cross-link #4 connects CaMKK2 AID-CBD Lys493 to CaM Lys78. Finally, the cross-link #6 connects the strand β4 in the

Table 2
Structural parameters determined from SAXS data.

	c (mg.mL^{-1})	R_g[a] (Å)	R_g[b] (Å)	D_{max} (Å)	V_p[c] (nm^3)	M_w[d,f] (kDa)	M_w[e,f] (kDa)
CaMKK2	3.0	32.3 ± 0.3	32.4 ± 0.3	125	93.7	47 ± 1	59
	2.3	32.3 ± 0.3	32.5 ± 0.3	126	98.4	46 ± 1	62
Ca^{2+}/CaM	3.9	22.2 ± 0.1	22.2 ± 0.1	71	27.6	20 ± 1	17
	1.9	22.2 ± 0.3	22.3 ± 0.1	67	28.1	21 ± 1	18
Complex	5.8	38.4 ± 0.5	38.6 ± 0.5	124	112.1	66 ± 1	70
(1:1)	2.4	37.1 ± 0.4	37.3 ± 0.4	120	110.0	64 ± 1	69

[a] Reciprocal space radius of gyration (R_g).
[b] Real space R_g.
[c] The excluded volume of the hydrated particle (the Porod volume).
[d] Molecular weight estimated by comparing the forward scattering intensity $I(0)$ with that of the reference solution of bovine serum albumin.
[e] Molecular weight estimated from the Porod volume ($M_w \approx V_p \times 0.625$) [32].
[f] Theoretical molecular weights of CaMKK2, Ca^{2+}/CaM and the CaMKK2:Ca^{2+}/CaM complex (with 1:1 stoichiometry) are 48, 17 and 65 kDa, respectively.

N-lobe of CaMKK2 KD containing Lys250 to the first N-terminal helix of CaM containing Lys14. Because the $C_\alpha - C_\alpha$ distances of lysine residues cross-linked by DSG and DSS are ~20 and ~24 Å, respectively, the presence of several cross-links between the CaMKK2-KD and CaM (cross-links #2, 5, and 6) indicates that Ca^{2+}/CaM, when bound to the CBD, directly interacts with the kinase domain of CaMKK2.

To visualize the transient interaction between the CaMKK2 KD and Ca^{2+}/CaM, docking simulation was performed using the program HADDOCK [36] with the crystal structure of the CaMKK2 KD (PDB ID: 5UY6), the solution structure of Ca^{2+}/CaM bound to the CBD of CaMKK1 (PDB ID: 1CKK) [23] and intermolecular distance constraints assessed in chemical cross-linking experiments. The final model, the structure with the lowest intermolecular energy, is consistent with most distance constraints assessed in chemical cross-linking experiments (Fig. 6) and suggests that the CaMKK2 KD interacts with Ca^{2+}/CaM preferentially through surfaces surrounding the C-terminal part of the helix αE. However, because substantial protection after 5 h of deuteration in the presence of Ca^{2+}/CaM was also observed in the $\beta2-\beta3$ and $\alpha EF-\beta11$ loops, Ca^{2+}/CaM may also interact with these regions.

3. Discussion

Previous structural studies on several CaMKs, including CaMKI, CaMKII and CaMKIV, have shown that the AID emerges from the base of

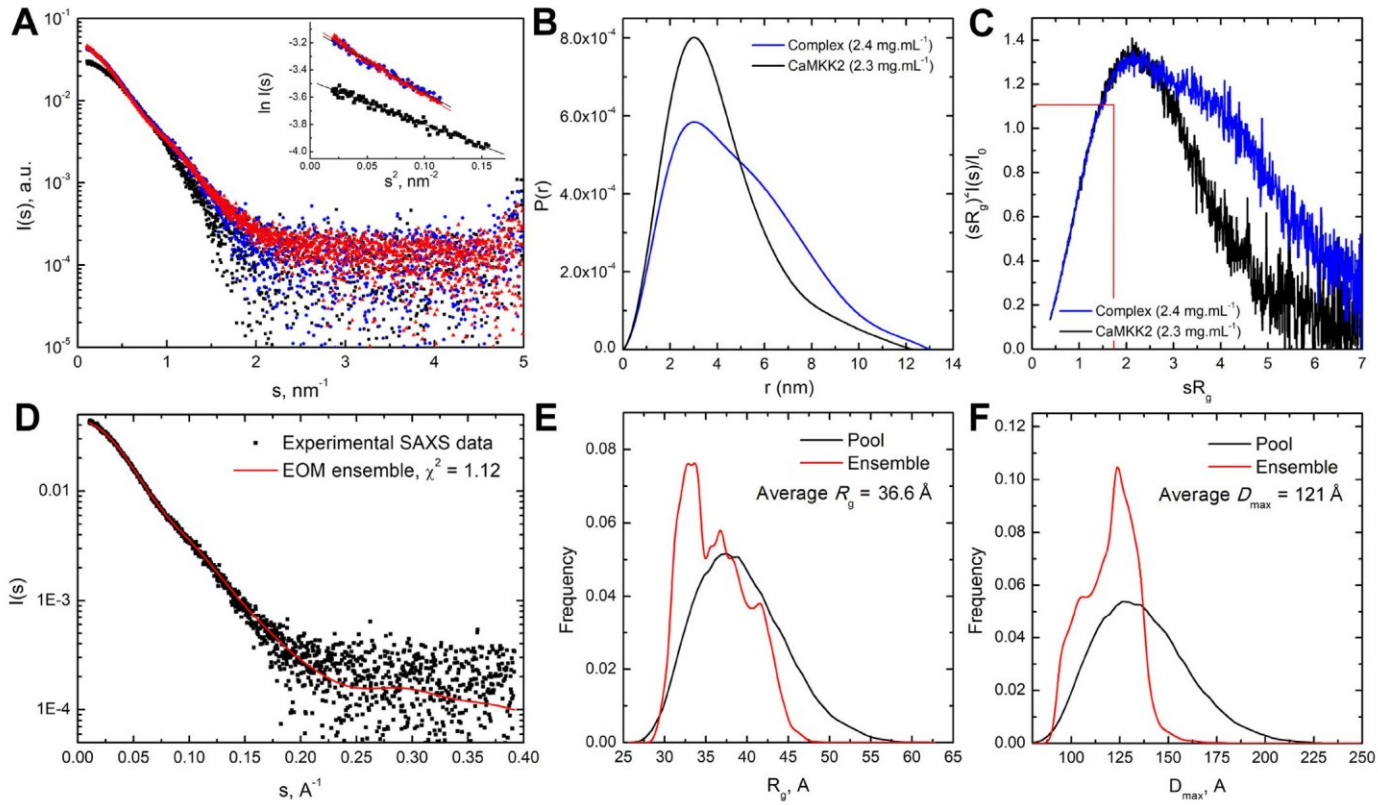

Fig. 5. SAXS Analysis of the CaMKK2:Ca^{2+}/CaM Complex. (A) Scattering intensity as a function of the scattering vector s ($s = 4\pi\sin(\theta/\lambda)$, where 2θ is the scattering angle, and λ is the wavelength) of CaMKK2 (2.3 mg.mL^{-1}, shown as black squares) and the CaMKK2:Ca^{2+}/CaM complex mixed at 2:1 M stoichiometry (2.4 and 5.8 mg.mL^{-1} shown as blue circles and red triangles, respectively). Guinier plots are shown in inset. (B) Distance distribution functions P(r) calculated from scattering data using the program GNOM [35]. (C) Dimensionless Kratky plots. Red lines mark the maximum at a value of 1.104 for $sR_g = 1.73$, which is typical of scattering data of compact globular proteins [33]. (D) Experimental scattering curve of the complex (at 2.4 mg.mL^{-1}) superimposed with the calculated curves of the ensemble selected by the program EOM (red). (E, F) Distributions of R_g and D_{max} values of the CaMKK2:Ca^{2+}/CaM complex conformations from ensemble selected by the program EOM [34].

Table 3
Intermolecular cross-links between CaMKK2 and CaM obtained with DSG and DSS.

		Cross-linked peptides		Cross-linked residues CaMKK2 – CaM	Observed mass	Theoretical mass	Error (ppm)	C_α-C_α distances from the model (Å)[d]
		CaMKK2	CaM					
DSG[a]	1	493-494	128-149	K493 – K149	2888.31	2888.31	0.40	15.7
	2	430–448	76–78	K441 – (K76, K78)[b]	2787.53	2787.53	−1.03	16.6, 19.9
DSS[a]	3	493–494	128-149	K493 – K149	2930.36	2930.36	0.06	15.7
	4	493–494	77–87	K493 – K78	1792.87	1792.87	0.19	28.5
	5	430–448	76–78	(K441 – K76, K78)	2829.58	2829.58	−1.30	16.6, 19.9
	6	243–250	1–14	K250 – K14[c]	2769.37	2769.37	0.57	24

[a] DSG, disuccinimidyl glutarate; DSG, disuccinimidyl suberate.
[b] Includes oxidation at CaM Met77.
[c] Includes acetylation and oxidation at CaM Met1.
[d] The model is shown in Fig. 6.

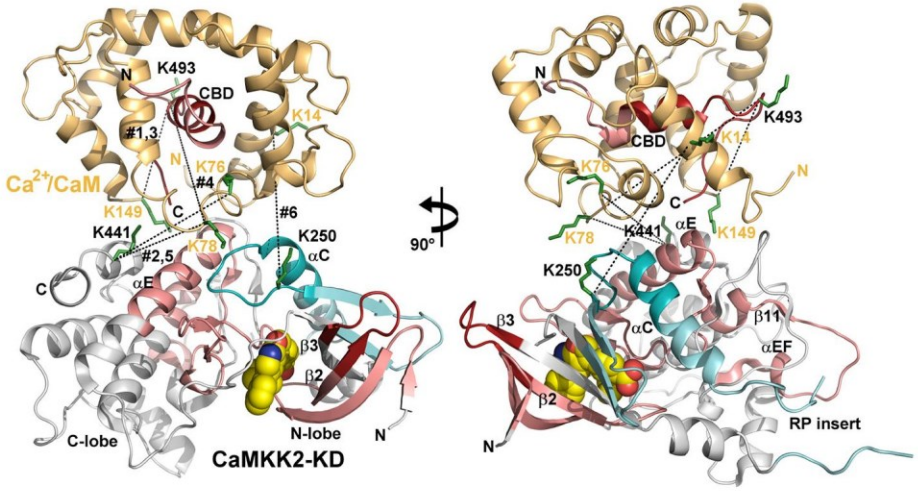

Fig. 6. Model of the CaMKK2 KD:Ca^{2+}/CaM complex. The model was prepared using the program HADDOCK [36] with the crystal structure of the CaMKK2 KD (PDB ID: 5UY6), the solution structure of Ca^{2+}/CaM bound to the CBD of CaMKK1 (PDB ID: 1CKK) [23], and intermolecular distance constraints assessed in chemical cross-linking experiments. The CaMKK2 KD is colored as in Fig. 3A, according to HDX-MS results. C_α-C_α distances derived from the model (dotted lines) are listed in Table 3.

the kinase domain and runs through the groove between helices αD and αE where it affects the position of the helix αD and subsequently the conformation of residues within the ATP binding site (Fig. 3B) [22, 28, 29]. In addition, the C-terminal part of AID of several CaMKs was also shown to occupy the ATP-binding pocket [28, 37]. However, the C-lobe of the CaMKK2 KD lacks the αD helix, and the sequence and length of the CaMKK AID differ from those of CaMKI and CaMKII [21], thus suggesting that the CaMKK AID may interact with different regions of the kinase domain, in contrast to other CaMKs. The HDX-MS results reported in this study indicate that the CaMKK2 AID interacts with surfaces formed by strands β4 and β5 and by the helix αC because peptides from these segments showed higher solvent exposure (increased exchange rate) upon Ca^{2+}/CaM binding. These surfaces are located on the opposite side of the kinase domain in relation to regions involved in interactions with the AID in other CaMKs (Fig. 3), thus corroborating the hypothesis that interactions between the CaMKK KD and the AID differ from those of other CaMKs [20, 21, 23]. Interestingly, three CaMKK2 point mutations (E268K, I328M and A329T), previously identified in large-scale human genetic studies and in various cancer tissues [38–41], are all located close to the ATP-binding pocket, in regions directly interacting with the loop between the αC helix and the β4 strand within the N-lobe, where the highest deprotection was observed upon Ca^{2+}/CaM binding (Figs. 3 and S4). O'Brien et al. [14] recently showed that these mutations substantially reduce Ca^{2+}/CaM-stimulated CaMKK2 activity and that the A329T mutation renders CaMKK2 completely insensitive to Ca^{2+}/CaM stimulation. Therefore, these findings further support the involvement of this N-lobe region in the interaction with the AID.

In addition to regions with increased exchange rate, several parts of the CaMKK2 KD, including the helix αE and segments containing strands β1-β2 and β6-β8, showed a decreased exchange rate upon complex formation. All these regions surround the ATP binding pocket and likely translate Ca^{2+}/CaM binding-induced conformational changes. This was further corroborated by the results of time-resolved tryptophan fluorescence measurements of Trp267, located within the strand β5 close to the ATP-binding pocket, and of Trp337, which is located within the activation segment (Fig. 4 and Table 1). Therefore, these data suggest that Ca^{2+}/CaM binding induces structural changes in regions surrounding the ATP-binding pocket, which likely contribute to the activation of CaMKK2. In addition, the regions with increased solvent exposure upon Ca^{2+}/CaM binding included the RP insert, a unique Arg-Pro-rich segment, which allows efficient targeting and subsequent activation of the downstream kinases CaMKI and CaMKIV [20]. This suggests that the CaMKK2 AID blocks the access to this region and that this interaction is relieved by Ca^{2+}/CaM binding to the CBD.

A structural study of DAPK, a CaMK involved in several apoptotic and autophagic cell death pathways [42], revealed that Ca^{2+}/CaM can, in addition to interacting with the CBD, simultaneously interact with the kinase domain [5]. Several regions of the CaMKK2 KD showed protection in the presence of Ca^{2+}/CaM, even after 5 h of deuteration (Fig. 2B). Such protection can be interpreted as either stabilization of secondary structure elements and/or decreased access to the solvent due to, for example, interaction with the AID-Ca^{2+}/CaM module. EOM analysis of SAXS data and the results of chemical cross-linking experiments suggested that a substantial portion of the CaMKK2:Ca^{2+}/CaM complex molecules is rather compact and that Ca^{2+}/CaM is located close to the kinase domain of CaMKK2 (Fig. 5 D-F and Table 3). Therefore, these results further supported the hypothesis that the kinase domain of CaMKK2 and the AID-Ca^{2+}/CaM module may directly

interact with each other. This interaction, however, would be rather transient, as suggested by the dimensionless Kratky plot (Fig. 5C), which indicated that the CaMKK2:Ca^{2+}/CaM complex shows substantial conformational flexibility.

The model of the CaMKK2:Ca^{2+}/CaM complex, which was build using the distance constraints assessed in chemical cross-linking experiments, suggested that the AID-Ca^{2+}/CaM module interacts with the region centered around the C-terminal part of helix αE (Fig. 6). In this position, the Ca^{2+}/CaM should not restrict the access to the active site, which is located on the opposite side of the kinase domain. The model of the CaMKK2:Ca^{2+}/CaM complex is consistent with all cross-linking data except for cross-link #4, which connects CaMKK2 AID-CBD Lys493 to CaM Lys78. The presence of this cross-link suggests that some portion of Ca^{2+}/CaM molecules binds in an opposite orientation to that observed in the complex between Ca^{2+}/CaM and the CBD peptide from CaMKKI [23] because this orientation would bring CaMKK2 Lys493 and CaM Lys78 close to each other.

In conclusion, our data contribute to understanding how Ca^{2+}/CaM interacts with and affects the structure of CaMKK2. Interactions between the CaMKK2 KD and the AID involve surfaces of the N-terminal lobe of the kinase domain, including the RP insert. Ca^{2+}/CaM binding affects the structure of regions surrounding the ATP-binding pocket as well as the activation segment. Moreover, our data also suggest that a substantial portion of the CaMKK2:Ca^{2+}/CaM molecules is rather compact, and the AID-bound Ca^{2+}/CaM transiently interacts with the kinase domain of CaMKK2. Thus, our results indicate that interactions between the CaMKK2 kinase domain and the AID differ from those of other CaMKs and that the AID inhibits CaMKK2 by blocking the RP insert and by affecting the structure of the ATP-binding pocket.

4. Materials and methods

4.1. Expression, purification and phosphorylation of CaMKK2

DNA encoding human CaMKK2 (residues 93–517) was ligated into pRSFDuet-1 (Novagen) using *Bam*HI and *Not*I sites. Modified pRSFDuet-1 containing the sequence of the His_6-tagged GB1 domain of protein G inserted into the first multiple cloning site was a gift from Evzen Boura (Institute of Organic Chemistry and Biochemistry AS CR, Prague, Czech Republic). CaMKK2 (93–517) was expressed as N-terminal His_6-GB1-tagged fusion protein in *Escherichia coli* BL21 (DE3) cells. Protein expression was conducted in autoinduction media for 5 h at 37 °C and then 16 h at 20 °C, and the protein was purified using Chelating Sepharose Fast Flow (GE Healthcare), according to the standard protocol. The eluted protein was dialyzed against the buffer containing 50 mM Tris-HCl (pH 8), 0.5 M NaCl, 4 mM 2-mercaptoethanol, 4 mM EDTA and 10% (*w/v*) glycerol and the His_6-GB1 tag was cleaved by incubation with TEV protease (250 U of TEV/mg of fusion protein) at 30 °C for 1 h. The final purification step was size-exclusion chromatography on a HiLoad 26/600 Superdex 75 column (GE Healthcare) in buffer containing 50 mM Tris-HCl (pH 8), 500 mM NaCl, 5 mM DTT, and 10% (w/v) glycerol. All mutants of CaMKK2 were generated using the QuikChange site-directed mutagenesis kit (Stratagene), and the mutations were confirmed by sequencing. The stability of mutants prepared was assessed by measuring the temperature of the unfolding transition (T_m) by differential scanning fluorimetry [43], and no significant differences in T_m were observed.

4.2. Expression and purification of CaM

Rat CaM was prepared as described previously [44].

4.3. Hydrogen/deuterium exchange coupled to mass spectrometry

HDX of $CaMKK2_{93–517}$ and the $CaMKK2_{93–517}$:Ca^{2+}/CaM complex was initiated by 10-fold dilution in a deuterated buffer containing 50 mM Tris-HCl (pH/pD 7.5), 150 mM NaCl, 1 mM TCEP and 1 mM $CaCl_2$. The final protein concentration was 3 μM. Aliquots (25 μL) were taken after 20 s, 1 min, 3 min, 10 min, 1 h, 3 h and 5 h of exchange. The exchange was quenched by adding 25 μL of 1 M glycine (pH 2.3) and fast freezing in liquid nitrogen. The deuterated samples (HPLC-MS) were analyzed on a HPLC column (1200 Agilent technologies, Waldbronn, Germany) connected to the ESI-FT-ICR MS (15 T solariX, Bruker Daltonics, Billerica, MA). The analysis started with quick thawing of the sample followed by digestion on a pepsin column (66 μL bed volume, flow rate 100 μL.min^{-1}). The resulting peptides were on-line desalted on a Peptide microtrap column (Optimize Technologies, Oregon City, OR) and separated on a C18 reversed phase column (ZORBAX 300SB-C18 3.5 μm, 0.5 × 35 mm, Agilent, Santa Clara, CA) using a linear gradient 10–45% B in 20 min, where solvent A was 2% acetonitrile/0.4% formic acid in water, solvent B 95% acetonitrile/5% water/0.4% formic acid. The injection and switching valve, the pepsin column, the peptide trap and the analytical column were placed in an icebox to minimize back exchange. Peptide identification (mapping, HPLC-MS/MS) was performed using the system described above, and the MS/MS spectra were searched by MASCOT against a database containing sequences of CaMKK2 and CaM. Spectra of partly deuterated peptides were processed using the software Data Analysis 4.2 (Bruker Daltonics, Billerica, MA) and an in-house software program termed DeutEx.

4.4. Chemical cross-linking combined with mass spectrometry

The $CaMKK2_{93–517}$ and the $CaMKK2_{93–517}$:Ca^{2+}/CaM complex were cross-linked with homobifunctional cross-linkers disuccinimidyl suberate (DSS) and disuccinimidyl glutarate (DSG). Cross-linkers DSS and DSG were used as 1:1 (mol/mol) mixtures of non-deuterated and four-times deuterated compounds (d0/d4). For the cross-linking reaction, the proteins were transferred to buffer containing 10 mM HEPES (pH 7.5) with 150 mM NaCl, 0.1 mM TCEP and 1 mM $CaCl_2$ and the protein concentration in all samples was 1 mg.mL^{-1}. Freshly prepared stock solutions of cross-linkers (10 mg.mL^{-1} in DMSO) were added to proteins in 20× or 50× molar excess in a total reaction volume of 20 μL. Reaction mixtures were incubated for 1 h at room temperature. Cross-linked samples were separated on NuPAGE 4–12% Bis–Tris gel using MES running buffer, and the bands corresponding to a monomeric cross-linked protein were excised. Cysteines were reduced with 50 mM DTT for 45 min at 60 °C, and free cysteines were alkylated with 100 mM iodoacetamide for 30 min at room temperature, in the dark. Trypsin digestion proceeded overnight at 37 °C with an enzyme/protein ratio of 1:20 (*w*/w). The resulting peptide mixtures were desalted on a Peptide microtrap column (Optimize Technologies, Oregon City, OR). Peptides extracted from the gel were loaded on a trap column (ZORBAX 300SB-C18, 5 μm, 5 × 0.3 mm, Agilent, Santa Clara, CA) and desalted for 5 min at flow rate 20 μL/min. Peptides were then separated by reversed phase C18 column (ZORBAX SB C18 RR 3.5u 150 × 0.3 mm, Agilent, Santa Clara, CA) at a flow rate 10 μL/min using capillary HPLC system (Agilent Technologies) under the following gradient conditions: 1–10% B in 1 min, 10–45% B in 19 min, 45–95% B in 5 min, where solvent A was 0.1% formic acid, 2.0% acetonitrile in water and solvent B was 0.1% formic acid in 98% acetonitrile. The column was heated at 50 °C and connected directly to an 15 T solariX FT-ICR mass spectrometer (Bruker Daltonics) using an electrospray ion source. The instrument was on line calibrated resulting in mass accuracy below 2 ppm. Data acquisition and data processing were performed by ftmsControl 2.1.0 and DataAnalysis 4.2 (Bruker Daltonics). The cross-links were identified using Links software [45]. The Links algorithm was set to consider the carbamidomethylation of cysteine and the possible single oxidation of methionine. The mass error threshold was kept below 2 ppm and all assigned fragments were verified manually.

4.5. Small angle x-ray scattering

SAXS data were collected at the European Molecular Biology Laboratory (EMBL) P12 beamline, at the storage ring PETRA III (Deutsches Elektronen Synchrotron (DESY), Hamburg, Germany). The SAXS measurements were conducted in buffer containing 50 mM Tris-HCl (pH 7.5), 150 mM NaCl, 1 mM TCEP, 1 mM $CaCl_2$, and 3% (*w/v*) glycerol, using 2.3–5 mg.mL^{-1} $CaMKK2_{93–517}$, 0.8–3.9 mg.mL^{-1} CaM and 2.4–10.7 mg.mL^{-1} $CaMKK2_{93–517}$:Ca^{2+}/CaM complex (1:1 M stoichiometry). The forward scattering $I(0)$ and the radius of gyration R_g were calculated using the Guinier approximation for a s ($s = 4\pi\sin(\theta)/\lambda$, where 2θ is the scattering angle and λ is the wavelength) range that satisfies the $sR_g < 1.3$ condition. The distance distribution functions $P(r)$ and the maximum particle dimensions D_{max} were computed using the program GNOM [35]. The solute apparent molecular mass (MM_{exp}) was estimated by comparing the forward scattering both with that of reference solutions of bovine serum albumin and with that of the excluded volume of the hydrated particle (the Porod volume) V_p [32]. V_P was computed using the program PRIMUS [46]. The analysis based on the ensemble optimization method was performed using the program EOM [34].

4.6. Time-resolved fluorescence measurements

Time-resolved fluorescence intensity and anisotropy decay measurements, as well as data analysis, were performed as previously described [47–49]. Tryptophan emission was excited at 298 nm by a tripled output of the Ti:Sapphire laser. Tryptophan fluorescence was isolated at 355 nm using a combination of monochromator and a stack of UG1 and BG40 glass filters (Thorlabs) placed in front of the input slit. Samples were placed in a thermostatic holder, and all experiments were performed at 23 °C in buffer containing 20 mM Tris-HCl (pH 7.5), 150 mM NaCl, 1 mM TCEP, 1 mM $CaCl_2$ and 10% (w/v) glycerol. The $CaMKK2_{93–517}$ and CaM concentrations were 15 and 30 μM, respectively.

4.7. Docking calculations

The docking simulation was performed using the program HADDOCK [36] with the crystal structure of the CaMKK2 KD (PDB ID: 5UY6), the solution structure of Ca^{2+}/CaM bound to the CBD of CaMKK1 (PDB ID: 1CKK) [23], and intermolecular distance constraints assessed in chemical cross-linking experiments. The residues in CaMKK2 KD that showed substantially lower deuterium incorporation (protection) after 5 h of deuteration in the presence of Ca^{2+}/CaM (regions 182–190, 292–341, and 354–373) were defined as the binding interface in HADDOCK calculation. The binding interface on the CaM molecule was defined based on the results from chemical cross-linking experiments. Ambiguous Interaction Restraints (AIRs) in both CaMKK2 KD and CaM molecules were defined according to the general HADDOCK rules [36].

Author contributions

V.O. and T.O. designed research; S.K., K.P., P.H., and T.O. performed research; S.K., K.P., P.H., V.O., and T.O. analyzed data; and V.O. and T.O. wrote the paper.

Conflict of interest

The authors declare no conflict of interest.

Acknowledgement

This study was supported by the Czech Science Foundation (Projects 16-02739S), the Grant Agency of the Charles University 1 (Project 368216), the Charles University Research Centre program No. UNCE/SCI/010, the Czech Academy of Sciences (Research Projects RVO: 67985823 of the Institute of Physiology), EU supported projects BIOCEV (CZ.1.05/1.1.00.02.0109) and Operational Programme "Research and Development for Innovation" (no. CZ.1.05/4.1.00/16.0340), and Czech Infrastructure for Integrative Structural Biology (CIISB) project LM2015043, funded by MEYS CR. We thank Dr. Petr Pompach for the mass spectrometry analyses and Dr. Carlos V. Melo for proofreading the article.

Appendix A. Supplementary data

Supplementary data to this article can be found online at https://doi.org/10.1016/j.bbagen.2018.07.025.

References

[1] T.R. Soderling, J.T. Stull, Structure and regulation of calcium/calmodulin-dependent protein kinases, Chem. Rev. 101 (2001) 2341–2352.
[2] M.T. Swulius, M.N. Waxham, Ca(2+)/calmodulin-dependent protein kinases, Cell. Mol. Life Sci. 65 (2008) 2637–2657.
[3] H. Tokumitsu, G.A. Wayman, M. Muramatsu, T.R. Soderling, Calcium/calmodulin-dependent protein kinase kinase: identification of regulatory domains, Biochemistry 36 (1997) 12823–12827.
[4] H. Tidow, P. Nissen, Structural diversity of calmodulin binding to its target sites, FEBS J. 280 (2013) 5551–5565.
[5] I. de Diego, J. Kuper, N. Bakalova, P. Kursula, M. Wilmanns, Molecular basis of the death-associated protein kinase-calcium/calmodulin regulator complex, Sci. Signal. 3 (2010) ra6.
[6] B. Haribabu, S.S. Hook, M.A. Selbert, E.G. Goldstein, E.D. Tomhave, A.M. Edelman, R. Snyderman, A.R. Means, Human calcium-calmodulin dependent protein kinase I: cDNA cloning, domain structure and activation by phosphorylation at threonine-177 by calcium-calmodulin dependent protein kinase I kinase, EMBO J. 14 (1995) 3679–3686.
[7] R.L. Hurley, K.A. Anderson, J.M. Franzone, B.E. Kemp, A.R. Means, L.A. Witters, The Ca2+/calmodulin-dependent protein kinase kinases are AMP-activated protein kinase kinases, J. Biol. Chem. 280 (2005) 29060–29066.
[8] K.A. Anderson, T.J. Ribar, F. Lin, P.K. Noeldner, M.F. Green, M.J. Muehlbauer, L.A. Witters, B.E. Kemp, A.R. Means, Hypothalamic CaMKK2 contributes to the regulation of energy balance, Cell Metab. 7 (2008) 377–388.
[9] L. Racioppi, A.R. Means, Calcium/calmodulin-dependent protein kinase kinase 2: roles in signaling and pathophysiology, J. Biol. Chem. 287 (2012) 31658–31665.
[10] H. Tokumitsu, M. Muramatsu, M. Ikura, R. Kobayashi, Regulatory mechanism of Ca2+/calmodulin-dependent protein kinase kinase, J. Biol. Chem. 275 (2000) 20090–20095.
[11] K.A. Anderson, R.L. Means, Q.H. Huang, B.E. Kemp, E.G. Goldstein, M.A. Selbert, A.M. Edelman, R.T. Fremeau, A.R. Means, Components of a calmodulin-dependent protein kinase cascade. Molecular cloning, functional characterization and cellular localization of Ca2+/calmodulin-dependent protein kinase kinase beta, J. Biol. Chem. 273 (1998) 31880–31889.
[12] M.F. Green, J.W. Scott, R. Steel, J.S. Oakhill, B.E. Kemp, A.R. Means, Ca2+/calmodulin-dependent protein kinase kinase beta is regulated by multisite phosphorylation, J. Biol. Chem. 286 (2011) 28066–28079.
[13] H. Tokumitsu, M. Iwabu, Y. Ishikawa, R. Kobayashi, Differential regulatory mechanism of Ca2+/calmodulin-dependent protein kinase kinase isoforms, Biochemistry 40 (2001) 13925–13932.
[14] M.T. O'Brien, J.S. Oakhill, N.M.X.Y. Ling, C.G. Langendorf, A. Hoque, T.A. Dite, A.R. Means, B.E. Kemp, J.W. Scott, Impact of genetic variation on human CaMKK2 regulation by Ca2+-calmodulin and multisite phosphorylation, Sci. Rep. 7 (2017).
[15] H. Tokumitsu, N. Hatano, T. Fujimoto, S. Yurimoto, R. Kobayashi, Generation of autonomous activity of Ca(2+)/calmodulin-dependent protein kinase kinase beta by autophosphorylation, Biochemistry 50 (2011) 8193–8201.
[16] J.W. Scott, E. Park, R.M. Rodriguiz, J.S. Oakhill, S.M. Issa, M.T. O'Brien, T.A. Dite, C.G. Langendorf, W.C. Wetsel, A.R. Means, B.E. Kemp, Autophosphorylation of CaMKK2 generates autonomous activity that is disrupted by a T85S mutation linked to anxiety and bipolar disorder, Sci. Rep. 5 (2015) 14436.
[17] G.A. Wayman, H. Tokumitsu, T.R. Soderling, Inhibitory cross-talk by cAMP kinase on the calmodulin-dependent protein kinase cascade, J. Biol. Chem. 272 (1997) 16073–16076.
[18] K. Psenakova, O. Petrvalska, S. Kylarova, D. Lentini Santo, D. Kalabova, P. Herman, V. Obsilova, T. Obsil, 14-3-3 protein directly interacts with the kinase domain of calcium/calmodulin-dependent protein kinase kinase (CaMKK2), Biochim. Biophys. Acta 1862 (2018) 1612–1625.
[19] T. Kitani, S. Okuno, H. Fujisawa, Regulation of Ca(2+)/calmodulin-dependent protein kinase kinase alpha by cAMP-dependent protein kinase: II. Mutational analysis, J. Biochem. 130 (2001) 515–525.
[20] H. Tokumitsu, N. Takahashi, K. Eto, S. Yano, T.R. Soderling, M. Muramatsu, Substrate recognition by Ca2+/Calmodulin-dependent protein kinase kinase. Role of the arg-pro-rich insert domain, J. Biol. Chem. 274 (1999) 15803–15810.
[21] M. Kukimoto-Niino, S. Yoshikawa, T. Takagi, N. Ohsawa, Y. Tomabechi, T. Terada,

M. Shirouzu, A. Suzuki, S. Lee, T. Yamauchi, M. Okada-Iwabu, M. Iwabu, T. Kadowaki, Y. Minokoshi, S. Yokoyama, Crystal structure of the Ca(2)(+)/calmodulin-dependent protein kinase kinase in complex with the inhibitor STO-609, J. Biol. Chem. 286 (2011) 22570–22579.
[22] O.S. Rosenberg, S. Deindl, R.J. Sung, A.C. Nairn, J. Kuriyan, Structure of the autoinhibited kinase domain of CaMKII and SAXS analysis of the holoenzyme, Cell 123 (2005) 849–860.
[23] M. Osawa, H. Tokumitsu, M.B. Swindells, H. Kurihara, M. Orita, T. Shibanuma, T. Furuya, M. Ikura, A novel target recognition revealed by calmodulin in complex with Ca2+ −calmodulin-dependent kinase kinase, Nat. Struct. Biol. 6 (1999) 819–824.
[24] M. Ikura, G.M. Clore, A.M. Gronenborn, G. Zhu, C.B. Klee, A. Bax, Solution structure of a calmodulin-target peptide complex by multidimensional NMR, Science 256 (1992) 632–638.
[25] W.E. Meador, A.R. Means, F.A. Quiocho, Modulation of calmodulin plasticity in molecular recognition on the basis of x-ray structures, Science 262 (1993) 1718–1721.
[26] W.E. Meador, A.R. Means, F.A. Quiocho, Target enzyme recognition by calmodulin: 2.4 a structure of a calmodulin-peptide complex, Science 257 (1992) 1251–1255.
[27] P. Rellos, A.C. Pike, F.H. Niesen, E. Salah, W.H. Lee, F. von Delft, S. Knapp, Structure of the CaMKIIdelta/calmodulin complex reveals the molecular mechanism of CaMKII kinase activation, PLoS Biol. 8 (2010) e1000426.
[28] J. Goldberg, A.C. Nairn, J. Kuriyan, Structural basis for the autoinhibition of calcium/calmodulin-dependent protein kinase I, Cell 84 (1996) 875–887.
[29] L.H. Chao, M.M. Stratton, I.H. Lee, O.S. Rosenberg, J. Levitz, D.J. Mandell, T. Kortemme, J.T. Groves, H. Schulman, J. Kuriyan, A mechanism for tunable autoinhibition in the structure of a human Ca2+/calmodulin- dependent kinase II holoenzyme, Cell 146 (2011) 732–745.
[30] J.R. Lakowicz, Principles of Fluorescence Spectroscopy, Third edition, Springer, New York, 2006.
[31] L. Rezabkova, M. Kacirova, M. Sulc, P. Herman, J. Vecer, M. Stepanek, V. Obsilova, T. Obsil, Structural modulation of phosducin by phosphorylation and 14-3-3 protein binding, Biophys. J. 103 (2012) 1960–1969.
[32] M.V. Petoukhov, D. Franke, A.V. Shkumatov, G. Tria, A.G. Kikhney, M. Gajda, C. Gorba, H.D. Mertens, P.V. Konarev, D.I. Svergun, New developments in the program package for small-angle scattering data analysis, J. Appl. Crystallogr. 45 (2012) 342–350.
[33] V. Receveur-Brechot, D. Durand, How random are intrinsically disordered proteins? A small angle scattering perspective, Curr. Protein Pept. Sci. 13 (2012) 55–75.
[34] G. Tria, H.D. Mertens, M. Kachala, D.I. Svergun, Advanced ensemble modelling of flexible macromolecules using X-ray solution scattering, IUCrJ 2 (2015) 207–217.
[35] D.I. Svergun, Determination of the regularization parameter in indirect-transform methods using perceptual criteria, J. Appl. Crystallogr. 25 (1992) 495–503.
[36] C. Dominguez, R. Boelens, A.M. Bonvin, HADDOCK: a protein-protein docking approach based on biochemical or biophysical information, J. Am. Chem. Soc. 125 (2003) 1731–1737.
[37] S.H. Hu, M.W. Parker, J.Y. Lei, M.C. Wilce, G.M. Benian, B.E. Kemp, Insights into autoregulation from the crystal structure of twitchin kinase, Nature 369 (1994) 581–584.
[38] M.R. Nelson, D. Wegmann, M.G. Ehm, D. Kessner, P. St Jean, C. Verzilli, J. Shen, Z. Tang, S.A. Bacanu, D. Fraser, L. Warren, J. Aponte, M. Zawistowski, X. Liu, H. Zhang, Y. Zhang, J. Li, Y. Li, L. Li, P. Woollard, S. Topp, M.D. Hall, K. Nangle, J. Wang, G. Abecasis, L.R. Cardon, S. Zollner, J.C. Whittaker, S.L. Chissoe, J. Novembre, V. Mooser, An abundance of rare functional variants in 202 drug target genes sequenced in 14,002 people, Science 337 (2012) 100–104.
[39] M. Lek, K.J. Karczewski, E.V. Minikel, K.E. Samocha, E. Banks, T. Fennell, A.H. O'Donnell-Luria, J.S. Ware, A.J. Hill, B.B. Cummings, T. Tukiainen, D.P. Birnbaum, J.A. Kosmicki, L.E. Duncan, K. Estrada, F. Zhao, J. Zou, E. Pierce-Hoffman, J. Berghout, D.N. Cooper, N. Deflaux, M. DePristo, R. Do, J. Flannick, M. Fromer, L. Gauthier, J. Goldstein, N. Gupta, D. Howrigan, A. Kiezun, M.I. Kurki, A.L. Moonshine, P. Natarajan, L. Orozco, G.M. Peloso, R. Poplin, M.A. Rivas, V. Ruano-Rubio, S.A. Rose, D.M. Ruderfer, K. Shakir, P.D. Stenson, C. Stevens, B.P. Thomas, G. Tiao, M.T. Tusie-Luna, B. Weisburd, H.H. Won, D. Yu, D.M. Altshuler, D. Ardissino, M. Boehnke, J. Danesh, S. Donnelly, R. Elosua, J.C. Florez, S.B. Gabriel, G. Getz, S.J. Glatt, C.M. Hultman, S. Kathiresan, M. Laakso, S. McCarroll, M.I. McCarthy, D. McGovern, R. McPherson, B.M. Neale, A. Palotie, S.M. Purcell, D. Saleheen, J.M. Scharf, P. Sklar, P.F. Sullivan, J. Tuomilehto, M.T. Tsuang, H.C. Watkins, J.G. Wilson, M.J. Daly, D.G. MaCarthur, C. Exome Aggregation, Analysis of protein-coding genetic variation in 60,706 humans, Nature 536 (2016) 285–291.
[40] S.A. Forbes, D. Beare, P. Gunasekaran, K. Leung, N. Bindal, H. Boutselakis, M. Ding, S. Bamford, C. Cole, S. Ward, C.Y. Kok, M. Jia, T. De, J.W. Teague, M.R. Stratton, U. McDermott, P.J. Campbell, COSMIC: exploring the world's knowledge of somatic mutations in human cancer, Nucleic Acids Res. 43 (2015) D805–D811.
[41] O.D. Abaan, E.C. Polley, S.R. Davis, Y.J. Zhu, S. Bilke, R.L. Walker, M. Pineda, Y. Gindin, Y. Jiang, W.C. Reinhold, S.L. Holbeck, R.M. Simon, J.H. Doroshow, Y. Pommier, P.S. Meltzer, The exomes of the NCI-60 panel: a genomic resource for cancer biology and systems pharmacology, Cancer Res. 73 (2013) 4372–4382.
[42] D. Gozuacik, A. Kimchi, DAPk protein family and cancer, Autophagy 2 (2006) 74–79.
[43] F.H. Niesen, H. Berglund, M. Vedadi, The use of differential scanning fluorimetry to detect ligand interactions that promote protein stability, Nat. Protoc. 2 (2007) 2212–2221.
[44] B. Holakovska, L. Grycova, J. Bily, J. Teisinger, Characterization of calmodulin binding domains in TRPV2 and TRPV5 C-tails, Amino Acids 40 (2011) 741–748.
[45] M.M. Young, N. Tang, J.C. Hempel, C.M. Oshiro, E.W. Taylor, I.D. Kuntz, B.W. Gibson, G. Dollinger, High throughput protein fold identification by using experimental constraints derived from intramolecular cross-links and mass spectrometry, Proc. Natl. Acad. Sci. U. S. A. 97 (2000) 5802–5806.
[46] P.V. Konarev, V.V. Volkov, A.V. Sokolova, M.H.J. Koch, D.I. Svergun, PRIMUS: a windows PC-based system for small-angle scattering data analysis, J. Appl. Crystallogr. 36 (2003) 1277–1282.
[47] D. Kosek, S. Kylarova, K. Psenakova, L. Rezabkova, P. Herman, J. Vecer, V. Obsilova, T. Obsil, Biophysical and structural characterization of the thioredoxin-binding domain of protein kinase ASK1 and its interaction with reduced thioredoxin, J. Biol. Chem. 289 (2014) 24463–24474.
[48] L. Rezabkova, E. Boura, P. Herman, J. Vecer, L. Bourova, M. Sulc, P. Svoboda, V. Obsilova, T. Obsil, 14-3-3 protein interacts with and affects the structure of RGS domain of regulator of G protein signaling 3 (RGS3), J. Struct. Biol. 170 (2010) 451–461.
[49] J. Vecer, P. Herman, Maximum entropy analysis of analytically simulated complex fluorescence decays, J. Fluoresc. 21 (2011) 873–881.

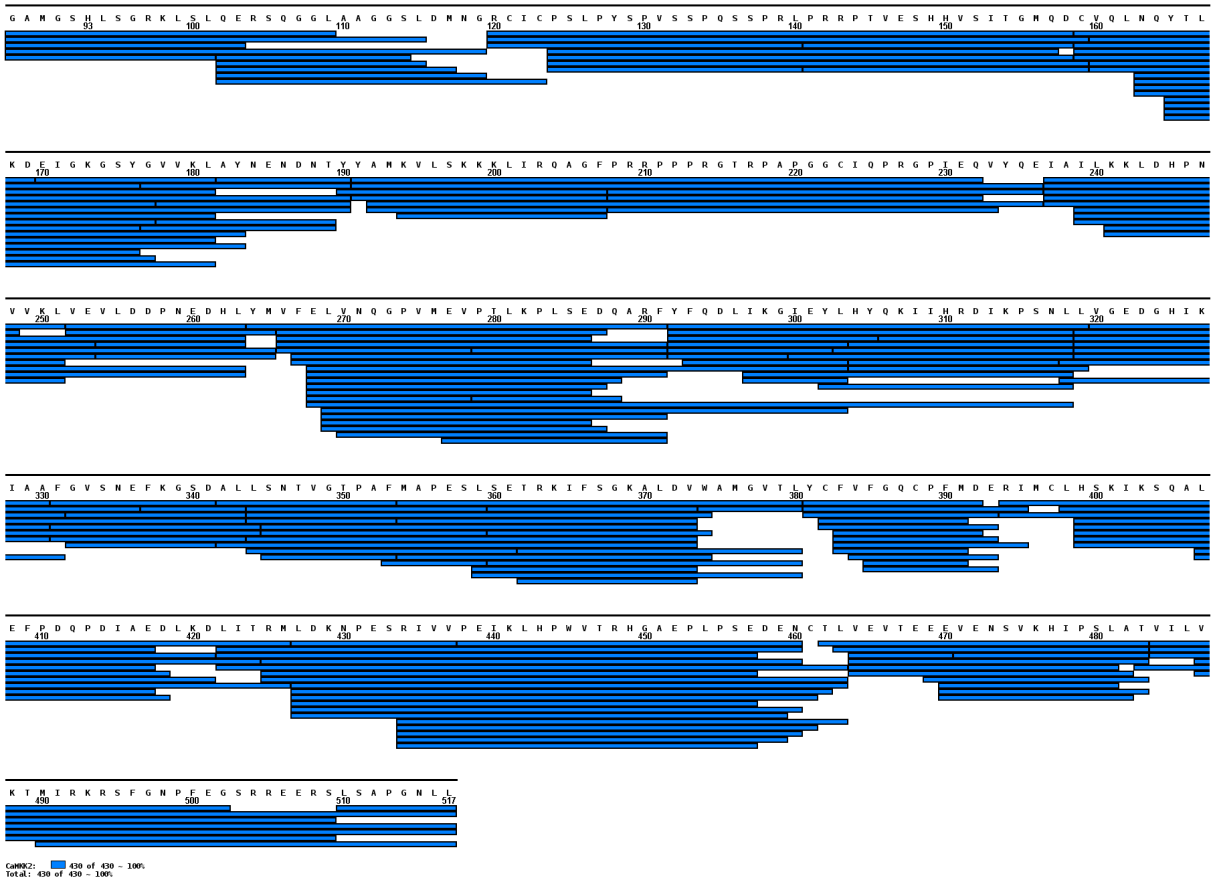

Figure S1. Related to Figure 2.

Peptide mapping of CaMKK2 after digestion with immobilized pepsin. All peptides identified by ESI-FT ICR-MS/MS analysis are shown as blue bars. The residues are numbered according to the native sequence (the first five residues are from the tag).

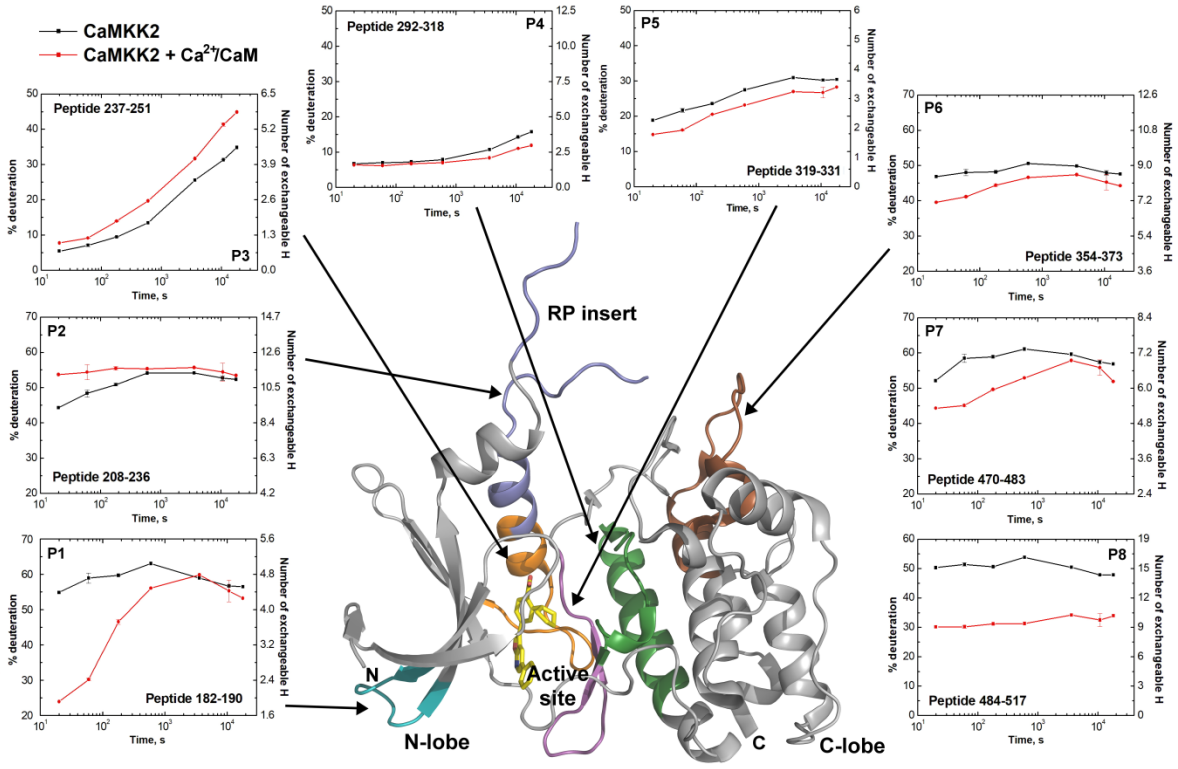

Figure S2. Related to Figure 2.

HDX kinetics for selected CaMKK2 peptides. The graphs represent the HDX kinetics of selected CaMKK2 regions that show changed deuterium exchange kinetics upon Ca^{2+}/CaM binding. Deuterium exchange is expressed as percentages relative to the maximum theoretical deuteration level (left vertical axis), as well as a number of exchangeable protons (right vertical axis) of selected CaMKK2 peptides alone (black squares) and in the presence of Ca^{2+}/CaM (red circles). The regions of the kinase domain (peptides P1–P6) are mapped on the surface representation of the CaMKK2 KD crystal structure (PDB ID: 5UY6). To estimate the measurement error, the HDX was repeated 3× for the time points 1 min, 3 min and 3 h, and the error bars are expressed the standard deviation of triplicate samples.

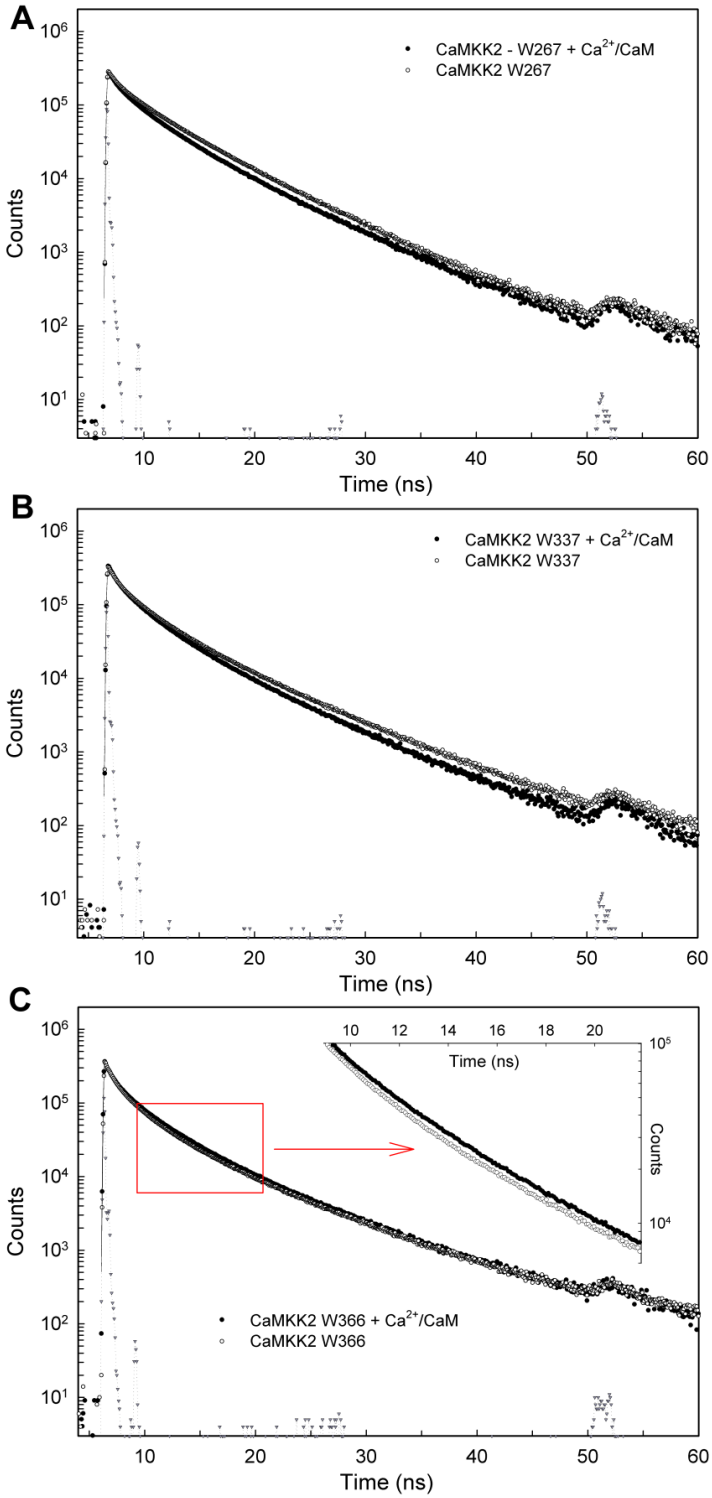

Figure S3. Related to Figure 4.

Time-resolved tryptophan fluorescence measurements. Fluorescence intensity decays of CaMKK2 W267 (A), CaMKK2 W337 (B) and CaMKK2 W366 (C) mutants in the absence and the presence of Ca^{2+}/CaM.

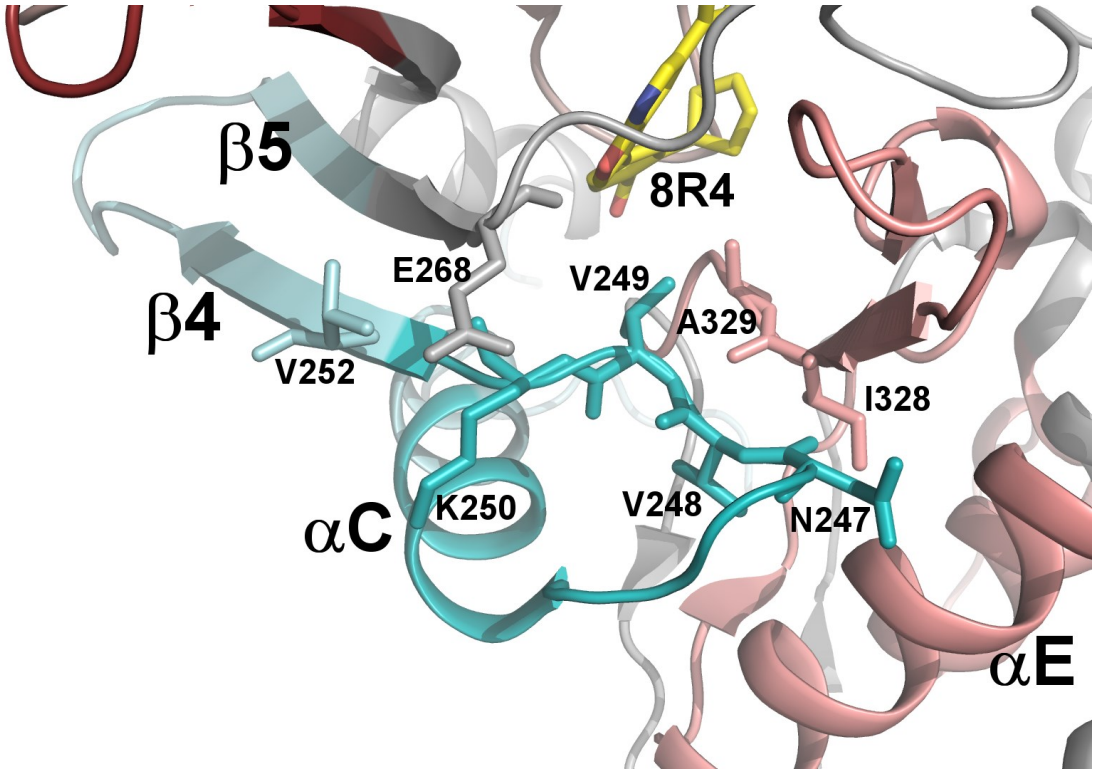

Figure S4. Related to Figure 3.

Detailed view of residues Glu268, Ile328 and Ala329 and of αC-β4 loop residues, which are located in their close vicinity. The crystal structure of CaMKK2 KD (PDB ID: 5UY6) showed that residues Glu268, Ile328 and Ala329, which are located close to the ATP-binding pocket, interact with αC-β4 loop residues 247-252. CaMKK2 KD is colored as in Fig. 3A, according to the HDX-MS results.

7.3 Supplement S3

7.3.1 Publication III: The role of 14-3-3 in the regulation of Caspase-2 protease activity

Smidova, A., Alblova, M., Kalabova, D., **Psenakova, K.,** Rosulek, M., Herman, P., Obsil, T. & Obsilova, V. 14-3-3 Protein Masks the Nuclear Localization Sequence of Caspase-2. *FEBS J.* **285**, 4196–4213 (2018).

My contribution: expression and purification of ^{15}N-labeled 14-3-3; sample preparation and further optimization for the NMR experiments; NMR experimental design and measurements; NMR data evaluation; docking calculations and refinement of the structural model based on the experimental data.

The FEBS Journal

14-3-3 protein masks the nuclear localization sequence of caspase-2

Aneta Smidova[1], Miroslava Alblova[1], Dana Kalabova[1,2], Katarina Psenakova[1,3], Michal Rosulek[4,5], Petr Herman[6], Tomas Obsil[1,3] and Veronika Obsilova[1]

1 Department of Structural Biology of Signaling Proteins, Division BIOCEV, Institute of Physiology of the Czech Academy of Sciences, Vestec, Czech Republic
2 2nd Faculty of Medicine, Charles University, Prague, Czech Republic
3 Department of Physical and Macromolecular Chemistry, Faculty of Science, Charles University, Prague, Czech Republic
4 Division BIOCEV, Institute of Microbiology of the Czech Academy of Sciences, Vestec, Czech Republic
5 Department of Biochemistry, Faculty of Science, Charles University, Prague, Czech Republic
6 Institute of Physics, Faculty of Mathematics and Physics, Charles University, Prague, Czech Republic

Keywords
14-3-3 protein; caspase-2; fluorescence; nuclear localization sequence; protein–protein interactions; small angle X-ray scattering

Correspondence
T. Obsil, Department of Physical and Macromolecular Chemistry, Faculty of Science, Charles University, Prague, Czech Republic
Fax: +420 224919752
Tel: +420 221951303
E-mail: obsil@natur.cuni.cz
and
V. Obsilova, Department of Structural Biology of Signaling Proteins, Division BIOCEV, Institute of Physiology of the Czech Academy of Sciences, 252 50 Vestec, Czech Republic
Fax: +420 241 062 488
Tel: +420 325 873 513
E-mail: veronika.obsilova@fgu.cas.cz

Aneta Smidova, Miroslava Alblova and Dana Kalabova contributed equally to this work

(Received 17 August 2018, accepted 28 September 2018)

doi:10.1111/febs.14670

Caspase-2 is an apical protease responsible for the proteolysis of cellular substrates directly involved in mediating apoptotic signaling cascades. Caspase-2 activation is inhibited by phosphorylation followed by binding to the scaffolding protein 14-3-3, which recognizes two phosphoserines located in the linker between the caspase recruitment domain and the p19 domains of the caspase-2 zymogen. However, the structural details of this interaction and the exact role of 14-3-3 in the regulation of caspase-2 activation remain unclear. Moreover, the caspase-2 region with both 14-3-3-binding motifs also contains the nuclear localization sequence (NLS), thus suggesting that 14-3-3 binding may regulate the subcellular localization of caspase-2. Here, we report a structural analysis of the 14-3-3ζ:caspase-2 complex using a combined approach based on small angle X-ray scattering, NMR, chemical cross-linking, and fluorescence spectroscopy. The structural model proposed in this study suggests that phosphorylated caspase-2 and 14-3-3ζ form a compact and rigid complex in which the p19 and the p12 domains of caspase-2 are positioned within the central channel of the 14-3-3 dimer and stabilized through interactions with the C-terminal helices of both 14-3-3ζ protomers. In this conformation, the surface of the p12 domain, which is involved in caspase-2 activation by dimerization, is sterically occluded by the 14-3-3 dimer, thereby likely preventing caspase-2 activation. In addition, 14-3-3 protein binding to caspase-2 masks its NLS. Therefore, our results suggest that 14-3-3 protein binding to caspase-2 may play a key role in regulating caspase-2 activation.

Database
The atomic coordinates and structure factors have been deposited in the Protein Data Bank, www.ww pdb.org (PDB ID codes 6GKF and 6GKG).

Abbreviations
CARD, caspase recruitment domain; CSP, chemical shift perturbation; NLS, nuclear localization sequence; NMR, nuclear magnetic resonance; PIDD, p53-induced protein with a death domain; proC2, caspase-2 residues 123-452 without the CARD domain; RAIDD, adaptor protein RIP-associated ICH-1/CAD-3 homologous protein with a death domain; SAXS, small angle X-ray scattering.

Introduction

Caspase activation coordinates the apoptotic pathway. Caspases cleave substrates at the C-terminal to aspartate residues. In particular, caspase-2 is a key switch between cellular metabolism and apoptosis and tumor suppressor [1]. This protease is crucial for human physiology and pathophysiology, as shown by its prominent downstream targets, such as protein kinase C delta and huntingtin protein. Accordingly, its activation must be strictly controlled in cells [2,3].

Caspase-2 is an initiator caspase (alongside caspase-8 and -9) activated by proximity-induced dimerization after recruitment to specific high molecular weight protein complexes and trans-cleavage of the caspase recruitment domain (CARD) and linker regions [4–7]. This results in the formation of the fully active enzyme, a heterodimer of two large (p19) and two small subunits (p12) which is responsible for triggering apoptosis. In turn, the PIDDosome, a complex formed by the scaffold protein p53-induced protein with a death domain (PIDD) and by the adaptor protein RIP-associated ICH-1/CAD-3 homologous protein with a death domain (RAIDD) [8,9] is a well-known caspase-2 activation platform.

In contrast to other caspases, endogenous caspase-2 is mainly localized in the nucleus and in the Golgi complex [10,11]. The nuclear localization of caspase-2 is driven by a classical nuclear localization sequence (NLS), located in the linker region between the CARD and the p19 domains (sequence P^{149}LYKKLRL^{156}), which is recognized by the importin α/β heterodimer [12]. Mutating a conserved Lys^{152} in this sequence has been shown to abolish caspase-2 nuclear localization and its binding to the importin α/β heterodimer. Moreover, a recent study has shown that DNA damage-induced caspase-2 activation primarily occurs in the nucleolus and depends on the PIDDosome and on the nucleolar phosphoprotein nucleophosmin. Conversely, cytoplasmic caspase-2 activation is driven by a PIDD-independent platform, albeit still requiring RAIDD [13].

In addition to the upstream regulation by its adaptor proteins, caspase-2 activation can also be fine-tuned by phosphorylation. In *Xenopus laevis*, abundant nutrient flux leads to strong Ser^{164} phosphorylation (human numbering), which blocks caspase-2 binding to RAIDD and induces caspase-2 binding to the scaffolding protein 14-3-3, thereby keeping caspase-2 inactive [14]. In addition, Ser^{340} phosphorylation by Cdk1 kinase has also been shown to prevent caspase-2 activation during normal mitosis [15].

14-3-3 proteins, highly homologous dimeric molecules present in all eukaryotic organisms, are the main regulators of key cellular processes such as apoptosis, signal transduction, cell cycle regulation, or tumorigenesis [16–19]. More than 2000 14-3-3 protein-binding partners have been predicted and several hundred have been experimentally validated thus far [20,21]. In most cases, 14-3-3 protein binding is triggered by phosphorylation of the target protein. Thus, 14-3-3 proteins function as master regulators of their binding partners by switching their active and inactive states in complex cell signaling networks [22,23].

Many 14-3-3-binding partners contain two or more 14-3-3-binding motifs, which could be simultaneously used to engage both protomers within the 14-3-3 dimer [21,24,25]. It has previously been suggested that the 14-3-3 protein binding to caspase-2 requires phosphorylation not only at Ser^{164} but also Ser^{139} (Fig. 1A) [14,26,27]. Indeed, we have recently shown that the complex formation between caspase-2 and 14-3-3 requires simultaneous phosphorylation of both these sites [28]. However, the structural details of this interaction and the exact role of 14-3-3 in regulating caspase-2 activation remain unclear. Moreover, the presence of both 14-3-3-binding motifs and of the NLS in the same caspase-2 region suggests that 14-3-3 binding may regulate the subcellular localization of caspase-2. Therefore, such mode of regulation likely requires a direct interaction between 14-3-3 and the NLS of caspase-2 that masks the interaction between the NLS and the nuclear import machinery, yet no such interaction has been shown thus far.

In this context, we aimed to analyze 14-3-3 protein binding to caspase-2 toward understanding how this interaction affects caspase-2 structure and regulation. For this purpose, we performed a structural analysis of the complex between 14-3-3ζ and phosphorylated caspase-2 using a combined approach based on small angle X-ray scattering (SAXS), NMR, chemical cross-linking, and fluorescence spectroscopy.

Results

The complex between caspase-2 and 14-3-3 has a globular and compact shape

The main goal of this work is to provide the structural basis for the role of 14-3-3 protein binding in regulating caspase-2 activation. Because all our previous attempts to crystallize the complex between Ser139- and Ser164-phosphorylated caspase-2 (residues 123–452 without the CARD domain) [28] (hereafter referred to as

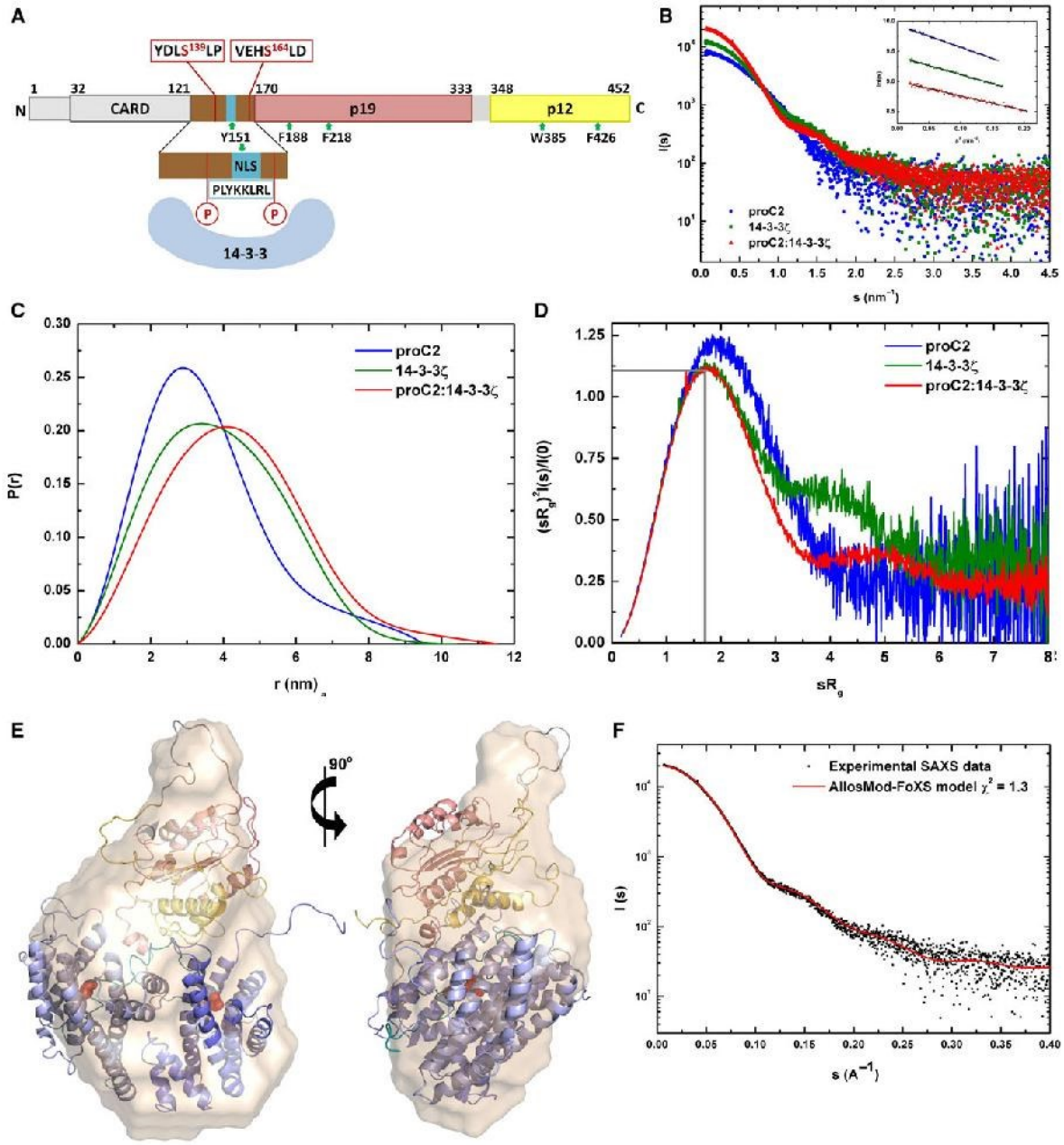

Fig. 1. SAXS data analysis. (A) Domain structure of human caspase-2. The N-terminal part with the CARD domain (not shown in the proC2 construct) is highlighted in gray, the linker sequence between the CARD and p19 domains in brown, the p19 domain in salmon and the p12 domain in yellow. The positions of phosphorylation sites and of the NLS are indicated in red and blue, respectively. The positions of Tyr and Phe residues mutated to Trp and used in fluorescence experiments are indicated by green arrows. (B) Experimental scattering intensity I(s) is plotted as a function of the scattering vector s ($s = 4\pi\sin(\theta)/\lambda$, where 2θ is the scattering angle, and λ is the wavelength). Data were collected at the following protein concentrations: proC2 (1.9 mg·mL^{-1}, blue), 14-3-3ζ (2.2 mg·mL^{-1}, green), and the proC2:14-3-3ζ complex mixed at 1 : 2 molar stoichiometry (3.6 mg·mL^{-1}, red). Guinier plots (ln[I(s) versus s2) for scattering curves are shown as inset. (C) Distance distribution functions P(r) calculated from scattering data using the program GNOM [56]. (D) Dimensionless Kratky plots. Gray lines mark the maximum at a value of 1.104 for $sR_g = 1.73$, a typical attribute of scattering data of compact globular proteins [35]. (E) *Ab initio* shape reconstruction of proC2:14-3-3ζ complex (wheat envelope) calculated from SAXS data with a superimposed AllosMod-FoXS model of the proC2:14-3-3ζ complex shown in two perpendicular views. The linker sequence in the groove, p19, p12 domains and phosphorylation sites are indicated in deep teal, salmon, yellow, and red spheres. The calculated molecular envelope was aligned to the structural model using the program SUPCOMB [66]. The *ab initio* shape reconstruction was performed using the program DAMMIF [67]. (F) Comparison of the calculated scattering curve of proC2 (red line) with the experimental scattering data (black line).

proC2) and 14-3-3ζ had been unsuccessful, we decided to use small angle X-ray scattering (SAXS) combined with NMR, with chemical cross-linking coupled to MS and with fluorescence spectroscopy to characterize the solution structure and conformational behavior of this complex. We and others have successfully used a similar approach to characterize conformationally flexible 14-3-3 protein complexes [29–34].

X-ray scattering data were collected for proC2, 14-3-3ζ, and the proC2:14-3-3ζ complex (mixed in 1 : 2 molar stoichiometry) at different concentrations (Table 1 and Fig. 1B). The complex was prepared at concentrations at least two orders of magnitude higher than the previously reported K_D value of ~ 230 nM [28]. The values of gyration radius (R_g), maximum particle distance (D_{max}), and Porod volume (V_p) were calculated from the measured SAXS profiles. The linearity of Guinier plots indicated the absence of aggregation in all samples (Fig. 1B). The apparent molecular masses of proC2, 14-3-3ζ, and the proC2:14-3-3ζ complex estimated from the forward scattering intensity $I(0)$ and V_p matched their expected M_w values (Table 1). The apparent M_w values of the proC2:14-3-3ζ complex and its V_p values are consistent with a 1 : 2 M stoichiometry, thus corroborating our previously published data [28].

The distance distribution functions $P(r)$ showed that the D_{max} values of the complex are only slightly larger than those of proC2 and 14-3-3ζ alone (Fig. 1C), thus suggesting that the proC2:14-3-3ζ complex adopts a rather compact conformation. This was further confirmed by dimensionless Kratky plots ($(sR_g)^2I(s)/I(0)$ versus sR_g), which indicate the conformational flexibility of a protein, regardless of its size [35]. In this plot, both the 14-3-3ζ dimer and the proC2:14-3-3ζ complex exhibited a bell-shaped profile, typical of a globular and rigid molecule with a maximum value of $(sR_g)^2I(s)/I(0)$ of 1.104 at $sR_g = 1.73$ (Fig. 1D). Conversely, the dimensionless Kratky plot of proC2 alone exhibits a higher maximum of 1.2 at $sR_g = 1.9$, thus indicating that the proC2 molecule has a greater flexibility than the complex.

Subsequently, we performed chemical cross-linking experiments using disuccinimidyl suberate (DSS) and disuccinimidyl glutarate (DSG) bifunctional agents to determine the distance restraints of the proC2:14-3-3ζ complex for structural modeling purposes. The intermolecular cross-links identified can be divided into three groups (Tables S1 and S2). The first group consists of cross-links connecting the N-terminal amino group of proC2 (Ser^{123}) to the loops between the helices H3-H4 (containing Lys^{68} and Lys^{75}) and H4-H5 (Lys^{138}) of 14-3-3ζ. The second group includes cross-links connecting Lys^{153} of proC2, located in the linker between the phosphorylation sites Ser^{139} and Ser^{164}, to the H3-H4 loop and to the helix H1 of 14-3-3ζ containing Lys^{68} and Lys^{11}, respectively. Cross-links from the last group connect Lys^{68} from the H3-H4 loop of 14-3-3ζ to either Lys^{372} or Lys^{381} located in the loop preceding the α6 helix of the proC2 p12 domain, thus indicating the proximity of this domain to the 14-3-3ζ surface.

The initial structural model of the complex was created using the crystal structures of 14-3-3ζ (PDB ID: IQJB) and caspase-2 (PDB ID: 3R7S) [36,37]. The two 14-3-3-binding motifs of caspase-2 are separated by 25 amino acid residues, similarly to the 14-3-3-binding motifs of yeast neutral trehalase Nth1, whose crystal

Table 1. Structural parameters determined from SAXS data.

	c (mg·mL^{-1})	c^a (μM)	R_g (Å)[b]	R_g (Å)[c]	D_{max} (Å)	V_p (nm^3)[d]	MM_{exp} (kDa)[e,f]	MM_{exp} (kDa)[g,f]
proC2	1.0	27	25.5 ± 1.6	26.7 ± 0.3	98	75	30	47
monomer	1.9	48	26.8 ± 1.7	27.6 ± 0.2	95	75	32	47
	3.7	96	32.2 ± 1.3	30.4 ± 0.1	93	80	41	50
14-3-3ζ	2.2	39	29.8 ± 1.7	30.1 ± 0.1	104	91	48	57
dimer	4.1	73	29.1 ± 0.9	29.6 ± 0.1	93	88	49	55
	8.1	144	27.3 ± 0.6	28.6 ± 0.1	81	79	47	49
Complex	1.7	18	32.9 ± 1.0	33.1 ± 0.1	119	152	83	95
proC2:14-3-3	3.6	38	33.3 ± 0.1	33.4 ± 0.1	115	155	81	97
(1 : 2)	6.6	70	33.5 ± 0.5	33.8 ± 0.1	119	162	84	101

[a] Molar concentration of the 14-3-3ζ dimer and the proC2(dp):14-3-3ζ complex with 1 : 2 molar stoichiometry. [b] Calculated using Guinier approximation. [c] Calculated using the program GNOM [56]. [d] The excluded volume of the hydrated particle (Porod volume). [e] Molecular weight was estimated by comparison of the forward scattering intensity $I(0)$ with that of the reference solution of bovine serum albumin. [f] The theoretical molecular weights of the proC2, 14-3-3ζ dimer and of the proC2(dp):14-3-3ζ complex (with 1 : 2 stoichiometry) are 38.2, 56 and 94.2 kDa, respectively. [g] Molecular weight was estimated from the Porod volume ($M_w = 0.625 \times V_p$).

structure in complex with 14-3-3 was recently reported by our group [38]. Therefore, the conformation of the proC2 N-terminal segment containing both 14-3-3-binding motifs and its interaction with the 14-3-3 dimer were modeled using the structure of the Nth1:14-3-3 complex (PDB ID: 5N6N). The Allos-Mod-FoXS method based on conformational sampling, combined with the rigid-body modeling of SAXS profiles and distance restrains assessed by intermolecular cross-links between 14-3-3ζ and the proC2 p12 domain, was used to calculate a structural model consistent with the experimental SAXS data [39]. The best-scoring model fitted the experimental SAXS data with χ^2 = 1.3 (Fig. 1F), and its theoretical R_g and D_{max} values of 33.1 Å and 123 Å, respectively, are consistent with the experimental values (Table 1). In this model, the proC2 p19 and p12 domains are positioned within the central channel of the 14-3-3 dimer and the α7 helix of the p12 domain interacts with the loop between helices H3 and H4 of 14-3-3ζ (Fig. 2A). The N-terminal segment of proC2 containing both 14-3-3-binding motifs and the NLS is located within the central channel of 14-3-3ζ, with the NLS region squeezed between the bottom of the 14-3-3 central channel and proC2 p12 domain helices α6 and α7. The positions of the proC2 p12 and p19 domains are apparently stabilized by interactions with the C-terminal H9 helices of both 14-3-3ζ protomers. The structural model of the proC2:14-3-3ζ complex is consistent with the *ab initio* molecular envelope calculated from the scattering data (Fig. 1E). The filtered averaged envelope of the complex shows a globular shape, and one side bulkier than the other. The superimposition shown in Fig. 1E suggests that the narrower part corresponds to the linker between the proC2 p19 and p12 domains. Projecting the cross-links identified (Tables S1 and S2) onto the structural model revealed that all observed cross-links are within the cross-linking distance limit for DSS and DSG (< 28 Å). The length of the spacer arm is 7.7 and 11.4 Å for DSG and DSS, respectively, thus adding 6.5 Å for each cross-linked lysine side-chain (20.7 and 24.4 Å) and allowing conformational dynamics (~ 30 Å) (Fig. 2B,C) [40].

14-3-3ζ proC2-binding surface mapping by NMR

We then performed a detailed analysis of the 14-3-3ζ proC2-binding surface by NMR spectroscopy. The previously published sequence-specific backbone assignment of 14-3-3ζΔC (protein construct missing the last C-terminal 12 amino acid residues) was used to analyze changes in 14-3-3ζ backbone amide signals [41]. NMR titration experiments revealed that numerous 14-3-3ζ residues showed either a change in signal intensity or a significant change in the NMR signal position upon proC2 addition (Figs 3 and 4), thus suggesting their involvement in the interaction or their conformational change induced by proC2 binding. The summary of chemical shift perturbations and intensity change analyses of the ^{1}H-^{15}N HSQC spectrum of 14-3-3ζΔC upon proC2 binding is shown in Fig. 4B. The most affected regions include not only segments from helices forming the ligand-binding groove (H3, H5, H7, and H9) but also helices H4, H8, and H6. These changes are consistent with the SAXS-based structural model which suggested that the p19 and p12 domains of proC2 are held within the 14-3-3ζ central channel through contacts with the C-terminal helix H9 (Fig. 1C). In addition, Fig. 4C analysis shows that the affected 14-3-3ζ residues are protruding from the inside of the dimer to the outer surface. We assume that the binding effect propagates to 14-3-3 protein residues with no direct interaction with proC2 due to allosteric structural changes, as previously shown for other proteins [30,42,43].

14-3-3 binding reduces the conformational flexibility of proC2 including the NLS region

To examine the 14-3-3-binding effect on the conformational behavior of proC2, we performed time-resolved tryptophan fluorescence intensity and anisotropy decay measurements. We prepared five single tryptophan containing proC2 mutants (Trp^{151}, Trp^{188}, Trp^{218}, Trp^{385}, Trp^{426}). However, the sequence of proC2 contains only one tryptophan residue at position Trp^{385}. Therefore, we prepared other mutants by mutating Trp^{385} to Phe and subsequently placing the tryptophan residue at the position of interest (mutations Y151W, F188W, F218W, and F426W). We assessed the stability of all mutants by measuring the midpoint temperatures of the protein-unfolding transition by differential scanning fluorimetry. No significant changes were observed, thus suggesting that the mutations introduced caused no change in the stability of the proC2 structure. This approach allowed us to monitor conformational changes in five different regions of proC2: Trp^{151} is located in the NLS region between the 14-3-3-binding motifs; Trp^{188} and Trp^{218} are located at the C terminus of helix α1 and the loop between the helix α2 and strand β1 of p19 domain, respectively; and Trp^{385} and Trp^{426} are located in the N terminus of helix α6 and the C-terminal segment of p12 domain, respectively (Figs 1A and 5A).

Then, we evaluated changes in the tryptophan environment induced by interaction with 14-3-3ζnoW

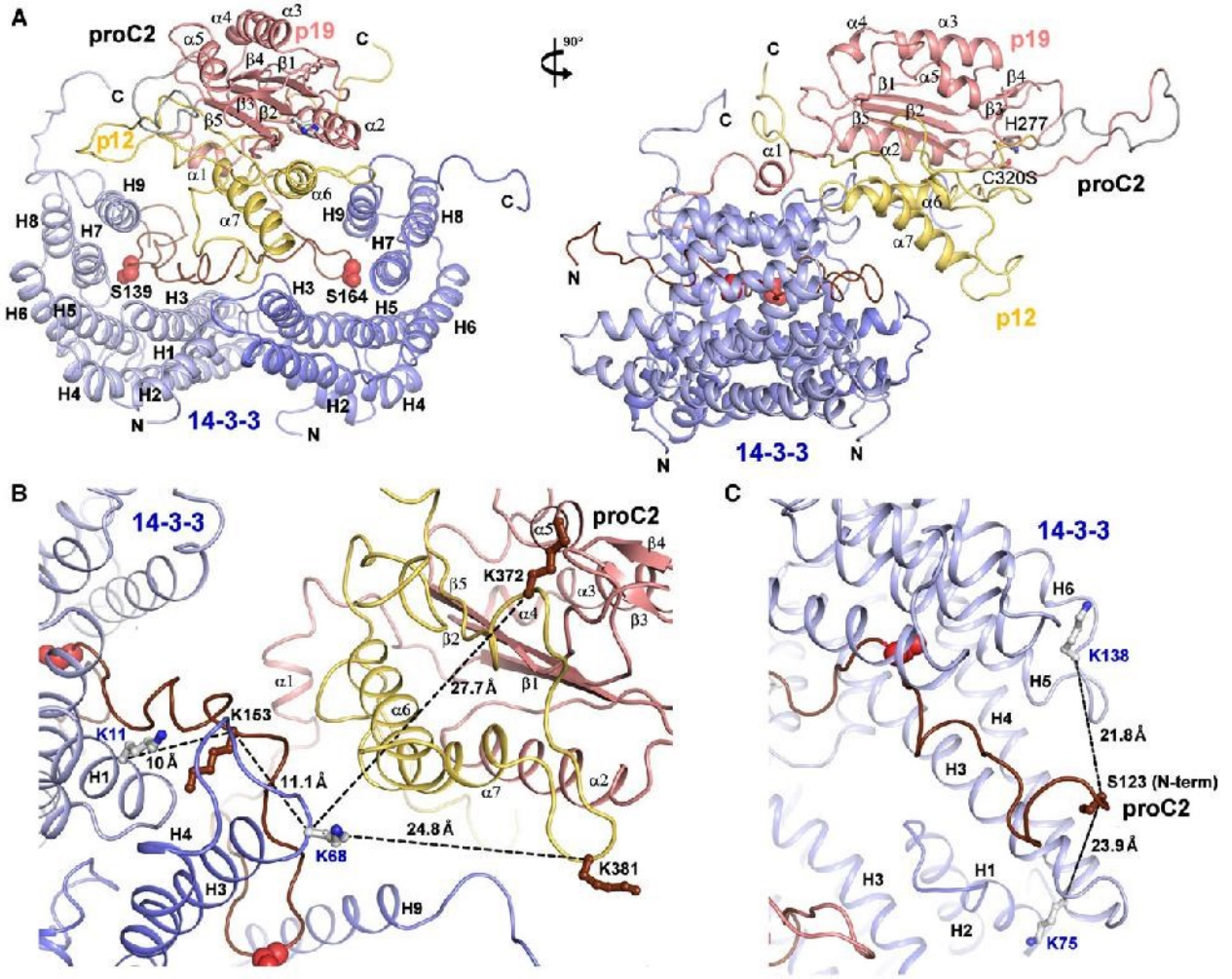

Fig. 2. SAXS-based structural modeling of the proC2:14-3-3ζ complex. (A) Best-scoring AllosMod-FoXS model of the proC2:14-3-3ζ complex shown in two perpendicular views. The N-terminal linker, the p19 and the p12 domains and phosphorylation sites are indicated in brown, salmon, yellow, and red spheres, respectively. The protomers of 14-3-3ζ are shown in blue. 14-3-3 helices are identified with capital letters, whereas proC2 helices and β-strands are identified with Greek letters. (B) Intermolecular cross-links connecting the NLS region of proC2 (Lys^{153}) to helices H1 and H3 of 14-3-3 (Lys^{11} and Lys^{68}); and the proC2 domain p12 (Lys^{372}, Lys^{381}) to the 14-3-3ζ helix H3 (Lys^{68}). Lysine residues of proC2 are shown in brown. (C) Cross-links between the N terminus of proC2 (Ser^{123}) and the 14-3-3ζ helix H4 and H5/H6 loop (Lys^{75}, Lys^{138}). Lysine residues of proC2 are shown in brown.

(fluorescently silent 14-3-3ζ containing W59F and W228F mutations) by time-resolved emission and fluorescence anisotropy decays. We have previously shown that these mutations have no effect on 14-3-3ζ-binding properties [44,45]. Because our single-tryptophan proC2 proteins exhibited complex multiexponential emission decays, we decided to use mean fluorescence lifetime (τ_{mean}) as a sensitive indicator reflecting changes in Trp microenvironment upon complex formation (Table 2 and Fig. 5B). A direct interaction between proC2 and 14-3-3ζnoW or a binding-induced conformational change of proC2 significantly increased the τ_{mean} of most mutants by approximately 0.4 ns. The only exception is the Trp^{188} mutant, which exhibits an unusually short lifetime, unresponsive to 14-3-3ζnoW binding. The increase in τ_{mean} likely resulted from the decrease in intramolecular quenching or from the increase in fluorophore shielding from solvent molecules in the presence of 14-3-3ζnoW.

The results from the time-resolved emission anisotropy experiments are summarized in Table 2. The hydrodynamic properties of all five proC2 mutants differ in the presence and absence of 14-3-3ζnoW. Three classes of correlation times were found. The first two include the fast Trp wobbling and the segmental motion reflected by the short correlation times ϕ_1 and

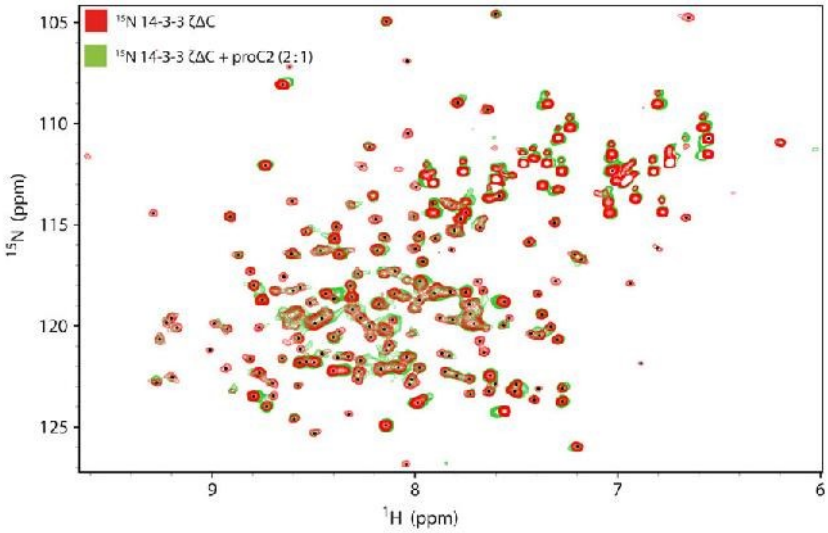

Fig. 3. proC2 binding-induced specific changes in the 2D ^{1}H-^{15}N HSQC NMR spectra of 14-3-3ζΔC. Comparison of the ^{1}H-^{15}N HSQC spectra of ^{15}N-labeled 14-3-3ζΔC recorded in the absence (red) or in the presence of a two-fold molar excess of unlabeled proC2 (green). The interaction changed the signal positions and intensity in the ^{1}H-^{15}N HSQC spectrum of 14-3-3ζΔC.

ϕ_2 located near 0.4 and 1.3–3.0 ns, respectively. The third class refers to the long correlation time ϕ_3, which can be assigned to the rotational motion of the whole molecule or molecular complex. Binding-induced changes in the rotational freedom of Trp within each mutant were assumed from the sum of $\beta_1 + \beta_2$, denoted as β_{FAST}, reflecting the overall amplitude of the fast motions. As shown in Fig. 5C and in Table 2, the Trp^{151} and Trp^{426} mutants exhibit a significantly lower β_{FAST} upon complex formation, which suggests rigidization of the Trp neighborhood upon 14-3-3ζnoW binding. The Trp mobility of the Trp^{188} mutant was also reduced in the complex. However, it should be noted that a rather short fluorescence lifetime prevents an accurate assessment of the long correlation times of this mutant. In contrast, Trp^{218} and Trp^{385} exhibited a rather rigid Trp microenvironment, which was only weakly modulated by the formation of the complex. Thus, these data suggested a decrease in the conformational flexibility of several regions of proC2, namely around Trp^{151} and Trp^{426}.

To further explore the 14-3-3-induced structural changes of proC2, we performed quenching experiments probing the fluorophore accessibility to acrylamide. The values of the bimolecular quenching constant k_q calculated from the Stern-Volmer plots are presented in Table S3 and compared in Fig. 5D. Trp^{151}, Trp^{218}, and Trp^{426} accessibility dramatically decreased by approximately 46% in the proC2:14-3-3ζnoW complex. Trp^{385} showed a smaller decrease (~ 32%), whereas Trp^{188} accessibility remained unchanged upon complex formation.

Together, these results suggested that the accessibility and mobility of Trp^{151} located in the NLS region and of Trp^{426} located in the C-terminal part of proC2 significantly decrease upon complex formation, thus corroborating the SAXS-based structural model in which these residues are opposite to each other on the interface between the two proteins (Fig. 5A). The behavior of Trp^{218}, located in the loop preceding the proC2 helix α2, exhibited an increase in both τ_{mean} and β_{FAST}, and a dramatic decrease in k_q upon the complex formation, likely resulting from improved shielding from the quencher upon complex formation. The Trp^{188} mutant behaves distinctly because neither its lifetime nor its accessibility to the quencher changes upon complex formation. However, after 14-3-3ζnoW binding, its motion virtually freezes. This is also consistent with the structural model proposed suggesting that this residue is located at the C terminus of the proC2 helix α1 located near the helix H9 of a 14-3-3ζ protomer.

14-3-3 protein binding protects proC2 from proteolytic degradation *in vitro*

Structural modeling together with chemical cross-linking and fluorescence spectroscopy data suggested that the 14-3-3ζ dimer extensively interacts with the whole proC2N-terminal linker region containing both 14-3-3-binding motifs and the NLS (Fig. 1A and Table 2, Tables S1 and S2). Therefore, complex formation presumably protects this region against proteolysis. To test this hypothesis, we performed limited proteolysis experiments. The results of protease digestion of proC2 alone and in complex with 14-3-3ζ by low levels of trypsin and chymotrypsin are presented in Fig. 6. Under the conditions used in this experiment, the proC2 alone was highly sensitive to proteolysis, and the cleavage resulted in the formation of a smaller fragment with an apparent M_w of 30 000 in both cases.

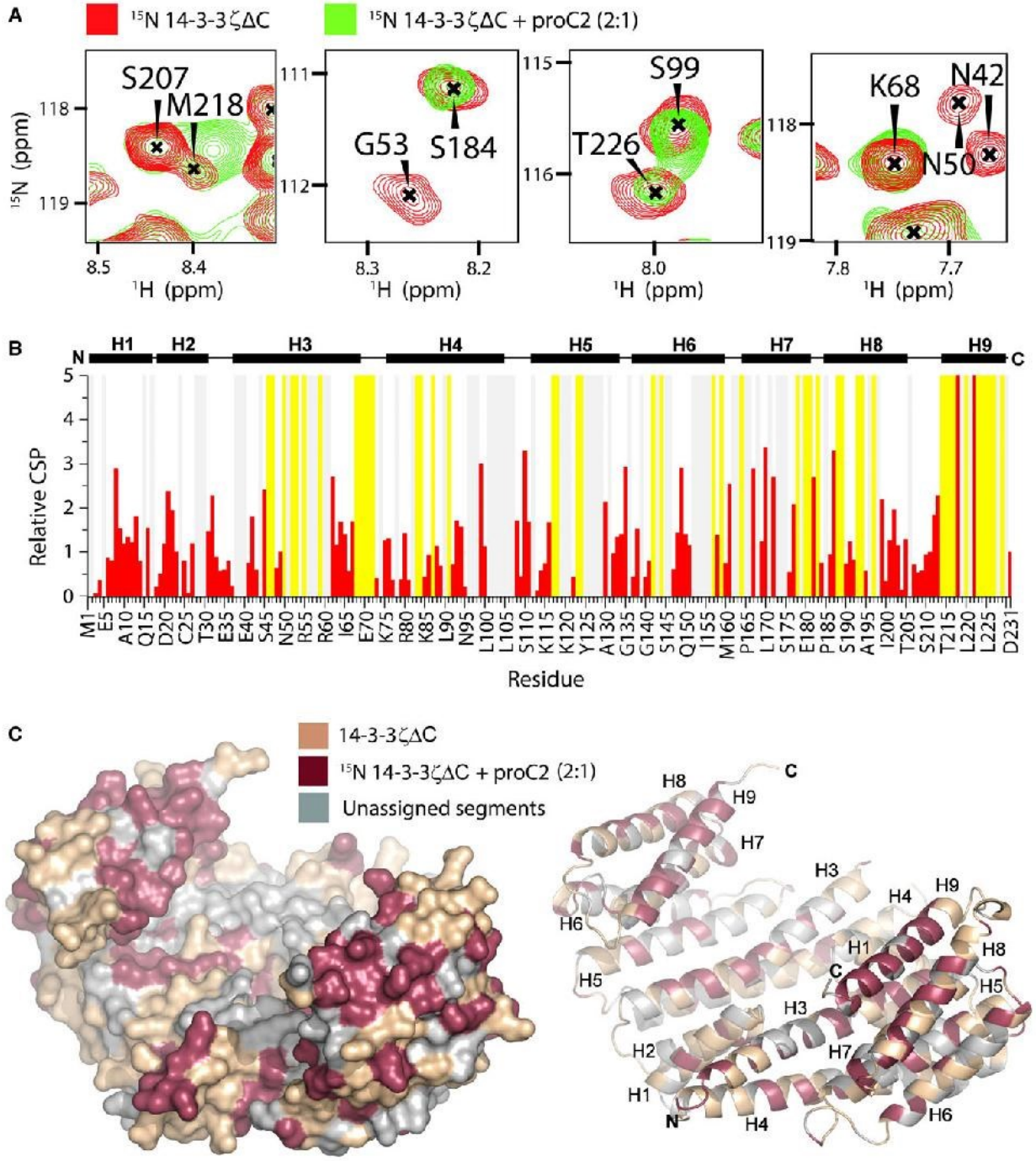

Fig. 4. Specific proC2 binding-induced changes in the NMR spectra of 14-3-3ζΔC. proC2 binding to 14-3-3ζ was evaluated by NMR titration of 150 μM of ^{15}N-labeled 14-3-3ζΔC with unlabeled proC2 to a final molar ratio 2 : 1. (A) Comparison of representative signals of free (red) and proC2-bound (green) 14-3-3ζΔC from the ^{1}H-^{15}N HSQC spectra. (B) The summary of chemical shift perturbations (CSPs) and intensity change analyses of the ^{1}H-^{15}N HSQC spectra of 14-3-3ζΔC upon proC2 binding. The relative CSPs were calculated as an averaged Euclidean chemical shift change: $d = \sqrt{\frac{1}{2}\left(\delta_H^2 + \frac{1}{5}\delta_N^2\right)}$, where δ_H and δ_N are the weighted average of shifts in the free and bound states for ^{1}H and ^{15}N, respectively [68]. The interaction induced both the change in positions (red bars) or a significant change in the intensities of the signals (yellow bars) in the ^{1}H-^{15}N HSQC spectrum of 14-3-3ζΔC. The regions of the protein backbone that could not be unambiguously assigned are highlighted in gray. The secondary structure elements of 14-3-3ζ are indicated at the top. (C) Range of the most significant CSPs and intensity changes mapped onto the 14-3-3ζ structure [36]. The 14-3-3ζ residues most affected by the proC2 binding are highlighted in dark red.

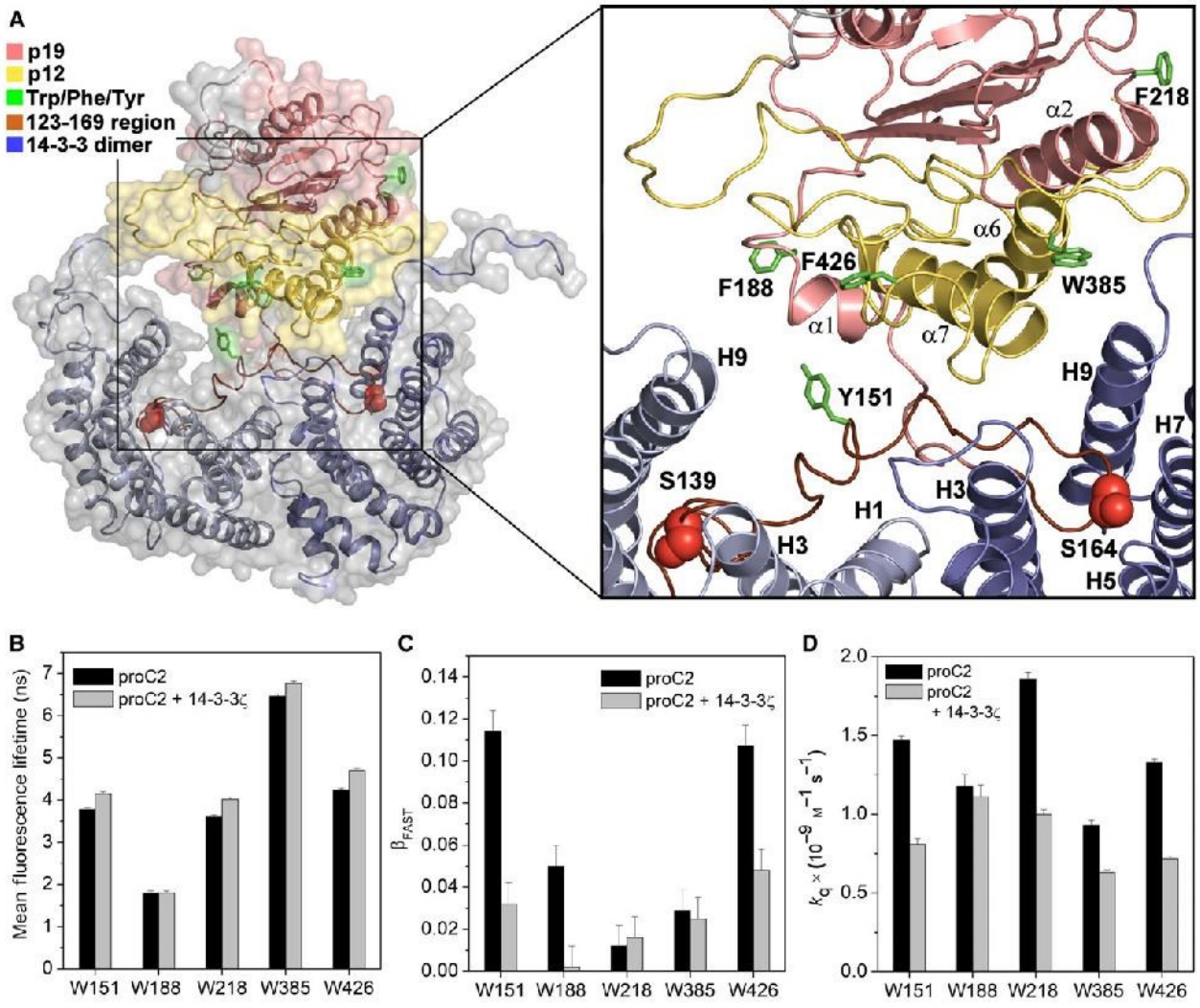

Fig. 5. Tryptophan fluorescence measurements of proC2 single Trp mutants and changes induced by the 14-3-3ζnoW protein binding to proC2. (A) Structural model of the proC2:14-3-3ζ complex. The N-terminal proC2 linker containing both 14-3-3 binding motifs is shown in brown; the p19 and the p12 domains and phosphorylation sites are shown in salmon, yellow, and red, respectively. The positions of the Tyr/Phe residues mutated to Trp residues are shown as green sticks. Time-resolved fluorescence measurements: (B) changes in mean fluorescence lifetimes in the absence and presence of 14-3-3ζnoW, (C) changes in amplitudes of Trp intramolecular mobility β_{FAST} in the absence and presence of 14-3-3ζnoW. (D) Steady-state fluorescence measurements: bimolecular quenching constant k_q from acrylamide quenching experiments in the absence and presence of 14-3-3ζnoW. Presented results are the means ± SD, $n = 3$.

The 14-3-3ζ protein was resistant to both proteases within the time course of this experiment, whereas the presence of 14-3-3ζ substantially slowed proC2 cleavage by both proteases. Mass spectrometry analysis of proC2 bands formed after 30 min of protease digestion by both trypsin and chymotrypsin revealed that the smaller fragment corresponds to the caspase-2 sequence 156-452 (the first identified peptide from the N-terminal part was peptide 156-161 phosphorylated at Ser^{164} with the m/z signal 692.29). The peptide containing the first phosphorylation site Ser^{139} (peptide 131–152 with the m/z signal 1965.95) was observed only in nonprotease-treated samples of proC2. These data indicate that the 14-3-3ζ masks the cleavage site located within the NLS region of proC2, thus corroborating the SAXS-based structural model of the complex.

Structural characterization of the 14-3-3-binding motifs of caspase-2

Previous studies have suggested that caspase-2 has two 14-3-3-binding motifs around pSer139 and pSer164 (Fig. 1A) [14,27,28]. Neither of these motifs is similar to canonical 14-3-3-binding motifs because they lack

Table 2. Summary of time-resolved tryptophan fluorescence measurements.

proC2 variant	τ_{mean} [a,b] (ns)	ϕ_1 [c] (ns)	β_1	ϕ_2 (ns)	β_2	ϕ_3 [d] (ns)	β_3	β_{inf} [e]	[f] $\beta_{FAST} = \beta_1 + \beta_2$
Trp^{151}	3.8	0.4	0.040	1.9	0.074	65	0.123		0.114
Trp^{151} + 14-3-3ζ [g]	4.2			1.5	0.032	20	0.069	0.136	0.032
Trp^{188}	1.8			3.0	0.050	28	0.187		0.050
Trp^{188} + 14-3-3ζ	1.8			2.5	0.002	20	0.217	0.018	0.002
Trp^{218}	3.6			1.8	0.012	21	0.188	0.037	0.012
Trp^{218} + 14-3-3ζ	4.0			1.2	0.016	65	0.221		0.016
Trp^{385}	6.5			1.3	0.029	18	0.153	0.055	0.029
Trp^{385} + 14-3-3ζ	6.8			2.0	0.025	26	0.087	0.125	0.025
Trp^{426}	4.2	0.5	0.039	2.8	0.068	42	0.130		0.107
Trp^{426} + 14-3-3ζ	4.7	0.5	0.013	2.1	0.035	65	0.189		0.048

[a] Mean lifetimes were calculated as $\tau_{mean} = \Sigma_i f_i \tau_i$, where f_i is an intensity fraction of the i-th lifetime component τ_i. [b] SD value is ± 0.05 ns. [c] Fluorescence anisotropies $r(t)$ were analyzed for a series of exponentials by a model-independent maximum entropy method without setting assumptions about the shape of the correlation time distributions, $r(t) = \Sigma_i \beta'_i \exp(-t/\phi'_i)$. The rotational correlation times, ϕ_i, and their amplitudes, β_i, represent the characteristics of the peaks in the corresponding distributions. [d] SD value is ± 5 ns. [e] Limiting anisotropy value of the longest correlation time related to the rotational diffusion of the whole protein or protein complex. Due to the short fluorescence lifetimes, the exact value of the correlation time was unresolved. [f] β_{FAST} represents the overall amplitude of fast molecular motions reflecting the rotational freedom of Trp within the molecule. Higher β_{FAST} indicates higher Trp mobility. [g] The human 14-3-3ζnoW protein mutant missing all Trp residues (mutations W59F and W228F) was used in all proC2 tryptophan measurements [44,45].

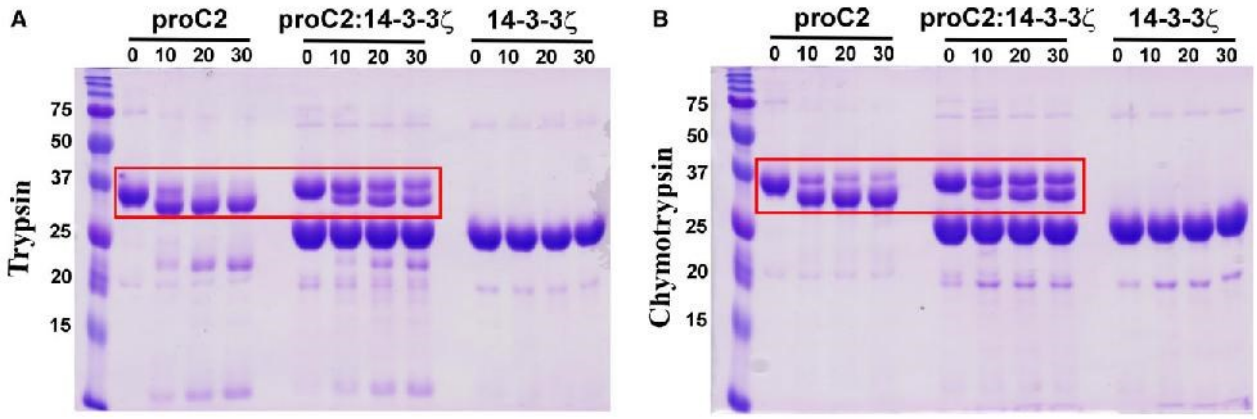

Fig. 6. Limited proteolysis of the proC2:14-3-3ζ complex. Limited proC2 proteolysis in the absence and in the presence of 14-3-3 digested with trypsin (A) and chymotrypsin (B) for 10, 20, and 30 min. The protease/proC2 ratio was 1 : 1000 (w/w). The reactions were stopped by boiling the samples with SDS/PAGE loading buffer at the times indicated before they were analyzed by SDS/PAGE. The resulting proC2 peptides were analyzed by MALDI-TOF-MS.

basic residues at positions -3 and -4 relative to the phosphorylated residue [36,46]. To elucidate the structural basis of interactions between 14-3-3 protein and the 14-3-3-binding motifs of caspase-2, we solved the crystal structures of phosphopeptides pepS139 (sequence YDLpSer^{139}LPFP) and pepS164 (sequence VEHpSer^{164}LDNK) with 14-3-3γΔC (ΔC denotes the missing ~15-residue-long flexible C-terminal tail). The 14-3-3γ isoform was selected based on crystal quality. The pepS139 and pepS164 phosphopeptide complex structures were determined at 2.6 and 2.8 Å resolution, respectively, with four 14-3-3 dimers with bound phosphopeptides in the asymmetric unit (Table 3). Both structures were solved by a molecular replacement with 14-3-3γ (PDB ID: 2B05) as search model. The final electron density allowed us to trace all eight residues of the pepS139 peptide in all eight 14-3-3γΔC protomers present in the asymmetric unit (Fig. 7A,B). In the case of pepS164, the electron density allowed us to build only six of eight peptides, and the longest traced peptide contained six residues. We were unable to trace the last two residues (Asn^{167} and Lys^{168}),

Table 3. Crystallographic data collection and refinement statistics.

Complex	14-3-3γΔC:pepS139	14-3-3γΔC:pepS164
Wavelength (Å)	0.9184	0.9184
Space group	P 41 21 2	P 41 21 2
Unit-cell parameters		
a, *b*, *c* (Å)	122.54, 122.54, 312.013	121.99, 121.99, 311.00
α, β, γ (°)	90.0, 90.0, 90.0	90.0, 90.0, 90.0
Asymmetric unit contents	Four dimers of 14-3-3γΔC with bound phosphopeptides	Four dimers of 14-3-3γΔC with bound phosphopeptides
Resolution range (Å)[a]	47.87–2.598 (2.691–2.598)	47.989–2.847 (2.949–2.847)
Unique reflections	74 062 (7245)	55 837 (5427)
Data multiplicity	26.7 (27.5)	26.5 (26.7)
Completeness (%)	99.83 (99.59)	99.79 (99.18)
$\langle I/\sigma(I)\rangle$	23.63 (2.17)	12.86 (1.49)
R_{meas}[b]	0.1318 (1.689)	0.3117 (2.578)
R_{work}	0.2416 (0.3075)	0.2312 (0.3314)
R_{free}	0.2881 (0.3553)	0.2868 (0.3922)
No. of protein atoms	1847	1830
No. of waters	114	0
Average B factors (Å^2)	64.94	57.23
Protein	65.01	57.23
Water	55.96	0
R.m.s.[c] deviations from ideal values		
Bond lengths (Å)	0.002	0.001
Bond angles (°)	0.37	0.33
Ramachandran favored (%)	98.69	98.77
Ramachandran allowed (%)	1.31	1.23
Ramachandran outliers (%)	0	0

[a] Values in parentheses are for the highest resolution shell. [b] $R_{meas} = \sum_{hkl}\{N(hkl)/[N(hkl)-1]\}^{1/2} \times \sum_i |I_i(hkl) - \langle I(hkl)\rangle| / \sum_{hkl}\sum_i I_i(hkl)$, where $I(hkl)$ is the intensity of reflection hkl, $\langle I(hkl)\rangle = \frac{1}{N(hkl)}\sum_i I_i(hkl)$, and $N(hkl)$ the multiplicity. [c] R.m.s., root mean square.

suggesting that these two residues are already disordered (Fig. 7C,D).

The recognition of the phosphate group, the main-chain conformation and other contacts in the 14-3-3-binding groove of both motifs are similar to those previously observed in other 14-3-3 protein complexes [25,36,38,47–49]. The pSer^{139} moiety of pepS139 is coordinated by the side-chains of the 14-3-3 residues Lys^{50}, Arg^{57}, Arg^{132}, and Tyr^{133}; other contacts include hydrogen bonds between the side-chains of the 14-3-3 residues Glu^{185}, Asn^{229}, and Asn^{178} and the main-chain atoms of the residues Tyr^{136}, Leu^{138}, and Leu^{140}, respectively (Fig. 7B). Very similar contacts were also observed in the case of the pepS164 peptide (Fig. 7D). The only differences are the presence of two intramolecular hydrogen bonds within the N-terminal half of the peptide and the contact between the side-chain of the 14-3-3 residue Lys^{50} and the main-chain carbonyl group of Leu^{165} of pepS164.

Discussion

Previous studies have shown that caspase-2 activation is inhibited by phosphorylation in a process involving interaction with the scaffolding 14-3-3 protein, which recognizes two 14-3-3-binding motifs within the linker between the CARD and the p19 domains of caspase-2 (Fig. 1) [14,26–28]. However, the inhibitory mechanism and the role of 14-3-3 in this process remain unresolved.

Caspase-2 is activated by proximity-induced dimerization after recruitment to specific high molecular weight protein complexes and trans-cleavage [4–7]. Caspase-2 dimerization has been previously shown to require both the CARD domain and residues from the C-terminal p12 domain [4]. The structural analysis of the complex between phosphorylated proC2 and 14-3-3ζ reported in this study suggested that most of the p12 domain surface is masked by 14-3-3ζ. In the model, the p12 domain faces the central channel of the 14-3-3ζ dimer, and its helix α7 interacts with the loop between 14-3-3ζ helices H3 and H4 and the proC2N-terminal linker, located at the bottom of the 14-3-3ζ dimer central channel (Fig. 2A). The proximity of the p12 domain to the 14-3-3ζ surface was confirmed by cross-linking experiments (Fig. 2B,C and Tables S1 and S2) and by fluorescence quenching measurements, which revealed that tryptophan residues Trp^{385} and

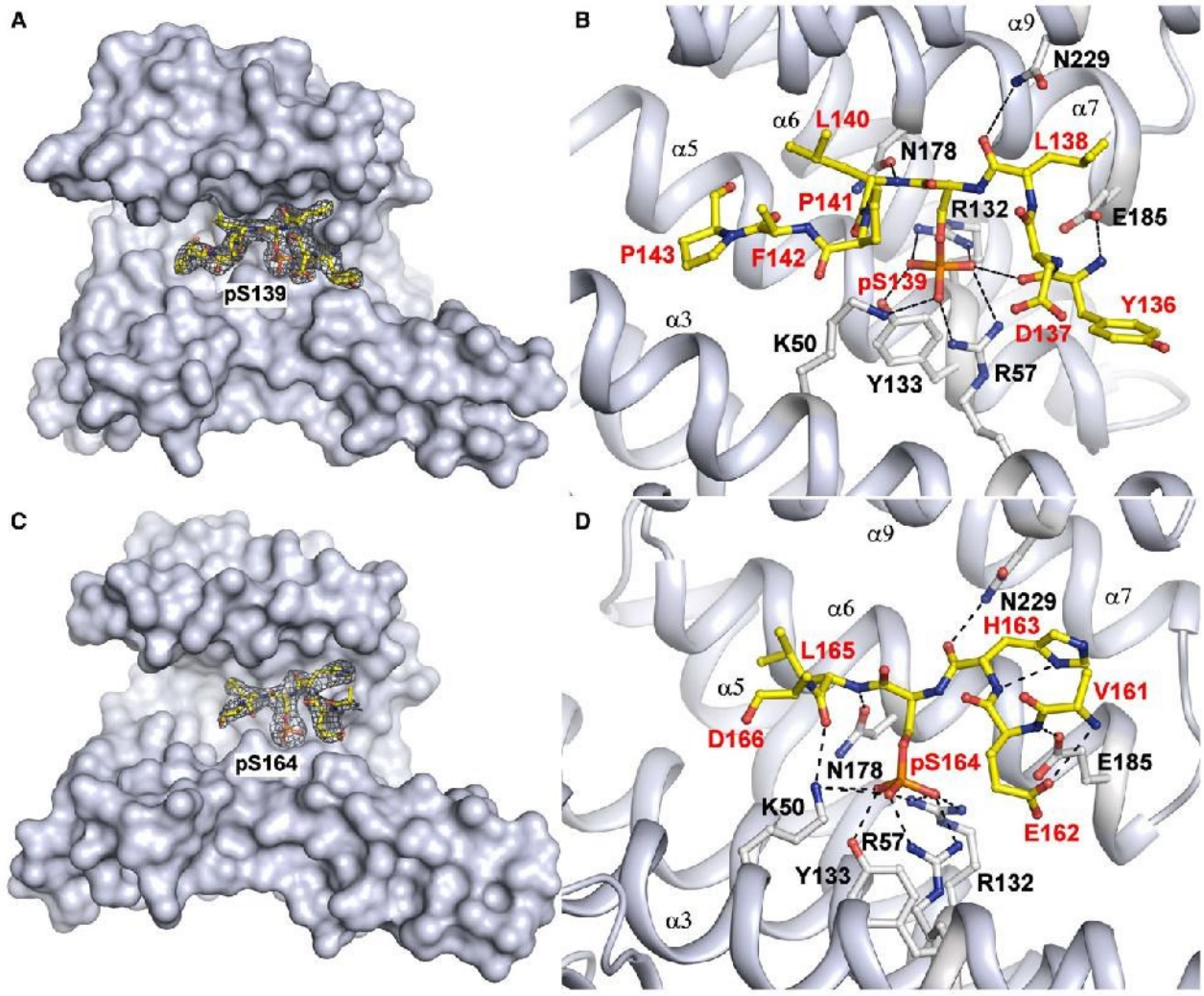

Fig. 7. Interactions between 14-3-3 and the 14-3-3-binding motifs of caspase-2. (A) Crystal structure of the 14-3-3γ:pepS139 complex. The $2F_o-F_c$ electron density map is contoured at 1σ. (B) Detailed view of contacts between 14-3-3γ and the pepS139 peptide. The caspase-2 residues are labeled in red, and the 14-3-3γ residues are labeled in black. (C) Crystal structure of the 14-3-3γ:pepS164 complex. The $2F_o-F_c$ electron density map is contoured at 1σ. (D) Detailed view of contacts between 14-3-3γ and the pepS164 peptide. The caspase-2 residues are labeled in red, and the 14-3-3γ residues are labeled in black.

Trp^{426}, both located within the p12 domain, are less exposed to the solvent upon complex formation (Fig. 5D). The proC2 construct used in this study (residues 123–452) did not include the N-terminal CARD domain (residues 32–121). However, because the linker between the CARD and the p19 domains containing both 14-3-3-binding motifs (residues 123–169) is buried within the central channel of the 14-3-3ζ dimer (Fig. 2A, shown in brown), the preceding CARD will likely be close to the 14-3-3ζ dimer surface also. Therefore, SAXS-based structural modeling together with chemical cross-linking and fluorescence data suggested that both regions required for caspase-2 dimerization are located close to the 14-3-3ζ surface, thus indicating that the 14-3-3 protein binding may prevent caspase-2 oligomerization and/or its binding to RAIDD.

Caspase-2 is the only known caspase that shuttles to the nucleus. The nuclear localization of caspase-2 zymogen is driven by the NLS, which is located between the 14-3-3-binding motifs within the linker connecting CARD and p19 domains [10–12]. 14-3-3 proteins are well-known regulators of the subcellular localization of their binding partners. Furthermore, because both 14-3-3-binding motifs and the NLS are located in the same region of caspase-2, 14-3-3 binding may play a role in the subcellular localization of caspase-2. However, such mode of regulation would likely require a direct interaction between 14-3-3 and NLS.

Our structural model of the proC2:14-3-3ζ complex suggested that the NLS region of caspase-2 is buried within the central channel of the 14-3-3 dimer constricted between the bottom of the channel and the p12 domain of proC2 (Fig. 2A). This position of NLS region on the interface between 14-3-3 and p12 was confirmed by chemical cross-linking experiments (Fig. 2B,C and Tables S1 and S2). In addition, fluorescence quenching and time-resolved fluorescence measurements of tryptophan residue inserted at position 151 within the NLS revealed a significant suppression of both its flexibility and solvent accessibility (Fig. 5C, D and Tables 2 and S3). Thus, these results indicated that the 14-3-3 protein binding masks the NLS region of caspase-2. However, whether this steric occlusion translates into the inhibition of caspase-2 nuclear localization *in vivo*, remains to be shown.

The SAXS-based structural analysis together with chemical cross-linking, NMR and fluorescence spectroscopy data revealed that phosphorylated proC2 and 14-3-3ζ form a compact and rigid complex in which the proC2 p19 and p12 domains are positioned within the central channel of the 14-3-3 dimer, where their position appears to be stabilized through interaction with the C-terminal helices H9 of both 14-3-3ζ protomers (Figs 1, 4 and 5). Compared with previously reported structures of 14-3-3 protein complexes, this architecture resembles the structures of complexes between 14-3-3ζ and serotonin N-acetyltransferase [50] and between 14-3-3ζ and the DNA-binding domain of the forkhead transcription factor FOXO4 [31] (Fig. 8). In addition, crystallographic analysis revealed that the phosphate group recognition, the main-chain conformation, and other contacts of both previously suggested 14-3-3-binding motifs of caspase-2 are similar to those observed in other 14-3-3 protein complexes [25,36,38,48,49]. Therefore, both phosphorylated motifs containing $pSer^{139}$ and $pSer^{164}$ are indeed the 14-3-3-binding motifs.

In conclusion, the structural analysis of the 14-3-3:caspase-2 complex reported in this study suggested that 14-3-3 protein binding may inhibit caspase-2 activation through interference with caspase-2 oligomerization and/or its nuclear localization by sterically occluding caspase-2 p12 domain as well as NLS, which is bordered by the two phosphorylated 14-3-3-binding motifs of caspase-2. Thus, these results corroborate the hypothesis that 14-3-3 binding is an important

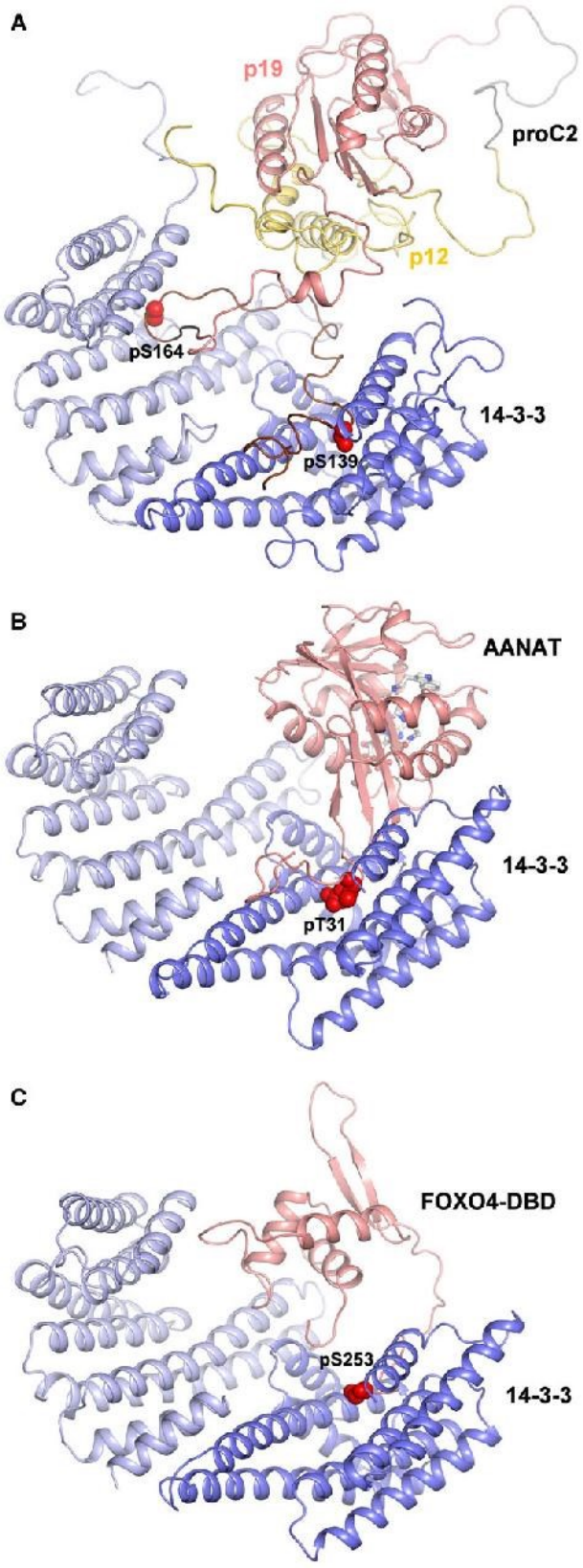

Fig. 8. Comparison of the structural model of the 14-3-3ζ:proC2 complex (A) with the crystal structure of the 14-3-3ζ:AANAT complex (B) [50] and with the model of the 14-3-3ζ:FOXO4-DBD complex (C) based on FRET experiments [31].

regulatory element of caspase-2 activation. Further research should be directed to study the effect of 14-3-3 on the caspase-2 dimerization and cellular localization *in vivo*.

Materials and methods

Heterologous expression, purification and phosphorylation of proC2

Human proC2 was expressed, purified and phosphorylated as previously described [28]. The mutants of proC2 containing a single-tryptophan residue (mutations Y151F, F188W, F218W, and F426W) were created using the QuikChange™ approach (Stratagene, San Diego, CA, USA). All mutations were confirmed by sequencing.

Heterologous expression and purification of 14-3-3 protein isoforms

The mutant version of human 14-3-3ζnoW with no tryptophan residues (mutations W59F and W228F) and 14-3-3ζΔC (residues 1–230) were prepared as previously described [44,50].

Crystallization, data collection, and structure determination

The 14-3-3γΔC and the pepS139 (sequence YDLpSer^{139}LPFP) or pepS164 (sequence VEHpSer^{164}LDNK) were mixed in a 1 : 10 M stoichiometry, respectively, in a buffer containing 20 mM HEPES (pH 7.0), 2 mM $MgCl_2$ and 2 mM TCEP. Crystallization was performed using the hanging-drop vapor-diffusion method at 293.15 K. Crystals of the 14-3-3γΔC:pepS139 peptide complex were grown from drops consisting of 3 μL of 8 mg·mL^{-1} protein and 3 μL of 100 mM Tris-HCl (pH 8.5), 32.5% (w/v) PEG 4000 and 200 mM sodium acetate. Crystals of the 14-3-3γΔC:pepS164 peptide complex were grown from drops consisting of 2 μL of 8 mg·mL^{-1} protein and 4 μL of 100 mM Tris-HCl (pH 8.5), 32.5% (w/v) PEG 4000, 200 mM lithium sulfate. Crystals were cryoprotected using 20% (v/v) PEG 400 and flash frozen in liquid nitrogen before data collection in oscillation mode at beamline 14.2 of the BESSY synchrotron. Diffraction data processing was performed using the packages XDS and XDSAPP [51,52]. Crystal structures of both complexes were solved by molecular replacement in MOLREP [53], using the structure 14-3-3γ (PDB ID: 2B05) as search models, and refined at resolutions of 2.6 and 2.85 Å, respectively, with PHENIX [54]. The atomic coordinates and structure factors of both complexes have been deposited in the RCSB PDB with accession codes 6GKF and 6GKG. All structural figures were prepared with PyMOL (https://pymol.org/2/).

Small angle X-ray scattering (SAXS)

SAXS data were collected on the European Molecular Biology Laboratory (EMBL) P12 beamline on the storage ring PETRA III (Deutsches Elektronen Synchrotron (DESY), Hamburg, Germany). The proC2 and 14-3-3ζ were measured in the concentration ranges of 0.5–3.7 and 1.2-8.1 mg·mL^{-1}, respectively. ProC2:14-3-3ζ protein complex was measured in the concentration range of 0.9–6.6 mg·mL^{-1} in a buffer containing 20 mM Tris-HCl (pH 7.5), 150 mM NaCl, 1 mM TCEP, 3% (w/v) glycerol. Data analysis was performed using the ATSAS software suite (ATSAS software, EMBL, Hamburg, Germany). The data were averaged after normalization to the intensity of the transmitted beam, and the scattering of the buffer was subtracted using PRIMUS [55]. The forward scattering $I(0)$ and the radius of gyration R_g were evaluated using the Guinier approximation. The distance distribution function $P(r)$ and the maximum particle dimension D_{max} were determined by the indirect Fourier transformation of the scattering data I(s) using GNOM [56]. The solute apparent molecular mass (MM_{exp}) was estimated by comparing the forward scattering with that from reference solutions of bovine serum albumin (molecular mass 72 kDa). The Porod volume, V_p (excluded volume of the hydrated particle), *ab initio* molecular envelopes were computed using DAMMIF. For each protein, 20 surfaces were generated and averaged using DAMAVER [57]. The averaged surfaces were then used as the final SAXS three-dimensional structure. Calculated molecular envelopes were superimposed to the structural models using the SUPCOMB program EMBL, Hamburg, Germany.

Structural modeling

The three-dimensional model of proC2 (residues 123–452) was generated using the AllosMod-FoXS method, SAXS data, and distance restrains calculated by intermolecular cross-links between 14-3-3ζ and the proC2 p12 domain [58]. For proC2 (123–452) modeling, the crystal structure of caspase-2 was used (PDB ID: 3R7S). The starting model of the complex was prepared using the crystal structure of caspase-2 and the 14-3-3ζ with phosphopeptides (PDB ID: 1QJB). The conformation of the proC2N-terminal segment containing both 14-3-3-binding motifs and its interaction with the 14-3-3 dimer were modeled using the structure of the Nth1:14-3-3 complex (PDB ID: 5N6N). The best-scoring AllosMod model was chosen according to the lowest χ^2 and the distances derived from intermolecular cross-links.

NMR spectroscopy

NMR spectra were acquired at 298 K on a Bruker Avance III™ HD 850 MHz spectrometer equipped with a $^{1}H/^{13}C/^{15}N$ cryoprobe. For NMR experiments, ^{15}N-labeled

14-3-3ζΔC was expressed in enriched minimal medium containing ^{15}N-ammonium sulfate. The sample volume was 160 μL of 150 μM ^{15}N-labeled 14-3-3ζΔC in the NMR buffer containing 50 mM sodium phosphate at pH 6.8, 100 mM NaCl and 10% D_2O/90% H_2O. One hundred and sixty out of 245 (65%) backbone amide signals in the 2D ^{1}H-^{15}N HSQC spectrum of 14-3-3ζΔC were assigned based on published sequence-specific backbone NMR assignment [41]. The binding of proC2 was evaluated by NMR titrations of 150 μM ^{15}N-labeled 14-3-3ζΔC with unlabeled proC2. A reference and four titration points were collected in 2 : 0.25, 2 : 0.5, 2 : 0.75, and 2 : 1 (14-3-3ζΔC:proC2) molar ratios. ^{1}H-^{15}N HSQC spectra were acquired at experimental times ranging from 90 min (16 scans, initial concentration) to 24 h (256 scans, final concentration).

Differential scanning fluorimetry

Thermofluor assay was performed using real-time PCR LightCycler 480 II (Roche, Basel, Switzerland) at a final protein concentration of 1 mg·mL^{-1}, as previously described [59].

Chemical cross-linking combined with mass spectrometry

ProC2 in the complex with 14-3-3ζ was cross-linked using DSS and DSG cross-linkers, and they were analyzed as described previously [40,60]. For cross-linking, all proteins were transferred to 20 mM HEPES (pH 7.5) buffer with 150 mM NaCl and 1 mM TCEP, assessing the following protein concentrations: 0.37 mg·mL^{-1} proC2(dp) and 0.53 mg·mL^{-1}14-3-3ζ. Eluting peptides were separated at 60 °C on a reversed-phase analytical Acclaim PepMap™ 100, C18 column (0.075 × 150 mm, 3 μm; Thermo Fisher Scientific, Waltham, MA, USA) UltiMate3000 RSLCnano System (Dionex, Sunnyvale, California, USA). The nano-UHPLC system was coupled to the CaptiveSpray ion source of a SolariX XR FT-ICR mass spectrometer (Bruker Daltonics, Billerica, Massachusetts, USA) equipped with a 12-T superconducting magnet. Data were acquired in positive broadband mode over the m/z range 245–2000, with 1M data points transient and 0.4 s ion accumulation and four scans were accumulated per spectrum. Data acquisition was performed using SOLARIX CONTROL program, Bruker Daltonics, Billerica, MA, USA.

Limited proteolysis and mass spectrometric analysis of proC2

Samples containing 11.8 μg of proC2 or 25.4 μg 14-3-3ζ and the proC2:14-3-3ζ complex were digested by trypsin or chymotrypsin for 10, 20, and 30 min at 25 °C in a buffer containing 20 mM Tris-HCl (pH 7.5), 150 mM NaCl, 1 mM TCEP, 10% (w/v) glycerol (protease/protein ratio was 1 : 1000, w/w). Undigested protein was used as a zero time point. The reactions were terminated by boiling in the presence of SDS/PAGE loading buffer. Protein bands were cut off the gel and destained. Cysteines were in gel reduced with 100 mM DTT for 45 min at 60 °C, and free cysteines were alkylated with 100 mM iodoacetamide for 30 min at room temperature in the dark. Trypsin digestion proceeded overnight at 37 °C. Extracted peptides were analyzed by MALDI-FT-ICR mass spectrometer (Bruker Daltonics). Data were processed by MMASS software [61].

Time-resolved fluorescence and tryptophan quenching

Time-resolved fluorescence intensity, fluorescence anisotropy, and tryptophan fluorescence quenching experiments were performed and analyzed as previously described [62–64]. For time-resolved measurements, tryptophan fluorescence was excited, at 298 nm, using a frequency-tripled Ti:saphire laser, and the emission was detected at 355 nm using monochromator with a stack of UG1 and BG40 glass filters placed in the front of input slit. Decays were accumulated in 1024 channels with a time resolution of 78 ps/channel, until typically 10^7 counts per decay were reached. Steady-state fluorescence quenching experiments were performed in a ISS PC1 photon counting fluorimeter, using a 1-nm bandpass on both excitation and emission monochromators. Stern-Volmer plots were constructed from changes in fluorescence intensity after adding acrylamide aliquots dissolved in the protein buffer. Trp emission was excited and measured at 297 and 340 nm, respectively; data were fitted and fitted with Eqn (1):

$$\frac{I_0}{I} = 1 + k_q \tau_{mean}[Q] e^{V[Q]}, \quad (1)$$

where I_0 and I is the fluorescence intensity in the absence and presence of quencher, respectively, $[Q]$ is acrylamide concentration; k_q is the bimolecular quenching constant, τ_{mean} denotes the mean fluorescence lifetime in the absence of quencher, and V is the static quenching constant. τ_{mean} was calculated as $\tau_{mean} = \Sigma_i f_i \tau_i$, where f_i is an intensity fraction of the i-th lifetime component τ_i. Corrections for the inner filter effect were performed as previously described [65]:

$$I_c = I \,\text{antilog}\left(\frac{A_{ex} + A_{em}}{2}\right), \quad (2)$$

where I_c is the corrected fluorescence intensity; I is the measured fluorescence intensity, and A_{ex} and A_{em} are sample absorbances at the excitation and emission wavelength, respectively.

All fluorescence experiments were performed at 23 °C in buffer containing 20 mM Tris (pH 7.5), 150 mM NaCl, 1 mM TCEP-HCl and 10% (w/v) glycerol (Sigma-Aldrich, St. Louis, MO, USA). The concentrations proC2 and 14-3-3ζnoW were 15 and 40 μM, respectively.

Acknowledgments

We thank EMBL SAXS beamline P12 (Petra III DESY, Hamburg) for the allocated experimental beam time. We thank Prof Jaroslav Vecer for the help with tryptophan fluorescence data analysis, Dr Vaclav Veverka with NMR analysis, Dr Petr Pompach with mass spectrometry analysis and Dr Petr Novak with cross-linking analyses, as well as Dr Carlos V. Melo for proofreading the article.

Funding

This study was funded by the Czech Science Foundation (VO, grant number 17-00726S), the Grant Agency of Charles University (DK, grant number 296216), the Czech Academy of Sciences (RVO:67985823 of the Institute of Physiology), project BIOCEV (CZ.1.05/1.1.00.02.0109) and MEYS CR (LM2015043 CIISB, Biocev, Biophysical methods, Structural Mass Spectrometry). PH acknowledges EU Operational Program OP VaVpI No. CZ.1.05/4.1.00/16.0340 and Center of Nano- and Bio-Photonics UNCE/SCI/010.

Author contributions

VO and TO designed research; AS, MA, DK, KP, MR, PH, and VO performed research; AS, KP, MR, PH, TO, and VO analyzed data; and TO and VO wrote the paper.

Conflict of interests

The authors declare that they have no competing interests.

References

1 Puccini J, Dorstyn L & Kumar S (2013) Caspase-2 as a tumour suppressor. *Cell Death Differ* **20**, 1133– 1139.
2 Panaretakis T, Laane E, Pokrovskaja K, Bjorklund AC, Moustakas A, Zhivotovsky B, Heyman M, Shoshan MC & Grander D (2005) Doxorubicin requires the sequential activation of caspase-2, protein kinase Cdelta, and c-Jun NH2-terminal kinase to induce apoptosis. *Mol Biol Cell* **16**, 3821–3831.
3 Hermel E, Gafni J, Propp SS, Leavitt BR, Wellington CL, Young JE, Hackam AS, Logvinova AV, Peel AL, Chen SF *et al.* (2004) Specific caspase interactions and amplification are involved in selective neuronal vulnerability in Huntington's disease. *Cell Death Differ* **11**, 424–438.
4 Butt AJ, Harvey NL, Parasivam G & Kumar S (1998) Dimerization and autoprocessing of the Nedd2 (caspase-2) precursor requires both the prodomain and the carboxyl-terminal regions. *J Biol Chem* **273**, 6763–6768.
5 Read SH, Baliga BC, Ekert PG, Vaux DL & Kumar S (2002) A novel Apaf-1-independent putative caspase-2 activation complex. *J Cell Biol* **159**, 739–745.
6 Muzio M, Stockwell BR, Stennicke HR, Salvesen GS & Dixit VM (1998) An induced proximity model for caspase-8 activation. *J Biol Chem* **273**, 2926–2930.
7 Baliga BC, Read SH & Kumar S (2004) The biochemical mechanism of caspase-2 activation. *Cell Death Differ* **11**, 1234–1241.
8 Garcia-Calvo M, Peterson EP, Rasper DM, Vaillancourt JP, Zamboni R, Nicholson DW & Thornberry NA (1999) Purification and catalytic properties of human caspase family members. *Cell Death Differ* **6**, 362–369.
9 Tinel A & Tschopp J (2004) The PIDDosome, a protein complex implicated in activation of caspase-2 in response to genotoxic stress. *Science* **304**, 843–846.
10 Mancini M, Machamer CE, Roy S, Nicholson DW, Thornberry NA, Casciola-Rosen LA & Rosen A (2000) Caspase-2 is localized at the Golgi complex and cleaves golgin-160 during apoptosis. *J Cell Biol* **149**, 603–612.
11 O'Reilly LA, Ekert P, Harvey N, Marsden V, Cullen L, Vaux DL, Hacker G, Magnusson C, Pakusch M, Cecconi F *et al.* (2002) Caspase-2 is not required for thymocyte or neuronal apoptosis even though cleavage of caspase-2 is dependent on both Apaf-1 and caspase-9. *Cell Death Differ* **9**, 832–841.
12 Baliga BC, Colussi PA, Read SH, Dias MM, Jans DA & Kumar S (2003) Role of prodomain in importin-mediated nuclear localization and activation of caspase-2. *J Biol Chem* **278**, 4899–4905.
13 Ando K, Parsons MJ, Shah RB, Charendoff CI, Paris SL, Liu PH, Fassio SR, Rohrman BA, Thompson R, Oberst A *et al.* (2017) NPM1 directs PIDDosome-dependent caspase-2 activation in the nucleolus. *J Cell Biol* **216**, 1795–1810.
14 Nutt LK, Buchakjian MR, Gan E, Darbandi R, Yoon SY, Wu JQ, Miyamoto YJ, Gibbons JA, Andersen JL, Freel CD *et al.* (2009) Metabolic control of oocyte apoptosis mediated by 14-3-3zeta-regulated dephosphorylation of caspase-2. *Dev Cell* **16**, 856–866.
15 Andersen JL, Johnson CE, Freel CD, Parrish AB, Day JL, Buchakjian MR, Nutt LK, Thompson JW, Moseley MA & Kornbluth S (2009) Restraint of apoptosis during mitosis through interdomain phosphorylation of caspase-2. *EMBO J* **28**, 3216–3227.
16 Morrison DK (2009) The 14-3-3 proteins: integrators of diverse signaling cues that impact cell fate and cancer development. *Trends Cell Biol* **19**, 16–23.
17 Hermeking H & Benzinger A (2006) 14-3-3 proteins in cell cycle regulation. *Semin Cancer Biol* **16**, 183–192.

18 Sluchanko NN & Gusev NB (2017) Moonlighting chaperone-like activity of the universal regulatory 14-3-3 proteins. *FEBS J* **284**, 1279–1295.
19 Mackintosh C (2004) Dynamic interactions between 14-3-3 proteins and phosphoproteins regulate diverse cellular processes. *Biochem J* **381**, 329–342.
20 Madeira F, Tinti M, Murugesan G, Berrett E, Stafford M, Toth R, Cole C, MacKintosh C & Barton GJ (2015) 14-3-3-Pred: improved methods to predict 14-3-3-binding phosphopeptides. *Bioinformatics* **31**, 2276–2283.
21 Johnson C, Crowther S, Stafford MJ, Campbell DG, Toth R & MacKintosh C (2010) Bioinformatic and experimental survey of 14-3-3-binding sites. *Biochem J* **427**, 69–78.
22 Tsuruta F, Sunayama J, Mori Y, Hattori S, Shimizu S, Tsujimoto Y, Yoshioka K, Masuyama N & Gotoh Y (2004) JNK promotes Bax translocation to mitochondria through phosphorylation of 14-3-3 proteins. *EMBO J* **23**, 1889–1899.
23 Pendergast AM (2005) Stress and death: breaking up the c-Abl/14-3-3 complex in apoptosis. *Nat Cell Biol* **7**, 213–214.
24 Yaffe MB (2002) How do 14-3-3 proteins work?–Gatekeeper phosphorylation and the molecular anvil hypothesis. *FEBS Lett* **513**, 53–57.
25 Molzan M & Ottmann C (2012) Synergistic binding of the phosphorylated S233- and S259-binding sites of C-RAF to one 14-3-3zeta dimer. *J Mol Biol* **423**, 486–495.
26 Ren K, Lu J, Porollo A & Du C (2012) Tumor-suppressing function of caspase-2 requires catalytic site Cys-320 and site Ser-139 in mice. *J Biol Chem* **287**, 14792–14802.
27 Tinti M, Madeira F, Murugesan G, Hoxhaj G, Toth R & Mackintosh C (2014) ANIA: ANnotation and Integrated Analysis of the 14-3-3 interactome. *Database (Oxford)* **2014**, bat085.
28 Kalabova D, Smidova A, Petrvalska O, Alblova M, Kosek D, Man P, Obsil T & Obsilova V (2017) Human procaspase-2 phosphorylation at both S139 and S164 is required for 14-3-3 binding. *Biochem Biophys Res Comm* **493**, 940–945.
29 Sluchanko NN, Tugaeva KV & Maksimov EG (2017) Solution structure of human steroidogenic acute regulatory protein STARD1 studied by small-angle X-ray scattering. *Biochem Biophys Res Comm* **489**, 445–450.
30 Milroy LG, Bartel M, Henen MA, Leysen S, Adriaans JM, Brunsveld L, Landrieu I & Ottmann C (2015) Stabilizer-guided inhibition of protein-protein interactions. *Angew Chem Int Ed Engl* **54**, 15720–15724.
31 Silhan J, Vacha P, Strnadova P, Vecer J, Herman P, Sulc M, Teisinger J, Obsilova V & Obsil T (2009) 14-3-3 protein masks the DNA binding interface of forkhead transcription factor FOXO4. *J Biol Chem* **284**, 19349–19360.
32 Rezabkova L, Man P, Novak P, Herman P, Vecer J, Obsilova V & Obsil T (2011) Structural basis for the 14-3-3 protein-dependent inhibition of the regulator of G protein signaling 3 (RGS3) function. *J Biol Chem* **286**, 43527–43536.
33 Kacirova M, Novacek J, Man P, Obsilova V & Obsil T (2017) Structural basis for the 14-3-3 protein-dependent inhibition of phosducin function. *Biophys J* **112**, 1339–1349.
34 Petrvalska O, Kosek D, Kukacka Z, Tosner Z, Man P, Vecer J, Herman P, Obsilova V & Obsil T (2016) Structural insight into the 14-3-3 protein-dependent inhibition of protein kinase ASK1 (Apoptosis Signal-regulating kinase 1). *J Biol Chem* **291**, 20753–20765.
35 Receveur-Brechot V & Durand D (2012) How random are intrinsically disordered proteins? A small angle scattering perspective. *Curr Protein Pept Sci* **13**, 55–75.
36 Rittinger K, Budman J, Xu J, Volinia S, Cantley LC, Smerdon SJ, Gamblin SJ & Yaffe MB (1999) Structural analysis of 14-3-3 phosphopeptide complexes identifies a dual role for the nuclear export signal of 14-3-3 in ligand binding. *Mol Cell* **4**, 153–166.
37 Tang Y, Wells JA & Arkin MR (2011) Structural and enzymatic insights into caspase-2 protein substrate recognition and catalysis. *J Biol Chem* **286**, 34147–34154.
38 Alblova M, Smidova A, Docekal V, Vesely J, Herman P, Obsilova V & Obsil T (2017) Molecular basis of the 14-3-3 protein-dependent activation of yeast neutral trehalase Nth1. *Proc Natl Acad Sci USA* **114**, E9811–E9820.
39 Weinkam P, Pons J & Sali A (2012) Structure-based model of allostery predicts coupling between distant sites. *Proc Natl Acad Sci USA* **109**, 4875–4880.
40 Young MM, Tang N, Hempel JC, Oshiro CM, Taylor EW, Kuntz ID, Gibson BW & Dollinger G (2000) High throughput protein fold identification by using experimental constraints derived from intramolecular cross-links and mass spectrometry. *Proc Natl Acad Sci USA* **97**, 5802–5806.
41 Killoran RC, Fan J, Yang D, Shilton BH & Choy WY (2015) Structural analysis of the 14-3-3zeta/Chibby interaction involved in Wnt/beta-catenin signaling. *PLoS One* **10**, e0123934.
42 Skerlova J, Kral V, Kachala M, Fabry M, Bumba L, Svergun DI, Tosner Z, Veverka V & Rezacova P (2015) Molecular mechanism for the action of the anti-CD44 monoclonal antibody MEM-85. *J Struct Biol* **191**, 214–223.
43 Tesina P, Cermakova K, Horejsi M, Prochazkova K, Fabry M, Sharma S, Christ F, Demeulemeester J, Debyser Z, De Rijck J *et al.* (2015) Multiple cellular proteins interact with LEDGF/p75 through a conserved unstructured consensus motif. *Nat Commun* **6**, 7968.

44 Obsilova V, Herman P, Vecer J, Sulc M, Teisinger J & Obsil T (2004) 14-3-3zeta C-terminal stretch changes its conformation upon ligand binding and phosphorylation at Thr232. *J Biol Chem* **279**, 4531–4540.
45 Silhan J, Obsilova V, Vecer J, Herman P, Sulc M, Teisinger J & Obsil T (2004) 14-3-3 protein C-terminal stretch occupies ligand binding groove and is displaced by phosphopeptide binding. *J Biol Chem* **279**, 49113–49119.
46 Yaffe MB, Rittinger K, Volinia S, Caron PR, Aitken A, Leffers H, Gamblin SJ, Smerdon SJ & Cantley LC (1997) The structural basis for 14-3-3:phosphopeptide binding specificity. *Cell* **91**, 961–971.
47 Ottmann C, Marco S, Jaspert N, Marcon C, Schauer N, Weyand M, Vandermeeren C, Duby G, Boutry M, Wittinghofer A *et al.* (2007) Structure of a 14-3-3 coordinated hexamer of the plant plasma membrane H+ -ATPase by combining X-ray crystallography and electron cryomicroscopy. *Mol Cell* **25**, 427–440.
48 Rose R, Rose M & Ottmann C (2012) Identification and structural characterization of two 14-3-3 binding sites in the human peptidylarginine deiminase type VI. *J Struct Biol* **180**, 65–72.
49 Sluchanko NN, Beelen S, Kulikova AA, Weeks SD, Antson AA, Gusev NB & Strelkov SV (2017) Structural basis for the interaction of a human small heat shock protein with the 14-3-3 universal signaling regulator. *Structure* **25**, 305–316.
50 Obsil T, Ghirlando R, Klein DC, Ganguly S & Dyda F (2001) Crystal structure of the 14-3-3zeta:serotonin N-acetyltransferase complex. a role for scaffolding in enzyme regulation. *Cell* **105**, 257–267.
51 Kabsch W (2010) XDS. *Acta Crystallogr D* **66**, 125–132.
52 Sparta KM, Krug M, Heinemann U, Mueller U & Weiss MS (2016) XDSAPP2.0. *J Appl Crystallogr* **49**, 1085–1092.
53 Vagin A & Teplyakov A (1997) MOLREP: an automated program for molecular replacement. *J Appl Crystallogr* **30**, 1022–1025.
54 Adams PD, Afonine PV, Bunkoczi G, Chen VB, Davis IW, Echols N, Headd JJ, Hung LW, Kapral GJ, Grosse-Kunstleve RW *et al.* (2010) PHENIX: a comprehensive Python-based system for macromolecular structure solution. *Acta Crystallogr D* **66**, 213–221.
55 Konarev PV, Volkov VV, Sokolova AV, Koch MHJ & Svergun DI (2003) PRIMUS: a Windows PC-based system for small-angle scattering data analysis. *J Appl Crystallogr* **36**, 1277–1282.
56 Svergun DI (1992) Determination of the regularization parameter in indirect-transform methods using perceptual criteria. *J Appl Crystallogr* **25**, 495–503.
57 Volkov VV & Svergun DI (2003) Uniqueness of ab initio shape determination in small-angle scattering. *J Appl Crystallogr* **36**, 860–864.
58 Schneidman-Duhovny D, Hammel M & Sali A (2010) FoXS: a web server for rapid computation and fitting of SAXS profiles. *Nucleic Acids Res* **38**, W540–W544.
59 Niesen FH, Berglund H & Vedadi M (2007) The use of differential scanning fluorimetry to detect ligand interactions that promote protein stability. *Nat Protoc* **2**, 2212–2221.
60 Kopecka M, Kosek D, Kukacka Z, Rezabkova L, Man P, Novak P, Obsil T & Obsilova V (2014) Role of the EF-hand-like motif in the 14-3-3 protein-mediated activation of yeast neutral trehalase Nth1. *J Biol Chem* **289**, 13948–13961.
61 Strohalm M, Kavan D, Novak P, Volny M & Havlicek V (2010) mMass 3: a cross-platform software environment for precise analysis of mass spectrometric data. *Anal Chem* **82**, 4648–4651.
62 Vecer J & Herman P (2011) Maximum entropy analysis of analytically simulated complex fluorescence decays. *J Fluoresc* **21**, 873–881.
63 Vecer J, Vesela P, Malinsky J & Herman P (2014) Sphingolipid levels crucially modulate lateral microdomain organization of plasma membrane in living yeast. *FEBS Lett* **588**, 443–449.
64 Kacirova M, Kosek D, Kadek A, Man P, Vecer J, Herman P, Obsilova V & Obsil T (2015) Structural characterization of phosducin and its complex with the 14-3-3 protein. *J Biol Chem* **290**, 16246–16260.
65 Eftink MR & Ghiron CA (1976) Fluorescence quenching of indole and model micelle systems. *J Phys Chem* **80**, 486–493.
66 Kozin MB & Svergun DI (2001) Automated matching of high- and low-resolution structural models. *J Appl Crystallogr* **34**, 33–41.
67 Franke D & Svergun DI (2009) DAMMIF, a program for rapid ab-initio shape determination in small-angle scattering. *J Appl Crystallogr* **42**, 342–346.
68 Williamson MP (2013) Using chemical shift perturbation to characterise ligand binding. *Prog Nucl Magn Reson Spectrosc* **73**, 1–16.

Supporting information

Additional supporting information may be found online in the Supporting Information section at the end of the article.

Table S1. Intermolecular cross-links between proC2 and 14-3-3ζ using DSG.

Table S2. Intermolecular cross-links between proC2 and 14-3-3ζ using DSS.

Table S3. Results of acrylamide quenching of tryptophan fluorescence.

Table S1.

Intermolecular cross-links between proC2 and 14-3-3ζ using DSG

#	Cross-linked peptides		Cross-linked residues	Observed mass	Error (ppm)
	proC2	14-3-3ζ	proC2–14-3-3ζ		
1	123-136+I	42-55	S123-K49	3177.69	1.24
2	123-136+I	61-74	S123-K68	3178.61	0.46
3	123-136+I	75-80	S123-K75	2435.23	0.29
4	123-136+S	84-103+S	S123-K85	3913.10	1.10
5	123-136+I	128-139	S123-K138	2953.48	0.91
6	137-153+P,I,I	61-74	K152-K68	3773.86	0.84
7	153-155	10-27+Ox,I,Ox	K153-K11	2644.25	0.75
8	153-155	42-55	K153-K49	2015.18	0.25
9	153-155	61-74	K153-K68	2016.10	0.33
10	362-378+S,I	61-74	K372-K68	3415.65	0.12
11	379-382	42-55	K381-K49	2117.18	0.63
12	379-382	61-74	K381-K68	2118.10	0.40

+ modification: P = phosphorylation, I = Iodoacetamide, Ox = oxidation, S = desulfocysteine
proC2 regions: 123-169, linker between CARD and p19 domains; 170-333, p19 domain; 334-347, linker between p19 and p12 domains; 348-452, p12 domain.

Table S2.

Intermolecular cross-links between proC2 and 14-3-3ζ using DSS

#	Cross-linked peptides		Cross-linked residues	Observed mass	Error (ppm)
	proC2	14-3-3ζ	proC2–14-3-3ζ		
1	123-136+I	10-18	S123-K11	2731.42	0.53
2	123-136+I	42-55	S123-K49	3219.73	1.11
3	123-136+I	75-80	S123-K75	2477.28	0.42
4	123-136+I	116-122	S123-K120	2644.40	0.79
5	123-136+S	121-127	S123-K122	2559.30	0.30
6	123-136+I	128-139	S123-K138	2995.52	0.81
7	123-136	61-74	H127-K68	3163.63	0.59
8	153-155	10-27+S	K153-K11	2565.31	0.88
9	153-155	61-74	K153-K68	2058.15	0.64
10	362-378+S,I	61-74	K372-K68	3457.70	0.69
11	379-382	42-55	K381-K49	2159.23	0.12
12	379-382	61-74	K381-K68	2160.15	0.20

+ modification: P = phosphorylation, I = Iodoacetamide, Ox = oxidation, S = desulfocysteine
proC2 regions: 123-169, linker between CARD and p19 domains; 170-333, p19 domain; 334-347, linker between p19 and p12 domains; 348-452, p12 domain.

Table S3.

Results of acrylamide quenching of tryptophan fluorescence

proC2 variant	$k_q \times (10^{-9}\ M^{-1}\ s^{-1})$[a,b,e]	Δk_q [d]
		%
Trp^{151}	1.47 ± 0.03	
Trp^{151} + 14-3-3ζ[c]	0.81 ± 0.04	-45
Trp^{188}	1.18 ± 0.07	
Trp^{188} + 14-3-3ζ	1.11 ± 0.08	-6
Trp^{218}	1.86 ± 0.04	
Trp^{218} + 14-3-3ζ	1.00 ± 0.03	-46
Trp^{385}	0.93 ± 0.03	
Trp^{385} + 14-3-3ζ	0.63 ± 0.02	-32
Trp^{426}	1.33 ± 0.02	
Trp^{426} + 14-3-3ζ	0.72 ± 0.01	-46

[a] For comparison, bimolecular quenching constant of Trp in aqueous environment is $k_q = 5.9 \times 10^{-9}\ M^{-1}\ s^{-1}$ [65]

[b] The bimolecular quenching constant (k_q) was calculated using Equation 2.

[c] The human 14-3-3ζnoW protein mutant missing all Trp residues (mutations W59F and W228F) was used in all proC2 tryptophan measurements [44- 45]

[d] Relative change in the bimolecular quenching constant after 14-3-3ζ binding

[e] Presented results are the means ± S.D., n=3.

7.4 Supplement S4

7.4.1 Publication IV: Inhibition of the FOXO3-DNA interaction by small molecule inhibitors

Hagenbuchner, J., Obsilova, V., Kaserer, T., Rass, B, **Psenakova, K.,** Docekal, V., Alblova, M., Kohoutova, K., Spoden, G., Schuster, D., Aneichyk, T., Kofler, R., Vesely, J., Obexer, P., Obsil, T. & Ausserlechner, M.J. Modulation of FOXO3 transcriptional activity by small molecule inhibitors. *Submitted*

My contribution: expression and purification of $^{13}C,^{15}N$-labeled FOXO3; sample preparation and further optimization for the NMR experiments; NMR experimental design and measurements; NMR assignment and data evaluation.

Modulation of FOXO3 transcriptional activity by small molecule inhibitors

Hagenbuchner, J.[1]*, Obsilova, V.[2]*, Kaserer, T.[5,8]*, Rass, B[8], Psenakova, K.[2,3], Docekal, V.[4], Alblova, M.[2], Kohoutova, K.[3], Spoden, G.[6,8], Schuster, D.[5], Aneichyk, T.[7] , Kofler, R.[7], Vesely, J.[4], Obexer, P. [1], Obsil, T.[2,3#], Ausserlechner, M.J.[5#]

[1]Department of Pediatrics II, Medical University Innsbruck, Innrain 66, Innsbruck, Austria
[2]Department of Structural Biology of Signaling Proteins, Institute of Physiology, Division BIOCEV, The Czech Academy of Sciences, Prague 14220, Czech Republic;
[3]Department of Physical and Macromolecular Chemistry, Faculty of Science, Charles University, Prague 12843, Czech Republic;
[4]Department of Organic Chemistry, Faculty of Science, Charles University, Prague 12843, Czech Republic;
[5]Institute of Pharmacy, Leopold Franzens University of Innsbruck, Innsbruck, Austria
[6]Tyrolean Cancer Research Institute, Innsbruck, Austria
[7]Division of Molecular Pathophysiology, Biocenter, Medical University Innsbruck, Innsbruck, Austria
[8]Department of Pediatrics I, Medical University Innsbruck, Innsbruck, Austria

* contributed equally to this work

address correspondence to

Abstract

FOXO transcription factors are critical regulators of cell homeostasis and steer cell death, differentiation and longevity in mammalian cells. Via combined pharmacophore-modelling-based *in silico* and fluorescence polarization-based screening we identified small molecules that physically interact with the DBD of FOXO3 and modulate the FOXO3 transcriptional program in human cells. The exact mode of interaction between compounds and the FOXO3-DBD was determined via NMR spectroscopy and docking studies. We demonstrate that compounds S9 and its oxalate salt S9OX interfere with FOXO3 target promoter binding, target gene transcription and modulate the physiologic program activated by FOXO3 in cancer cells. These small molecules prove the druggability of FOXO transcription factors and provide a basis for modulating these important homeostasis regulators in normal and malignant cells.

Keywords:

Small compounds, transcription factor

The mammalian forkhead box O (FOXO) transcription factor family (FOXO1/FKHR, FOXO3/FKHRL1, FOXO4/AFX, and FOXO6) is involved in multiple cellular processes ranging from apoptosis induction to longevity[1]. In mammals, FOXO3 and its family members recognize and bind the same core DNA elements (TTGTTTAC) to control the transcription of direct target genes. However, despite sharing the same consensus sequences, FOXO members serve distinct functions and may act as tissue-specific homeostasis regulators.

FOXO3 was initially considered as a tumor suppressor that induces apoptosis and cell-cycle arrest.[2] However, its functions in cellular detoxification,[3, 4] and drug-resistance,[5, 6], maintains cancer stem cells [7] as well as inhibition of other death-inducers such as TP53[8] suggest also a tumor-promoting role in certain types of cancer.

Multiple cellular signaling pathways converge on FOXO3, most importantly the pro-proliferative PI3K-PKB pathway that inactivates target gene transcription. On the other hand, stress conditions, such as genotoxic stress, reactive oxygen species (ROS) or hypoxic stress, override growth-factor-mediated phosphorylation of FOXO3, which results in the relocation of FOXO3 to the nucleus.[9, 10] Thereby, stress induced signaling kinases, such as JNK or MST1 that cause FOXO3 activation and nuclear accumulation also in presence of PKB signaling critically contribute to FOXO3-triggered therapy-resistance programs that protect cancer cells during therapy[7, 8, 11]. In addition, FOXO3 regulates the differentiation of naïve regulatory T-cell differentiation *via* its transcriptional target FOXP3[12, 13], which limits cytotoxic anti-cancer T-cell response by immune-suppressive regulatory T-cells that infiltrate tumor tissue. A reversible inhibition of FOXO3 activity by small compounds thereby might boost anti-tumor immune responses and limit side effects of FOXO3 functional inactivation.

In contrast to the small, defined substrate binding pockets on catalytic enzymes the DBD of transcription factors are usually regarded as “undruggable” due to the large surfaces and the fact that the only known ligand is a DNA molecule. Small molecules have been described for the transcription factor FOXM1[14, 15] and one compound was shown to regulate FOXO1 activity [16], but no compounds have been discovered that directly physically interact with DBD of FOXO proteins to regulate their transcriptional activity. By a pharmacophore model-based, virtual *in silico* screening approach we identified compound

S9 and demonstrate that this substance inhibits FOXO3-binding to target promoters, affects the cell-wide transcriptional program of FOXO3, as well as FOXO3 effects on cellular ROS production and cell growth in 2D and 3D cell culture systems. By NMR we demonstrate that S9 directly interacts with FOXO3 DBD, define the mode of binding and how this substance structurally interferes with FOXO3 transcriptional activity.

Results

Identification of compound S9 as a putative FOXO-DBD ligand

In the absence of known small molecule ligands, a structure-based modeling workflow (Supplemental Figure 1a) was developed, employing the crystal structure of FOXO3 DNA binding domain (DBD) in complex with a 13 bp FOXO3 consensus sequence DNA strand (PDB entry 2UZK[17]). The site to be targeted within the large interaction surface was defined using experimentally observed FOXO3-DNA interactions (Supplemental Fig. 1b), consensus sites predicted by four pocket prediction algorithms (Pocket-Finder Pocket Detection, Molecular Operating Environment (MOE v. 11.2011))[18-22], and literature data on crucial residues and less flexible sites as suggested by mutational studies and posttranslational modifications[17] and a molecular dynamics simulation on the related FOXO4[23], respectively. Due to the limited amount of available data, we aimed to elucidate interaction patterns of potential ligands by combining data from the interactions observed in the protein-DNA complex (Supplemental Fig. 1b), interaction hotspots on the protein surface calculated with MOE (Fig. 1a), and binding modes predicted by docking of Drugbank[24] version 2.5 into the binding site (Fig. 1b). The identified binding patterns were represented by six pharmacophore models, which were subsequently used for virtual screening of the Specs (www.specs.net) and Maybridge (www.maybridge.com) databases. 76 virtual hits for which the desired binding mode was confirmed by further docking studies were selected for experimental testing. Among others, compound S9 (1-(4,6-dimethylpyrimidin-2-yl)-3-(4-propoxyphenyl)guanidine) was identified by pharmacophore model 1 (Fig. 1c).

Primary biochemical validation of hit-compounds was performed via fluorescence polarization analyses using recombinant FOXO3-DBD (residues 156-269) and FAM-labeled oligonucleotides containing the IRE consensus sequence (CTA TCA AAA CAA

CGC). As shown in Fig. 1d, compounds S9 and S9OX (the oxalate salt S9OX was prepared to increase the S9 solubility in water) reduced the interaction of FOXO3-DBD to the FAM-IRE oligonucleotide at a concentration of 0.5 μM. To validate these biochemical screening results in living cells we used SH-EP/FOXO3 neuroblastoma cells stably expressing a 4-hydroxy-tamoxifen (4OHT)-regulated FOXO3(A3)ERtm transgene that undergo apoptotic cell death upon activation of FOXO3[11, 25]. As shown in Fig. 1e, addition of compound S9 and to a lesser extend also S9OX significantly reduced FOXO3-induced cell death, demonstrating that S9 transduces the cytoplasma membrane and modulates FOXO3 function in living cells. Based on these primary screening results we defined S9 as a promising FOXO3-modulatory compound worth for further biochemical, cell biological and structural characterization.

Mapping of the S9-binding site in FOXO3-DBD

Structural characterization of the interaction between FOXO3-DBD and S9 was performed using nuclear magnetic resonance (NMR) spectroscopy. First, ^{1}H saturation transfer difference (STD) NMR measurements were used to further assess S9 binding to FOXO3-DBD. STD signals were detected for several protons of both S9 and its oxalate salt, thus confirming their interaction with FOXO3-DBD (Figs. 2a and S1a). In the case of S9OX, pronounced STD signals were observed for H1, H3, H5, and H7 protons, whereas less pronounced signals were observed for H4 and H6 protons. In the case of S9, whose STD spectra were acquired in the presence of 10% DMSO due to its low solubility in water, strong STD signal was observed for H3 protons and less pronounced signals were recorded for H1, H5, H6 and H7 protons. These data suggested that both aromatic moieties as well as the aliphatic part of S9 are involved in direct interactions with FOXO3-DBD.

Because the previously published NMR sequential assignment of human FOXO3-DBD[26] was obtained for shorter construct (residues 151–251) compared to the construct used in this study (residues 156–269), standard triple resonance experiments were used to obtain a sequence specific backbone assignment of our FOXO3-DBD$_{156\text{-}269}$ construct. The ^{1}H-^{15}N heteronuclear single quantum coherence (HSQC) spectrum of ^{15}N-labeled FOXO3-DBD with obtained resonance assignment is shown in Fig. S1b. The data analysis provided a resonance assignment for 99 out of 114 residues (87% of the FOXO3-DBD sequence). To identify the S9-binding site in FOXO3-DBD, the ^{15}N-labeled FOXO3-DBD was titrated

with S9OX and ^{1}H and ^{15}N chemical shift perturbations (CSPs) of the backbone amide groups of FOXO3-DBD were followed in ^{1}H-^{15}N HSQC spectra (Fig. S1c). The oxalate salt of S9 was used for its higher solubility in water, thus avoiding the use of DMSO and the associated chemical interferences. The presence S9OX induced significant dose-dependent CSPs of backbone amide groups of fifteen FOXO3-DBD residues (the chemical shift change was greater than σ^{0}_{corr} above the mean), thus suggesting their involvement in the interaction or their conformational change induced by S9 binding (Fig. 2b). When these residues were mapped onto the solution structure of FOXO3-DBD[26], they revealed the binding surface for S9 in the region formed by the DNA recognition α-helix H3 and the N-terminal part of β-strand S2 (Fig. 2c). The most affected residues (the chemical shift change was greater than $2\sigma^{0}_{corr}$ above the mean) were Arg211, His212, Asn213, Ser215 and Leu216 from the helix H3; Phe220 and Asn237 from the wing W2; and Thr167 from the helix H1. In addition, the gradual shift of resonances during titration indicated fast exchange of the ligand on the NMR time scale, thus suggesting that the S9OX binding is of moderate affinity. This was confirmed by plotting the normalized chemical shifts against the S9OX concentration, which revealed the binding affinity (K_D value) of 0.5 ± 0.2 mM (Fig. S1d).

To obtain greater insight into the interaction of S9 with FOXO3-DBD, docking calculations using Autodock Vina[27] were performed. The S9 binding surface (the residues treated as flexible) included residues identified in ^{1}H-^{15}N HSQC experiment as well as several additional residues with high CSPs located close to them (Fig. 2d). The calculated poses with the lowest binding energy were extracted and further validated against results from STD NMR measurements. The final pose is consistent with results from both STD and ^{1}H-^{15}N HSQC experiments and suggests that S9 binds into the groove formed by residues Arg211, His212 and Ser215 at the C-terminus of α-helix H3 and residues Met221 and Arg222 from the N-terminus of β-strand S2. This region is a crucial part of the FOXO3-DBD/DNA interface as the DNA recognition α-helix H3 is responsible for most of the direct base contacts with DNA and the N-terminal part of β-strand S2 is involved in contacts with the DNA backbone.[17] Therefore, these data indicate that S9 binding blocks the DNA binding surface of FOXO3-DBD in the region of the recognition α-helix H3.

Compounds S9 and S9OX affect FOXO3 transcriptional program

To analyze the effect of compound S9 on mRNA steady state levels of FOXO3-regulated genes we assessed genome-wide regulatory events by mRNA expression profiling. SH-EP/FOXO3 cells were treated with 50 nM 4OHT for three hours in presence or absence of 50 μM compound S9 and transcriptome was measured with Affymetrix U133 2.0 whole genome chips. 1262 mRNAs were induced and 889 mRNAs showed statistically significant repression upon activation of ectopic FOXO3(A3)ERtm. When 4OHT-driven activation of ectopic FOXO3 was combined with S9 the expression of 208 mRNAs was altered with only 35 mRNAs being regulated in common with FOXO3 activation alone. This suggests that S9 inhibited FOXO3-mediated induction of 1227 mRNAs (97.2 %), but also increased steady state levels of 173 mRNAs that were not regulated by ectopic FOXO3. These changes in mRNA expression might result from differences in target gene regulation between ectopic FOXO3(A3)ERtm and endogenous FOXO3, as ectopic FOXO3(A3)ERtm carries mutations at the major PKB phosphorylation sites (T32, S253 and S315) or off-target effects. This effect of S9 is well visualized in the heatmap analysis (Fig. 3a) where S9 attenuates the strong induction of a large cluster of genes (top-part of heatmaps) or repressed highly expressed FOXO3 targets by its own (bottom part of heat map). Interestingly, S9 also *per se* induced a cluster of strongly repressed FOXO3-targets (middle part of heatmaps) and, for a small number of genes, S9 interestingly increased FOXO3-mediated induction (arrows). Therefore, although S9 mainly exerts an inhibitory effect on FOXO3 transcriptional activity, this compound also induces mRNA expression of a small number of FOXO3 target genes.

To verify genome-wide gene expression results we selected four genes previously identified as FOXO3 targets in neuroblastoma cells and evaluated the effect of compound S9 and its oxalate salt S9OX on mRNA expression by quantitative RT-PCR analyses. As shown in Figure 3c-f, activation of ectopically-expressed FOXO3(A3)ERtm by 4OHT significantly induced steady state expression of the pro-apoptotic BH3-only proteins BIM and NOXA, as well as of the detoxifying proteins SESN3 and DEPP1 similar to previously published data from our group[4, 9, 25, 28]. S9 or S9OX caused no statistically significant changes in steady state expression of these genes compared to solvent-treated controls. However, when combined with activation of ectopic FOXO3, S9 as well S9OX

significantly counteracted mRNA induction of all four *bona fide* FOXO3 targets suggesting that this compound efficiently interferes with specific mRNAs induction by FOXO3.

FOXO3-modulatory compounds S9 and S9OX inhibit the induction of FOXO3 target proteins, binding of FOXO3 to target promotors and promotor transactivation.

Next, we quantified the effects of compound S9 and S9OX *via* immunoblot analyses to assess whether regulations observed on mRNA steady state level were also translated into changes in protein expression. As shown in Fig. 4a-d the activation of the 4OHT-regulated FOXO3(A3)ERtm transgene in SH-EP/FOXO3 neuroblastoma cells elevated the protein levels of the proteins BIM, NOXA, SESN3 and DEPP1. Consistent with quantitative RT-PCR results in Fig. 3d-g, both, S9 and S9OX prevented FOXO3-mediated induction of BIM, NOXA and SESN3 above background level and significantly attenuated the strong induction of DEPP1, demonstrating that S9 and S9OX efficiently interfere with the regulation of FOXO3 target proteins in living cells. The combined data suggest that S9 and S9OX both modulate FOXO3-transcriptional program and target protein regulation. Biochemical results from fluorescence polarization analyses and NMR-based structural analyses suggest that *in vitro* the compounds S9 / S9OX bind to the DBD of FOXO3 and inhibit DBD – DNA interaction. To address, whether S9 directly interferes with FOXO3 target promoter recognition in living cells we next performed chromatin immunoprecipitation (ChIP) analyses and assessed the binding of FOXO3 to the promotors of BIM, NOXA, SESN3 and DEPP1. As demonstrated in Fig. 4e, activation of the conditional FOXO3 allele for three hours significantly increased FOXO3 promoter binding, which is consistent with the previously demonstrated induction of these FOXO3 targets on mRNA and protein level. Importantly, for all investigated promoters, the addition of S9 almost completely reduced the interaction of FOXO3 with endogenous promoters to control level. To assess, whether this reduced promoter binding also correlates with reduced transactivation we used a luciferase reporter vector containing a 544 bp DEPP1 promoter fragment that carries three putative FOXO3 consensus sites[4]. As demonstrated in Fig. 4f, compound S9 reduced luciferase activity in a dose-dependent manner with approximately 50% reduction at 12.5 µM. These results confirm the biochemical binding studies between compounds S9 and S9OX and FOXO3-DBD (Figs. 1d and 2) and demonstrate that S9 inhibits binding of FOXO3 to target promoters and their activation in living cells.

Compounds S9 and S9OX prevent ROS-induction and cell death by FOXO3 in 2D and 3D cell culture models.

We previously demonstrated that FOXO3-activation induces a bi-phasic reactive oxygen species (ROS) wave that critically contributes to induction of apoptotic cell death in human neuroblastoma cells[9]. To assess the effect of S9 and S9OX on ROS accumulation by FOXO3 we either activated ectopic FOXO3(A3)ERtm by 4OHT treatment (Fig. 5a) or treated the cells with 20 µg/ml etoposide to activate endogenous FOXO3 *via* DNA-damage response (Fig. 5b). Direct activation of ectopic FOXO3 by 4OHT or etoposide treatment cause significant accumulation of cellular ROS as demonstrated by live-cell fluorescence microscopy using the ROS-sensitive dye reduced mitotracker red. Both, S9 and S9OX completely prevent ROS accumulation in 4OHT- and etoposide-treated cells demonstrating that S9 and S9OX efficiently prevent cellular ROS accumulation in response to FOXO3 activation. Since results obtained with 2D cell culture only partially reflect drug effects in tissues or solid tumors we assessed the effect of S9 and its oxalate salt S9OX in 3D spheroids of neuroblastoma cells formed by magnetic bioprinting and magnetic levitation culture. For these experiments the FOXO3-sensitive, high-stage neuroblastoma cell line NB15/FOXO3-GFP was used to directly image cell growth / viability by fluorescence microscopy. To define at which concentrations S9and S9OX are still biologically active and how long physiologic effects may be observed upon single treatment we reduced the concentrations of S9 and S9OX to 5µM. Tumor spheres grown for 72 hours floating in a magnetic field were treated with 10 nM 4OHT for 72 hours in presence or absence of S9 and S9OX and then cultured for another week. After this time, sphere-size and number of spheres per well were analyzed by fluorescence microscopy (Fig. 5c-e). Metabolic activity and cell viability was assessed by measuring ATP-content (Fig. 5f) and reduction of resazurin salt (Fig. 5g), respectively. Both, S9 and S9OX prevented FOXO3-induced cell death in 3D tumor spheroids at a concentration of 5 µM and after single administration. Although sphere diameter was slightly reduced in S9 / S9OX + 4OHT-treated cells compared to controls, still normal numbers of well-formed tumor spheres were present. Importantly, ATP-content and resazurin salt reduction, which are both parameters for cell viability, demonstrated that S9 and S9OX preserved the viability of tumor spheres and strongly inhibited the apoptosis-inducing effect of FOXO3 in this 3D tumor model. The

combined data demonstrate that S9 and its oxalate salt S9OX physically interact with the FOXO3-DBD, inhibit FOXO3 transcriptional program and modulate FOXO3 physiologic function in the low micromolar range in living cells.

Discussion

In this manuscript we describe for the first time small compounds that inhibit FOXO3 transcriptional activity by direct binding to the FOXO3-DBD. Based on structural data of FOXO1, FOXO3 and FOXO4 we developed six different pharmcophore-models that were then used for *in silico* screening of structural compound databases. Candidate compounds were tested biochemically by fluorescence polarization analysis and for biological efficacy in a cell system stably expressing a conditional FOXO3(A3)ERtm allele that can be activated by the addition of 4OHT. By this we selected for compounds that hamper FOXO3-DNA interaction and enter living cells. From successful candidate compounds we choose S9 due to its relatively high solubility in water, established the whole chemical synthesis pathway (Supplemental Information page 3ff) and synthesized an oxalate salt of S9 with increased solubility in water. This was a prerequisite for using solution NMR to gain insight into the molecular basis for S9-mediated inhibition of FOXO3 transcriptional activity.

NMR measurements together with molecular docking simulations revealed that S9 binds to the pocket formed by the C-terminal part of α-helix H3 and the wing W1 (Fig. 2d). This region is a crucial part of the DNA binding surface as it includes residues important for DNA recognition: Arg211, His212 and Ser215 from α-helix H3.[34] Furthermore, residues Arg222 and Trp234 from the β-strand S2 at the stem of wing W1 are involved in contact with the phosphate group of the DNA backbone. Therefore, the S9 binding could obstruct FOXO3-DBD interaction with the target DNA, thus blocking its transcriptional activity.

Gene expression profiling provided an interesting three hours snap-shot on the mRNA changes induced by ectopic FOXO3 activation in presence or absence of compound S9. S9 strongly prevented the induction of FOXO3-induced genes or by its own repressed clusters of highly expressed FOXO3 targets, which is consistent with its interaction to a region in FOXO3-DBD including R211, H212 and S215 which all contribute to helix H3-DNA interaction[17]. On the other hand, S9 *per se* strongly induced a cluster of genes that was

actively repressed by ectopically switched on FOXO3 suggesting that these genes are permanently repressed by endogenous FOXO3 in manner that requires the DNA-binding domain either for protein-DNA or protein-protein interaction and that this repression is abrogated by S9. A small cluster of genes was identified that was only moderately induced by ectopic FOXO3, but strongly up-regulated in presence of S9. One explanation for this phenomenon might be that DNA-binding independent transactivation by endogenous FOXO3 is further supported by S9 preventing intra-molecular protein-protein interaction of the C-terminal FOXO3 transactivation domain with the FOXO3-DBD as it involves the C-terminus of α-helix H3, which is part of the S9 binding pocket.[26] These aspects concerning inhibition of intra- or inter-molecular protein-protein interaction at FOXO3-DBD by S9 are investigated in currently ongoing studies.

Besides genome-wide regulation we tested the effect of S9 and S9OX on physiological FOXO3 downstream targets. The BCL2-family members BIM and NOXA are mediators of FOXO3-induced intrinsic cell death and BIM critically triggers transitory accumulation of ROS at the mitochondria, which is counteracted by the parallel induction of the detoxifying protein SESN3[9]. DEPP1 sensitizes neuroblastoma cells for ROS and is strongly induced by FOXO3 via three functional FOXO consensus sequences in its promoter.[4, 28] We demonstrated that FOXO3 induction of these four *bona fide* targets was efficiently reduced by both S9 and S9OX on mRNA level as well as on protein expression level. To further prove direct inhibition of FOXO3-DBD-DNA interaction in living cells, ChIP analyses on the four *bona fide* targets was performed which demonstrated that increased FOXO3 binding upon ectopic FOXO3-activation was almost completely abrogated by S9 (Fig. 4e). This was consistent with results from primary FP analysis (Fig. 1d) and dose-dependent repression of promoter activity by S9 and S9OX as demonstrated luciferase reporter assay (Fig. 4f). Consistent with the repression of target gene regulation, also FOXO3-induced ROS accumulation[4, 9] was efficiently prevented by S9 and S9OX providing evidence that S9 directly interferes with physiological effects of FOXO3 in living cells. As affinity measurements using recombinant protein fragments provide only limited information about biologically effective concentrations, we generated magnetic 3D tumor spheres that allowed us on one hand to assess possible long term toxicity of S9 / S9OX in 3D culture and on the other to test effective doses of these compounds. S9 / S9OX neither reduced

sphere-numbers nor diameter when spheres were treated 72 hours with 5 μM of these drugs, but efficiently prevented FOXO3-induced cell death. Interestingly, the growth-inhibitory effects of FOXO3 were only partially inhibited, which corresponds to the observation that gene-dosage effects of FOXO3 lead to, in part, contrary physiological outcomes.[11]

FOXO transcription factors have been implicated in a plethora of different cellular functions, in cancer immunity where loss of FOXO3 exerts anti-cancer effects, but also hampers other arms of the immune system[29], in neuronal development and plasticity[30], cancer angiogenesis and metabolism[31]. This excludes the permanent ablation of FOXO activity in mammals as a therapeutic option. More complexity is added by the fact that the DBD of FOXO transcription factors participates in intra-, but also intermolecular interactions with other cellular key regulators of death and longevity, such as p53[26] and thereby also steers e.g. aging of the whole organism [32]. Due to its mode of binding, S9 might well interfere with some of these protein-protein interactions. The effect of small drugs like S9 on specific tissues has be investigated in detail to define, whether S9 can serve as a chemical starting point for developing FOXO-regulatory compounds that steer distinct target gene subsets / functions of FOXO transcription factors. The advantage of small drugs like S9 is the strict control of application-dose and -time and the fact that they are not immunogenic allowing repeated applications – so dose- and application time can be adjusted to damage cancer cells or boost anti-cancer immunity, but also limit unwanted side effects of FOXO-inhibition on stem cells and other somatic tissues.

Methods

Analysis of Foxo3a-DNA interactions and generation of interaction maps. The experimentally observed interactions of the FOXO3 consensus sequence DNA strand and the FOXO3-DBD were extracted in LigandScout[33] version 3.0 and represented by pharmacophore features (Fig. 1b). The pdb entry 2UZK[17, 34] was loaded into MOE version 11.2011. The protein was protonated using the default settings and interaction maps were generated using the N1:: (sp3 NH with lone pair), O (carbonyl oxygen), and DRY (hydrophobic) probes with -4 kcal/mol, -3.5 kcal/mol, and -2.5 kcal/mol cut-offs, respectively (Fig. 1c).

Docking, pharmacophore modeling, virtual screening, and selection of test compounds. GOLD[35] version 3.1 was used for docking. Hydrogen atoms were added to the protein and all water molecules and ligands were deleted. The area of 20.0 Å around His212 was defined as binding site and the GoldScore was used for scoring. Up to 10 different docking poses were reported for each input molecule and analyzed using LigandScout version 3.0. Pharmacophore models were created using LigandScout[33] version 3.0 based on docking poses of molecules from Drugbank[36] version 2.5 (Fig. 1d). In particular, one docking pose of DB00878 (model 1), DB02056 (model 2+3), DB00430 (model 4), DB02141 (model 5), and DB01274 (model 6) was used, respectively. Automatically generated models were manually refined to reflect interaction patterns observed in the crystal structure, highlighted by the interaction maps, or involved residues either crucial for binding or which are posttranslational modification sites such as Asn208, Ser209, Arg211, His212, and Ser215. Compound libraries for virtual screening were generated by calculating up to 250 conformations for each molecule in the Specs (version April 2010, www.specs.net) and Maybridge (version 2010, www.maybridge.com) databases. Pharmacophore hits were docked into the binding site using the protocol described above and docking poses were analyzed using LigandScout version 3.0. 76 compounds, for which docking poses reflected the identified interaction patterns, were selected for experimental testing.

Synthesis of S9 and S9OX. The synthesis of S9 and S9OX and all corresponding NMR spectra are described in Supplemental information.

Expression and purification of recombinant FOXO3-DBD. Recombinant FOXO3-DBD protein was produced as previously described for FOXO4-DBD[23]. Briefly, DNA encoding human FOXO3-DBD (residues 156−269) was ligated into the pGEX-6P-1 (GE Healthcare), using the BamHI and XhoI sites. FOXO3-DBD was expressed as N-terminal GST-tagged fusion protein in E. coli BL21(DE3). Protein expression in LB-media was induced by isopropyl β-D-1-thiogalactopyranoside for 18 h at 20 °C, and the protein was purified using Glutathione Sepharose 4 Fast Flow (GE Healthcare) according to a standard protocol. Protein was dialyzed against buffer containing 20 mM Tris-HCl, 100 mM NaCl, 1 mM EDTA, 1 mM DTT, 10% (wt/vol) glycerol at pH 7.5. The affinity tag was removed by PreScission Protease cleavage overnight at 4 °C (10 U/mg recombinant protein). After the

cleavage, FOXO3-DBD was purified by size-exclusion chromatography (HiLoad Superdex 75; GE Healthcare) in 20 mM phosphate buffer containing 50 mM KCl, 2 mM TCEP, and 10% (wt/vol) glycerol at pH 6.5. Isotopically labeled proteins for NMR experiments were expressed using the same procedure in minimal medium with [^{15}N]NH_4Cl and/or [^{13}C]glucose as the sole nitrogen and carbon sources, respectively, and purified as unlabeled FOXO3-DBD.

Fluorescence polarization (FP) analyses. To determine the binding of a compound S9 to FOXO3-DBD *in vitro* FP-measurements were carried out in black 96-well plates with flat bottom (HVD Life Sciences, Vienna, Austria) in a chameleon plate reader (Hidex, Turku, Finland). For FP-Assays, recombinant FOXO3 was only purified via affinity chromatography and gel-filtration chromatography. Two microliters S9 (500nM final concentration) were added to 100 µl reaction mix containing 125 nM FOXO3-DBD and 25 nM FAM-labeled double strand FOXO3 consensus sequence oligonucleotides in assay buffer (20 mM TrisHCl, 100mM NaCl, 1mM EDTA, pH 7.5). Positive (only assay buffer and FAM-labeled oligonucleotide) and negative (FOXO3-DBD and FAM-labeled oligonucleotide) controls were analyzed on each plate. Millipolarization values (mP) were measured at an excitation wavelength of 485 nm and an emission wavelength of 530 nm.

NMR data collection and analysis. NMR data were acquired on Bruker Avance III™ HD 600 MHz and 850 MHz spectrometers both equipped with a ^{1}H/^{13}C/^{15}N cryoprobe at 25 °C. The sequence-specific backbone resonance assignment was obtained using a series of standard triple-resonance spectra (HNCO, HN(CA)CO, HNCACB, and CBCA(CO)NH experiments). The obtained assignments were in a good agreement with the sequence-specific backbone NMR assignment obtained for shorter FOXO3-DBD construct.[26] Chemical shift perturbations (CSPs) were assessed using ^{1}H-^{15}N heteronuclear single quantum coherence (HSQC) spectra. For these experiments, ^{1}H-^{15}N HSQC spectra were collected for samples containing 250 µM FOXO3-DBD alone and in the presence of 1.5–7 mM S9OX. All NMR experiments were performed in buffer containing 20 mM sodium phosphate (pH 6.5), 50 mM KCl and 10% D_2O. STD-NMR experiments were acquired at 25 °C using samples containing 15 µM unlabeled FOXO3-DBD in the presence of 1 mM ligand. 10% dimethyl sulfoxide (DMSO) was added to the buffer used in STD

experiments with S9 to increase its solubility. The dissociation constant for S9OX binding to FOXO3-DBD was determined by a nonlinear least squares analysis using the equation

$$\mathrm{CSP}_{obs} = \mathrm{CSP}_{sat} \times \frac{[\mathrm{L}] + [\mathrm{P}] + \mathrm{K}_D - \sqrt{([\mathrm{L}] + [\mathrm{P}] + \mathrm{K}_D)^2 - 4 \times [\mathrm{L}] \times [\mathrm{P}]}}{2 \times [\mathrm{P}]}$$

where CSP_{obs} is the observed CSP at the given total S9OX concentration [L], CSP_{sat} is the CSP at saturation, and [P] is the total concentration of FOXO3-DBD [37].

Molecular docking. Docking experiments were performed using Autodock Vina[27]. The solution structure of FOXO3-DBD (PDB ID: 2K86) and the S9 compound were modeled in Autodock Tools. The search space was defined as a 24×22×22 Å box centered on the helix H3 of the FOXO3-DBD. Flexible residues were selected based on CSP NMR analysis. The 20 lowest energy solutions were then analyzed and the lowest energy solution consistent with results from both STD and ^{1}H-^{15}N HSQC experiments was selected as the final pose.

Cell lines, culture conditions, and reagents. The neuroblastoma cell lines SH-EP/FOXO3 and NB15/FOXO3-GFP were cultured in RPMI1640 (Lonza, Basel, Switzerland) containing 10% fetal bovine serum (GIBCO BRL, Paisley, UK), 100 U/ml penicillin, 100 µg/ml streptomycin and 2 mM L-glutamine (Sigma-Aldrich, Vienna, Austria) at 5% CO_2. All cultures were routinely tested for mycoplasma contamination using the Venor^{R} GeM-mycoplasma detection kit (Minerva Biolabs, Berlin, Germany). All reagents were purchased from Sigma-Aldrich (Vienna, Austria) unless indicated otherwise.

Spheroids. Spheroids were formed by ferromagnetic bioprinting according to manufacturer's instructions (Pelobiotech GmbH, Germany). Spheroids were grown for 72 h before treatment with 4OHT / 4OHT + S9/S9OX. After 72 hours treatment substances were removed by centrifugation and remaining spheroids were grown for one week. Finally, spheroids were collected and re-plated in 100 µl fresh media into white 96well plates for ATP measurement or clear plates for resazurin reduction. Size was monitored regularly by live-cell microscopy. ATP-amount was measured by CellTiter-Glow-3D-cell-viability-assay according to manufacturer's instruction (Promega, Germany), resazurin salt reduction

was assessed *via* fluorescence measurement in a chameleon plate reader (Hidex, Turku, Finland).

Quantitative RT-PCR. To quantify mRNA-levels real-time qPCR was performed using Maxima™-SYBR-Green-qPCR-Master-Mix (Thermo Scientific, Waltham, USA) and GAPDH as reference-gene as previously described[38]: total-RNA was isolated from 5 x 10^6 cells using TRI-Reagent® (Sigma-Aldrich, St. Louis, USA) and 1 µg was reverse-transcribed to cDNA using RevertAid-H-Minus-cDNA-Synthesis Kit (Thermo Scientific, Waltham, USA). Oligonucleotides for BIM, NOXA, DEPP1, SESN3, and GAPDH are listed in Supplemental Table S1. qRT-PCR-reactions were performed in triplicates in a Bio-Rad-iCycler-instrument and repeated 3-times. After normalization to GAPDH, regulation was calculated between treated and untreated cells.

Microarray expression profiling. Generation of the Affymetrix microarray data set was performed at the Expression Profiling Unit of the Medical University Innsbruck according to the manufacturer's protocols. Total RNA was prepared from SH-EP/FOXO3 cells treated for three hours with/without 50 nM 4OHT and/or 50 µM compound S9 and RNA quantity and quality was determined in a 2100 Bioanalyzer (Agilent Technologies, Palo Alto, USA). 250 ng of high quality RNA was processed, hybridized to twelve Human Genome U133 Plus 2.0 arrays (three independent biological replicates per treatment) and scanned according to manufacturer's instructions as described.[39] The data analysis was performed in R (version). Raw data has been pre-processed using the GCRMA method.[40]

Immunoblot analyses. Total protein was prepared as described in Hagenbuchner et al.[41] Proteins were separated by SDS-PAGE and blotted on nitrocellulose membrane (GE Healthcare, Chalfot, UK). After blocking, membranes were incubated with primary antibodies (Supplemental Table S2), washed and incubated with horseradish-peroxidase conjugated secondary antibody (GE Healthcare, UK). The immunoblots were developed by enhanced chemiluminescence (GE Healthcare, Chalfont, UK) according to manufacturer's instructions and analyzed using an AutoChemi detection system (UVP, Cambridge, UK). Densitometry was performed using Labworks software version 4.5 (UVP, UK).

Chromatin-immunoprecipitation (ChIP). ChIP was performed using Magna-ChIP-Kit (Millipore, Darmstadt, GER) as described [4]. 20 µl protein-G-magnetic-beads were

coupled to 7.5 µl of FOXO3 antibody (Santa Cruz, Dallas, USA) or control-IgG and incubated with nuclear lysates of shredded DNA from 2 x 10^7 cells. After precipitation, protein was digested by proteinase-K and DNA was concentrated with ChIP-DNA-Clean-&-Concentrator-Kit (Zymo Research, Irvine, USA). FOXO3-binding to DNA was quantified by qPCR using promoter-specific primers for FOXO3-targets (Supplemental Table S3).

ROS measurements by live cell analyses. Cells were grown on LabTek Chamber Slides™ (Nalge Nunc International, Rochester, USA), coated with 0.1 mg/ml collagen. ROS measurements were performed by incubating the cells with MitoTrackerRed CM-H_2XROS (Invitrogen, Carlsbad, CA, USA) according to the manufacturer's instructions (final concentration 500 nM). Images were acquired with an Axiovert200M microscope (Zeiss, Vienna, Austria). Fluorescence intensity was quantified using Axiovision Software (Zeiss, Vienna, Austria) and relative ROS levels were expressed as % of untreated controls.

Acknowledgment

We thank Patrick Markt and Anna Filipek for technical support, Vaclav Veverka and Lukas Vrzal for help with NMR measurements. This work was supported by COMET center of excellence ONCOTYROL, MFF-Tirol (Project Nr. 296), Czech Science Foundation (Project 17-33854L), the "Provita Kinderleukämiestiftung", the Austrian Science Fund (FWF) (I3089-B28) and the "Tirol-Kliniken GmbH".

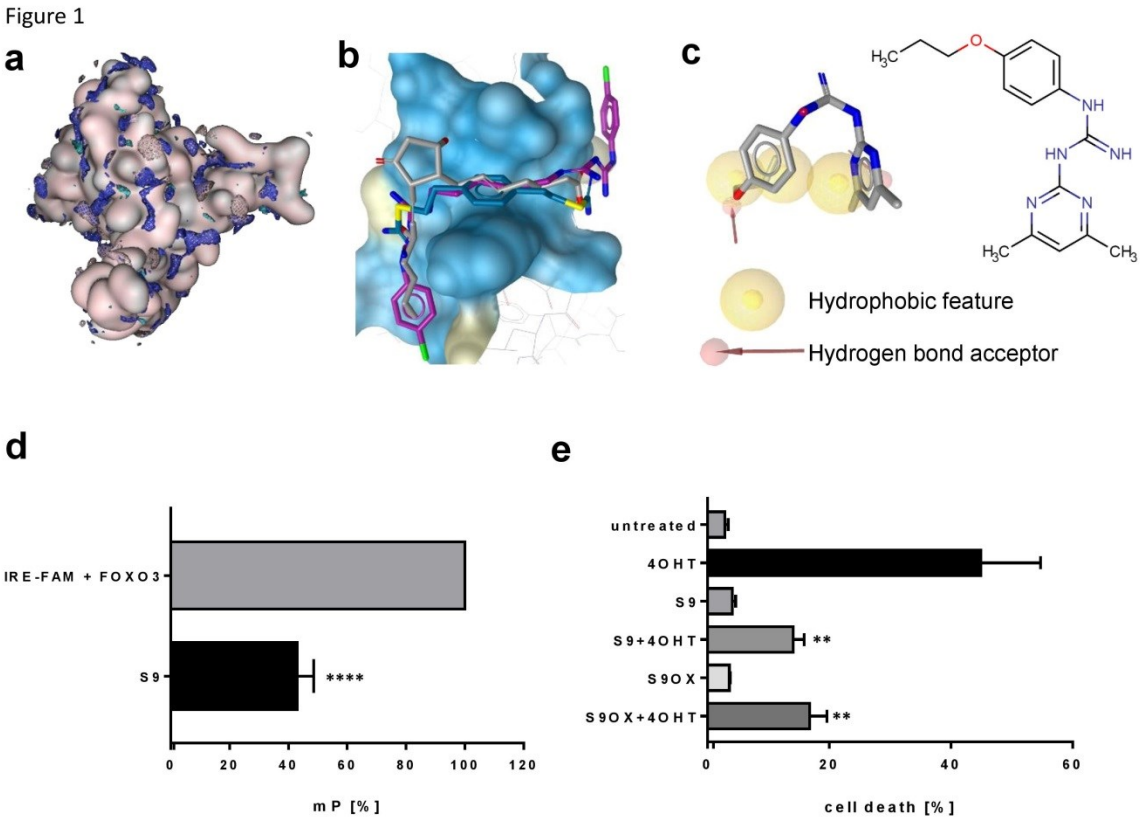

Figure 1: Pharmacophore model based screening for small compounds that interact with FOXO3-DBD. Binding of S9 to the DBD affects FOXO3's apoptotic function. Interaction maps highlight areas on the FOXO3a DBD surface (depicted in rose) where the defined probes can interact with the protein (a). Docking poses of compound S9 and additional compounds binding to the Foxo3a DBD (b). Compound **1** maps the pharmacophore model 1 (c). Fluorescence polarization assay (FP-Assay) of recombinant FOXO3-DBD (50 nM) and FAM- labeled IRE oligonucleotide (10 nM). A final concentration of 500nM S9 was used to displace the FAM-IRE. Shown is the mean of four independent experiments +SD (****p<0.0001) (d). PI-FACS analyses of SH-EP/FOXO3 cells treated with 50 nM 4OHT alone or in combination with 50 µM S9 or S9OX for 48 hours. Shown is the mean +SD of three independent experiments (e). Statistical differences between 4OHT and S9+4OHT or S9OX+4OHT were assessed by students t-test **p<0.01.

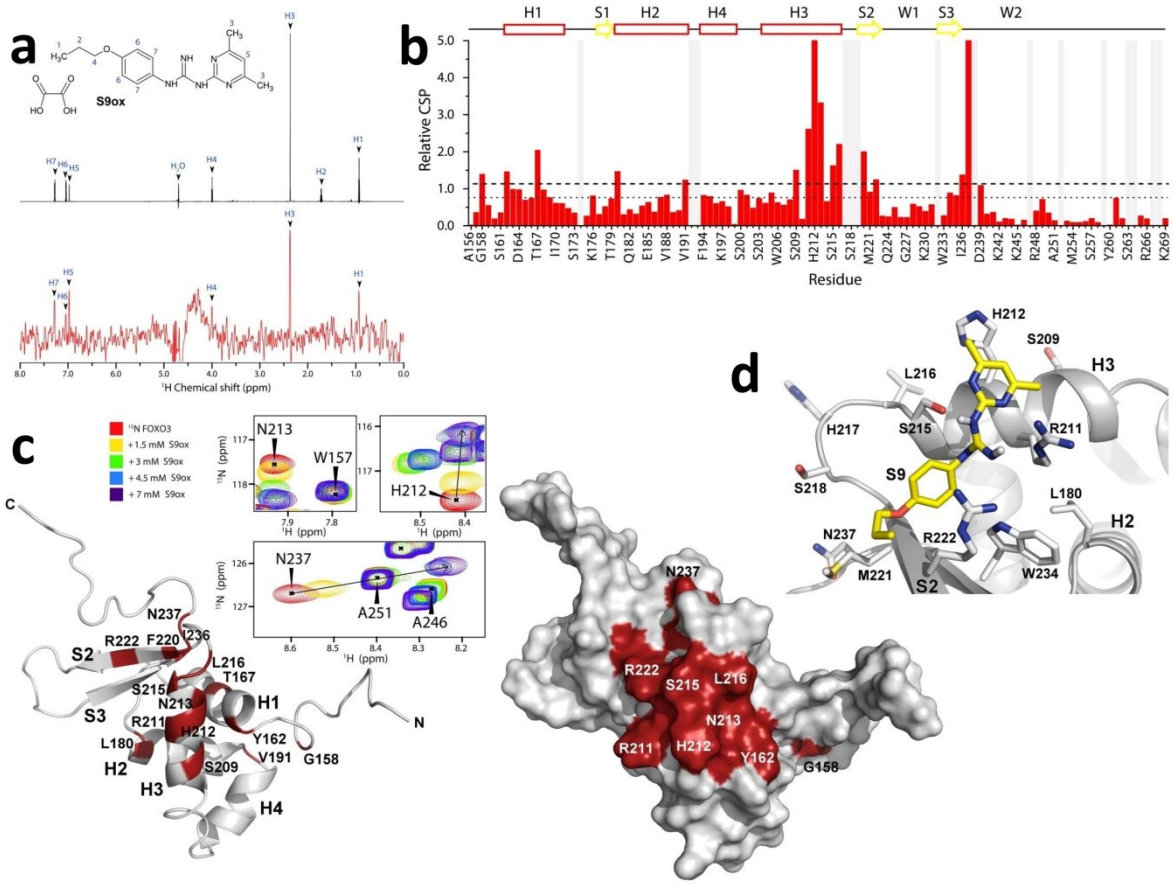

Figure 2: Compounds S9 / S9OX blocks the DNA binding surface of FOXO3-DBD. (a) 1D ^{1}H STD-NMR experiments for S9OX compound in the presence of the 15 μM FOXO3-DBD. The reference spectrum of S9OX is shown in black, the corresponding STD-NMR spectrum is shown in red. Chemically equivalent hydrogens in S9 molecule are numbered from 1 to 7. (b) The summary of quantified chemical shift perturbations (CSPs) obtained for FOXO3-DBD in the presence of 1.5 mM S9OX. The changes in chemical shift resonances were calculated using weighted combination of chemical shifts given by: $CSP = \sqrt{\Delta\delta_H^2 + (\frac{1}{5}\Delta\delta_N)^2}$, where $\Delta\delta_H$ and $\Delta\delta_N$ are differences in chemical shifts of ^{1}H and ^{15}N, respectively, in the free and bound states.[42] The regions of the protein backbone that could not be unambiguously assigned are highlighted in grey. The secondary structure of FOXO3-DBD is indicated on top. The dotted and dashed lines indicate changes greater than the mean and the mean + $1\sigma^{0}_{corr}$, respectively. (c) Observed CSPs mapped onto the solution structure of FOXO3-DBD.[26] Ribbon and surface representations are shown at right and left, respectively. Thirteen residues whose ^{1}H-^{15}N resonances were significantly perturbed

($1\sigma^0_{corr}$ above the mean) are shown in red. Selected signals from the ^1H-^{15}N HSQC spectra of 250 µM FOXO3-DBD in the presence of various concentrations of S9OX are shown in inset. (d) Structural model of FOXO3-DBD with bound S9. The best flexible docking solution consistent with data from ^1H-^{15}N HSQC and STD measurements is shown.

Figure 3

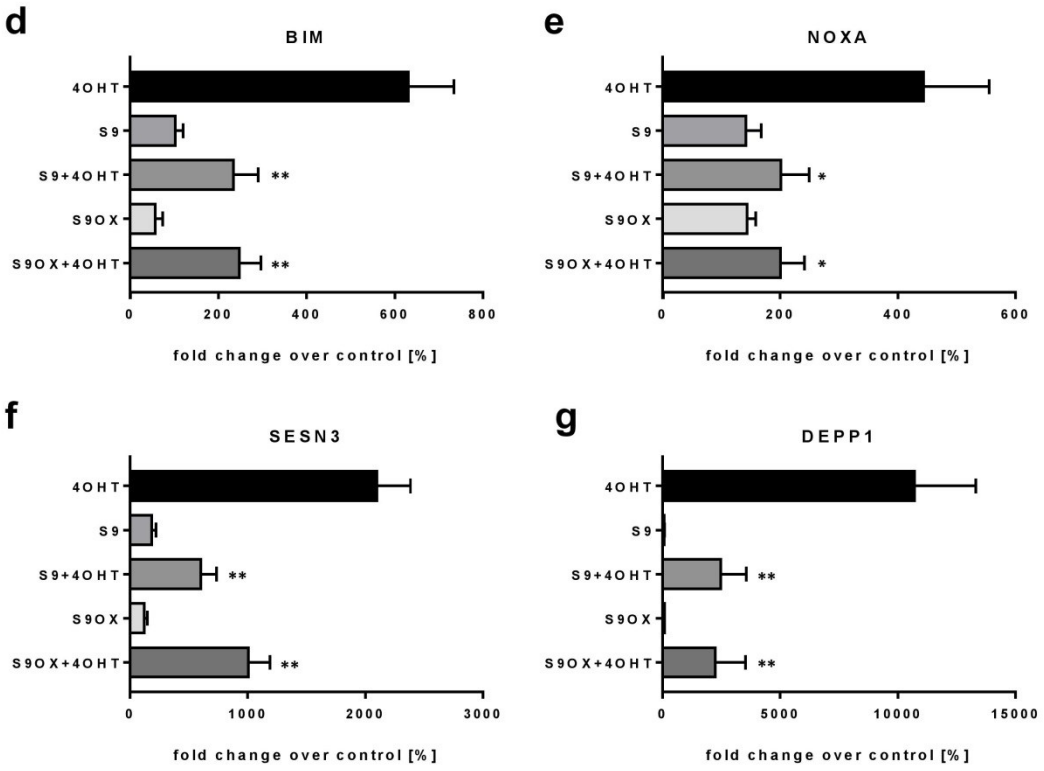

Figure 3: Compounds S9 / S9OX affect induction of FOXO3 target gene mRNAs. (a) Heatmaps of Affymetrix microarray analyses (U133 plus 2.0 expression profiling chips). Total RNA was prepared of SH-EP/FOXO3 cells treated with 100 nM 4OHT alone or in combination with 50 µM S9 for 3 hours. Expression heatmap shows average expression of the differentially expressed genes within three replicates in each condition. The rows were scaled around 0 (b) Venn diagram showing number of genes regulated in common when cells with activated FOXO3 were treated with S9 or solvent as control. BIM (c), NOXA (d), SESN3 (e), and DEPP1 (f) mRNA levels were measured by quantitative RT-PCR in SH-EP/FOXO3 cells after treatment with 100 nM 4OHT for 3 hours alone in combination with 50 µM S9 or S9OX (cells were preincubated with substances for 30 minutes). Bars represent mean +SD of three independent experiments, each performed in triplicates (fold

over untreated control (100%)). Significant differences between 4OHT treatment and S9+4OHT or S9OX+4OHT: *p<0.05, **p<0.01 (students t-test).

Figure 4

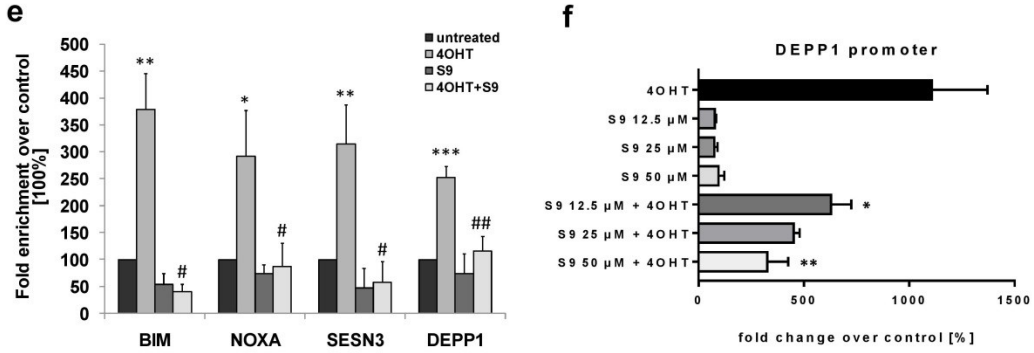

Figure 4: Compound S9 /S9OX inhibit protein expression of FOXO3 regulated proteins and prevent binding of FOXO3 to target promoters. SH-EP/FOXO3 cells were treated for 8 hours (a,b) or 24 hours (c,d) with 100 nM 4OHT alone or in combination with 50 µM S9 or S9OX. Cell lysates were subjected to immunoblot analyses using anti-bodies against NOXA and BIM (8 hours) or SESN3 and DEPP1 (24 hours). Shown are representative immunoblots (a,c) or densitometric analyses of three independent cell lysates +SD. Regulations are expressed as fold over DMSO-control (100%). Significant differences between 4OHT treatment and S9+4OHT or S9OX+4OHT were analyzed by students t-test: *p<0.05, **p<0.01, ***p<0.001. (e) ChIP analyses were performed in SH-EP/FOXO3 cells treated with 100 nM 4OHT for 3 hours alone or on combination with 50 µM S9. Binding of FOXO3 to the promoter regions of BIM, NOXA, SESN3, and DEPP1 was quantified by qRT-PCR. Shown is the mean value +SD of three independent experiments, each performed in duplicates. Significantly different to untreated cells: *P<0.05, **p<0.01, ***p<0.001; significant differences between 4OHT-treatment and S9+4OHT treatment: #P<0.05. ##P<0.01(students t-test). (f) Binding of FOXO3 to the promoter region of DEPP1 was assessed after transfection of a DEPP1-luciferase reporter plasmid into SH-EP/FOXO3 cells. 24 hours after transfection cells were seeded into 24 well plates. After adherence for another 24 hours, cells were treated for 3 hours with 100 nM 4OHT with or without increasing amounts of S9 (preincubated for 30 minutes). Firefly-luciferase was analyzed using Luciferase Assay System (Promega). The increase of light emission was calculated as fold over untreated controls (100%). Shown are mean values +SD of three

independent experiments, each performed in triplicates. Significant differences between 4OHT treatment and S9+4OHT: *p<0.05, **p<0.01 (students t-test).

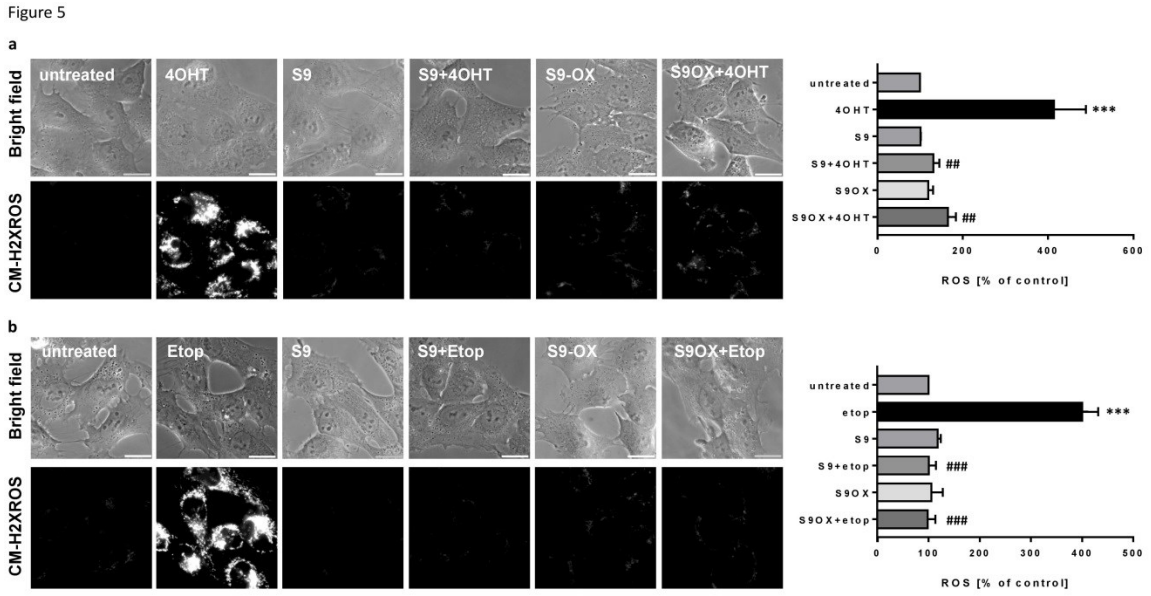

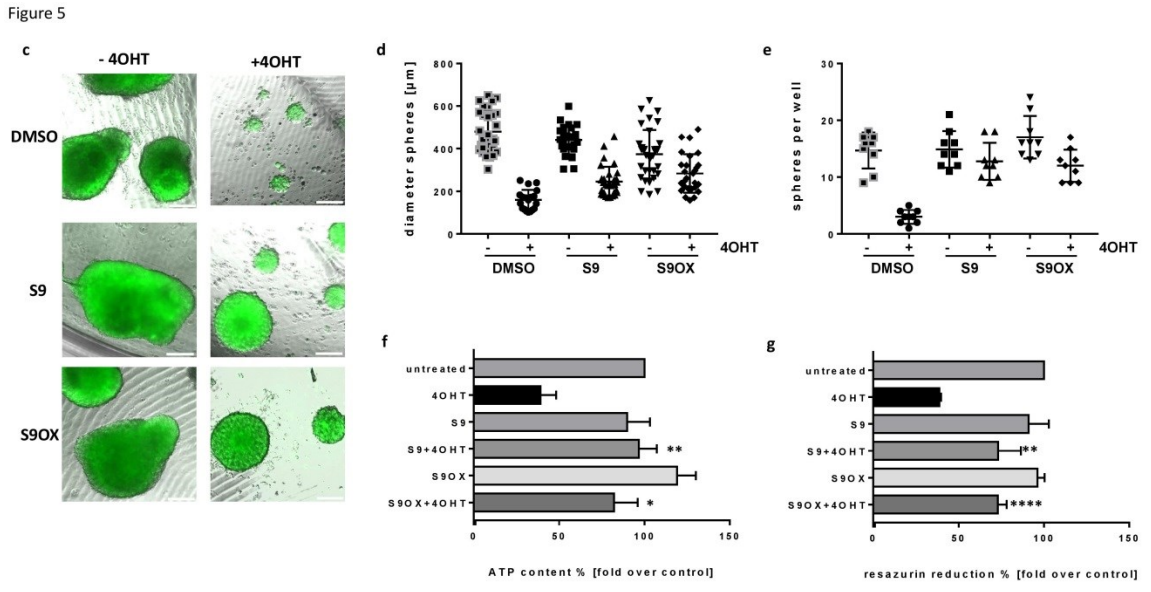

Figure 5: Effects of compounds S9 / S9OX on FOXO3-induced ROS and sphere growth in 3D cell culture models. SH-EP/FOXO3 cells were treated either for 4 hours with 100 nM 4OHT (a) or for 2 hours with 20 µg/ml etoposide (b). 50 µM S9 or S9OX were pre-incubated for 15 minutes. ROS accumulation was analyzed using CM-H2XROS (500 nM). Images were acquired by live-cell imaging using an Axiovert200M microscope, equipped

with a 63x oil objective, bar 20 µm. Shown are representative images (left panel) or densitometric analyses of three independent experiments (more than 15 cells per experiment were quantified) using AxioVision software version 4.8; Significantly different to untreated cells: ***P<0.001; significantly different between 4OHT-treatment and S9+4OHT or S9OX+4OHT cells: ##P<0.01, ###P<0.001 (students t-test). 3D spheroids of NB15/FOXO3-GFP cells were formed by magnetic bioprinting for 72 hours before treatment with 10 nM 4OHT alone or in combination with 5 µM S9 or S9OX for another 72 hours. After one week, spheroids were analyzed by live cell microscopy and further used for viability analyses. Shown are representative images (a) and sphere size / mean diameter (b) as well as the number of spheroids per well (c) out of three independent experiments. Statistical differences between single 4OHT treatment or combinational treatment were assessed by Mann-Whitney test ****P<0.001. Viability of spheroids was assessed by measuring of ATP content (d) or resazurin reduction (e). Shown are mean values +SD of three independent experiment, each performed with spheres of 8 different wells. Statistical differences were assessed by students t-test between 4OHT-DMSO and 4OHT-compound (*P<0.05, **P<0.01, ****p<0.0001).

References

1. Hornsveld, M., Dansen, T.B., Derksen, P.W. & Burgering, B.M.T. Re-evaluating the role of FOXOs in cancer. *Seminars in cancer biology* **50**, 90-100 (2018).
2. Calnan, D.R. & Brunet, A. The FoxO code. *Oncogene* **27**, 2276-2288 (2008).
3. de Keizer, P.L., Burgering, B.M. & Dansen, T.B. Forkhead box o as a sensor, mediator, and regulator of redox signaling. *Antioxidants & redox signaling* **14**, 1093-1106 (2011).
4. Salcher, S. et al. C10ORF10/DEPP, a transcriptional target of FOXO3, regulates ROS-sensitivity in human neuroblastoma. *Mol Cancer* **13**, 224 (2014).
5. Hui, R.C. et al. Doxorubicin activates FOXO3a to induce the expression of multidrug resistance gene ABCB1 (MDR1) in K562 leukemic cells. *Mol Cancer Ther* **7**, 670-678 (2008).
6. Wilson, M.S., Brosens, J.J., Schwenen, H.D. & Lam, E.W. FOXO and FOXM1 in cancer: the FOXO-FOXM1 axis shapes the outcome of cancer chemotherapy. *Current drug targets* **12**, 1256-1266 (2011).
7. Naka, K. et al. TGF-beta-FOXO signalling maintains leukaemia-initiating cells in chronic myeloid leukaemia. *Nature* **463**, 676-680 (2010).
8. Rupp, M. et al. FOXO3-mediated chemo-protection in high-stage neuroblastoma depends on wild-type TP53 and SESN3. *Oncogene* **36**, 6190-6203 (2017).
9. Hagenbuchner, J. et al. FOXO3-induced reactive oxygen species are regulated by BCL2L11 (Bim) and SESN3. *J Cell Sci* **125**, 1191-1203 (2012).
10. Hagenbuchner, J., Kuznetsov, A.V., Obexer, P. & Ausserlechner, M.J. BIRC5/Survivin enhances aerobic glycolysis and drug resistance by altered regulation of the mitochondrial fusion/fission machinery. *Oncogene* **32**, 4748-4757 (2013).
11. Hagenbuchner, J. et al. Nuclear FOXO3 predicts adverse clinical outcome and promotes tumor angiogenesis in neuroblastoma. *Oncotarget* **7**, 77591-77606 (2016).
12. Kerdiles, Y.M. et al. Foxo transcription factors control regulatory T cell development and function. *Immunity* **33**, 890-904 (2010).
13. Harada, Y. et al. Transcription factors Foxo3a and Foxo1 couple the E3 ligase Cbl-b to the induction of Foxp3 expression in induced regulatory T cells. *The Journal of experimental medicine* **207**, 1381-1391 (2010).
14. Gormally, M.V. et al. Suppression of the FOXM1 transcriptional programme via novel small molecule inhibition. *Nature communications* **5**, 5165 (2014).
15. Hegde, N.S., Sanders, D.A., Rodriguez, R. & Balasubramanian, S. The transcription factor FOXM1 is a cellular target of the natural product thiostrepton. *Nature chemistry* **3**, 725-731 (2011).
16. Nagashima, T. et al. Discovery of novel forkhead box O1 inhibitors for treating type 2 diabetes: improvement of fasting glycemia in diabetic db/db mice. *Molecular pharmacology* **78**, 961-970 (2010).
17. Tsai, K.L. et al. Crystal structure of the human FOXO3a-DBD/DNA complex suggests the effects of post-translational modification. *Nucleic acids research* **35**, 6984-6994 (2007).
18. Le Guilloux, V., Schmidtke, P. & Tuffery, P. Fpocket: An open source platform for ligand pocket detection. *BMC Bioinformatics* **10**, 168 (2009).

19. Obexer, P. & Ausserlechner, M.J. X-linked inhibitor of apoptosis protein - a critical death resistance regulator and therapeutic target for personalized cancer therapy. *Front Oncol* **4**, 197 (2014).
20. Kulharia, M., J, B.S., S., G.R. & Jackson, R.M. InCa-SiteFinder: a method for structure-based prediction of inositol and carbohydrate binding sites on proteins. *J Mol Graph Model.* **28**, 297-303 (2009).
21. ULC, C.C.G., Edn. 11.2011 (1010 Sherbooke St. West, Suite #910, Montreal, QC, Canada, H3A 2R7; 2011).
22. Le Guilloux, V., Schmidtke, P. & Tuffery, P. Fpocket: an open source platform for ligand pocket detection. *BMC bioinformatics* **10**, 168 (2009).
23. Boura, E. et al. Both the N-terminal loop and wing W2 of the forkhead domain of transcription factor Foxo4 are important for DNA binding. *J Biol Chem* **282**, 8265-8275 (2007).
24. Wishart, D.S. et al. DrugBank: a knowledgebase for drugs, drug actions and drug targets. *Nucleic acids research* **36**, D901-906 (2008).
25. Obexer, P., Geiger, K., Ambros, P.F., Meister, B. & Ausserlechner, M.J. FKHRL1-mediated expression of Noxa and Bim induces apoptosis via the mitochondria in neuroblastoma cells. *Cell Death Differ* **14**, 534-547 (2007).
26. Wang, F. et al. Biochemical and structural characterization of an intramolecular interaction in FOXO3a and its binding with p53. *Journal of molecular biology* **384**, 590-603 (2008).
27. Trott, O. & Olson, A.J. AutoDock Vina: improving the speed and accuracy of docking with a new scoring function, efficient optimization, and multithreading. *Journal of computational chemistry* **31**, 455-461 (2010).
28. Salcher, S., Hermann, M., Kiechl-Kohlendorfer, U., Ausserlechner, M.J. & Obexer, P. C10ORF10/DEPP-mediated ROS accumulation is a critical modulator of FOXO3-induced autophagy. *Mol Cancer* **16**, 95 (2017).
29. Luo, C.T. & Li, M.O. Foxo transcription factors in T cell biology and tumor immunity. *Seminars in cancer biology* **50**, 13-20 (2018).
30. McLaughlin, C.N. & Broihier, H.T. Keeping Neurons Young and Foxy: FoxOs Promote Neuronal Plasticity. *Trends in genetics : TIG* **34**, 65-78 (2018).
31. Yadav, R.K., Chauhan, A.S., Zhuang, L. & Gan, B. FoxO transcription factors in cancer metabolism. *Seminars in cancer biology* **50**, 65-76 (2018).
32. Baar, M.P. et al. Targeted Apoptosis of Senescent Cells Restores Tissue Homeostasis in Response to Chemotoxicity and Aging. *Cell* **169**, 132-147.e116 (2017).
33. Wolber, G. & Langer, T. LigandScout: 3-D Pharmacophores Derived from Protein-Bound Ligands and Their Use as Virtual Screening Filters. *Journal of Chemical Information and Modeling* **45**, 160-169 (2005).
34. Tsai, K.-L. et al. Crystal structure of the human FOXO3a-DBD/DNA complex suggests the effects of post-translational modification. *Nucleic Acids Research* **35**, 6984-6994 (2007).
35. Jones, G., Willett, P., Glen, R.C., Leach, A.R. & Taylor, R. Development and validation of a genetic algorithm for flexible docking. *Journal of Molecular Biology* **267**, 727-748 (1997).
36. Wishart, D.S. et al. DrugBank: a knowledgebase for drugs, drug actions and drug targets. *Nucleic Acids Research* **36**, D901-D906 (2008).

37. Yokogawa, M. et al. NMR analyses of the interaction between the FYVE domain of early endosome antigen 1 (EEA1) and phosphoinositide embedded in a lipid bilayer. *J Biol Chem* **287**, 34936-34945 (2012).
38. Hagenbuchner, J. et al. The tubulin inhibitor MG-2477 induces autophagy-regulated cell death, ROS accumulation and activation of FOXO3 in neuroblastoma. *Oncotarget* **8**, 32009-32026 (2017).
39. Schmidt, S. et al. Identification of glucocorticoid-response genes in children with acute lymphoblastic leukemia. *Blood* **107**, 2061-2069 (2006).
40. Wu, Z., Irizarry, R.A., Gentleman, R., Martinez-Murillo, F. & Spencer, F. A Model-Based Background Adjustment for Oligonucleotide Expression Arrays. *Journal of the American Statistical Association* **99**, 909-917 (2004).
41. Hagenbuchner, J., Kiechl-Kohlendorfer, U., Obexer, P. & Ausserlechner, M.J. BIRC5/Survivin as a target for glycolysis inhibition in high-stage neuroblastoma. *Oncogene* **35**, 2052-2061 (2016).
42. Williamson, M.P. Using chemical shift perturbation to characterise ligand binding. *Progress in nuclear magnetic resonance spectroscopy* **73**, 1-16 (2013).

Figure S1

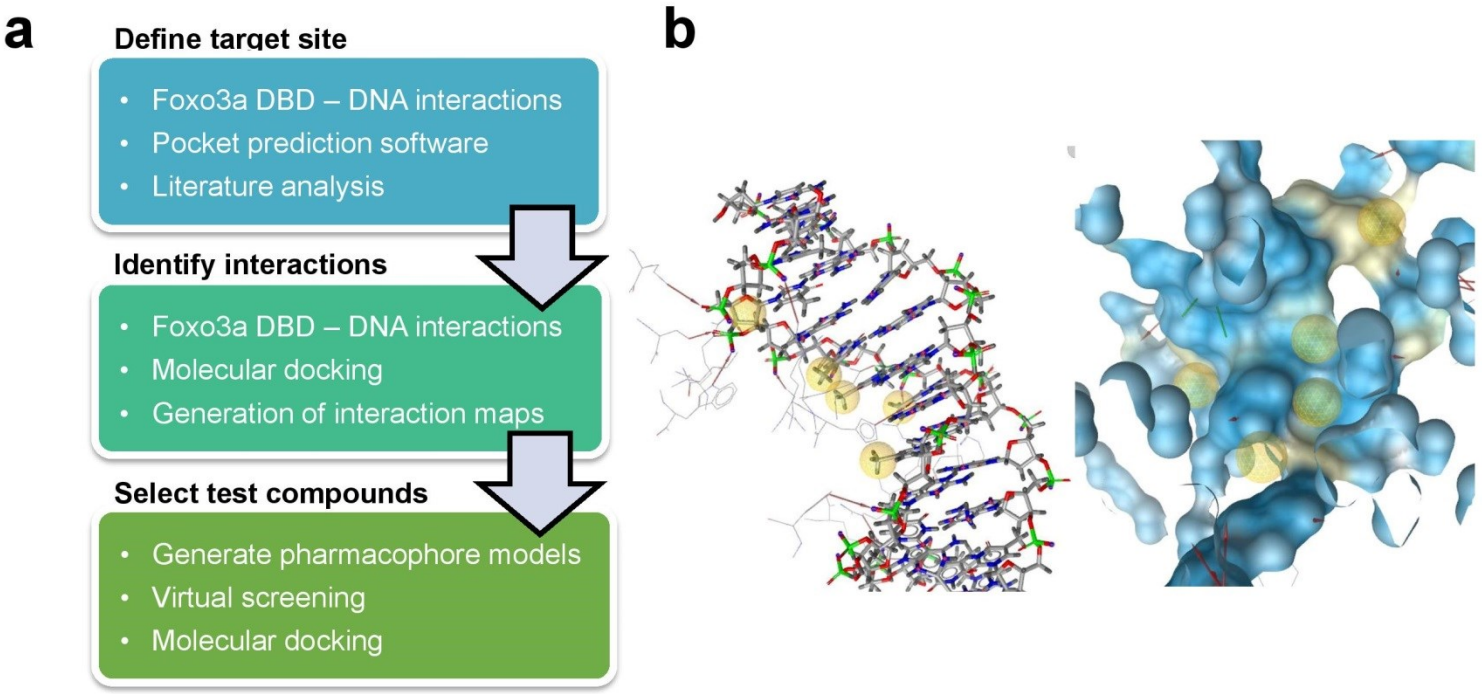
a
Define target site
• Foxo3a DBD – DNA interactions
• Pocket prediction software
• Literature analysis
Identify interactions
• Foxo3a DBD – DNA interactions
• Molecular docking
• Generation of interaction maps
Select test compounds
• Generate pharmacophore models
• Virtual screening
• Molecular docking
b

Figure S2

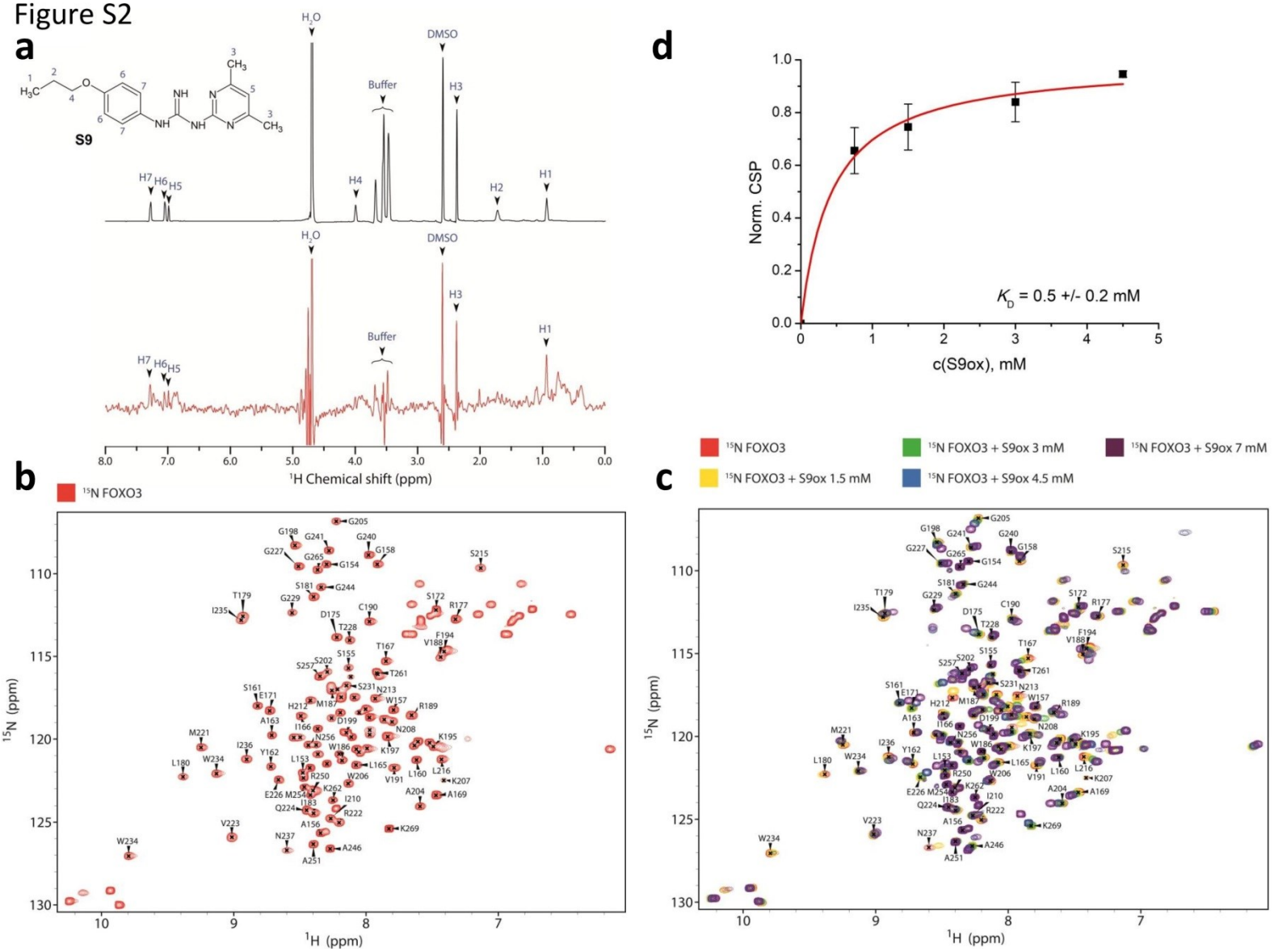
a
S9
H2O
DMSO
Buffer
H3
H1
H2
H4
H5
H6
H7
1H Chemical shift (ppm)
d
Norm. CSP
c(S9ox), mM
KD = 0.5 +/- 0.2 mM
b
15N FOXO3
15N (ppm)
1H (ppm)
c
15N FOXO3
15N FOXO3 + S9ox 1.5 mM
15N FOXO3 + S9ox 3 mM
15N FOXO3 + S9ox 4.5 mM
15N FOXO3 + S9ox 7 mM

Supplemental Figure 1.

Strategy to identify small molecule compounds that interact with FOXO3-DBD. (a) Overview of the *in silico* workflow employed to identify FOXO3 inhibitors. (b) Interactions between FOXO3 DBD and the 13 bp DNA strand were represented as pharmacophore features. DNA is shown as sticks and FOXO3 DBD residues as lines (left) and the pharmacophore features were mapped onto the FOXO3 DBD protein surface (blue, right).

Supplemental Figure S2.

S9 binding to FOXO3-DBD. (a) 1D ^{1}H STD-NMR experiments for S9 compound in the presence of the 15 μM FOXO3-DBD. The reference spectrum of S9 is shown in black, the corresponding STD-NMR spectrum is shown in red. Chemically equivalent hydrogens in S9 molecule are numbered from 1 to 7. 10% dimethyl sulfoxide (DMSO) was added to the buffer to increase the S9 solubility. (b) ^{1}H-^{15}N HSQC spectrum of ^{15}N-labeled FOXO3-DBD. (c) ^{1}H-^{15}N HSQC spectra of ^{15}N-labeled FOXO3-DBD in the absence of S9ox (red) and in the presence of various concentrations of S9ox. The interaction induced both the change in signal positions or significant signal intensity reduction in the ^{1}H-^{15}N HSQC spectrum of FOXO3-DBD. (d) Representative binding isotherm used to calculate the dissociation constant of the interaction between FOXO3-DBD and S9ox.

Synthesis of S9 and S9ox

General

Chemicals and solvents were either purchased from commercial suppliers. For thin-layer chromatography (TLC), silica gel plates Merck 60 F254 were used and compounds were visualized by irradiation with UV light and/or by treatment with a solution ninhydrine followed by heating. Column chromatography was performed using silica gel Merck 60 (particle size 0.063-0.200 mm). ^{1}H-NMR, ^{13}C-NMR spectra were recorded on Bruker AVANCE III 400. Chemical shifts for protons are given in δ relative to tetramethylsilane (TMS) and are referenced to residual protium in the NMR solvent (DMSO-d_6: δ = 2.50 ppm, Methanol-d_4: δ = 4.87 ppm). Chemical shifts for carbon are referenced to the carbon in NMR solvent (DMSO-d_6: δ = 39.52 ppm,, Methanol-d_4: δ = 49.00 ppm. The coupling constants J are given in Hz. IR DRIFT spectras were recorded with Nicolet AVATAR 370 FT-IR in cm^{-1}. High-resolution mass spectras were recorded with LCQ Fleet spectrometer.

Reaction scheme

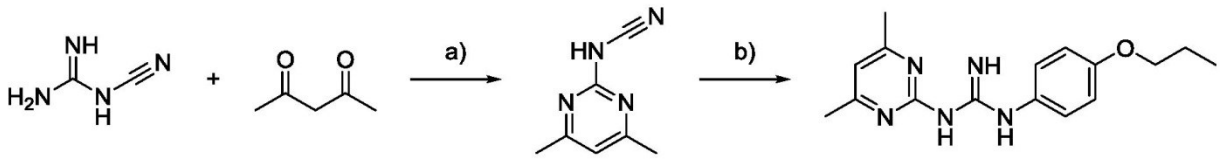

Scheme 1: Synthetic route to S9. Reagents and conditions: a) NaOH, H_2O, reflux, 22% yield, b) 4-propoxyaniline, EtOH, reflux, 47% yield.

Preparation of substrates

N-(4,6-Dimethylpyrimidin-2-yl)cyanamide

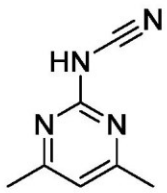

N-(4,6-Dimethylpyrimidin-2-yl)cyanamide was prepared according to previously reported procedure.[1]

Cyanoguanidine (5.0 g, 60 mmol), acetylacetone (9.0 g, 90 mmol) were added to a solution of NaOH (0.3M, 40 ml) and the reaction mixture was stirred under reflux 48 h. Then the mixture was cooled to 4 °C, solids were filtered and washed with minimal amount of water. Filtrate cake was recrystallized from boiling ethanol (approx. 120 ml).

22% **yield**, white solid, **m.p.** = 228.7 °C, **^{1}H-NMR:** (400 MHz, DMSO-d_6) δ = 12.58 (s, 1H), 6.63 (s, 1H), 2.31 (s, 6H). ppm, **^{13}C-NMR:** (101 MHz, DMSO-d_6) δ = 166.8, 160.2 (2C), 115.8, 109.7, 21.9 (2C) ppm, **IR** (KBr) ν = 3503, 3282, 3249, 3064, 3010, 2980, 2857, 2842, 2815, 2621, 2319, 2244, 2202, 2175, 2089, 1838, 1727, 1649, 1610, 1422, 1362, 1323, 1231, 1195, 1165, 1036, 1018, 985 cm^{-1}, **HRMS** (ESI+) *m*/*z*: calcd. for $C_7H_9N_4$ $[M+H]^+$: 149.0827, found: 149.0792.

1-(4,6-Dimethylpyrimidin-2-yl)-3-(4-propoxyphenyl)guanidine

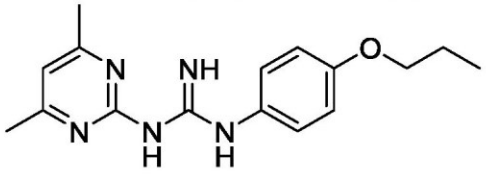

4-Propoxyaniline (307 mg, 2.03 mmol, 1.5 eq.) was added dropwise to a suspension of *N*-(4,6-dimethylpyrimidin-2-yl)cyanamide (200 mg, 1.35 mmol; 1.0 eq.) in anhydrous EtOH (4 ml). Solids were dissolved during addition of aniline. Reaction mixture was heated to reflux. At this temperature reaction mixture was stirred for 72 h and monitored by TLC (eluent: MeOH). Then reaction mixture was cooled to -35 °C and solution of NaOH (10 ml, 10% w/w) was added dropwise. Solids were filtered and washed with Et_2O (4 × 20 ml). Filtrate cake was dissolved in MeOH and purified by column chromatography on silica with MeOH as an eluent.

47% **yield**, white solid, **m.p.** = 191.5 °C, $\boldsymbol{R_f}$ **=** 0.36 (MeOH, ninhydrine), **^{1}H-NMR:** (400 MHz, Methanol-d_4) δ = 7.21 – 7.08 (m, 2H), 6.92 – 6.83 (m, 2H), 6.61 (s, 1H), 3.89 (t, J = 6.5 Hz, 2H), 3.27 (p, J = 1.6 Hz, 1H), 2.31 (s, 6H), 1.83 – 1.65 (m, 2H), 1.01 (t, J = 7.4 Hz, 3H) ppm, **^{13}C-NMR:** (101 MHz, Methanol-d_4) δ = 168.6 (2C), 165.2, 158.1, 157.3, 133.7, 126.6 (2C), 116.4 (2C), 112.9, 70.9, 23.74 (2C), 23.69, 10.9 ppm, **IR** (KBr) ν = 3312, 3106, 3088, 2959, 2893, 2869, 1631, 1577, 1527, 1509, 1419, 1383, 1344, 1237, 1171, 1117, 1075, 1048, 1024 cm^{-1}, **HRMS** (ESI+) *m*/*z*: calcd. for $C_{16}H_{22}N_5O$ $[M+?]^+$: 300.1824, found: 300.1773.

[1] WO2013/53726, **2013**, *A1*.

NMR spectra

N-(4,6-Dimethylpyrimidin-2-yl)cyanamide

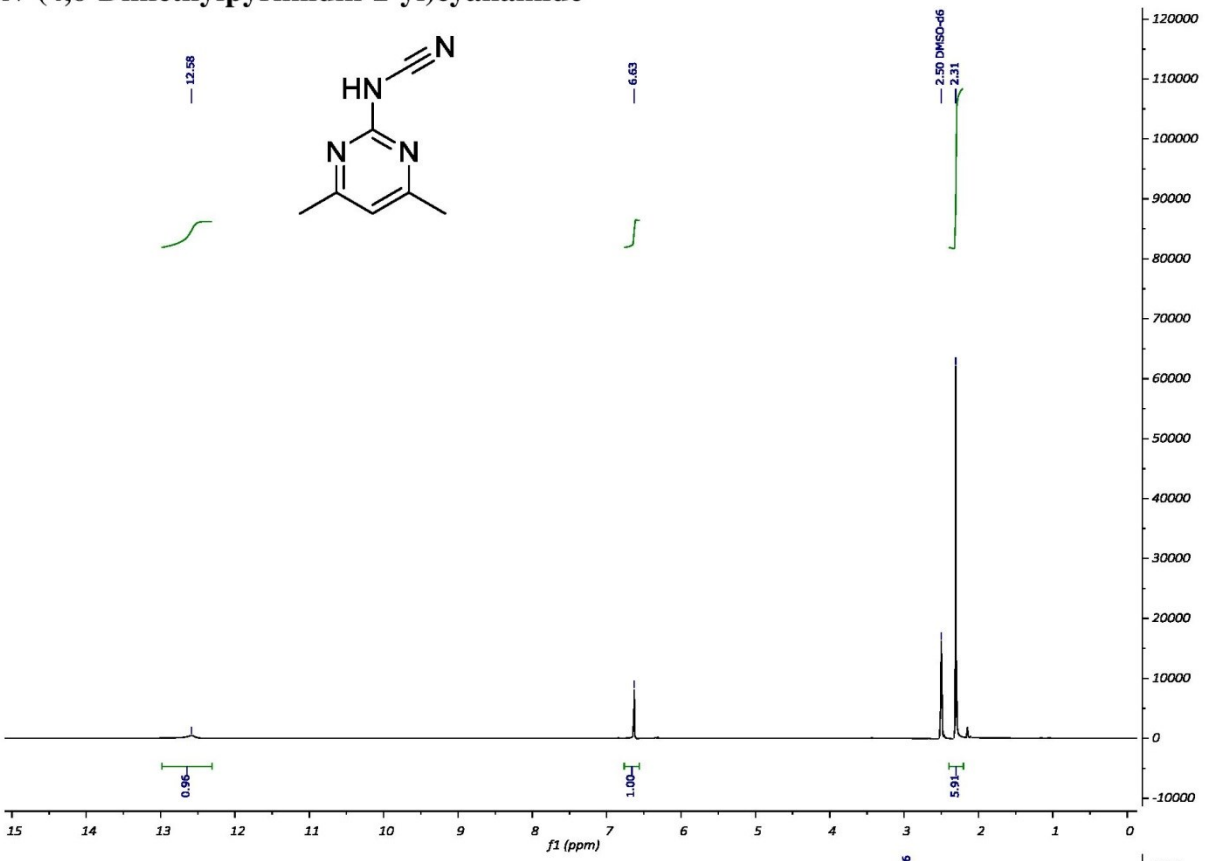

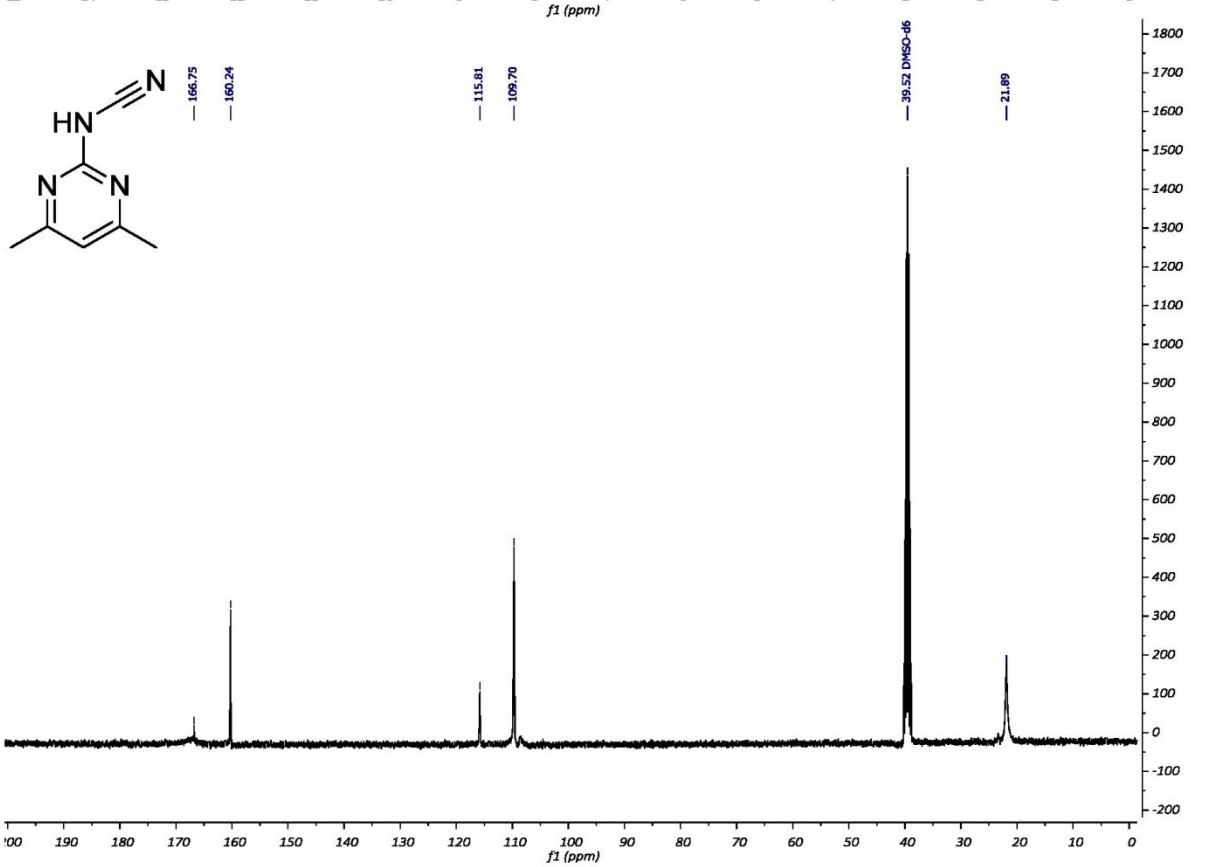

DEPT-135

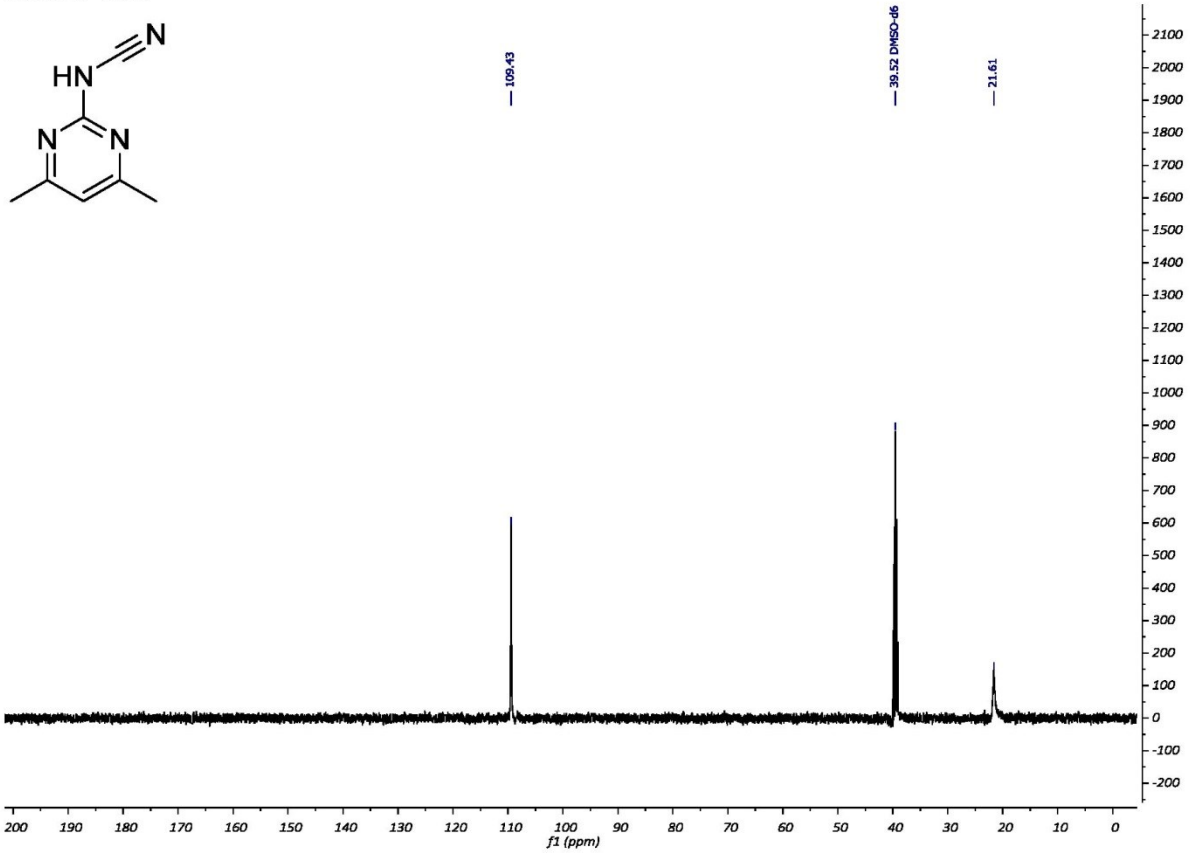

COSY

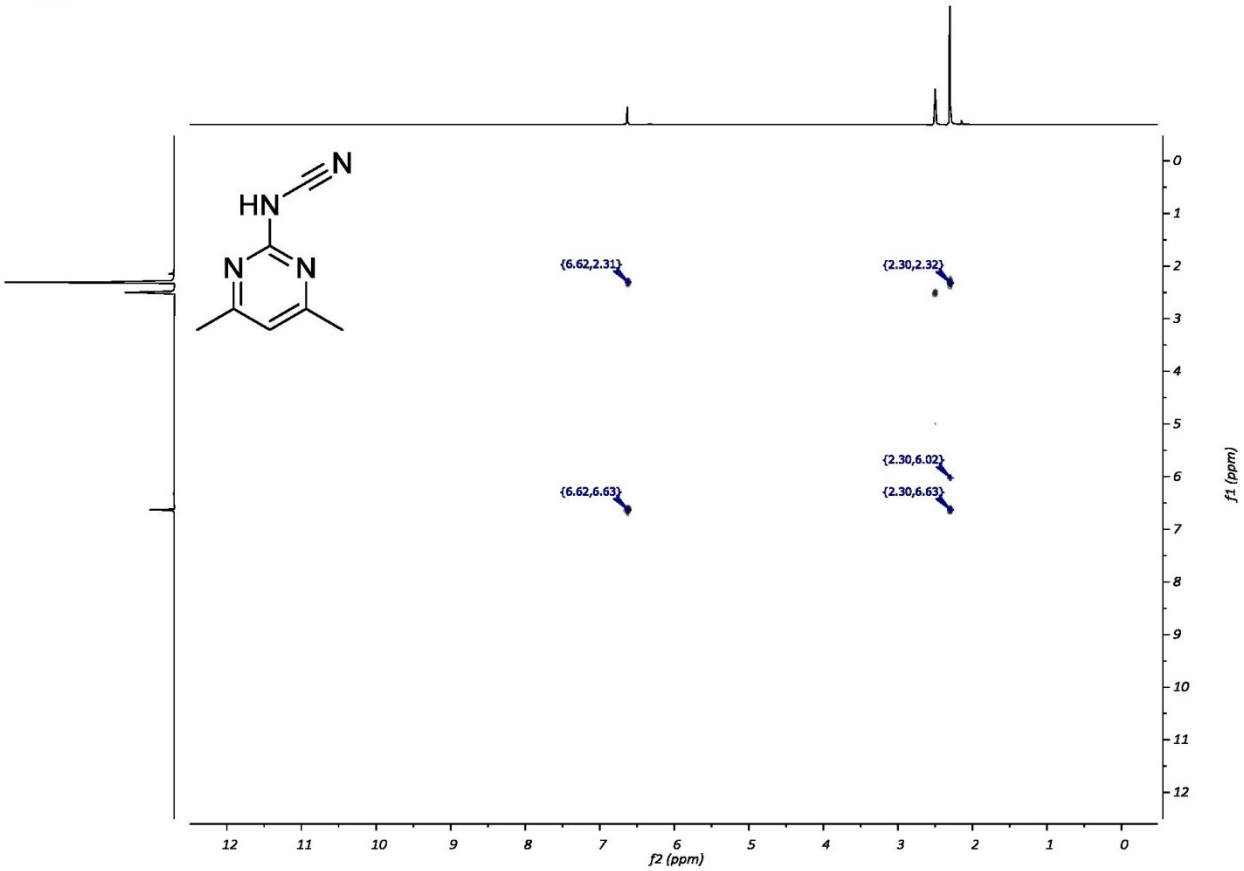

HSQC

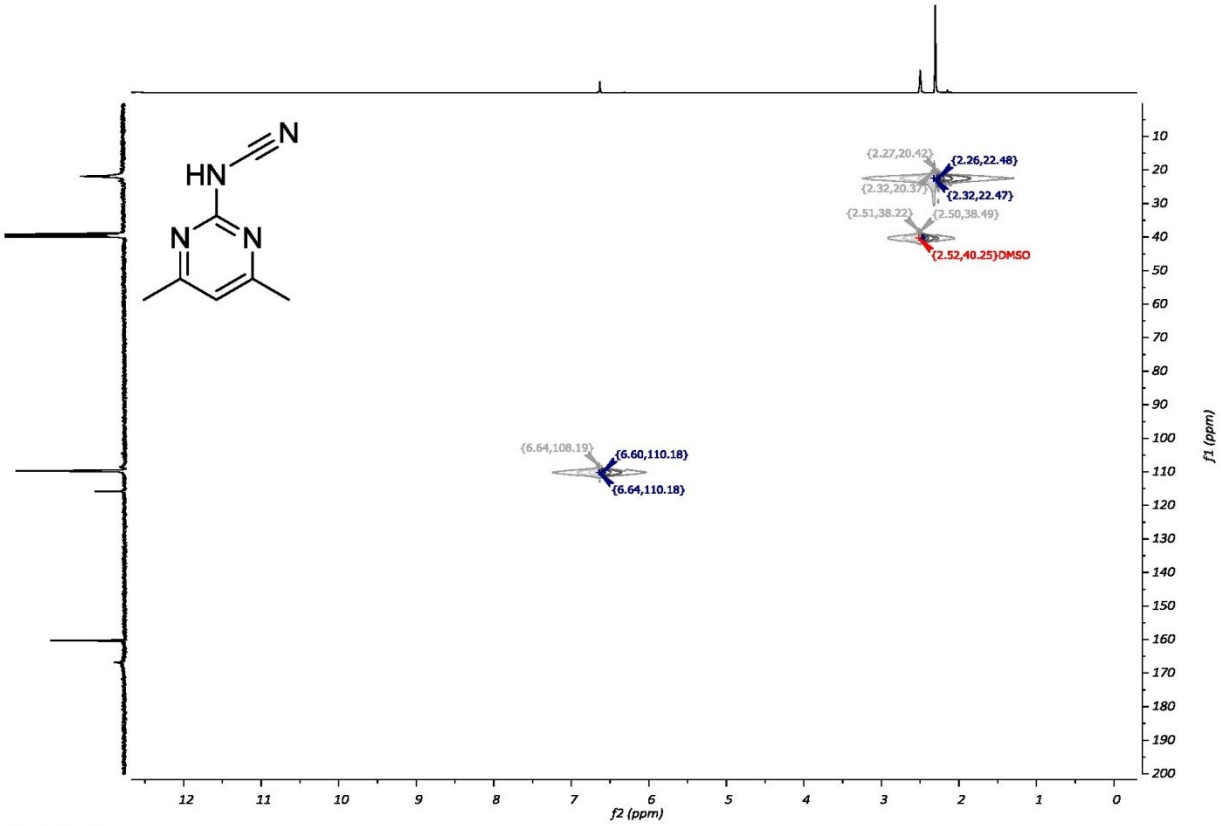
HN
N
N
{2.27,20.42}
{2.26,22.48}
{2.32,20.37}
{2.32,22.47}
{2.51,38.22}
{2.50,38.49}
{2.52,40.25}DMSO
{6.64,108.19}
{6.60,110.18}
{6.64,110.18}
f2 (ppm)
f1 (ppm)

HMBC

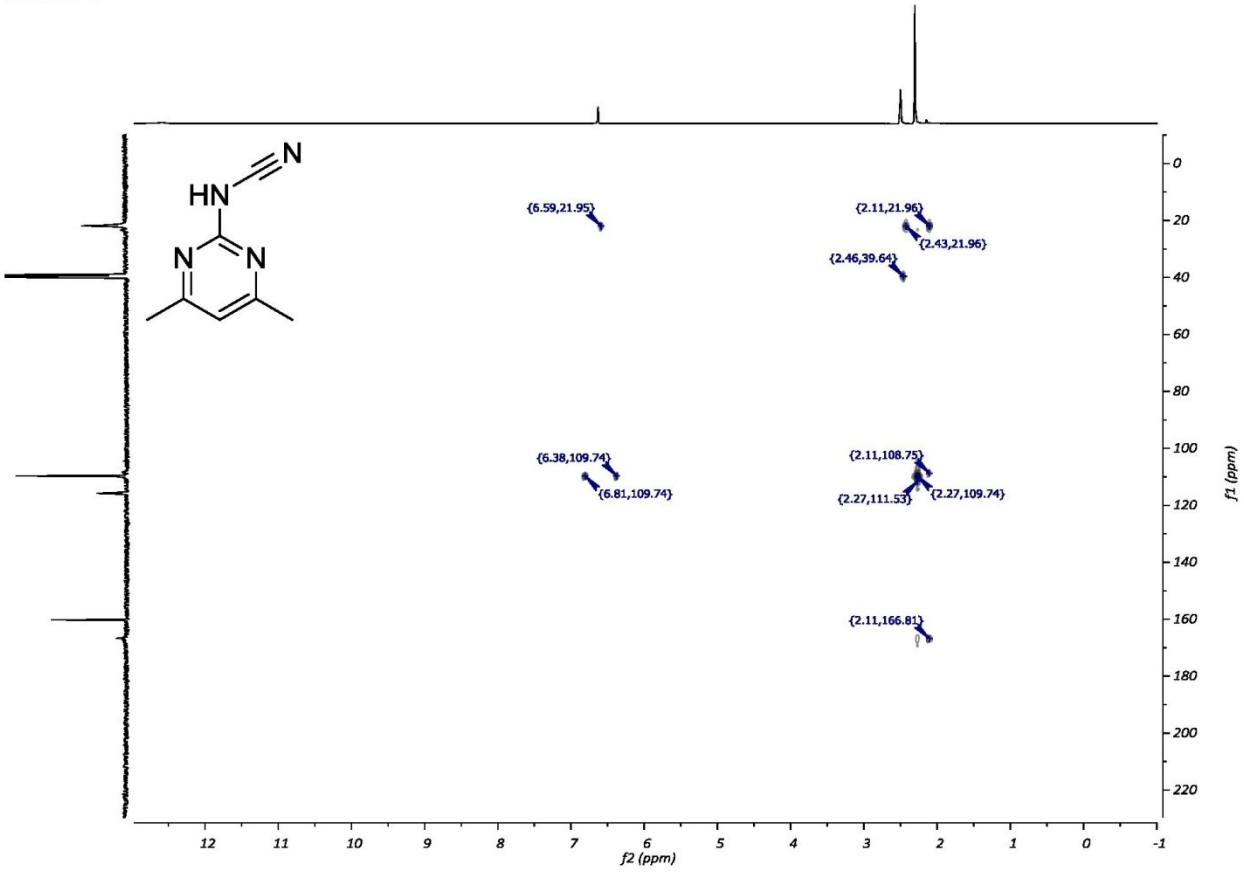
HN
N
N
{6.59,21.95}
{2.11,21.96}
{2.43,21.96}
{2.46,39.64}
{6.38,109.74}
{6.81,109.74}
{2.11,108.75}
{2.27,111.53}
{2.27,109.74}
{2.11,166.81}
f2 (ppm)
f1 (ppm)

1-(4,6-Dimethylpyrimidin-2-yl)-3-(4-propoxyphenyl)guanidine

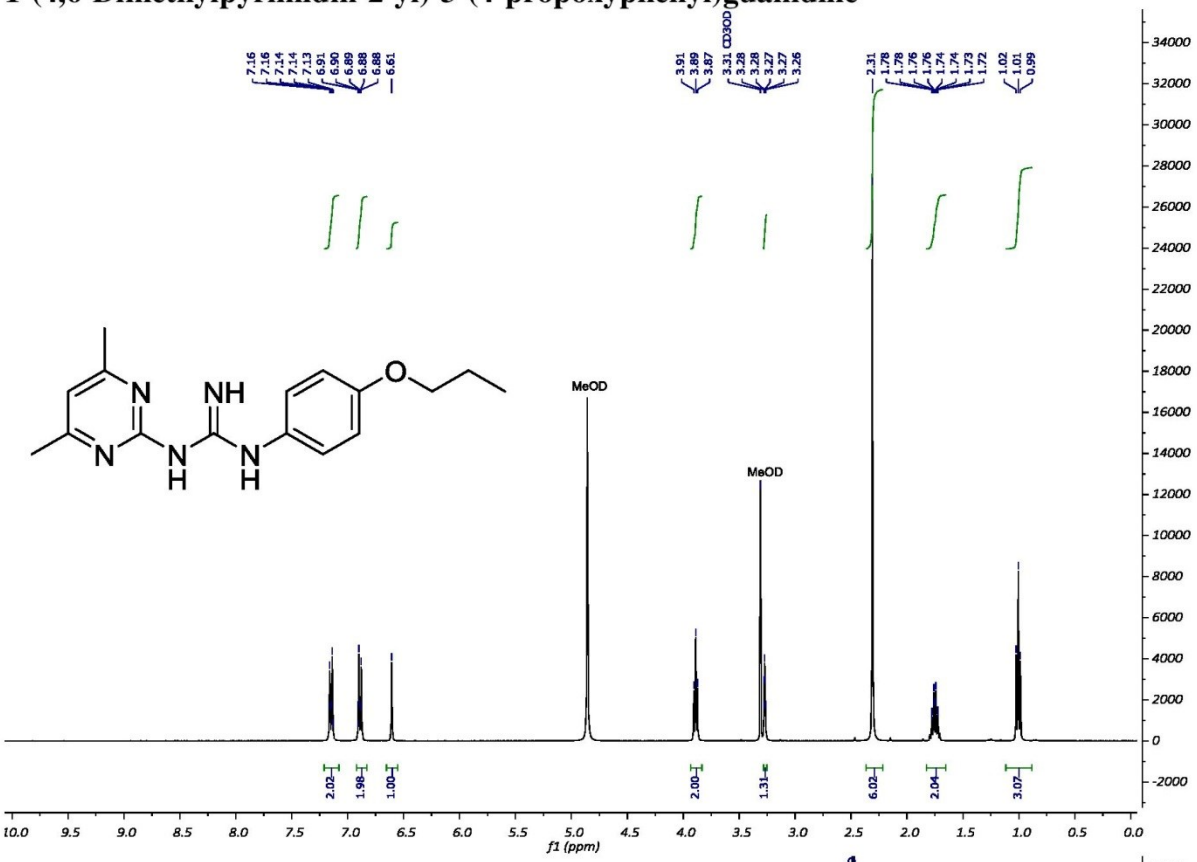

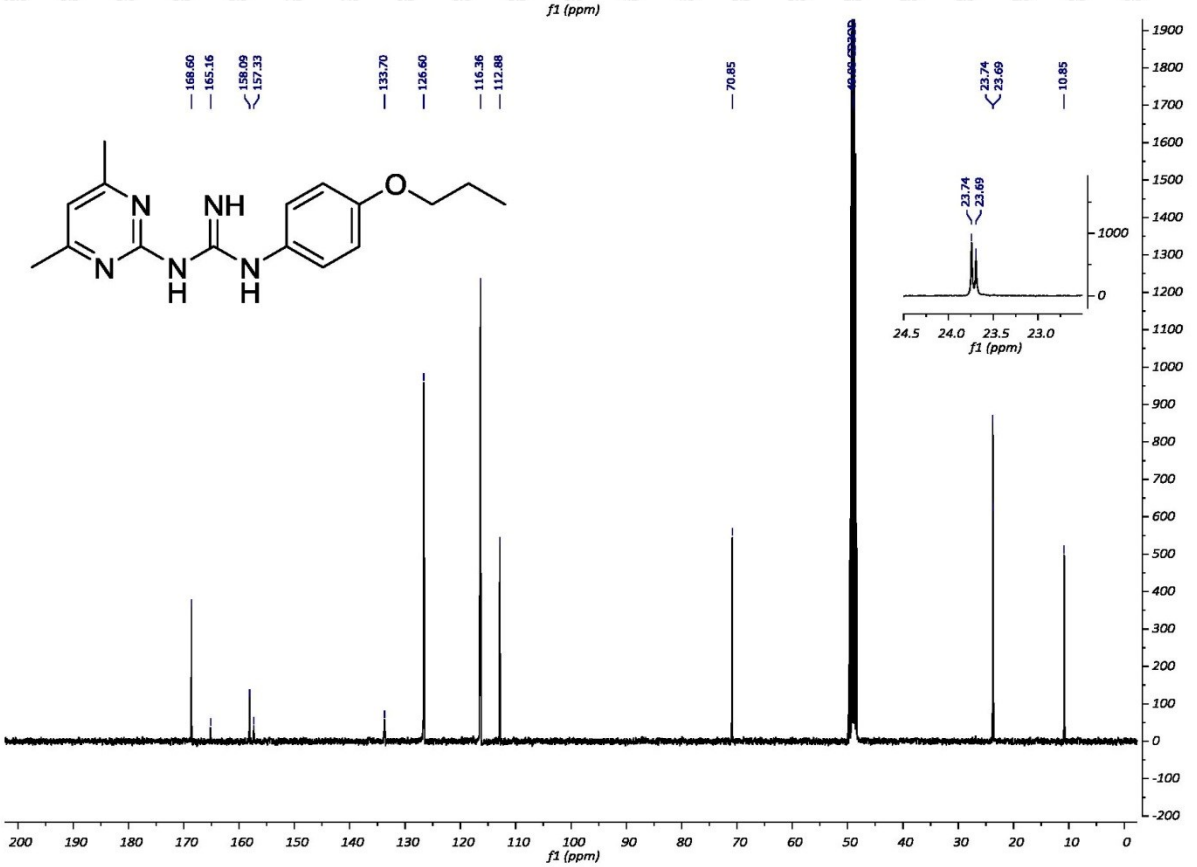

DEPT-135

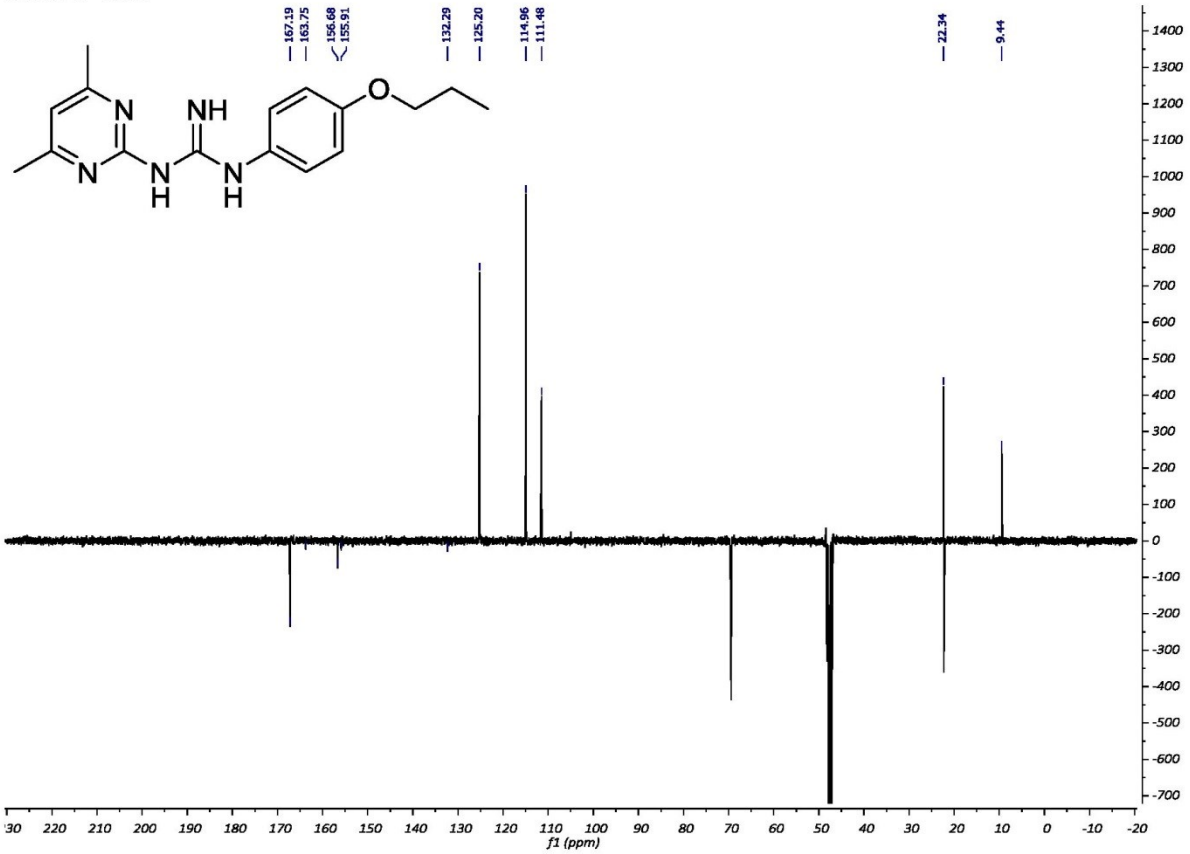

COSY

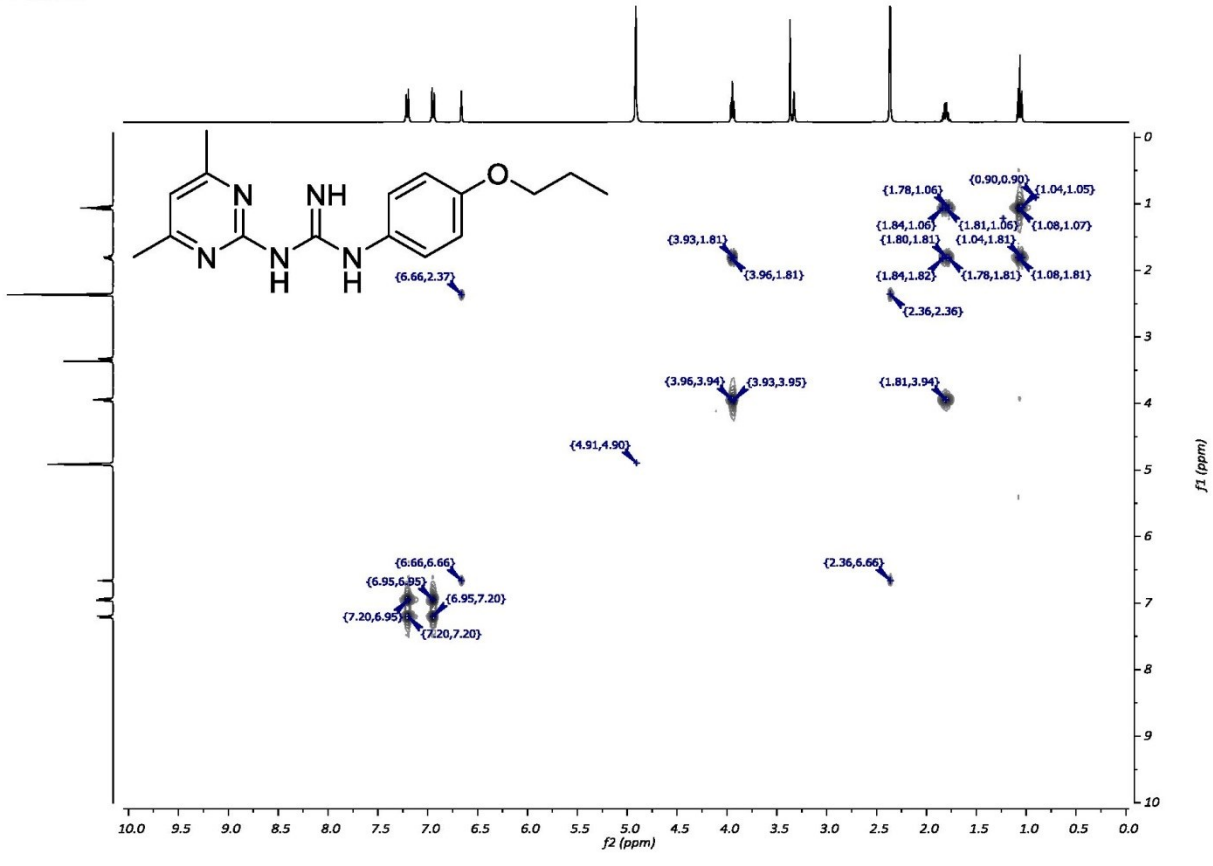

HSQC

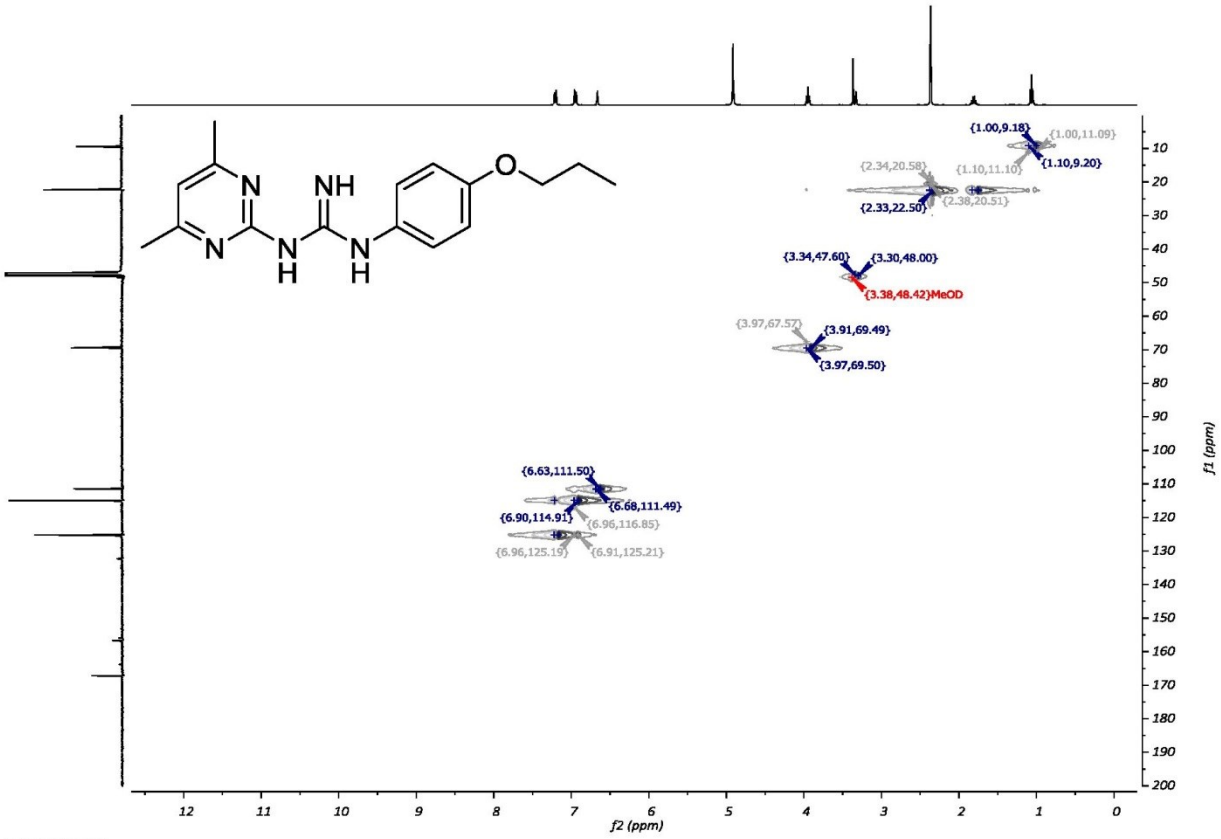
{1.00,9.18}
{1.00,11.09}
{1.10,9.20}
{2.34,20.58}
{1.10,11.10}
{2.33,22.50}
{2.38,20.51}
{3.34,47.60}
{3.30,48.00}
{3.38,48.42}MeOD
{3.97,67.57}
{3.91,69.49}
{3.97,69.50}
{6.63,111.50}
{6.68,111.49}
{6.90,114.91}
{6.96,116.85}
{6.96,125.19}
{6.91,125.21}
f2 (ppm)
f1 (ppm)

HMBC

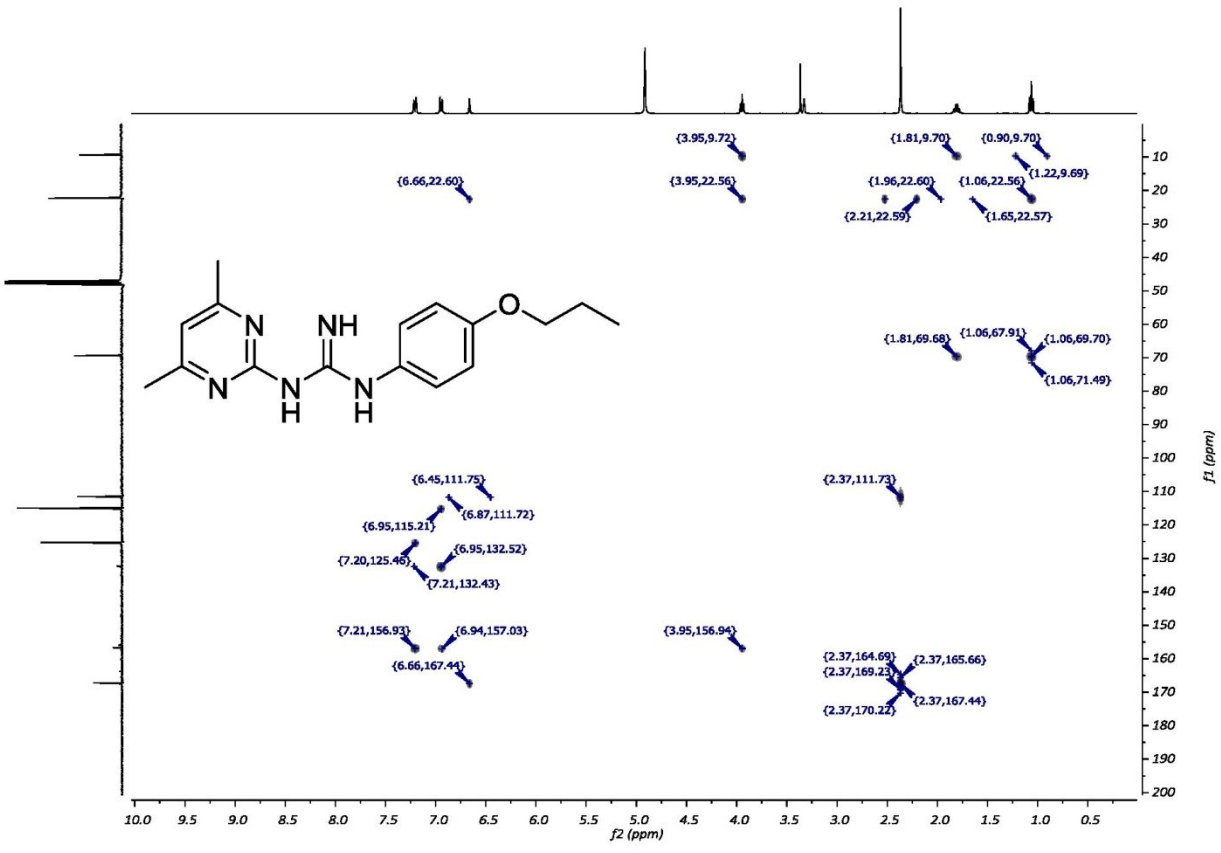
{3.95,9.72}
{1.81,9.70}
{0.90,9.70}
{1.22,9.69}
{6.66,22.60}
{3.95,22.56}
{1.96,22.60}
{1.06,22.56}
{2.21,22.59}
{1.65,22.57}
{1.81,69.68}
{1.06,67.91}
{1.06,69.70}
{1.06,71.49}
{6.45,111.75}
{2.37,111.73}
{6.87,111.72}
{6.95,115.21}
{7.20,125.46}
{6.95,132.52}
{7.21,132.43}
{7.21,156.93}
{6.94,157.03}
{3.95,156.94}
{6.66,167.44}
{2.37,164.69}
{2.37,165.66}
{2.37,169.23}
{2.37,167.44}
{2.37,170.22}
f2 (ppm)
f1 (ppm)

Preparation of oxalate salt derived from S9

Corresponding oxalate salt derived from 1-(4,6-dimethylpyrimidin-2-yl)-3-(4-propoxyphenyl)guanidine was prepared according to previously reported procedure.[2]
Oxalate acid dihydrate (27.1 mg; 0.167 mmol; 1.0 eq.) was dissolved in distilled water (1.0 ml). To this solution was added 1-(4,6-dimethylpyrimidin-2-yl)-3-(4-propoxyphenyl) (20.0 mg, 0.167 mmol, 1.0 eq.). Reaction mixture was stirred for 24 h at room temperature. Water was evaporated. Resulting solid was used directly to further studies.
quantitative **yield**, white solid, **^{1}H-NMR:** (400 MHz, DMSO-d_6) δ = 9.18 (s, 2H), 7.38 – 7.22 (m, 2H), 7.18 – 6.94 (m, 3H), 3.96 (t, J = 6.5 Hz, 2H), 2.42 (s, 6H), 1.74 (q, J = 7.0 Hz, 2H), 0.99 (t, J = 7.4 Hz, 3H) ppm, **^{13}C-NMR:** (101 MHz, DMSO-d_6) δ = 168.1 (2C), 165.2, 157.9, 157.2, 154.1 (2C), 127.5 (2C), 126.7, 115.7 (2C), 115.5, 69.3, 23.4 (2C), 22.0, 10.5 ppm.
168.6 (2C), 165.2, 158.1, 157.3, 133.7, 126.6 (2C), 116.4 (2C), 112.9, 70.9, 23.74 (2C), 23.69, 10.9 ppm, **IR** (KBr) ν = 3375, 3294, 3111, 2959, 2881, 1736, 1652, 1613, 1545, 1512, 1428, 1356, 1341, 1299, 1240, 1207, 1180, 1099, 1078, 1054, 1015 cm^{-1}.

[2] Israel, M.; Zoll, E. C.; Muhammad, N.; Modest, E. *J. Med. Chem.* **1973**, *16*, 1-5.

^{1}H-NMR

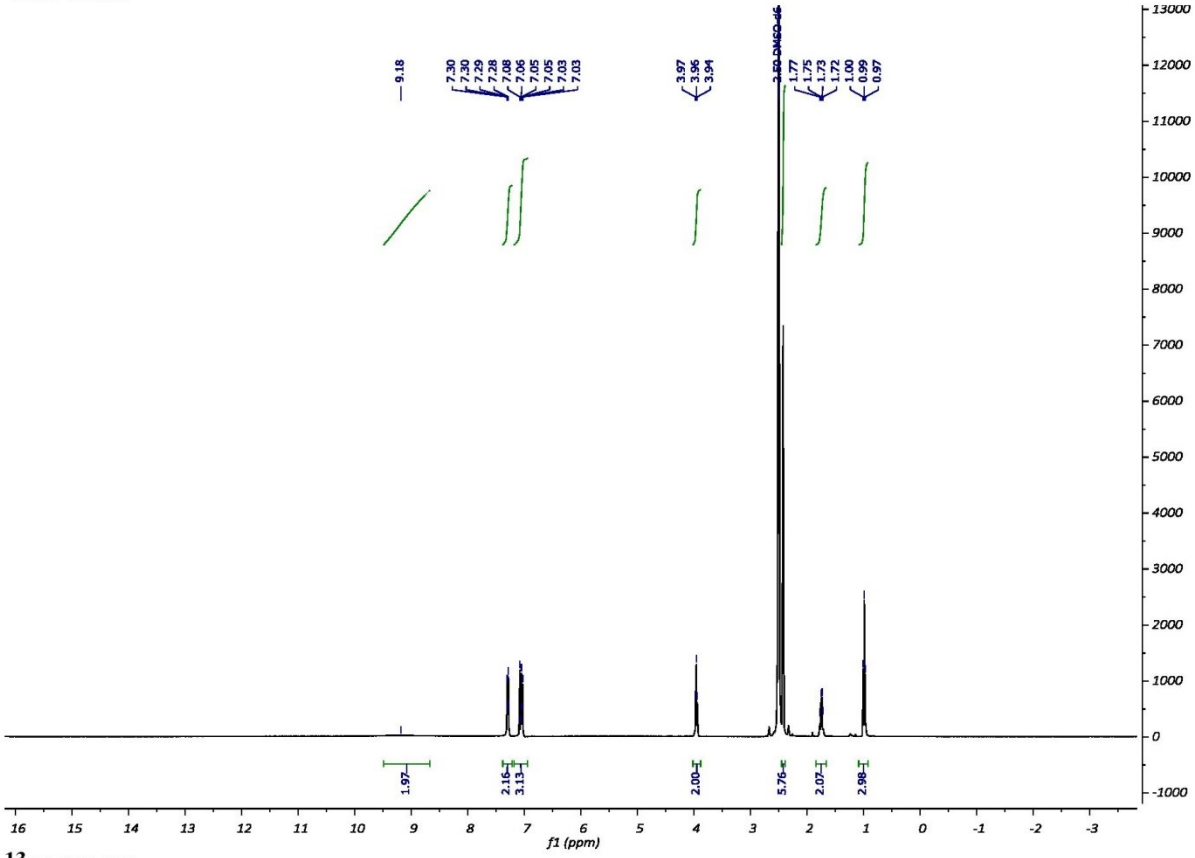

^{13}C-NMR

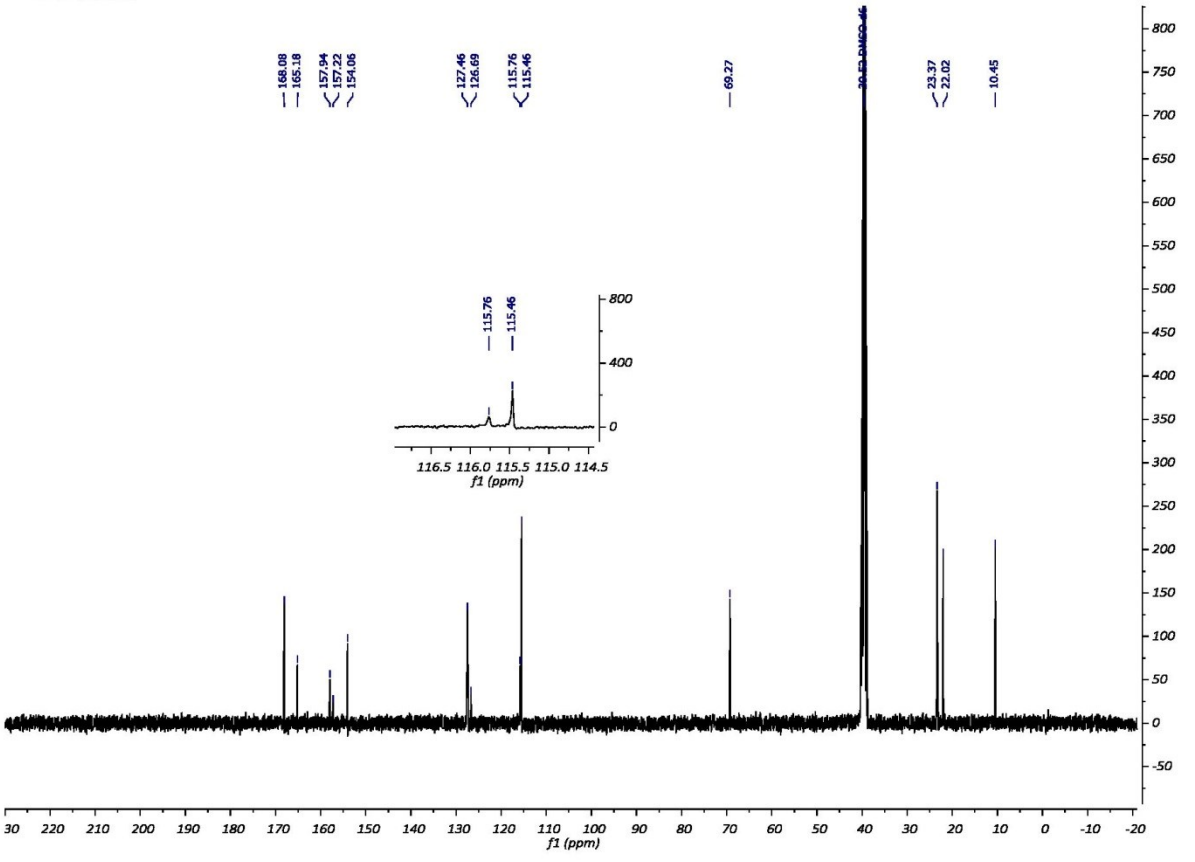

DEPT-135

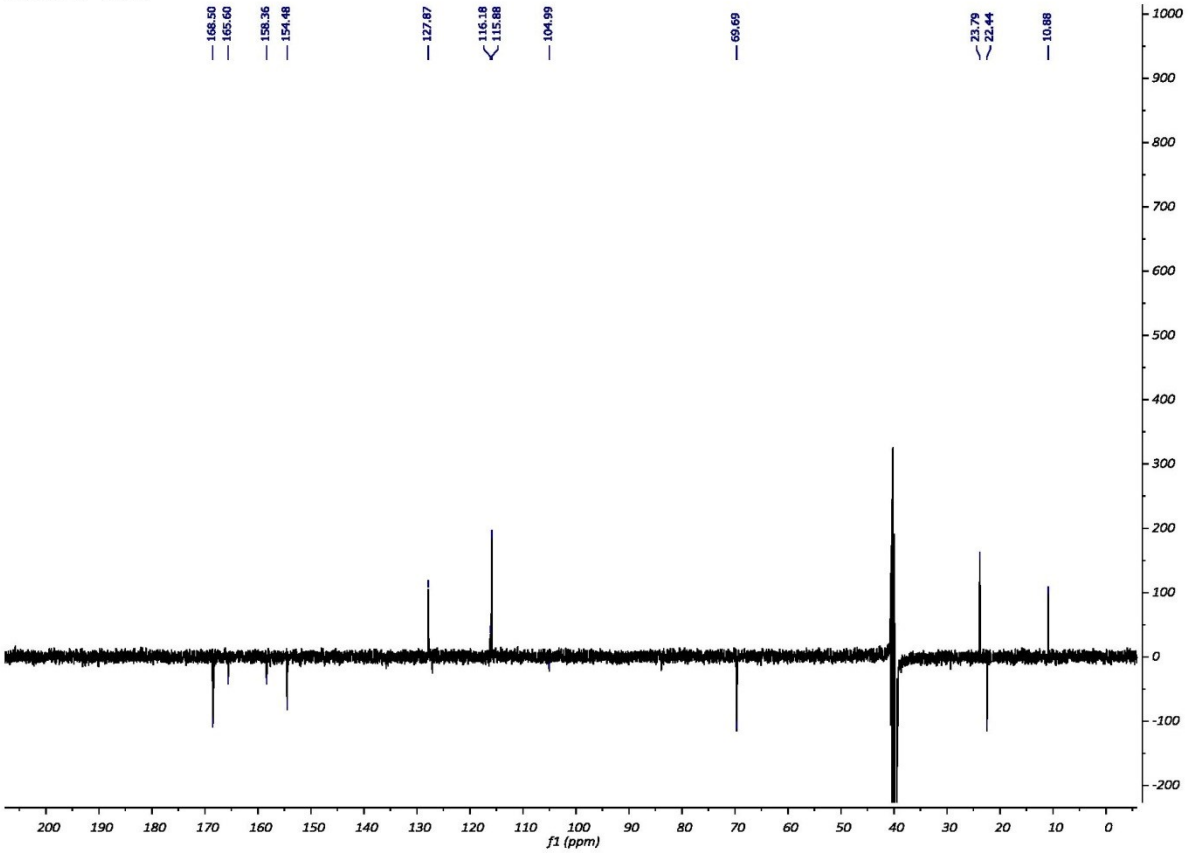

COSY

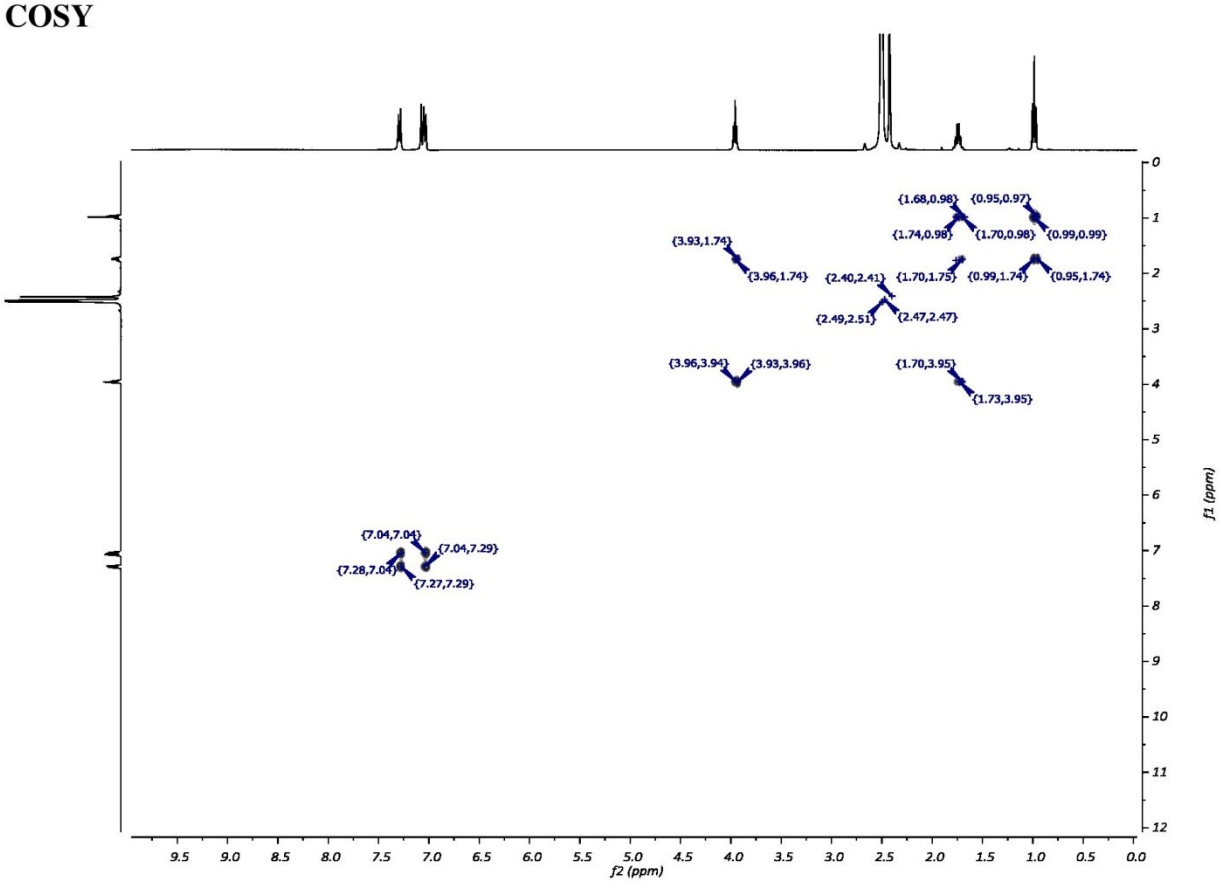

HSQC

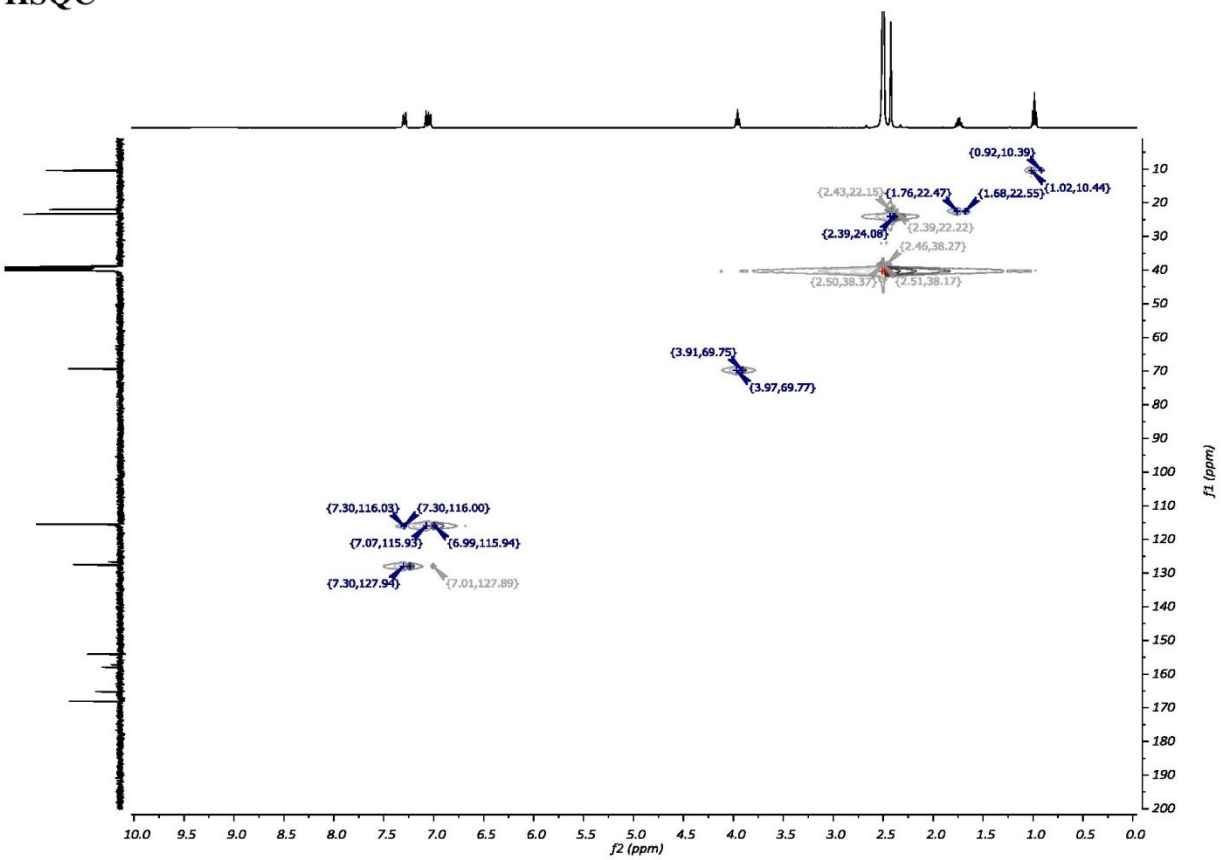
{0.92,10.39}
{1.02,10.44}
{1.68,22.55}
{1.76,22.47}
{2.43,22.15}
{2.39,22.22}
{2.39,24.08}
{2.46,38.27}
{2.50,38.37}
{2.51,38.17}
{3.91,69.75}
{3.97,69.77}
{7.30,116.03}
{7.30,116.00}
{7.07,115.93}
{6.99,115.94}
{7.30,127.94}
{7.01,127.89}
f2 (ppm)
f1 (ppm)

HMBC

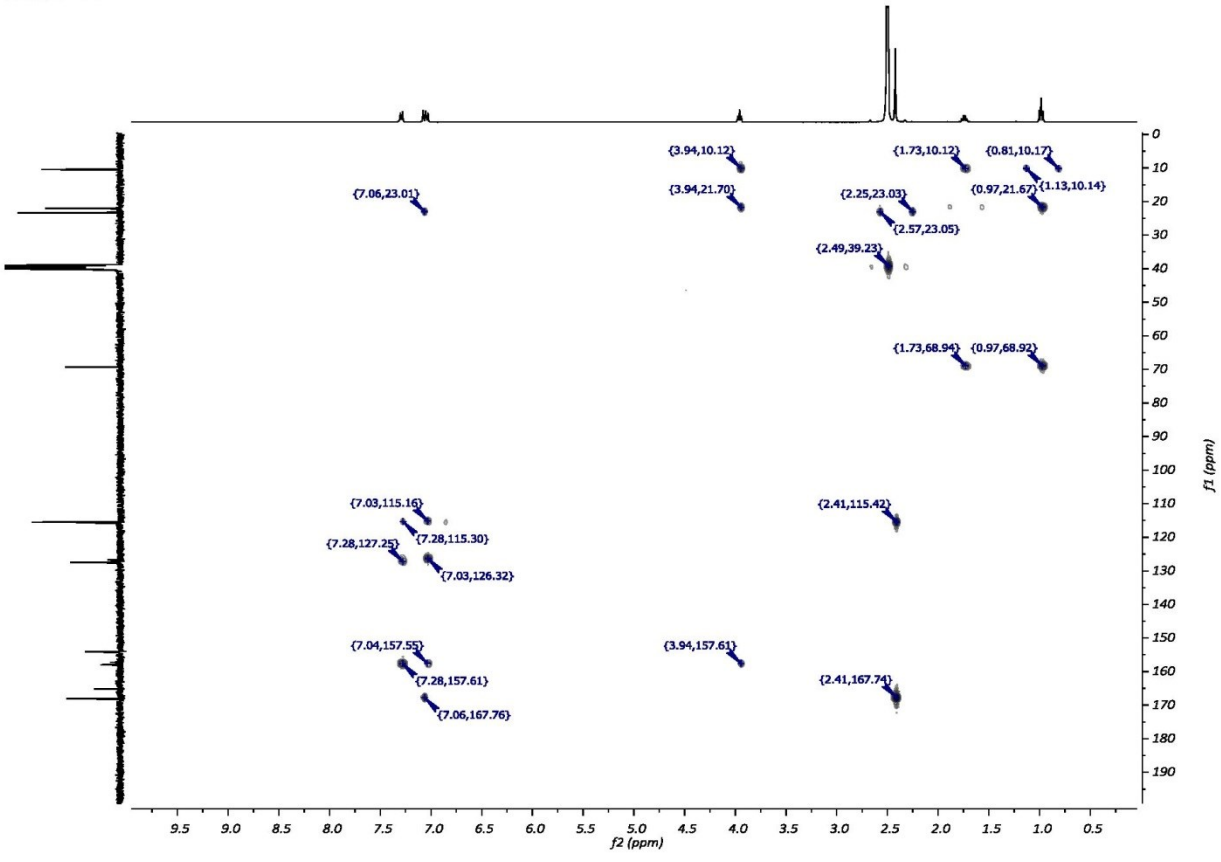
{3.94,10.12}
{1.73,10.12}
{0.81,10.17}
{1.13,10.14}
{0.97,21.67}
{3.94,21.70}
{7.06,23.01}
{2.25,23.03}
{2.57,23.05}
{2.49,39.23}
{1.73,68.94}
{0.97,68.92}
{7.03,115.16}
{2.41,115.42}
{7.28,127.25}
{7.28,115.30}
{7.03,126.32}
{7.04,157.55}
{3.94,157.61}
{7.28,157.61}
{2.41,167.74}
{7.06,167.76}
f2 (ppm)
f1 (ppm)

7.5 Supplement S5

7.5.1 Publication V: The role of cysteines in the regulation of Apoptosis signal-regulating kinase 1 by thioredoxin

Kylarova, S., Kosek, D., Petrvalska, O., **Psenakova, K.,** Man, P., Vecer, J., Herman, P., Obsilova, V. & Obsil, T. Cysteine residues mediate high-affinity binding of thioredoxin to ASK1. *FEBS J.* **283**, 3821–3838 (2016).

My contribution: expression and purification of TRX, ASK1-TBD and cysteine and tryptophan mutants of ASK1-TBD, sample preparation and further optimization for tryptophan fluorescence; native gel electrophoresis experiments.

The FEBS Journal

FEBS PRESS science publishing by scientists

Cysteine residues mediate high-affinity binding of thioredoxin to ASK1

Salome Kylarova[1,2], Dalibor Kosek[1,2], Olivia Petrvalska[1,2], Katarina Psenakova[1,2], Petr Man[3,4], Jaroslav Vecer[5], Petr Herman[5], Veronika Obsilova[2] and Tomas Obsil[1,2]

1 Department of Physical and Macromolecular Chemistry, Faculty of Science, Charles University, Prague, Czech Republic
2 Institute of Physiology, The Czech Academy of Sciences, Prague, Czech Republic
3 BioCeV – Institute of Microbiology, The Czech Academy of Sciences, Vestec, Czech Republic
4 Department of Biochemistry, Faculty of Science, Charles University, Prague, Czech Republic
5 Institute of Physics, Faculty of Mathematics and Physics, Charles University, Prague, Czech Republic

Keywords
ASK1; cysteine; disulfide bond; mass spectrometry; TRX

Correspondence
T. Obsil, Department of Physical and Macromolecular Chemistry, Faculty of Science, Charles University, Prague, Czech Republic
Fax: +420 224919752
Tel: +420 221951303
E-mail: obsil@natur.cuni.cz
V. Obsilova, Institute of Physiology, The Czech Academy of Sciences, Prague, Czech Republic
Fax: +420 241062488
Tel: +420 241062191
E-mail: veronika.obsilova@fgu.cas.cz

(Received 3 August 2016, accepted 1 September 2016)

doi:10.1111/febs.13893

Apoptosis signal-regulating kinase 1 (ASK1, MAP3K5) activates p38 mitogen-activated protein kinase and the c-Jun N-terminal kinase in response to proinflammatory and stress signals. In nonstress conditions, ASK1 is inhibited by association with thioredoxin (TRX) which binds to the TRX-binding domain (ASK1-TBD) at the N terminus of ASK1. TRX dissociates in response to oxidative stress allowing the ASK1 activation. However, the molecular basis for the ASK1:TRX1 complex dissociation is still not fully understood. Here, the role of cysteine residues on the interaction between TRX1 and ASK1-TBD in both reducing and oxidizing conditions was investigated. We show that from the two catalytic cysteines of TRX1 the residue C32 is responsible for the high-affinity binding of TRX1 to ASK1-TBD in reducing conditions. The disulfide bond formation between C32 and C35 within the active site of TRX1 is the main factor responsible for the TRX1 dissociation upon its oxidation as the formation of the second disulfide bond between noncatalytic cysteines C62 and C69 did not have any additional effect. ASK1-TBD contains seven conserved cysteine residues which differ in solvent accessibility with the residue C250 being the only cysteine which is both solvent exposed and essential for TRX1 binding in reducing conditions. Furthermore, our data show that the catalytic site of TRX1 interacts with ASK1-TBD region containing cysteine C200 and that the oxidative stress induces intramolecular disulfide bond formation within ASK1-TBD and affects its structure in regions directly involved and/or important for TRX1 binding.

Introduction

Apoptosis signal-regulating kinase 1 (ASK1, also known as MAP3K5), a member of the mitogen-activated protein kinase kinase kinase (MAP3K) family, activates the p38 mitogen-activated protein kinase and the c-Jun N-terminal kinase in response to proinflammatory and stress signals [1]. ASK1 is activated by various types of stimuli, such as oxidative stress, endoplasmic reticulum stress, calcium influx, tumor necrosis factor α, and lipopolysaccharide and its activity plays a key role in the pathogenesis of several diseases including cancer, neurodegeneration, and cardiovascular diseases (reviewed by [2,3]). According to the

Abbreviations
ASK1, apoptosis signal-regulating kinase 1; ASK1-TBD, thioredoxin-binding domain of ASK1; AUC, analytical ultracentrifugation; DSF, differential scanning fluorimetry; IAA, 2-iodoacetamide; SV, sedimentation velocity; TRX, thioredoxin.

current model of ASK1 regulation in oxidative stress, ASK1 forms a silent high molecular mass complex called ASK1 signalosome in nonstress conditions by direct interaction through the C-terminal, coiled-coil domain [4]. In this complex, the ASK1 activity is inhibited by association with thioredoxin (TRX) interacting with the N-terminal region of ASK1, and the 14-3-3 protein recognizing phosphorylated motif at the C terminus of the kinase domain [5–7]. In response to oxidative stress, TRX and the 14-3-3 protein dissociate allowing the recruitment of tumor necrosis factor receptor-associated factors 2 and 6 to the N-terminal region of ASK1. This, in turn, results in homo-oligomerization of ASK1 through its N-terminal coiled-coil motif, autophosphorylation of activation loop at T838 and ASK1 activation [8,9].

Thioredoxins, a class of small dithiol oxidoreductases, perform various biological functions including the reduction of protein disulfide bonds, the supply of reducing equivalents to redox enzymes, and the regulation of transcription factors and proteins through either a direct reduction of their cysteine groups or different mechanisms (reviewed by [10]). The sequence of mammalian TRX1 contains five cysteine residues (Fig. 1A) from which two (C32 and C35) are embedded within the highly conserved catalytic motif $W^{31}CGPC^{35}$, where they provide the sulfhydryl groups responsible for TRX-dependent redox activity [11]. The formation of an intramolecular disulfide bond between these two cysteine residues upon their oxidation is thought to cause the dissociation of TRX1 from signalosome resulting in the activation of ASK1 under oxidative stress conditions [5,7,8]. The three nonactive-site cysteines of TRX1 are located at positions 62, 69, and 73 and it has been suggested that these three residues are also important for the function of TRX1 [12]. In addition, residues C62 and C69 have been shown to form a second intramolecular disulfide bond under oxidizing conditions [13,14], but whether its formation plays any role in TRX1 dissociation from ASK1 is unknown.

It has recently been shown that the N-terminal TRX-binding domain of ASK1 (ASK1-TBD) is a monomeric protein which binds reduced TRX1 with 1:1 molar stoichiometry through the relatively large binding interface without undergoing any dramatic conformational change [15]. However, the molecular basis for the ASK1-TBD:TRX1 complex dissociation upon the oxidative stress is still not fully understood. For example, it is still unclear how the intramolecular disulfide bond formation within the catalytic site of TRX1 causes the complex dissociation and whether this process is the only factor responsible for the complex dissociation under the oxidative stress. Moreover, the sequence of ASK1-TBD contains seven conserved Cys residues (Fig. 1B) and it is entirely possible that some of these residues might form intra- and/or intermolecular disulfide bond(s) under the oxidative stress, thus affecting the structure of ASK1-TBD. If this is the case then the oxidation of ASK1-TBD might be another factor that contributes to the dissociation of its complex with TRX1.

In this work, we investigated the role of cysteine residues on the interaction between TRX1 and ASK1-TBD in both reducing and oxidizing conditions. We show that from the two catalytic cysteines of TRX1 the residue C32 is responsible for the high-affinity binding of TRX1 to ASK1-TBD in reducing conditions. The disulfide bond formation between C32 and C35 within the active site of TRX1 is the main factor responsible for the TRX1 dissociation upon its oxidation as the formation of the second disulfide bond between non-catalytic C62 and C69 did not have any additional effect. We also show that cysteine residues of ASK1-TBD differ in solvent accessibility with C250 being the only cysteine which is both solvent exposed and essential for TRX1 binding in reducing conditions. Furthermore, our data show that the catalytic site of TRX1 interacts with ASK1-TBD region containing cysteine C200 and that the oxidative stress induces intramolecular disulfide bonds formation within ASK1-TBD and affects its structure in regions directly involved and/or important for TRX1 binding.

Results

Residue C32 of TRX1 is crucial for the high-affinity binding of TRX1 to ASK1-TBD in reduced conditions

Main objective of this work was to investigate the importance of individual cysteine residues for the interaction between TRX1 and ASK1-TBD. First, we focused our attention on TRX1 (Fig. 1A) and used site-directed mutagenesis to assess the role of its cysteines in the binding to ASK1-TBD. In our previous work, the sedimentation velocity analytical ultracentrifugation (SV AUC) was used to show that the TRX1 C73S mutant binds ASK1-TBD in reducing conditions with K_D value of ~ 0.3 μM [15]. Therefore, the remaining TRX1 cysteine mutants (C32S, C35S, C62S, and C69S) were prepared and their binding to ASK1-TBD was characterized using the same approach. Mutations of these residues are known to

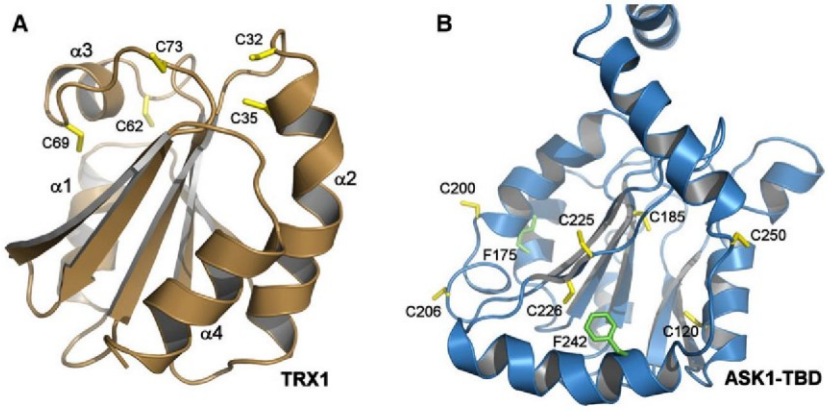

Fig. 1. Crystal structure of TRX1 and a theoretical model of ASK1-TBD. (A) Crystal structure of reduced human TRX1 [17]. Cysteine residues are shown as sticks. (B) Theoretical model of human ASK1-TBD (sequence 88-302) [15]. Cysteine residues are shown as yellow sticks. Phenylalanine residues (F175 and F242) that were replaced by tryptophans for time-resolved fluorescence experiments are shown in green.

have no significant effect on TRX1 structure [16,17]. For each TRX1 mutant, a range of different molar ratios of ASK1-TBD with reduced TRX1 were examined using SV AUC and the values of the apparent equilibrium dissociation constant (K_D) were estimated by analyzing the isotherms of weight-averaged sedimentation coefficients (s_w isotherms) as a function of TRX1 concentration (Fig. 2, panels A–E, Table 1). The normalized continuous sedimentation coefficient distributions $c(s)$ underlying the s_w data points obtained from SV experiments of mixtures of ASK1-TBD WT and TRX1 mutants are shown in insets in Fig. 2. These experiments revealed that only the TRX1 C32S mutant binds ASK1-TBD with a significantly lower binding affinity with the best-fit K_D of 12 ± 3 μM, whereas all other TRX1 mutants bind ASK1-TBD with similar affinities as TRX1 WT with the best-fit K_D values of < 0.6 μM. This strongly suggests that from the two catalytic cysteines of TRX1 the residue C32 is the one responsible for the high-affinity binding of TRX1 to ASK1-TBD under reducing conditions.

Disulfide bond formation between C32 and C35 is the main factor responsible for the ASK1-TBD: TRX1 complex dissociation upon TRX1 oxidation

Several studies suggested that the disulfide bond formation between the active-site cysteines, C32 and C35, is responsible for TRX1 dissociation from ASK1 [5,7,8]. However, the TRX1 oxidation has been shown to generate, besides this disulfide, also a second disulfide bond between the nonactive-site cysteines, C62 and C69, with a predicted effect on TRX structure as C62 and C69 are 17 Å apart in the TRX1 molecule (Fig. 1A) [12,13,17]. To investigate the role of this second disulfide in the TRX1 dissociation from ASK1-TBD, TRX1 was oxidized using H_2O_2 for 15 min at 37 °C at two different molar ratios (protein:H_2O_2) of 1:5 (denoted here as 'low-ox' conditions) and 1 : 100 (denoted here as 'high-ox' conditions). Oxidation of TRX1 under high-ox conditions has been shown to induce the formation of two disulfide bonds, (C32–C35 and C62–C69) whereas oxidation under low-ox conditions produces TRX1 containing only one disulfide bond involving active-site cysteines C32 and C35 [12]. However, SV AUC experiments revealed that TRX1 WT forms dimers upon the oxidation even under low-ox conditions (Fig. 3A), likely due to the intermolecular disulfide bond formation by the nonactive-site cysteine C73 [17]. The dimerization via C73 blocks the active site due to the catalytic motif $W^{31}CGPC^{35}$ being part of the dimer interface [17] and since it is considered to be an *in vitro* artifact we decided to use TRX1 C73S mutant instead of TRX1 WT in these experiments. The quantification of free thiol groups before and after TRX1 C73S oxidation under low-ox and high-ox conditions revealed expected decrease in the number of free thiols consistent with the formation of one and two disulfides, respectively (Table 2). The analysis of the s_w isotherm determined for ASK1-TBD and TRX1 C73S oxidized under low-ox conditions revealed the best-fit K_D of 4 ± 2 μM using a 1 : 1 Langmuir binding model, thus significantly lower binding affinity compared to reduced TRX1 C73S (Fig. 2F and Table 1). We have previously shown that TRX1 C73S oxidized under high-ox conditions binds to ASK1-TBD with the K_D value of

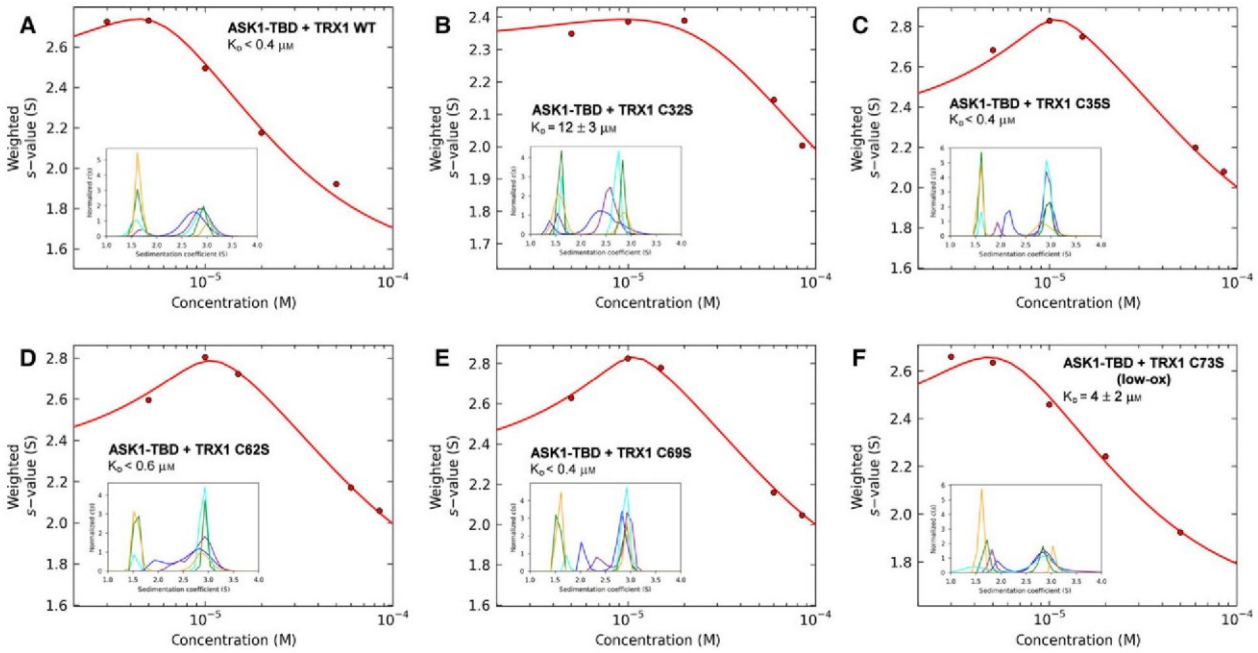

Fig. 2. Sedimentation velocity analytical ultracentrifugation analysis of complexes between TRX1 variants and ASK1-TBD. (A) Reduced TRX WT and ASK1-TBD WT. (B) Reduced TRX C32S and ASK1-TBD WT. (C) Reduced TRX C35S and ASK1-TBD WT. (D) Reduced TRX C62S and ASK1-TBD WT. (E) Reduced TRX C69S and ASK1-TBD WT. (F) Oxidized TRX C73S (low-ox conditions) and ASK1-TBD WT in buffer without reducing agents. Isotherm of weight-averaged sedimentation coefficients s_w were obtained from SV AUC experiments of mixtures of ASK1-TBD WT (5 μM) and TRX1 (3–85 μM). The insets show the sedimentation coefficient distributions *c(s)* of mixtures of ASK1-TBD and TRX1 at various concentrations underlying the s_w data points (panels B–E: 5 μM TRX1 blue, 10 μM TRX1 purple, 20 μM TRX1 cyan, 60 μM TRX1 green, 85 TRX1 μM orange; panels A and F: 3 μM TRX1 blue, 5 μM TRX1 purple, 10 μM TRX1 cyan, 20 μM TRX1 green, 50 μM TRX1 orange).

Table 1. Binding affinities of TRX1 Cys mutants for ASK1-TBD.

TRX1 variant	K_D[a], μM
WT reduced	< 0.4
C32S reduced	12 ± 3
C35S reduced	< 0.4
C62S reduced	< 0.6
C69S reduced	< 0.4
C73S reduced[b]	0.3 ± 0.1
C73S low-ox	4 ± 2
C73S high-ox[b]	6 ± 2

[a] K_D values and their uncertainties were determined by analyzing the isotherms of weight-averaged sedimentation coefficients (s_w isotherm) as a function of TRX1 concentration using the SEDPHAT software [30,31].
[b] These K_D values were reported in Kosek *et al.* [15].

6 ± 2 μM [15]. No significant difference in binding affinities of TRX1 C73S oxidized in low-ox and high-ox conditions for ASK1-TBD suggests that the formation of the second disulfide bond between the nonactive-site cysteines C62 and C69 does not play any significant role in the dissociation of the TRX1:ASK1-TBD complex upon TRX1 oxidation.

Cysteine residues of ASK1-TBD differ in solvent accessibility

Apoptosis signal-regulating kinase 1-TBD contains seven conserved cysteine residues C120, C185, C200, C206, C225, C226, and C250 (Fig. 1B). Previous studies revealed that C250 is important for the TRX1 binding to ASK1 as its mutations (C250A, C250S) inhibited this interaction [15,18,19]. However, the role of other cysteine residues of ASK1-TBD, especially upon its oxidation, is unclear. Since the three-dimensional structure of ASK1-TBD is still unknown, we first investigated the solvent accessibility and reactivity of all cysteine residues from this domain. Here, we employed the experimental setup primarily designed for hydrogen/deuterium exchange mass spectrometry (HDX-MS) [20]. In this methodology the acidified protein sample is digested on immobilized pepsin column and directly analyzed by LC-MS/MS. LC-MS/MS analysis of peptides from ASK1-TBD treated by 2-iodoacetamide (IAA) under native conditions revealed that out of seven ASK1-TBD cysteine residues the cysteine C120 is the only one inaccessible as no modification of this residue was detected under conditions used in this experiment

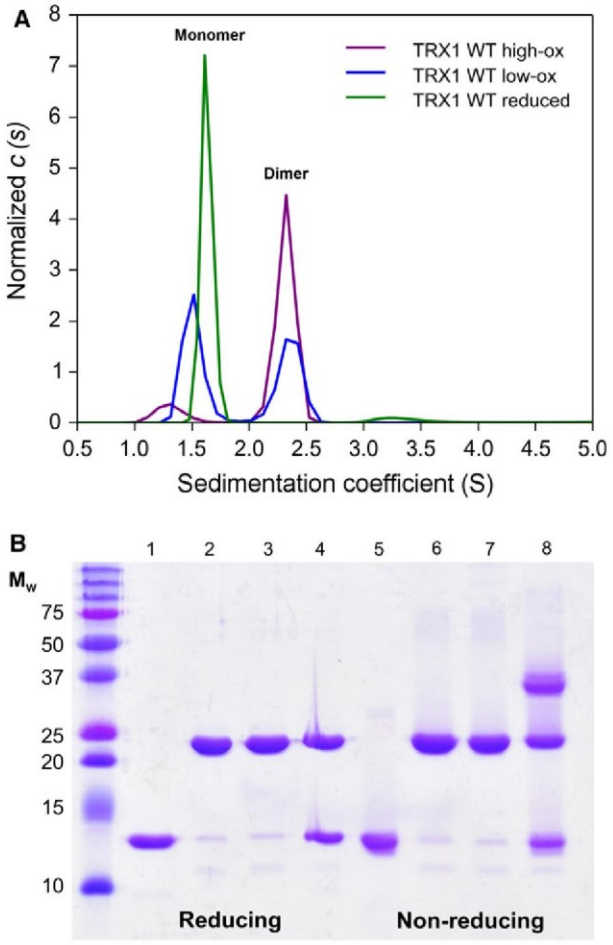

Fig. 3. Oligomerization of TRX1 and ASK1-TBD upon oxidation. (A) The normalized continuous sedimentation coefficient distributions, *c(s)*, for reduced TRX1 WT (green), TRX1 WT oxidized under high-ox (purple) and low-ox (blue) conditions. As noticed, TRX1 WT forms dimers upon oxidation with H_2O_2. (B) 15% SDS/PAGE gel with ASK1-TBD WT and TRX1 C35,73S. Proteins (300 pmol TRX1 C35,73S and/or 300 pmol ASK1-TBD) were desalted into buffer containing 20 mM Tris-HCl (pH 7.5) and 200 mM NaCl. Then, selected samples of ASK1-TBD (samples 3 and 7) were oxidized under low-ox conditions. Nonoxidized samples were incubated at 4 °C for 24 h. All samples were then separated on SDS/PAGE under either reducing (samples 1–4) or nonreducing (samples 5–8) conditions. ASK1-TBD was oxidized by incubating with fivefold excess of H_2O_2 for 15 min at 37 °C. Oxidation reaction was stopped by adding five units of catalase. Lane 1: TRX1 C35,73S, lane 2: ASK1-TBD, lane 3: oxidized ASK1-TBD, lane 4: ASK1-TBD + TRX1 C35,73S, lane 5: TRX1 C35,73S, lane 6: ASK1-TBD, lane 7: oxidized ASK1-TBD, lane 8: ASK1-TBD + TRX1 C35,73S.

(Fig. 4A). All other cysteine residues reacted with the alkylating reagent to various extents. Residues C200, C206, and C250 were modified by IAA either completely or almost completely, (Fig. 4C, E) whereas just ~ 40% of the peptide containing residue C185 was alkylated (Fig. 4B). In addition, approx. 80% of the peptide containing pair of adjacent cysteines, C225 and C226, was doubly alkylated while ~ 20% of this peptide was alkylated on just one cysteine residue (Fig. 4D). Detailed inspection of the MS/MS data, however, failed to prove whether there is any preference for modification of either of the two vicinal Cys residues. Altogether, these data suggest that the residue C185 and one from the pair C225, C226 are not fully exposed to the surface of ASK1-TBD.

Table 2. The number of free thiol groups in reduced and oxidized samples of TRX1 and ASK1-TBD.

Protein	Reduced	Oxidized under low-ox conditions	Oxidized under high-ox conditions
TRX1 WT	4.9 ± 0.1	3.1 ± 0.4	0.4 ± 0.1
TRX1 C73S	3.8 ± 0.4	2.1 ± 0.4	0.1 ± 0.1
ASK1-TBD	7.1 ± 0.3	4.7 ± 0.2	n.d.

The values are shown as the mean ± SD of five experiments.

Oxidation of ASK1-TBD leads to the formation of two intramolecular disulfide bonds

Next, the formation of disulfide bond(s) upon the ASK1-TBD oxidation was investigated. In these experiments, ASK1-TBD was oxidized using low-ox conditions as high-ox conditions caused heavy precipitation of the protein. The nonreducing SDS/PAGE revealed no significant formation of disulfide-linked ASK1-TBD homodimers or other multimers upon the oxidation (Fig. 3B, compare lanes 3 and 7). However, the quantification of free thiol groups before and after ASK1-TBD oxidation revealed a decrease in the number of free thiols from 7.1 ± 0.3 to 4.7 ± 0.2, (Table 2) thus suggesting at least one intramolecular disulfide bond formation. This was further investigated by high-resolution mass spectrometry. Samples of ASK1-TBD were first analyzed directly (intact mass measurement). Details of the ultrahigh resolution ESI-FTMS spectra of intact ASK1-TBD in the presence of DTT, without DTT and after the oxidation are shown in Fig. 5A–C. The shift of the main peak toward the lower mass corresponds to the formation of 1–2 disulfide bonds upon oxidation while no such effect was observed to be induced by air oxidation (sample without DTT). In addition, virtually no Met, Trp or His oxidation was caused by H_2O_2 treatment under low-ox conditions and only the traces of sodiated and potassiated adducts were detectable. In order to obtain semi-quantitative estimation of the number of disulfide bonds formed upon oxidation, ASK1-TBD was also analyzed after oxidation followed by non-native

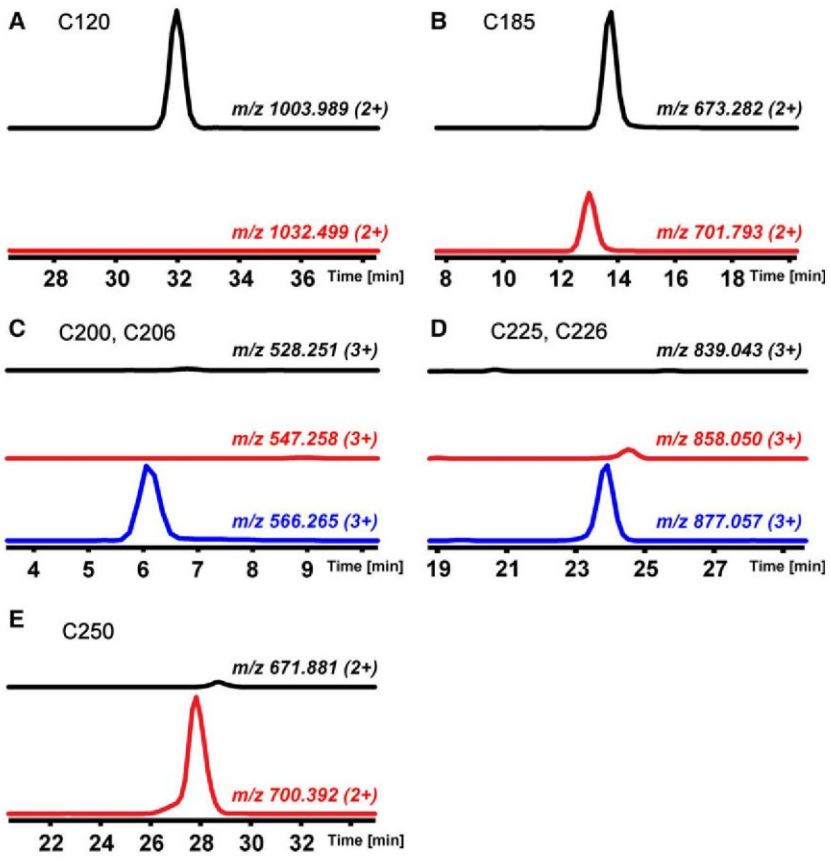

Fig. 4. Accessibility and reactivity of Cys residues in ASK1-TBD probed by alkylation with iodoacetamide. Extracted ion chromatograms for selected peptic peptides covering cysteines in the ASK1-TBD sequence are shown. Traces are colored according to the extent of modification—unmodified (black), singly (red), and doubly (blue) alkylated. The panels represent the following peptides: (A) ESEALQSLREACETVGATL (C120); (B) YCDTNSDSLQSL (C185); (C) KEIICQKNTMCTGN (C200 and C206); (D) YTFVPYMITPHNKVYCCDSSF (C225 and C226); (E) ELLLGPICL (C250). Mass-to-charge (m/z) ratios used to plot the chromatograms are indicated above each trace.

alkylation (reaction carried out in the presence of denaturing agent). ASK1-TBD fully alkylated under denaturing conditions was used here as a control. Figure 5D–F shows details of the 22+ charge state of intact ASK1-TBD fully reduced (panel D), fully alkylated (panel E), and oxidized prior to the non-native alkylation (panel F). The spectrum of ASK1-TBD alkylated under denaturing conditions (Fig. 5E) shows the presence of seven to eight carbamidomethylations suggesting that besides all seven cysteine residues an additional carbamidomethylation also occurs on some other residue. The spectrum of oxidized and then alkylated ASK1-TBD (Fig. 5F) reveals the presence of two peak series. The more intense one validates the presence of ASK1-TBD containing three, five, or seven carbamidomethylations that correspond to the presence of two, one, and none disulfide bridges, respectively. The presence of proteins containing four, six, and eight carbamidomethylations (the less intense peak series in the spectrum) is due to the modification of one noncysteine residue in the sequence of ASK1-TBD. These proteoforms, however, still correspond to the ASK1-TBD with two, one, and none disulfide bonds, respectively.

Following intact mass measurements we performed detailed analysis of the disulfide bonds pattern and of the extent to which these bonds are formed. For this, two different approaches were used, however, in both cases, ASK1-TBD after full alkylation and ASK1-TBD that underwent oxidation followed by alkylation, were digested with protease and the resulting peptides were identified by LC-MS/MS. In the first set of analyses the individual ASK1-TBD samples were digested with trypsin prior to the MS analysis. Several disulfide-linked peptides were identified leading to the assignment of the disulfide bond pattern as follows. C120 was not involved in any disulfide linkage at all. On the other hand, C200 formed disulfide with C206, while C225 was found to be bonded with C226. Interestingly weaker MS signals were also found for

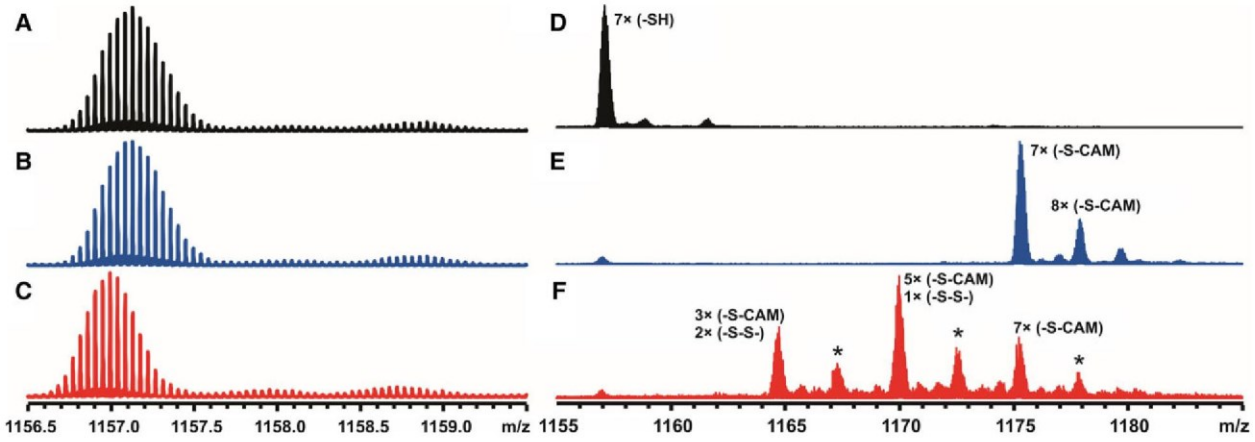

Fig. 5. Formation of disulfide bonds in ASK1-TBD monitored by high-resolution mass spectrometry. Detail of the isotopic profile of 22+ charge state of intact ASK1-TBD in the fully reduced form (A), after removal of DTT (B) and after oxidation under low-ox conditions (C). The apparent shift of the isotopic envelope toward the lower masses (panel C) corresponds to the formation of one to two disulfides. The mass region above the main peak also shows that the treatment with the peroxide caused virtually no oxidation beside the disulfide bond closing. (D–F) Monitoring of the disulfide bonds formation using alkylalytion and intact mass measurement. Detail of the 22+ charge state of intact ASK1-TBD for the fully reduced protein (D), protein alkylated by iodoacetamide under denaturing conditions (E) and protein alkylated under denaturing conditions after oxidation (F). Non-native alkylation (panel E) leads to full modification of all cysteine residues, however, slight overmodification on protein N terminus and/or some noncysteine residues can also be observed. Alkylation after oxidation (panel F) helps to estimate portion of the protein with no disulfide bond (7 × CAM), one disulfide (5 × CAM, 1× -S-S-), and two disulfides (3 × CAM, 2× -S-S-). CAM stands for carbamidomethylation, disulfide is described as '-S-S-'and free sulfhydryl as '-SH'. Peaks labeled with an asterisk correspond to ASK1-TBD with CAM on noncysteine residue.

linkages C185–C200 and for C250 linked either to C225 or C226 (Fig. 6).

In order to obtain estimation of the extent to which these disulfide bonds were created, we employed the HDX-MS setup mentioned above. Based on this data, the assessment of protein amount injected in individual analyses was performed using noncystein peptides (Fig. 7). This showed that the amount of the analyzed protein is virtually identical for fully alkylated and oxidized and then alkylated ASK1-TBD, which is a necessary prerequisite for further comparisons. Next, the intensities of extracted ion chromatograms for selected Cys-containing peptides were plotted and compared. Based on the Fig. 7B we can conclude that the peptide bearing C185 was not changing its intensity upon oxidation and thus remained as a free sulfhydryl. On the other hand, the largest intensity decrease was observed for peptides covering C200, C206, C225, and C226, thus supporting their preferential involvement in disulfide bonds. Moreover, moderate signal drop was also observed for C185 and C250. Finally, these analyses also confirmed part of the results arising from trypsin digestion, namely formation of disulfide bonds C200–C206 and C225–C226. Altogether these data corroborated our previous findings from the native ASK1-TBD alkylation as well as from the disulfide bond assignment and from the intact mass measurements.

Disulfide bonds formation upon oxidation induces conformational change of ASK1-TBD

In our previous work, four ASK1-TBD mutants containing single tryptophan residues inserted at four different positions within the ASK1-TBD (positions 132, 175, 242, and 272) were used to study the flexibility of this domain [15]. Structural model of ASK1-TBD indicated that tryptophan residues inserted at positions 175 and 242 (using mutations F175W and F242W) might be located relatively close to cysteine residues involved in disulfide bonds formation upon oxidation (C200–C206 and C225–C226) (Fig. 1B). We therefore decided to use these two mutants to study potential structural changes induced by oxidation and disulfide bonds formation. The stability of all prepared mutants was checked using differential scanning fluorimetry (DSF). Mutants F175W and F242W did not exhibit any significant change in T_m compared to ASK1-TBD WT (Table 3). Fluorescence decay measurements revealed that the oxidation (low-ox conditions) significantly decreased the mean excited state lifetime τ_{mean} of ASK1-TBD F242W from 4.88 ± 0.02 ns, which was observed for the reduced protein, to 4.66 ± 0.05 ns obtained for the oxidized sample (Table 4). Statistical significance of the observed difference is supported by the bootstrap confidence-interval

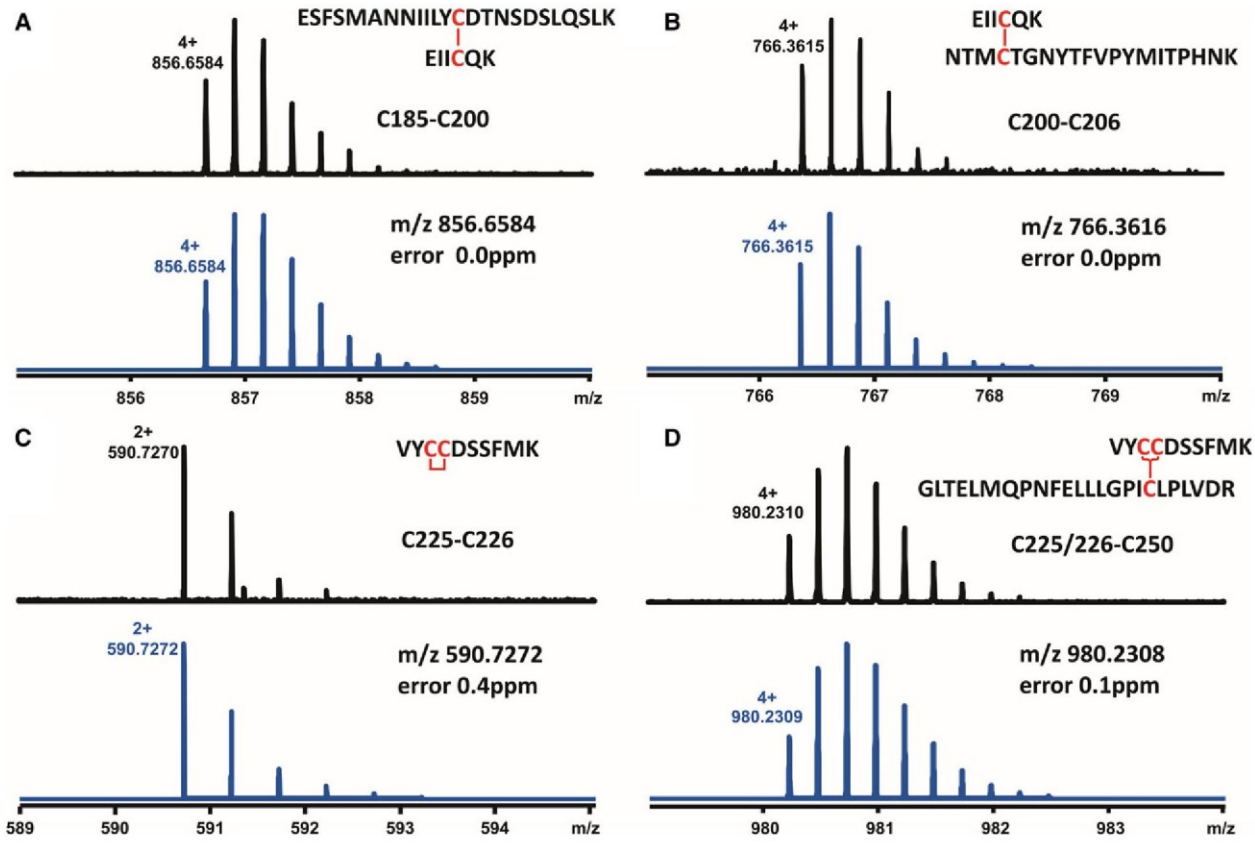

Fig. 6. Identification of disulfide bonds upon peroxide-mediated oxidation of ASK1-TBD. Detail of the isotopic pattern for each identified dipeptide is shown together with the theoretical spectrum (blue). Peptide sequences and the disulfide bond they contain are indicated in each panel together with the information about m/z value and the error of MS measurement.

analysis presented in Fig. 8A,B [21]. As can be noticed from the lifetime distribution analysis in Fig. 8C, the decrease in τ_{mean} is caused mainly by the oxidation-induced shortening of the three longest lifetime peaks representing together about 97% of the total fluorescence intensity. These three peaks dominate the mean excited state lifetime, since $\tau_{mean} = \Sigma_i (f_i \tau_i)$, where f_i represent intensity fraction of the i-th lifetime component τ_i [22]. The suppression of τ_{mean} of ASK1-TBD F242W indicates an increase in polarity and/or change in quenching interactions in the vicinity of W242 upon the oxidation and the disulfide bonds formation. On the other hand, no significant effect on τ_{mean} was found upon the oxidation of ASK1-TBD F175W (Table 4).

Analysis of the time-resolved emission anisotropy decays of reduced and oxidized samples of ASK1-TBD revealed two correlation times, one short (ϕ_1 = 0.4–1.2 ns) and the second close to 15 ns (ϕ_2). While the ϕ_1 likely reflects fast segmental motions, the ϕ_2 corresponds to the rotation of globular protein with M_w about 30 kDa and can be therefore assigned to the overall rotational motion of ASK1-TBD [22]. While no change in segmental motion was observed upon the oxidation of ASK1-TBD F175W, the oxidation of ASK1-TBD F242W resulted in increased flexibility of an otherwise very rigid region containing W242, since the amplitude β_1 of almost undetectable segmental motion (β_1 = 0.003) increases upon oxidation to the value of 0.14 as documented in Table 4. Taken together, results of time-resolved tryptophan fluorescence measurements suggest that the oxidative stress induces structural change within the C terminal part of ASK1-TBD in the region containing residue 242 likely as a result of disulfide bond(s) formation.

The catalytic site of TRX1 interacts with ASK1-TBD region containing cysteine C200

Next, we attempted to measure the binding affinity of oxidized ASK1-TBD for TRX1 using the catalytically inactive TRX1 C35,73S mutant as these two mutations do not affect the complex formation (Fig. 2, Table 1).

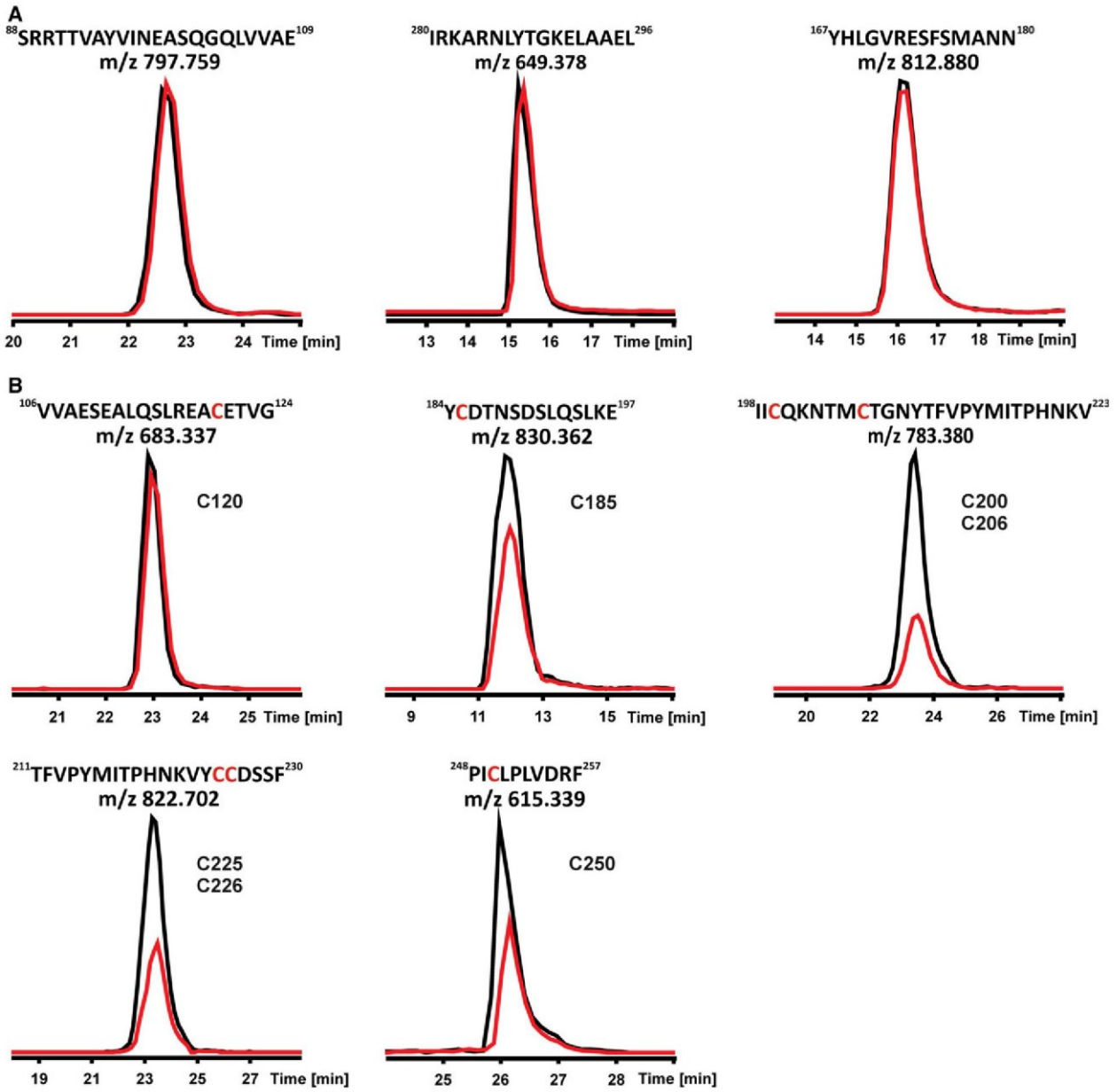

Fig. 7. Estimation of the involvement of cysteine residues in the disulfide bonds formation. Extracted ion chromatograms are compared for fully alkylated ASK1-TBD (black) and ASK1-TBD alkylated after oxidation/disulfide bond formation (red). Virtually identical loading in the analyses was verified by comparing chromatographic traces for noncysteine peptides (A). Decrease in the intensity of the chromatographic peak (B) indicates involvement of the particular Cys in disulfide bond. Sequence of the peptide with highlighted Cys residue in red, m/z value of the peptide and the number of the Cys residue on in ASK1-TBD sequence are shown in each panel.

However, and not surprisingly, the oxidized ASK1-TBD and TRX1 C35,73S in buffer without reducing agents formed the covalent adduct that prevented the binding affinity measurements. The catalytically inactive TRX1 with missing C35 is commonly used to identify proteins that interact with TRX1 as this mutation enables the formation of covalent complexes containing mixed disulfide bond involving the N-terminal catalytic cysteine C32 [23]. ASK1-TBD and TRX1 C35,73S when incubated in buffer without reducing agents formed an adduct with molecular mass corresponding to the cross-linked ASK1-TBD:TRX1 complex (Fig. 3B, lane #8, theoretical M_w =38.6 kDa). The LC-MS/MS analysis of this adduct revealed that

Table 3. Midpoint temperatures of the protein-unfolding transition (T_m) for ASK1-TBD mutants as determined using differential scanning fluorimetry (DSF).

ASK1-TBD variant	T_m, °C[a]
WT	49.2 ± 0.8
C120S	42.0 ± 0.1
C185S	47.3 ± 0.3
C200S	50.4 ± 0.3
C206S	49.5 ± 0.9
C225S	48.4 ± 0.1
C226S	47.9 ± 0.2
C250S	49.8 ± 0.1
F175W	49.0 ± 0.2
F242W	52.1 ± 0.1

[a] Standard deviations were calculated from three different experiments.

Table 4. Summary of time-resolved tryptophan fluorescence measurements of ASK1-TBD mutants

Sample		τ_{mean}[a], ns	ϕ_1, ns	β_1[b]	ϕ_2, ns	β_2
ASK1-TBD F175W	Reduced	5.46 ± 0.02	1.2	0.027	15.0	0.21
	Oxidized	5.44 ± 0.02	1.1	0.033	15.5	0.20
ASK1-TBD F242W	Reduced	4.88 ± 0.02	1.2	0.003	14.5	0.23
	Oxidized	4.66 ± 0.05	0.4	0.014	14.0	0.22

[a] Mean lifetimes were calculated as $\tau_{mean} = \Sigma_i f_i \tau_i$, where f_i is an intensity fraction of the i-th lifetime component τ_i.

[b] The anisotropies $r(t)$ were analyzed for a series of exponentials by a model-independent maximum entropy method without setting assumptions about the shape of the correlation time distributions [34], $r(t) = \Sigma_i \beta_i \exp(-t/\phi_i)$, where amplitudes β_i represent the distribution of the correlation times ϕ_i. Presented values are peak vales of the multimodal distribution, amplitudes are integrated across corresponding peaks.

ASK1-TBD and TRX1 C35,73S are connected through disulfide bond connecting C32 of TRX1 and C200 of ASK1-TBD (Fig. 9). No other linkages involving other ASK1-TBD cysteine residues were detected. This strongly suggests that the catalytic site of TRX1 interacts with ASK1-TBD region containing residue C200.

Serine-scanning mutagenesis of Cys residues of ASK1-TBD

The serine-scanning mutagenesis was used to assess the importance of individual Cys residues of ASK1-TBD in TRX1 binding. To verify that the introduced mutations did not result in an overall destabilization of the ASK1-TBD structure, the stability of purified ASK1-TBD cysteine mutants (C120S, C185S, C200S, C206S, C225S, C226S, and C250S) was checked by measuring the thermally induced protein denaturation using DSF. No significant differences in the temperature of the unfolding transition (T_m) were observed for prepared ASK1-TBD mutants with the exception of the C120S variant with the $T_m \sim 7$ °C lower compared to WT (Table 3). Significantly lower value of T_m indicates that this mutation destabilized the tertiary structure of ASK1-TBD. Moreover, modification of ASK1-TBD by iodoacetamide revealed that cysteine C120 is buried (Fig. 4A) suggesting that this residue cannot participate in TRX1 binding. Therefore, we decided to exclude the C120S mutant from further experiments. The binding of ASK1-TBD cysteine mutants (C185S, C200S, C206S, C225S, and C226S) to TRX1 WT under reducing conditions was investigated using SV AUC. The analysis of s_w isotherms revealed no significant differences in binding affinities of prepared mutants compared to ASK1-TBD WT (Tables 1 and 5, Fig. 10). This indicates that sulfhydryl groups of ASK1-TBD cysteine residues C185, C200, C206, C225, and C226S are not essential for the binding of TRX1 in reducing conditions. Thus, the only ASK1-TBD cysteine which is both solvent exposed and whose mutation significantly affects interaction with TRX1 is C250 [15,18,19]. This suggests that this residue is either directly involved in TRX binding and/or its replacement induces structural change within the TRX1-binding surface but without destabilizing the overall tertiary structure as indicated by DSF measurements (Table 3).

Discussion

Main aim of this study was to provide an insight into the role of cysteine residues in the interaction between ASK1-TBD and TRX1 which is disrupted by the oxidative stress. Previous studies suggested that the oxidation of TRX1 is the main factor responsible for the dissociation of this complex under oxidative stress conditions [5,7,8]. TRX1 oxidation leads to the formation of an intramolecular disulfide bond between the catalytic cysteines C32 and C35, and since structural studies revealed no dramatic conformational changes in TRX1 upon this disulfide bond formation [16,17], it is reasonable to speculate that one or both of these cysteine residues directly participate in TRX1 binding to ASK1-TBD. Binding experiments with TRX1 cysteine mutants revealed that only TRX1 C32S mutant failed to bind ASK1-TBD with high affinity, thus strongly suggesting that from the two catalytic cysteines the residue C32 is the prominent one required for the high-affinity binding of TRX1 to ASK1-TBD

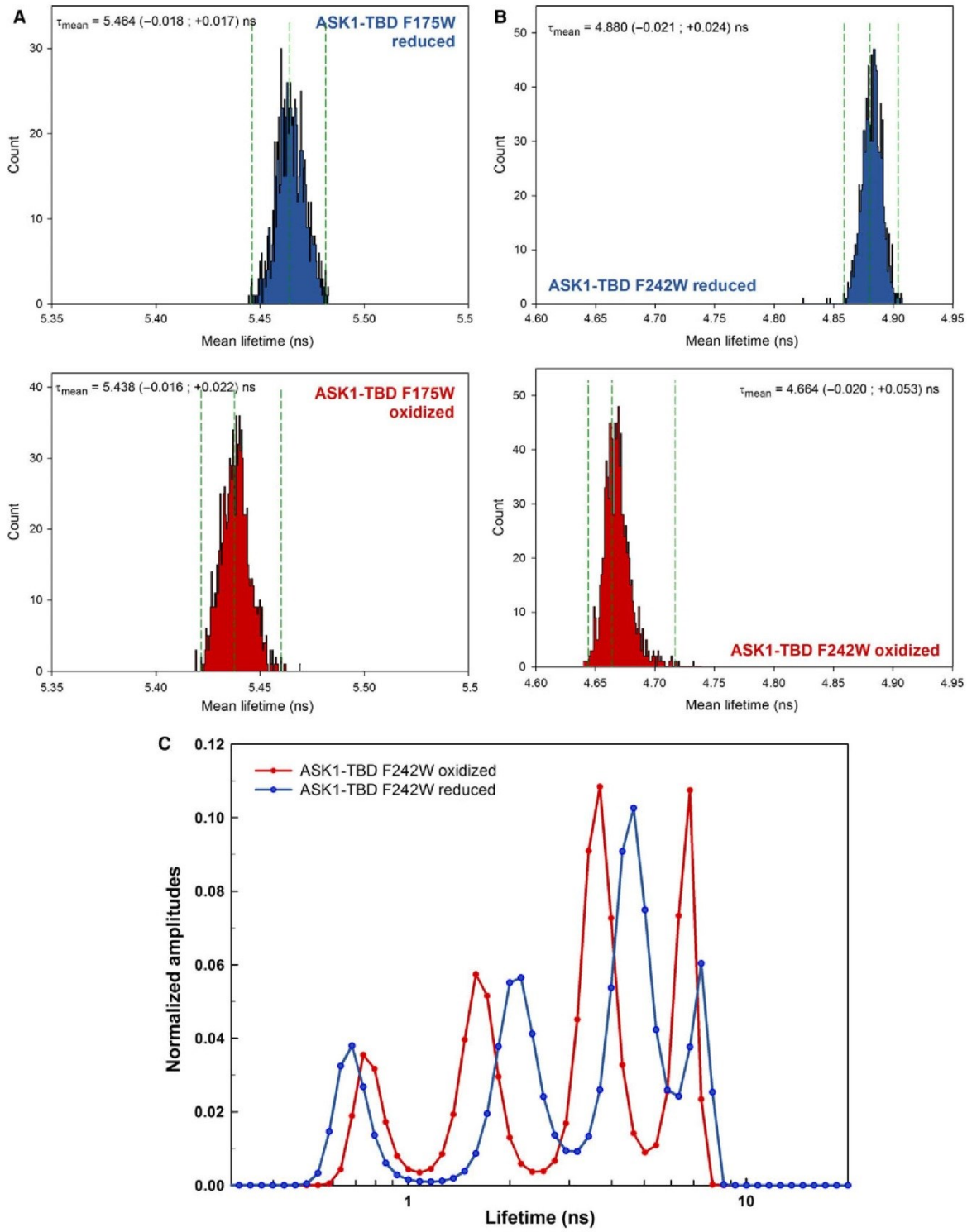

Fig. 8. Time-resolved tryptophan fluorescence measurements. Statistical confidence-interval analysis of the mean fluorescence lifetimes of ASK1-TBD F175W (A) and ASK1-TBD F242W (B) mutants in reduced and oxidized states. Histograms represent an occurrence frequency of the particular τ_{mean} as a result of 3000 bootstrap fitting cycles of raw data [21]. The distributions of ASK1-TBD F242W mutant show that the most probable τ_{mean} values are close to 4.88 and 4.66 ns with 99% confidence interval (three standard deviations) bordered by dashed lines. It is seen that confidence intervals given in Table 4 are therefore realistic estimates. (C) Excited state lifetime distributions of ASK1-TBD F242W in reduced (blue distribution) and oxidized (red distribution) states. As can be noticed, the three longest lifetime peaks dominating the mean excited state lifetime become shortened upon the ASK1-TBD oxidation. As a consequence, τ_{mean} of W242 is reduced.

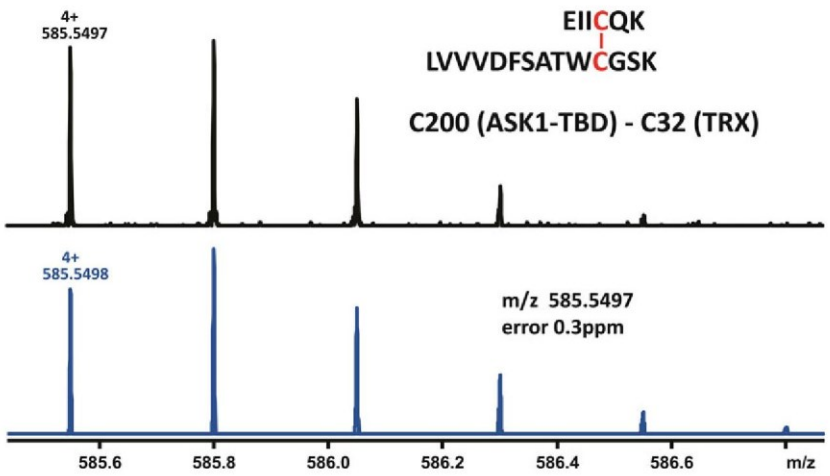

Fig. 9. Identification of the interprotein (ASK1-TBD:TRX1 C35,73S) disulfide bond. The upper spectrum shows detail of the isotopic envelope for quadruply charged ion at m/z 585.54966 corresponding to the ASK1-TBD:TRX1 C35,73S adduct peptide EIIC^{200}QK–LVVVDFSATWC^{32}GPSK. The lower spectrum (blue) shows the theoretical spectrum which together with very low mass error of the assignment (0.3 ppm) verifies unambiguous identification of the interprotein linkage.

Table 5. Binding affinities of ASK1-TBD Cys mutants for TRX1 WT in reducing conditions.

ASK1-TBD mutant	K_D, μM[a]
C185S	< 0.5
C200S	< 0.5
C206S	< 0.5
C225S	< 0.5
C226S	< 0.5
C250S[b]	50 ± 10

[a] K_D values and their uncertainties were determined by analyzing the isotherms of weight-averaged sedimentation coefficients (s_w isotherm) as a function of TRX1 concentration using the SEDPHAT software [30,31].

[b] This K_D value was reported in Kosek *et al.* [15] using the reduced TRX1 C73S mutant.

in reducing conditions (Table 1 and Fig. 2). Cysteine C32 is located just next to the tryptophan W31 which has also been shown to participate in TRX1 binding to ASK1-TBD, [15] thus further confirming that the catalytic W^{31}CGPC^{35} motif forms an important part of the ASK1-binding surface of TRX1. In comparison with cysteine C35, the residue C32 is located at the surface of TRX1 (Fig. 1A) and possesses a significantly lower pK_a (~ 6.7) [24]. Whether this is of importance for the interaction between TRX1 and ASK1-TBD is unclear but it is entirely possible that the thiolate of TRX1 cysteine C32 might be involved in either coulombic and/or sulfur–aromatic interactions with ASK1-TBD and the disulfide bond formation between C32 and C35 removes these interactions, thus destabilizing the complex.

Human TRX1 possesses three nonactive-site cysteines located at positions 62, 69, and 73, out of which C62 and C69 form an intramolecular disulfide bond under stronger oxidizing conditions and this disulfide bond formation is predicted to significantly affect TRX1 conformation by disrupting the helix α3 of TRX1 (Fig. 1A) [13,14]. Therefore, we next investigated whether this disulfide bond formation has any additional effect on binding affinity between oxidized TRX1 and ASK1-TBD. However, our binding affinity experiments revealed that TRX1 containing just one intramolecular disulfide bond between the catalytic cysteine residues (C73S mutant oxidized under low-ox conditions) binds to ASK1-TBD with the similar affinity as TRX1 containing two disulfide bonds (C73S mutant oxidized under high-ox conditions [15]) (Fig. 2F and Table 1). This suggests that (a) the intramolecular disulfide bond formation between C32 and C35 is the main factor responsible for the complex dissociation upon the oxidation of TRX1, and that (b) the region containing cysteines C62 and C69 (the helix α3, Fig. 1A) is not a part of the ASK1-TBD-binding surface of TRX1.

It has previously been suggested that the oxidation of ASK1 might also participate in the activation of ASK1 kinase function [19,25]. ASK1-TBD possesses seven conserved Cys residues, (Fig. 1B) thus it is reasonable to speculate that some of these residues might form intra- or intermolecular disulfide bond(s) under oxidative stress conditions. Since the structure of ASK1-TBD is still unknown, we first investigated the solvent accessibility of these residues. Since we

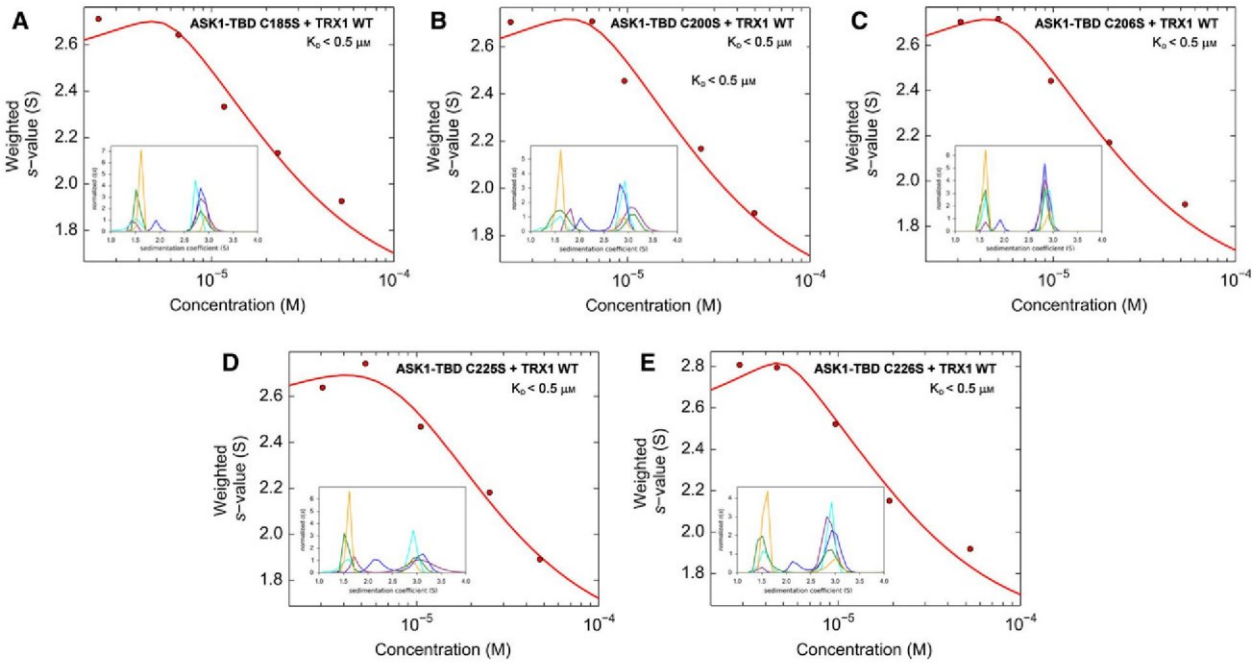

Fig. 10. Sedimentation velocity analytical ultracentrifugation analysis of complexes between reduced TRX1 WT and ASK1-TBD variants: ASK1-TBD C185S (A), ASK1-TBD C200S (B), ASK1-TBD C206S (C), ASK1-TBD C225S (D), and ASK1-TBD C226S (E). Isotherms of weight-averaged sedimentation coefficients s_w were obtained from SV AUC experiments of mixtures of ASK1-TBD (5 μM) and TRX1 WT (3–50 μM). The insets show the sedimentation coefficient distributions *c(s)* of mixtures of ASK1-TBD and TRX1 at various concentrations underlying the s_w data points (3 μM TRX1 blue, 5 μM TRX1 purple, 10 μM TRX1 cyan, 20 μM TRX1 green, 50 μM TRX1 orange).

expected sample with only partially blocked Cys residues and under classical proteomic digestion protocol (pH neutral to slightly basic) spontaneous disulfide bond formation can be a problem, we employed an alternative setup based on HDX-MS protocol. The advantages of this methodology include immediate sample processing at low pH and low temperature during the analysis. Under such conditions artificial disulfide bond scrambling can be ruled out. In addition, pepsin digestion using immobilized pepsin column provides a set of overlapping peptides and when properly tuned, full sequence coverage can be easily reached. Alkylation experiments revealed that residues C200, C206, and C250 are fully exposed to the solvent, whereas residue C120 is completely buried and residues C185 and one from the pair C225, C226 are just partially exposed to the solvent (Fig. 4). These differences are consistent with the previously published theoretical model of ASK1-TBD [15] which predicted that residues C120 and C185 are buried within the compact N-terminal part with the 3-layer α/β sandwich architecture, whereas residues C200, C206, C225, C226, and C250 are located at the periphery of ASK1-TBD (Fig. 1B). This theoretical model also indicated that residues C200 and C206, besides adjacent residues C225 and C226, are located close enough to each other to form a disulfide bond. Indeed, the analysis of ASK1-TBD oxidized under low-ox conditions suggested intramolecular disulfide bond formation C200–C206 and C225–C226 and to a small extent also C185–C200 and C225/C226–C250 (Figs 6 and 7). However, the functional impact of these changes is still unclear. We made an attempt to assess the binding affinity of oxidized ASK1-TBD for TRX1 using the catalytically inactive TRX1 C35,73S. However, the covalent adduct formation between these two proteins in the absence of reducing agents prevented the binding affinity measurement (Fig. 3B). Further analysis of this covalent adduct suggested that the catalytic site of TRX1 (residue C32) interacts with the ASK1-TBD region containing residue C200 (Fig. 9) which belongs to cysteines involved in intramolecular disulfide bonds formation (Fig. 6). Out of the residues forming disulfide bonds, only C250 is essential for the high-affinity binding of TRX1 to ASK1-TBD (Table 5). In addition, time-resolved fluorescence measurements with the tryptophan residue inserted at position 242 revealed that the oxidation of ASK1-TBD induces a significant conformational change in this region likely as a result of disulfide bonds formation (Table 4 and Fig. 8).

Thus, we can conclude that the disulfide bonds formation affects ASK1-TBD regions involved in and/or important for the TRX1 binding.

These findings allowed us to update the theoretical model of the ASK1-TBD:TRX1 complex [15]. The model was prepared using a rigid-body docking search with the theoretical model of ASK1-TBD alone [15] and the crystal structure of reduced TRX1 [17] used as a receptor and a ligand, respectively. The best scoring complex in which the TRX1 residue C32 was located close to the residue C200 of ASK1-TBD was further refined using the ALLOSMOD-FOXS program [26,27] to generate model consistent with the previously reported small angle X-ray scattering (SAXS) data of the ASK1-TBD:TRX1 complex [15]. The best scoring AllosMod model (Fig. 11A) is consistent with the SAXS data ($\chi = 0.78$, Fig. 11B) and predicts that the TRX1-binding site is located within the C-terminal half of ASK1-TBD containing cysteines C200, C206, C225, C226, and C250. The predicted ASK1-TBD-binding surface of TRX1 includes the active site with residues W31 and C32, the N-terminal part of helix α2, the loop between helix α3 and strand β3, and the C-terminal strand β4 and helix α4. The predicted TRX1-binding surface of ASK1-TBD also includes residue F242 which was replaced by tryptophan in mutant used for time-resolved fluorescence measurements, (Table 4 and Fig. 8) thus indicating that the observed oxidation-induced conformational change affects the TRX1-binding surface of ASK1-TBD.

Taken together, our results show that the residue C32 of reduced TRX1 is responsible for its high-affinity binding to ASK1-TBD. The disulfide bond formation between C32 and C35 is the main factor responsible for the complex dissociation upon the oxidation of TRX1. Cysteine residues of ASK1-TBD differ in solvent accessibility with C250 being the only cysteine which is both solvent exposed and essential for TRX1 binding in reducing conditions. Furthermore, our data show that the catalytic site of TRX1 interacts with ASK1-TBD region containing cysteine C200 and that the oxidative stress could induce intramolecular disulfide bonds formation within ASK1-TBD and affect its structure in regions directly involved and/or important for the TRX1 binding.

Materials and Methods

Preparation of ASK1-TBD and TRX1

Human ASK1-TBD (sequence 88-302) and human TRX1 were expressed and purified as described previously [15]. All mutants of ASK1-TBD and TRX1 were generated by using the QuikChange site-directed mutagenesis kit (Stratagene, La Jolla, CA, USA) and mutations were confirmed by sequencing.

Oxidation of ASK1-TBD and TRX1

Fully reduced ASK1-TBD, TRX1 WT, and TRX1 C73S (the complete reduction was confirmed by measuring the number of free thiol groups) were desalted on a Zeba™ Spin Desalting Column (Thermo Scientific, Prague, Czech Republic) equilibrated with 20 mM Tris-HCl (pH 7.5) and 200 mM NaCl. Proteins (15–20 μM) were oxidized by incubating with either 5-fold (low-ox conditions) or 100-fold (high-ox conditions) excess of H_2O_2 for 15 min at 37 °C [12]. Oxidation reaction was stopped by adding five units of catalase (Sigma Aldrich, Prague, Czech Republic).

Determination of total thiol groups

Protein free thiol quantitation Ellman's reagent (5,5′-Dithiobis-[2-nitrobenzoic acid];DTNB) assay was used to quantitate free cysteine residues [28]. Reduced or oxidized proteins (15–20 μM) in 20 mM Tris-HCl (pH 7.5) and 200 mM NaCl were incubated in the dark with 6 M guanidine hydrochloride and 1 mM DTNB (Sigma Aldrich) in a final volume of 350 μL of 200 mM Tris-HCl (pH 8.0). A molar extinction coefficient of TNB^{2-} anion of 13 600 M^{-1} cm^{-1} at 412 nm was used to calculate the number of free thiol groups.

Native alkylation of ASK1-TBD cysteine residues by iodoacetamide

Reduced ASK1-TBD (15–20 μM) in buffer containing 20 mM Tris-HCl (pH 7.5), 200 mM NaCl, and 5 mM DTT was mixed with 500 mM iodoacetamide stock solution in 20 mM Tris-HCl (pH 7.5) and 200 mM NaCl to yield a 5:1 molar ratio of iodoacetamide to DTT. The mixture was incubated in the dark for 30–60 min at room temperature and results of the alkylation reaction were analyzed by MS.

Mass spectrometry analysis of ASK1-TBD

Mass spectrometry techniques were used to analyze ASK1-TBD reduced, oxidized, alkylated under native-like conditions (preceding paragraph) or after non-native alkylation. This modification was done in 8 M urea and both reduced and oxidized ASK1-TBD were used for this modification. The proteins for intact mass measurement 15T FT-ICR mass spectrometer (Solarix XR, Bruker Daltonics, Billerica, MA, USA) were desalted using offline protein microtrap (Optimize Technologies, Oregon City, OR, USA) prior to the analysis. For the detailed analysis of disulfide bond linkages two sample preparation methods were used. First one employed LC system primarily designed for H/D

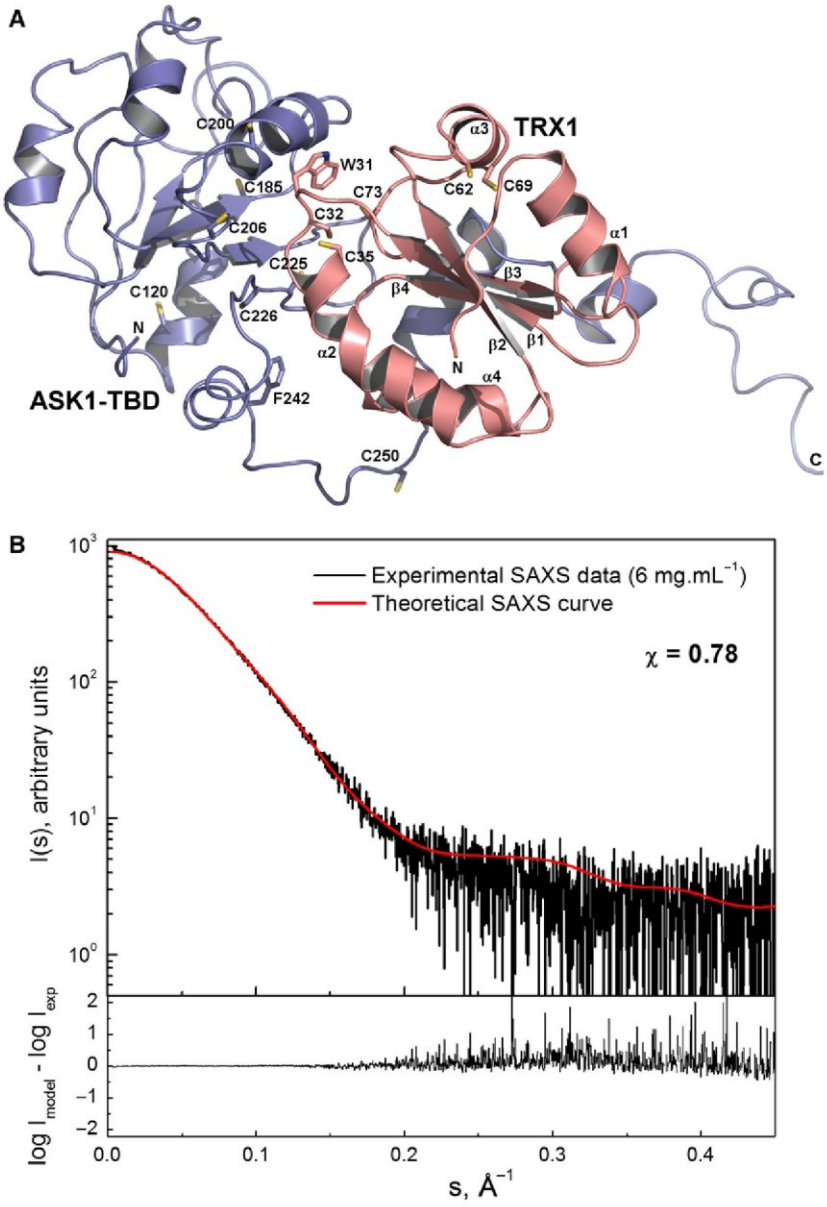

Fig. 11. Structural model of the ASK1-TBD:TRX1 complex. (A) The best scoring AllosMod model of the ASK1-TBD:TRX1 complex. The starting model of the complex for the AllosMod-FoXS simulation was obtained using the FRODOCK program [32]. AllosMod-FoXS [26,27] calculation was used to generate structure consistent with the previously reported SAXS data of the ASK1-TBD:TRX1 complex [15]. (B) Comparison of the calculated scattering curve of the best scoring AllosMod model of the ASK1-TBD:TRX1 complex (red line) with the previously reported scattering data of the complex at protein concentration 6 mg·mL^{-1} [15]. Theoretical scattering curve of the model was calculated using the FOXS program [33].

exchange [20]. Briefly the protein was acidified, mixed with guanidine hydrochloride (final concentration 3 M) and injected onto an immobilized pepsin column where it was digested. The resulting peptides were trapped on a reversed phase trap column (peptide MicroTrap, Optimize Technologies), desalted and after that separated on an analytical reversed phase column (Zorbax 300SB-C18 5 μm, 0.5 × 35 mm, Agilent Technologies, Santa Clara, CA, USA) by acetonitrile gradient from 10 to 25% in 8 min (0.4% formic acid was used as an ion pairing agent). Outlet of the column was connected to an ESI source of 15T FT-ICR mass spectrometer (Solarix XR, Bruker Daltonics) operating in data-dependent MS/MS mode. The data were searched by MASCOT algorithm against a single-protein database containing ASK1-TBD sequence. Based on the sample origin, some or all of the following modifications were considered as possible—formation of SS bonds, Cys carbamidomethylation, and methionine oxidation.

Alternatively, the ASK1-TBD was digested with trypsin (37 °C, 6 h). Peptide mixtures were loaded into vials and subjected to LC-MS/MS analysis. After quick online desalting the peptides were separated by an acetonitrile gradient (5–40% acetonitrile in 40 min, 0.2% formic acid was used as the ion pairing agent). The analytical column used for these analyses was Zorbax 300SB-C18 3.5 μm, 0.3 × 150 mm (Agilent Technologies). The data-dependent MS/MS data searching using MASCOT were done as described above. In addition, disulfide-linked peptides were

identified by Links algorithm based on the AUTOMATED SPECTRUM ASSIGNMENT Program [29]. Other data processing was done in DATAANALYSIS 4.4 (Bruker Daltonics).

Mass spectrometry analysis of the ASK1-TBD: TRX1 C35,73S adduct

The band corresponding to the ASK1-TBD:TRX1 C35,73S adduct was excised from the gel, destained, and modified with IAA. Trypsin digestion was carried out overnight at 37 °C. Peptide mixture was loaded into a vial and analyzed as described above for the trypsin digest of ASK1-TBD.

Analytical ultracentrifugation

Sedimentation velocity (SV) experiments were performed using a ProteomeLab™ XL-I analytical ultracentrifuge (Beckman Coulter, Brea, CA, USA). Samples were dialyzed against the buffer containing 20 mM Tris-HCl (pH 7.5), 200 mM NaCl and 5 mM 2-mercaptoethanol before analysis. Samples containing oxidized proteins were analyzed in the same buffer but without reducing agents. The buffer density, viscosity, and partial specific volume of all proteins were estimated using the program SEDNTERP (http://sednterp.unh.edu/). SV AUC experiments with ASK1-TBD, TRX WT, and their mutants were conducted at various loading concentrations and molar ratios in charcoal-filled Epon centerpieces with 12-mm optical path length at 20 °C and 185 462 ***g*** rotor speed (An-50 Ti rotor, Beckman Coulter). All sedimentation profiles were collected with interference and absorbance optics at 280 nm. The sedimentation coefficients $c(s)$ distributions were calculated from the raw interference data using SEDFIT software package. The procedure was followed by integration of calculated distributions to establish the weight-average s-values (s_w). Calculated s_w values were plotted as a function of TRX1 concentration to construct s_w isotherms. Obtained isotherms were fitted with $A + B \rightleftharpoons AB$ model as implemented in the SEDPHAT software package with previously known s values of each component. Resulting parameters were verified and loading concentrations were corrected using global Lamm equation modeling also implemented in the SEDPHAT software [30,31].

Differential scanning fluorimetry

The thermal shift assay was performed using a real-time PCR LightCycler 480 II (Roche Applied Science, Penzberg, Germany). The proteins at a concentration of 0.5 $mg \cdot mL^{-1}$ were incubated with 8× concentrated Sypro Orange (Sigma-Aldrich) in a total reaction volume of 25 μL in the LightCycler 480 Multiwell Plate 96 (Roche Applied Science). The plate was covered with the LightCycler 480 Sealing Foil (Roche Applied Science). Temperature gradient ranged from 20 to 95 °C with a rate of 0.01 $°C \cdot s^{-1}$ and fluorescence excitation and emission wavelength were 465 and 580 nm, respectively. The melting temperature values, T_m, corresponding to the minima of the negative first derivative of melting curves, were determined using the ROCHE LIGHTCYCLER 480 SW 1.5 software.

Time-resolved fluorescence measurements

Time-resolved tryptophan fluorescence intensity and anisotropy decay measurements as well as data analysis were performed as has been described previously [15]. Tryptophan emission was excited at 298 nm by a tripled output of the Ti:Sapphire laser. Tryptophan fluorescence was isolated at 355 nm by a combination of monochromator and a stack of UG1 and BG40 glass filters (Thorlabs, Newton, NJ, USA) placed in front of the input slit. All samples were blank-corrected and intensity decays were measured under the 'magic angle' conditions to remove rotational bias of the protein [22]. ASK1-TBD samples (15 μM) were placed in a thermostatic holder, and all experiments were performed at 23 °C in buffer containing 20 mM Tris-HCl (pH 7.5), 200 mM NaCl, and 1 mM EDTA. Samples measured under reduced conditions also contained 5 mM DTT.

Structural modeling of the ASK1-TBD:TRX1 complex

A rigid-body protein–protein docking search was performed using the FRODOCK program [32]. The theoretical model of ASK1-TBD [15] and the crystal structure of reduced TRX1 [17] were used as a receptor and a ligand, respectively. The AllosMod-FoXS server [26,27] was used to generate structure consistent with the previously reported SAXS data of the ASK1-TBD:TRX1 complex (at a protein concentration of 6 $mg \cdot mL^{-1}$) [15]. Theoretical scattering curve of the model was calculated using FoXS [33].

Acknowledgements

This work was supported by the Czech Science Foundation (Project 14-10061S), the Grant Agency of Charles University (Project 161116), and the Czech Academy of Sciences (Research Project RVO: 67985823 of the Institute of Physiology). Access to the MS facility was enabled through the following financial sources—EU project CZ.1.05/1.1.00/02.0109 and by the Czech Infrastructure for Integrative Structural Biology (LM2015043).

Author contributions

SK, DK, OP, and KP conducted most of the experiments and analyzed the results. PM performed LC-MS experiments, data analysis, and interpretation. PH and JV performed time-resolved fluorescence experiments,

data analysis, and interpretation. VO and TO conceived the idea for the project, analyzed the results, and wrote the manuscript.

Conflict of interest

The authors declare that they have no conflicts of interest with the contents of this article.

References

1 Ichijo H, Nishida E, Irie K, ten Dijke P, Saitoh M, Moriguchi T, Takagi M, Matsumoto K, Miyazono K & Gotoh Y (1997) Induction of apoptosis by ASK1, a mammalian MAPKKK that activates SAPK/JNK and p38 signaling pathways. *Science* **275**, 90–94.

2 Shiizaki S, Naguro I & Ichijo H (2013) Activation mechanisms of ASK1 in response to various stresses and its significance in intracellular signaling. *Advan Biol Regul* **53**, 135–144.

3 Kawarazaki Y, Ichijo H & Naguro I (2014) Apoptosis signal-regulating kinase 1 as a therapeutic target. *Expert Opin Ther Targets* **18**, 1–14.

4 Tobiume K, Saitoh M & Ichijo H (2002) Activation of apoptosis signal-regulating kinase 1 by the stress-induced activating phosphorylation of pre-formed oligomer. *J Cell Physiol* **191**, 95–104.

5 Saitoh M, Nishitoh H, Fujii M, Takeda K, Tobiume K, Sawada Y, Kawabata M, Miyazono K & Ichijo H (1998) Mammalian thioredoxin is a direct inhibitor of apoptosis signal-regulating kinase (ASK) 1. *EMBO J* **17**, 2596–2606.

6 Zhang L, Chen J & Fu H (1999) Suppression of apoptosis signal-regulating kinase 1-induced cell death by 14-3-3 proteins. *Proc Natl Acad Sci USA* **96**, 8511–8515.

7 Liu Y & Min W (2002) Thioredoxin promotes ASK1 ubiquitination and degradation to inhibit ASK1-mediated apoptosis in a redox activity-independent manner. *Circ Res* **90**, 1259–1266.

8 Fujino G, Noguchi T, Matsuzawa A, Yamauchi S, Saitoh M, Takeda K & Ichijo H (2007) Thioredoxin and TRAF family proteins regulate reactive oxygen species-dependent activation of ASK1 through reciprocal modulation of the N-terminal homophilic interaction of ASK1. *Mol Cell Biol* **27**, 8152–8163.

9 Liu H, Nishitoh H, Ichijo H & Kyriakis JM (2000) Activation of apoptosis signal-regulating kinase 1 (ASK1) by tumor necrosis factor receptor-associated factor 2 requires prior dissociation of the ASK1 inhibitor thioredoxin. *Mol Cell Biol* **20**, 2198–2208.

10 Hanschmann EM, Godoy JR, Berndt C, Hudemann C & Lillig CH (2013) Thioredoxins, glutaredoxins, and peroxiredoxins–molecular mechanisms and health significance: from cofactors to antioxidants to redox signaling. *Antioxid Redox Signal* **19**, 1539–1605.

11 Holmgren A, Soderberg BO, Eklund H & Branden CI (1975) Three-dimensional structure of *Escherichia coli* thioredoxin-S2 to 2.8 A resolution. *Proc Natl Acad Sci USA* **72**, 2305–2309.

12 Hashemy SI & Holmgren A (2008) Regulation of the catalytic activity and structure of human thioredoxin 1 via oxidation and S-nitrosylation of cysteine residues. *J Biol Chem* **283**, 21890–21898.

13 Watson WH, Pohl J, Montfort WR, Stuchlik O, Reed MS, Powis G & Jones DP (2003) Redox potential of human thioredoxin 1 and identification of a second dithiol/disulfide motif. *J Biol Chem* **278**, 33408–33415.

14 Cheng Z, Zhang J, Ballou DP & Williams CH Jr (2011) Reactivity of thioredoxin as a protein thiol-disulfide oxidoreductase. *Chem Rev* **111**, 5768–5783.

15 Kosek D, Kylarova S, Psenakova K, Rezabkova L, Herman P, Vecer J, Obsilova V & Obsil T (2014) Biophysical and structural characterization of the thioredoxin-binding domain of protein kinase ASK1 and its interaction with reduced thioredoxin. *J Biol Chem* **289**, 24463–24474.

16 Qin J, Clore GM & Gronenborn AM (1994) The high-resolution three-dimensional solution structures of the oxidized and reduced states of human thioredoxin. *Structure* **2**, 503–522.

17 Weichsel A, Gasdaska JR, Powis G & Montfort WR (1996) Crystal structures of reduced, oxidized, and mutated human thioredoxins: evidence for a regulatory homodimer. *Structure* **4**, 735–751.

18 Zhang R, Al-Lamki R, Bai L, Streb JW, Miano JM, Bradley J & Min W (2004) Thioredoxin-2 inhibits mitochondria-located ASK1-mediated apoptosis in a JNK-independent manner. *Circ Res* **94**, 1483–1491.

19 Nadeau PJ, Charette SJ & Landry J (2009) REDOX reaction at ASK1-Cys250 is essential for activation of JNK and induction of apoptosis. *Mol Biol Cell* **20**, 3628–3637.

20 Kadek A, Mrazek H, Halada P, Rey M, Schriemer DC & Man P (2014) Aspartic protease nepenthesin-1 as a tool for digestion in hydrogen/deuterium exchange mass spectrometry. *Anal Chem* **86**, 4287–4294.

21 Johnson ML (2008) Nonlinear least-squares fitting methods. *Methods Cell Biol* **84**, 781–805.

22 Lakowicz JR (1999) Principles of Fluorescence Spectroscopy, 2nd edn. Kluwer Academic/Plenum Publishers, New York.

23 Balmer Y, Vensel WH, Tanaka CK, Hurkman WJ, Gelhaye E, Rouhier N, Jacquot JP, Manieri W, Schurmann P, Droux M *et al.* (2004) Thioredoxin links redox to the regulation of fundamental processes of plant mitochondria. *Proc Natl Acad Sci USA* **101**, 2642–2647.

24 Kallis GB & Holmgren A (1980) Differential reactivity of the functional sulfhydryl groups of cysteine-32 and cysteine-35 present in the reduced form of thioredoxin from *Escherichia coli*. *J Biol Chem* **255**, 10261–10265.
25 Nadeau PJ, Charette SJ, Toledano MB & Landry J (2007) Disulfide Bond-mediated multimerization of Ask1 and its reduction by thioredoxin-1 regulate H(2)O (2)-induced c-Jun NH(2)-terminal kinase activation and apoptosis. *Mol Biol Cell* **18**, 3903–3913.
26 Weinkam P, Pons J & Sali A (2012) Structure-based model of allostery predicts coupling between distant sites. *Proc Natl Acad Sci USA* **109**, 4875–4880.
27 Schneidman-Duhovny D, Hammel M & Sali A (2010) FoXS: a web server for rapid computation and fitting of SAXS profiles. *Nucleic Acids Res* **38**, W540–W544.
28 Ellman GL (1959) Tissue sulfhydryl groups. *Arch Biochem Biophys* **82**, 70–77.
29 Young MM, Tang N, Hempel JC, Oshiro CM, Taylor EW, Kuntz ID, Gibson BW & Dollinger G (2000) High throughput protein fold identification by using experimental constraints derived from intramolecular cross-links and mass spectrometry. *Proc Natl Acad Sci USA* **97**, 5802–5806.
30 Dam J, Velikovsky CA, Mariuzza RA, Urbanke C & Schuck P (2005) Sedimentation velocity analysis of heterogeneous protein-protein interactions: Lamm equation modeling and sedimentation coefficient distributions c(s). *Biophys J* **89**, 619–634.
31 Schuck P (2000) Size-distribution analysis of macromolecules by sedimentation velocity ultracentrifugation and lamm equation modeling. *Biophys J* **78**, 1606–1619.
32 Garzon JI, Lopez-Blanco JR, Pons C, Kovacs J, Abagyan R, Fernandez-Recio J & Chacon P (2009) FRODOCK: a new approach for fast rotational protein-protein docking. *Bioinformatics* **25**, 2544–2551.
33 Schneidman-Duhovny D, Hammel M, Tainer JA & Sali A (2013) Accurate SAXS profile computation and its assessment by contrast variation experiments. *Biophys J* **105**, 962–974.
34 Vecer J & Herman P (2011) Maximum entropy analysis of analytically simulated complex fluorescence decays. *J Fluorescen* **21**, 873–881.